08:32:52 OCA PAD AMENDMENT - PROJECT HEADER INFORMATION 09/20/90

Active

Project #: E-21-F50 Cost share #: Rev #: 2
Center # : 10/24-6-R6776-1A0 Center shr #: OCA file #:
Work type : RES
Contract#: 1 R03 EY08402-01 Mod #: Document : GRANT
Prime #: Contract entity: GTRC

Subprojects ? : N
Main project #:

Project unit: ELEC ENGR Unit code: 02.010.118
Project director(s):
RHODES W T ELEC ENGR (404)894-2929

Sponsor/division names: DHHS/PHS/NIH / NATL INSTITUTES OF HEALTH
Sponsor/division codes: 108 / 001

Award period: 890801 to 910731 (performance) 911031 (reports)

Sponsor amount	New this change	Total to date
Contract value	0.00	36,239.00
Funded	0.00	36,239.00
Cost sharing amount		0.00

Does subcontracting plan apply ?: N

Title: CORNEAL ENDOTHELIUM EVALUATION BY FOURIER TRANSFORMS

PROJECT ADMINISTRATION DATA

OCA contact: Kathleen R. Ehlinger 894-4820

Sponsor technical contact	Sponsor issuing office
PETER A.DUDLEY, PH.D.	GAYE LYNCH
(301)496-5884	(301)496-5884
EXTRAMURAL PROGRAM DIRECTOR	GRANTS MANAGEMENT SPECIALIST
CORNEAL DISEASES PROGRAM	EXTRAMURAL SERVICES BRANCH
NATIONAL EYE INSTITUTE	NATIONAL EYE INSTITUTE

Security class (U,C,S,TS) : U ONR resident rep. is ACO (Y/N): N
Defense priority rating : N/A NIH supplemental sheet
Equipment title vests with: Sponsor GIT X

Administrative comments -
ISSUED TO EXTEND TERMINATION DATE FROM 7/31/90 TO 7/31/91.

GEORGIA INSTITUTE OF TECHNOLOGY
OFFICE OF CONTRACT ADMINISTRATION

NOTICE OF PROJECT CLOSEOUT

Closeout Notice Date 06/22/92

Project No. E-21-F50_____ Center No. 10/24-6-R6776-1A0_

Project Director RHODES W T_____ School/Lab ELEC ENGR_____

Sponsor DHHS/PHS/NIH/NATL INSTITUTES OF HEALTH_____

Contract/Grant No. 1 R03 EY08402-01_____ Contract Entity GTRC

Prime Contract No. _____

Title CORNEAL ENDOTHELIUM EVALUATION BY FOURIER TRANSFORMS_____

Effective Completion Date 910731 (Performance) 911031 (Reports)

Closeout Actions Required:	Y/N	Date Submitted
Final Invoice or Copy of Final Invoice	Y	911113
Final Report of Inventions and/or Subcontracts	Y	_____
Government Property Inventory & Related Certificate	N	_____
Classified Material Certificate	N	_____
Release and Assignment	N	_____
Other _____	N	_____

Comments_____
_____

Subproject Under Main Project No. _____

Continues Project No. _____

Distribution Required:

Project Director	Y
Administrative Network Representative	Y
GTRI Accounting/Grants and Contracts	Y
Procurement/Supply Services	Y
Research Property Managment	Y
Research Security Services	N
Reports Coordinator (OCA)	Y
GTRC	Y
Project File	Y
Other _____	N
_____	N

NOTE: Final Patent Questionnaire sent to PDPI.

CORNEAL ENDOTHELIUM EVALUATION BY FOURIER TRANSFORMS

Final Report to the National Institutes of Health
on Contract No. R03 EY08402-01

Prepared by

William T. Rhodes, Ph.D.
School of Electrical Engineering
Georgia Institute of Technology
Atlanta, Georgia 30332-0250
(404) 894-2929

Abstract

There is a need for efficient and reliable evaluation of the shape, size, orientation, density, and regularity of the cells of the endothelial layer of the cornea. High speed parallel opto-electronic methods were investigated for performing such evaluation. A coherent optical Fourier transform system was used to obtain the Fraunhoffer pattern associated with edge-enhanced cell patterns. This pattern was sampled by a wedge-ring detector and functions relating to angular and radial characteristics calculated. These were used in successful evaluation of cell density and shape. A nonlinear image processing algorithm was developed for enhancing the raw endothelial cell imagery and preparing it for use in the Fourier transforming system. The algorithm, based on a parallel optical convolver using a rotating kernel, can be applied to a variety of image enhancement and pattern recognition operations.

I. Introduction

Motivation for this research arose from the need for efficient and reliable evaluation of the shape, size, orientation, density, and regularity of the cells of the endothelial layer of the cornea. It is thought by ophthalmologists that associated statistics can be used as an important tool in the diagnosis of corneal endothelial tissue in normal and pathological conditions. The purpose of the research was to conduct preliminary investigations of hybrid optical/digital methods for enhancing raw endothelial cell imagery and for obtaining the desired statistical measures in near real time. The proposed effort included the development of realtime analysis techniques for cell size and shape statistics based on both global and regional analysis; a comparison of regional and global morphological statistics; the development of parallel optical preprocessing techniques for enhancing cell-boundary definition; and preliminary characterization of hardware and software for general analysis of ophthalmic imagery.

II. Summary of Research Results

The results of the research program are reported in detail in two attachments. The first is entitled "Fourier Transform Method for Statistical Evaluation of Corneal Endothelial Morphology," by Barry R. Masters, Yim-Kul Lee, and William T. Rhodes, published in **Noninvasive Diagnostic Techniques in Ophthalmology**, B. Masters, ed. (Springer-Verlag, 1990), Chapter 8 (pp. 122-141). The second is the doctoral dissertation, "Nonlinear Image Processing and Pattern Analysis by Rotating Kernel Transformation and Optical Fourier Transform," by Yim Kul Lee. A brief summary of the key results are presented in the following sections.

A. Pattern Analysis by Optical Fourier Transform

In preliminary studies, high-contrast tracings of human endothelial widefield specular images were obtained from Keeler Instruments. These were used as inputs to an optical Fourier transforming system, which produced as output Fraunhoffer diffraction patterns of the illuminated region of the tracings. The diffraction patterns were sampled, and weighted sums of the sample values taken to emphasize radial and azimuthal structures in the patterns. Results of the preliminary study, summarized in Attachment 1 and in Chapter 2 of Attachment 2, indicated clearly that the Fourier transforms can be analyzed to yield average cell size as well as the distribution of sizes. However, it was also made clear in this preliminary study that raw endothelial cell imagery is not satisfactory to use as input to the Fourier transform system, because of noise and low contrast. It is imperative that the raw imagery undergo some enhancement to delineate the boundaries between cells. For this purpose, the rotating kernel min-max transformation, discussed next, was developed.

B. Rotating Kernel Min-Max Transformation

The rotating kernel min-max transformation (RKMT) is a nonlinear image processing operation particularly well suited to enhancing straight line structures in noisy imagery. The operation, which was invented in the course of this research, is well suited to high-speed parallel implementation with a hybrid opto-electronic image processing system. In this operation an input image is convolved with a long, narrow kernel which is rotated through 360 degrees, either continuously or discretely in a large number of small steps. As the kernel rotates, the output of the convolver is monitored and the minimum and maximum result at each point are recorded. The output of the transformation is some function f(max,min) of those maximum and minimum values at each point. A wide variety of kernels can be combined with a wide variety of nonlinear functions f(.,.) for image enhancement operations. A number of variations on the basic RKMT algorithm were studied. The RKMT is discussed in detail in Chapter 3 of Attachment 2.

C. Nonlinear Preprocessing of Imagery

The RKMT was successfully applied to the enhancement of the cell boarders in raw endothelial cell imagery and to the location of the vertices of the cell structures (see p. 51 and Chapter 4 of Attachment 2). Methods for binarizing the enhanced images were then studied and comparisions made with alternative enhancement methods.

D. Invariant Pattern Recognition

Investigation of the RKMT methodology led to the invention of a new means for characterizing objects that is invariant to object scale and orientation angle. The so-called angular signature method is discussed in Chapter 5 of Attachment 2. Although it was not studied in detail, it holds promise for some forms of scale- and orientation-invariant pattern recognition operations.

E. Edge Detection and Enhancement

Edge detection and enhancement represent logical extensions of the cell border enhancement operations performed on the endothelial cell imagery. Chapter 6 of Attachment 2 presents general results on such application of the RKMT operation, both for grayscale and binary edge structures.

III. Concluding Remarks

Because of the clear need for enhancement preprocessing of the endothelial cell imagery, the research program did not go as far as originally planned in the direction of highspeed opto-electronic systems to implement the statistical analysis operations. On the other hand, the development of the rotating kernel image processing operations and associated applications represents a very significant step in the general development of

nonlinear image processing algorithms.

Important research has followed that conducted under this grant. Of particular significance is work presented in the paper "Morphological Image Processing and Network Analysis of Cornea Endothelial Cell Images," by Luc Vincent and Barry Masters, to appear in Proceedings of the SPIE, Vol. 1769, Image Algebra and Morphological Image Processing III (published by SPIE, Bellingham, Washington), July 1992. This paper introduces remarkably successful morphological methods for enhancing the raw endothelial cell imagery and associated network analysis tools for extracting the desired statistical information.

IV. Publications and Presentations Resulting from Research

1. Yim-Kul Lee and William T. Rhodes, "Nonlinear image processing by a rotating kernel transformation," **Optics Letters**, vol. 15, No. 23 (1 December 1990), pp. 1383-1385.

2. Yim-Kul Lee and William T. Rhodes, "Feature Detection and Enhancement by a Rotating Kernel Min-Max Transformation," in **Hybrid Image & Signal Processing II**, D. Casasent and A. Tescher, eds. (Proc. SPIE, Vol. 1297, 1990), pp.

3. Yim-Kul Lee and William T. Rhodes, "Scale- and Rotation-Invariant Pattern Recognition by a Rotating Kernel Min-Max Transformation," in **Optical Information Processing Systems and Architectures II**, B. Javidi, ed. (Proc. SPIE, Vol. 1347, 1990), pp.

4. Barry R. Masters, Yim-Kul Lee, and William T. Rhodes, "Fourier transform method to determine human corneal endothelial morphology," Presented at OELASE'90 SPIE Conference, paper No. #1239.

5. Barry R. Masters, Yim-Kul Lee, and William T. Rhodes, "Fourier Transform Method for Statistical Evaluation of Corneal Endothelial Morphology," in **Noninvasive Diagnostic Techniques in Ophthalmology**, Barry R. Masters, ed. Springer-Verlag, 1990

6. Yim-Kul Lee and William T. Rhodes, "Edge Enhancement by Hybrid Optical Rotating Kernel Min-Max Transformation," presented at the Optical Society of America 1990 Annual Meeting (1990 Technical Digest Series, Vol. 15, p. 142).

7. Yim-Kul Lee, **Nonlinear Image Processing and Pattern Analysis by Rotating Kernel Transformation and Optical Fourier Transform**, Ph.D. Dissertation, Georgia Institute of Technology, December 1990.

ATTACHMENT 1

Fourier Transform Method for Statistical Evaluation of Corneal Endothelial Morphology, by Barry R. Masters, Yim-Kul Lee, and William T. Rhodes, from **Noninvasive Diagnostic Techniques in Ophthalmology** (Springer, New York, 1990), Chapt. 8.

CHAPTER 8

Fourier Transform Method for Statistical Evaluation of Corneal Endothelial Morphology

BARRY R. MASTERS, YIM-KUL LEE, and WILLIAM T. RHODES

The human cornea is about 0.52 mm thick at its center. It is composed of several layers, the innermost being the endothelium, which is a single layer of cells in contact with the aqueous humor. The endothelium consists of some 350,000 to 500,000 polygonal cells, approximately 5 mm thick, with straight-sided borders about 20 μm across. In a newborn baby the cells are almost all hexagonal and close-packed[1]; the cell density is approximately 4500 cells/sq mm. By the ninth decade of life the cell density can decrease to fewer than 1000 cells/sq mm, and the hexagons are less regular and mixed in with pentagons, heptagons, and other polygonal shapes.[2-4]

Specular microscopy, a routine clinical tool for in vivo evaluation of the cornea, provides qualitative and quantitative information on the morphology of the corneal endothelium.[5-7] (Evaluation of cell function requires other types of analysis, such as redox fluorometry.[8,9]) Photographs are made of the endothelium using a flash lamp; alternatively, the images are detected with a video system connected to video cassette recorder. In the latter case the video monitor is photographed to obtain the endothelial images. The negatives are enlarged, and the cell boundaries are traced. Usually a fraction of the cells in the print have indistinct cell boundaries, which must be filled in by hand. A digitizing pad is used to digitize the cell borders, and a computer program then calculates the following parameters: number of cells, average cell area, cell density, cell perimeter, coefficient of variation (CV; given by the standard deviation divided by the mean) of the cell area, percent of cells that are hexagons, and the border length per square millimeter. The variation in cell size (polymegethism) and cell shape (pleomorphism) are determined from histograms of cell size and shape.[10]

Quantitative information is obtained from manual digitization of the images or through automated morphometric analysis.[11-16] Automated analysis works best for high-contrast, wide-field specular images. Several systems are available for automated endothelial analysis, most requiring human intervention for 5 to 10% of the cells. All of the analytic methods treat the endothelial cells as discrete independent entities without consideration of cell position or neighborhood. This method is analogous to cutting out the individual endothelial cells on a specular photomicrograph, mixing them, and randomly choosing a particular cell for analysis. The average morphologic parameters are obtained from an arithmetic mean of the parameters of the individual cells. This approach removes all spatial information about the global cellular pattern and effectively randomizes the positions of the cells. There is thus no possibility of obtaining correlative information between individual cells as a function of position, size, shape, and orientation. Because there is a reasonable possibility that such information has diagnostic value, and because existing morphometric analysis methods

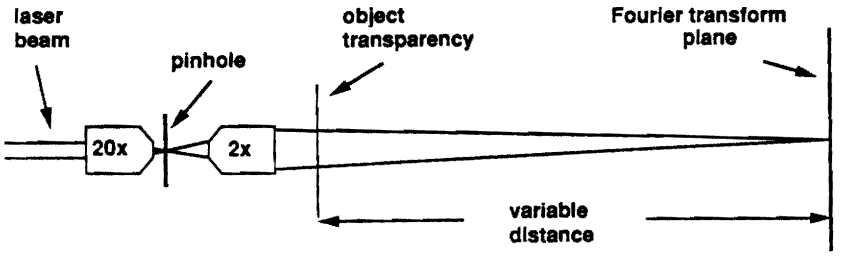

FIGURE 8.1. Optical system for evaluating Fourier transform distributions. A phototransparency of the input pattern is illuminated by a converging light beam from a helium-neon laser. The squared magnitude (intensity) of the Fourier transform distribution appears in the plane of convergence for the beam.

are relatively slow, an alternative approach to cell morphometrology is under development in our laboratory.

The method is based on an analysis of the two-dimensional (2-D) Fourier transform of the cell-boundary pattern.[17] Preliminary results indicate that the method can provide reliable measures of average cell size, cell size variation, and angular orientation characteristics of the cell patterns indicative of the mixture of polygonal shapes. Of particular importance, the method is capable of being implemented essentially in real-time using opto-electronic techniques. In addition, the method can be used equally well for both local and global morphologic measures of cell characteristics.

In the following sections the 2-D Fourier transform is reviewed and those characteristics that are particularly well suited for the endothelial cell measurements are discussed. Basic methods and results are outlined, the method and its possible extensions are discussed, and an opti-electronic system for making the measurements at high speed is described.

Characteristics of Fourier Transforms

The 2-D Fourier transform F(u,v) of an image distribution f(x,y) is given by

$$F(u,v) = \int_{-\infty}^{\infty} f(x,y)\exp[-i2\pi(ux + vy)dxdy \quad (1)$$

where i denotes the square root of -1.[18] In shorthand notation, $f(x,y) \rightarrow F(u,v)$. If x and y have units of distance, then u and v have units of cycles per unit distance, or spatial frequency. The 2-D Fourier transform provides a measure of the spatial frequency content of the image. The Fourier transform is generally complex valued; however, in signal or image analysis, what is typically measured is the magnitude $|F(u,v)|$ or its square. The squared magnitude is often referred to as the Fourier *intensity distribution*. The Fourier transform can be obtained using either a digital computer or an optical system similar to the one illustrated in Figure 8.1.

The Fourier-transforming optical system, which operates in accord with the laws of diffraction of light waves, has the advantage of performing the computation virtually instantaneously.[19,20] The system we use to obtain such optical transforms employs a 2 mW HeNe laser for the light source. A 20× microscope objective is used to bring the beam down to a small point, which is focused onto a 25-mm pinhole to remove light scattered by dust on the laser output window. After expanding to a diameter of approximately 6 mm, the laser beam is passed through a 2× objective, which focuses the beam to a spot on an observation screen 2 meters away. It is in this plane that the Fourier transform distributions are observed and photographed when a photo transparency of the input pattern is placed in the beam near the 2× objective end. By moving the transparency closer to or farther away from the observation plane, the Fourier transform is made smaller or larger. If necessary, the film transparency can be immersed in a refractive-index-matching liquid (xylene), which reduces

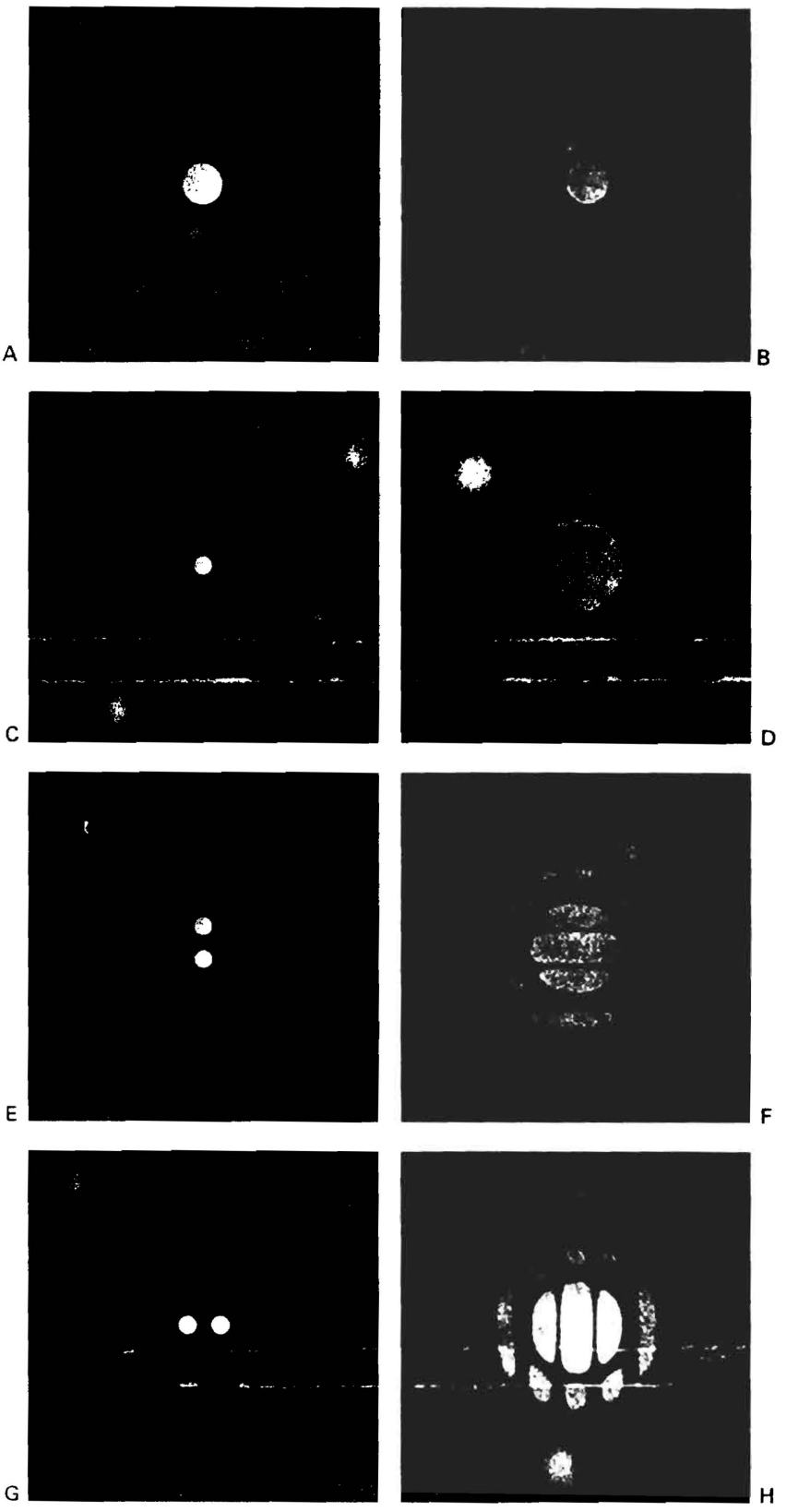

FIGURE 8.2. Examples of Fourier transforms obtained with an optical system. Input patterns appear on the

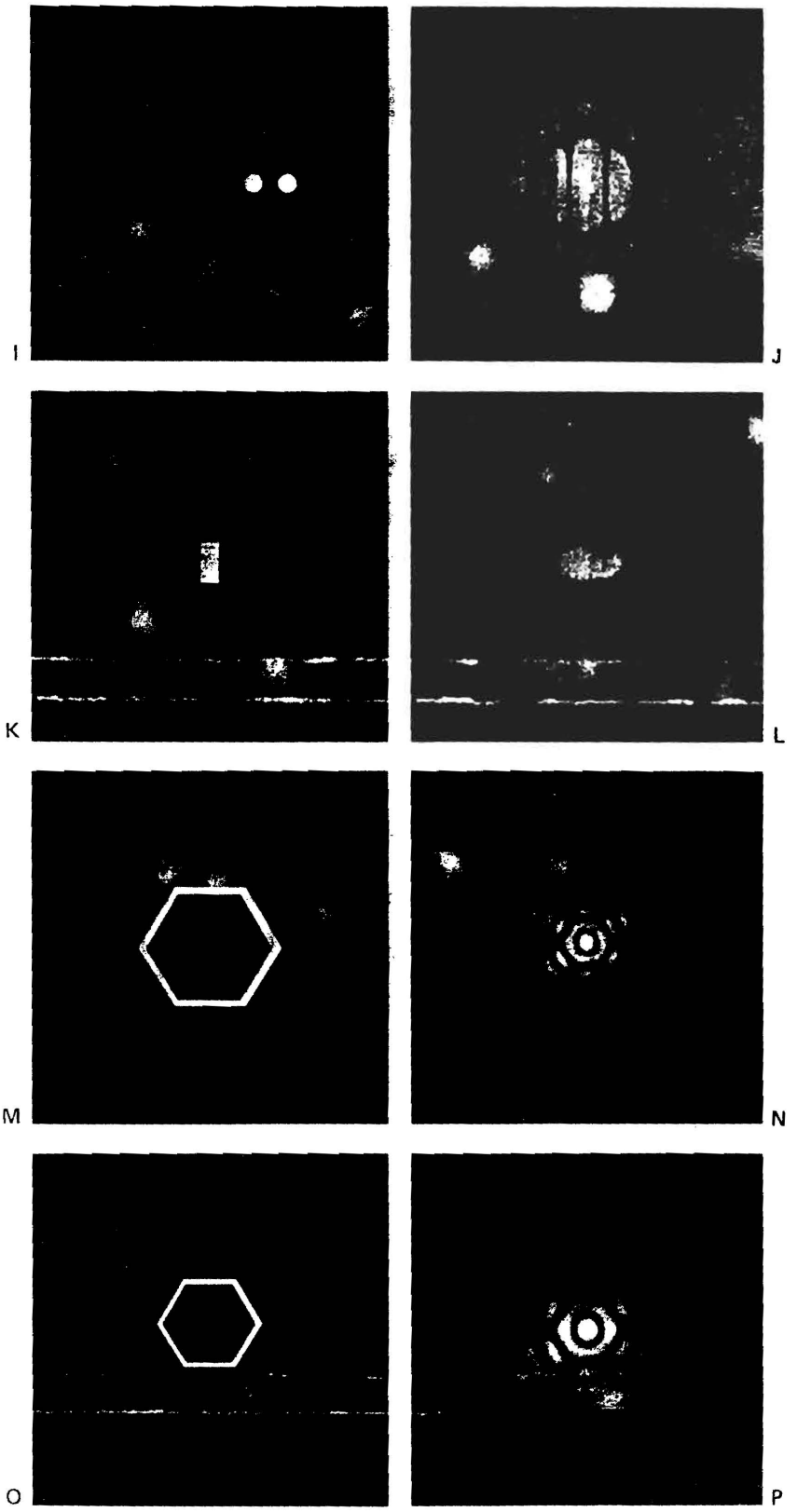

left. Fourier transforms on the right. Note that all Fourier transform intensity patterns are symmetric through the origin.

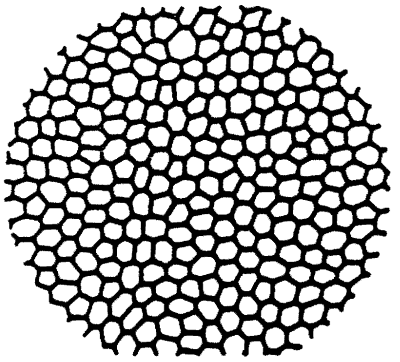

A

FIGURE 8.3. Typical endothelial cell boundary tr
ing (**A**) and examples of Fourier transform inten
patterns from such tracings. Patterns **B** through
were obtained optically. Patterns **G** and **H** (showr
a different scale) were obtained digitally. In
cases, the cell size CV was 0.2. Average cell den
was, respectively, 1000, 1500, 2000, 2500, and 3
cells/sq mm for **B** to **F** and 1000 and 3000 cells/sq r
for **G** and **H** (see page 128).

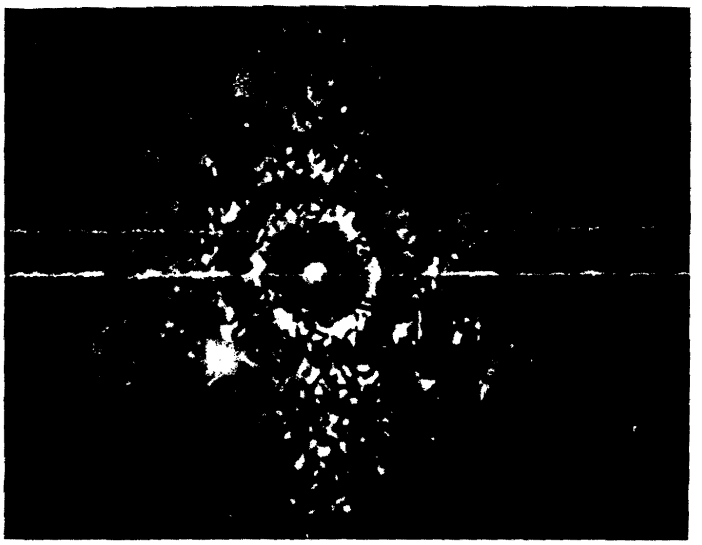

B

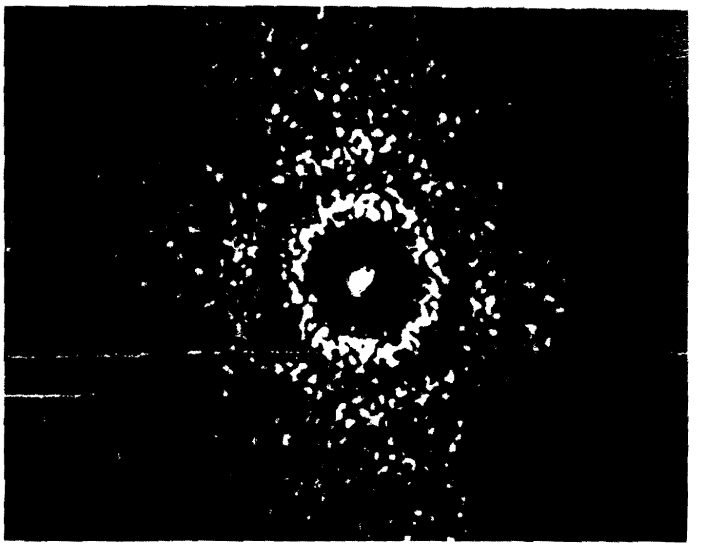

C

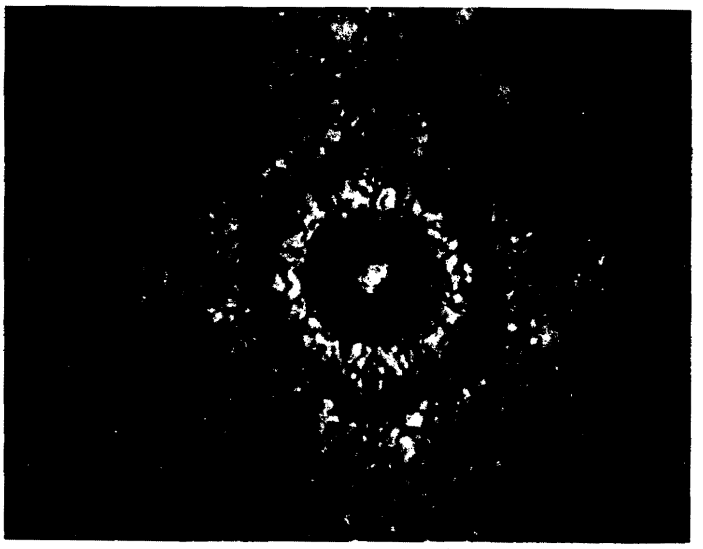

D

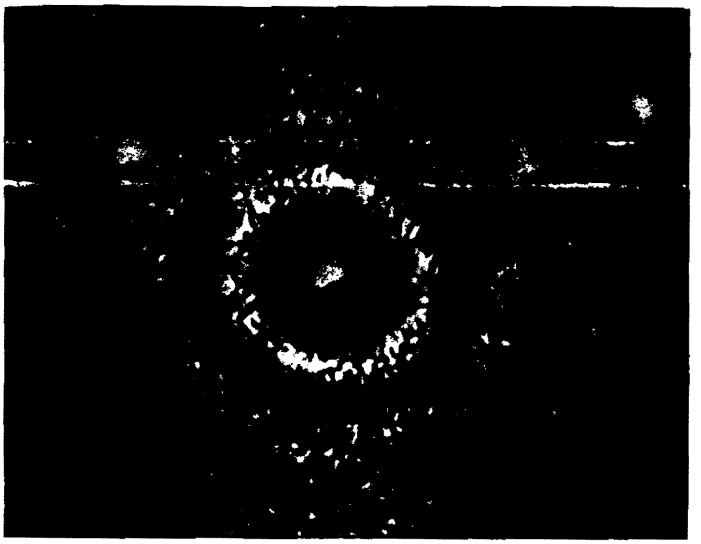

E

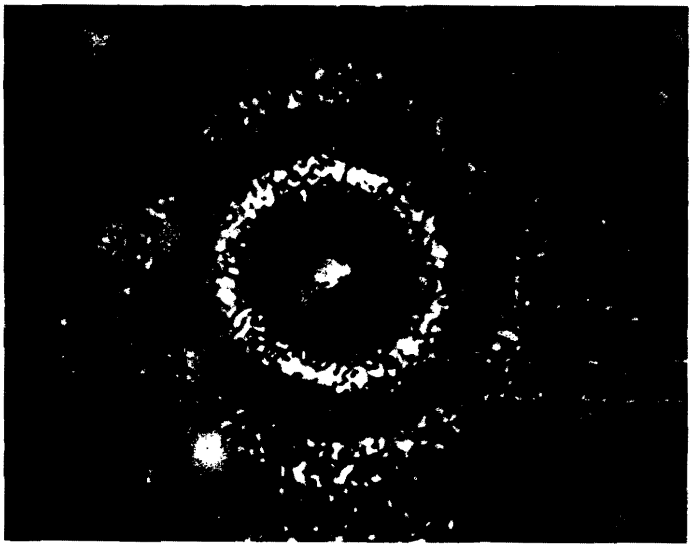

F

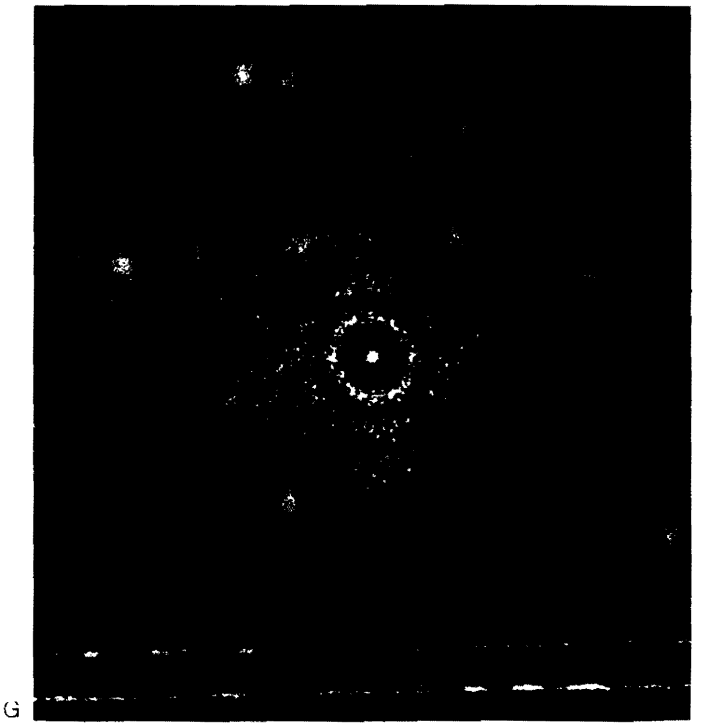

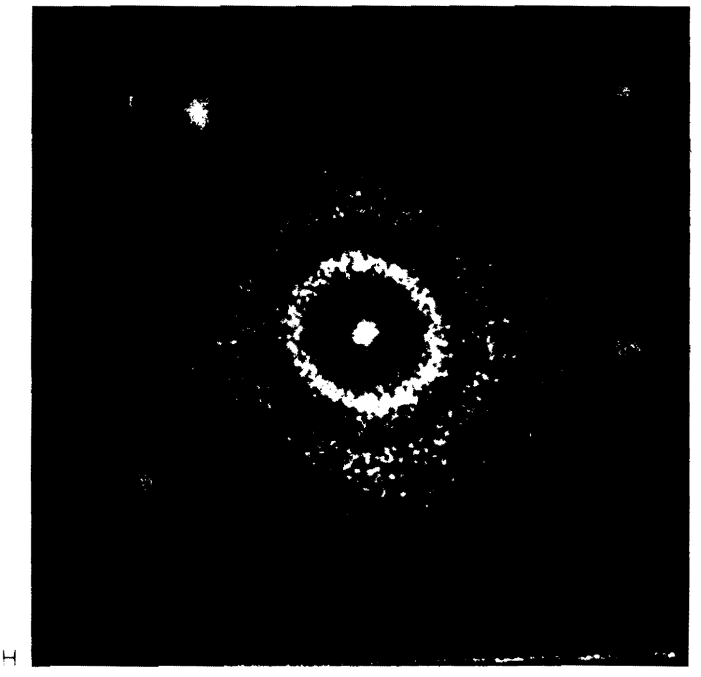

FIGURE 8.3.

or eliminates the effects of film emulsion thickness variations on the recorded Fourier intensities.[19] Such systems have been applied successfully in the past to a variety of inspection and pattern characterization operations.[20,21,23–26] Examples of Fourier transforms obtained optically are shown in Figure 8.2. Numerous other examples can be found in refs. 22 and 27.

Several characteristics, or properties, of the Fourier transform,[18] some of which are evident in Figure 8.2, are particularly important to the cell measurement problem.

1. The magnitude of the Fourier transform is insensitive to change in position of the input image. Thus f(x,y) and f(x − a, y − b) yield the same intensity pattern $|F(u,v)|^2$, illustrated by the patterns in Figure 8.2 (g) and (i) and their respective transforms.
2. There is an inverse scale relation between an image and its Fourier transform; specifically, if f(x,y) transforms to F(u,v), the Fourier transform of f(ax,by) is proportional to F(u/a,v/b). This characteristic is seen clearly by comparing the Fourier transform pair illustrated in Figure 8.2 (a) and (b) with that in (c) and (d). Similarly, compare (m) and (n) with (o) and (p).
3. Rotation of the input image produces rotation of its Fourier transform through the same angle. In Figure 8.2 compare (e) and (f) with (g) and (h).
4. The Fourier transform of a real-valued input (all image distributions are real-valued) has a symmetric magnitude. Thus for a real input, the Fourier intensity $|F(u,v)|^2$ is symmetric about the origin. This characteristic is evident throughout Figure 8.2.

Of special interest are (n) and (p) in Figure 8.2, which show the Fourier transform intensities of hexagonal cells. Note that there is a bright central lobe surrounded by dark and bright rings. Through property 2 (above), the mean diameters of the rings are in inverse proportion to the sizes of the hexagons and can thus be used to estimate hexagon size. In addition, the distributions show spoked patterns that relate to the orientation of the sides of the hexagons. This characteristic can also be exploited, as discussed below.

The feasibility of using Fourier transforms to evaluate corneal endothelial cell patterns was first proposed by Masters.[17] The basic thesis presented was that the Fourier transform of the cell border tracings could serve to measure global shape characteristics of the cells, including average size, and thus provide clinically useful diagnostic information. The following section provides evidence, based on subsequent investigation, that the Fourier transform patterns do indeed contain useful and easily evaluated information on endothelial cell morphology.

Methods and Results

High-contrast tracings of human endothelial widefield specular images were obtained from Keeler Instruments. Each panel had a different coefficient of variation, and cell density varied from 1000 to 3000 cells/sq mm. A section of a typical cell tracing is shown in Figure 8.3A. Fourier transform intensity patterns obtained for different cell tracings are shown in the remainder of Figure 8.3. Those in Figure 8.3B–F were obtained using the optical system of Figure 8.1. Groups of approximately 50 cells served as the input patterns for obtaining these Fourier transform distributions. The coefficient of variation of cell size was the same in all cases (0.2), but the average cell density differed. Note the increase in diameter of the now speckled ring patterns as the cell density goes up. Photographs of the Fourier transform intensity patterns were scanned and digitized in a 512×512 sample format using an image scanner connected to a MegaVision XM1024 digital image processor. Care was taken to ensure that the zero spatial frequency point (the origin of the u,v coordinate system) was correctly centered in the field of view of the MegaVision system. For comparison, several cell tracings (again with a coefficient of size variation of 0.2) were also scanned and digitized and their Fourier transform distributions calculated digitally. The resultant transform

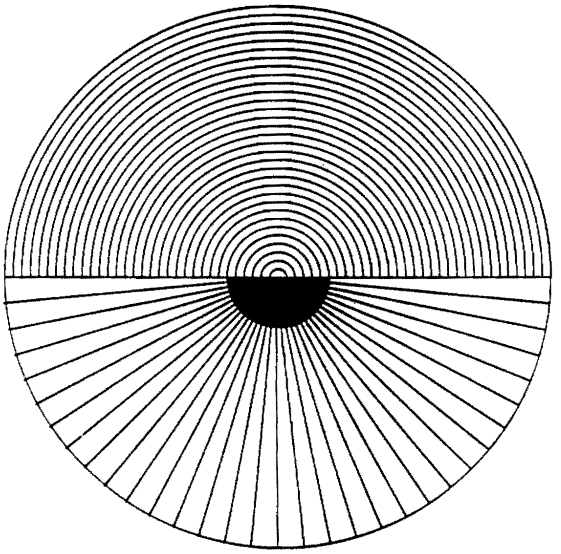

FIGURE 8.4. Wedge-ring mask for calculating angular and radial projection coefficients in Fourier space. Only 32 of the 64 wedges and semiannular rings are shown. Because the Fourier intensity distribution is symmetric through the origin, the pattern sampled by the wedges is the same as the pattern sampled by the annular rings.

patterns are shown in Figure 8.3G, H to slightly different scale.

To reduce the amount of data to a manageable amount, we worked with the theta projection of $|F(u,v)|^2$, given by

$$P_\theta(\theta) = \int_0^\infty |F_p(r,\theta)|^2 dr \qquad (2)$$

where $F_p(r,\theta)$ denotes the Fourier transform expressed in polar coordinates. A discretized version, appropriate for the sampled computer distributions, was obtained by calculating the average Fourier intensity within wedge-shaped areas such as those shown in Figure 8.4. The result was a set of 64 numbers (Q_n) given by

$$Q_n = \frac{1}{N_n} \int_{(n-1)\Delta\theta}^{n\Delta\theta} \int_0^\infty |F_p(r,\theta)|^2 \, r \, dr \, d\theta,$$

$$1 \leq n \leq 64 \qquad (3)$$

where N_n is a normalizing factor corresponding to the number of pixels within the nth wedge, and where $\Delta\theta = 180°/64$. To eliminate the effects of the angular orientation of the cell pattern and of the cells within the pattern, we calculated the discrete angular correlation function (C_m), given by

$$C_m = \frac{\sum_{i=1}^{64} Q_i Q_{i+m}}{\sum_{i=1}^{64} Q_i Q_i}, \quad 0 \leq m \leq 63 \qquad (4$$

In this calculation, Q_i assumes the value Q_{i-6} for $65 \leq i \leq 128$. A plot of C_m versus m for the Fourier transform of a close-packed array of perfect hexagons is shown in Figure 8.5. Because of property 4, above, the 180° to 360° range repeats the 0° to 180° range shown. The angle between the peaks of the plot is a direct measure of the relative orientation of the sides of the hexagon. In general, for an array of regular polygons oriented the same way, the angular separation between peaks is given by 180°/N for N odd or 180°/(N/2) for N even, where N is the number of sides of the polygon.

The angular correlation function for the cell border pattern of actual endothelial cells is much less peaked than that of Figure 8.5 because of the irregularity in shape and orientation of the cells (Fig. 8.6). The absence of a strong angular dependence of the Fourier transform results from averaging a large number of cells of different types and angular orientations.

To obtain more useful shape information from cell transform patterns, it appears to be necessary to (1) limit the input to small region roughly the size of a single cell, scanning over a large number of cells, and (2) average the angular correlation functions rather than the cell transforms themselves. Figure 8.7 illustrates the basic idea. Figure 8.7A shows a small region of the cell outline transparency. Each of the numbered cells was Fourier-transformed optically by illuminating it with a beam of laser light slightly larger than a cell. (The beam had a gaussian intensity profile, its radius being given by the distance at which the intensity is 1/e times its value at the beam center.) Some of the optical transforms are shown in Figure 8.7B–D, and their angular correlation functions are shown in Figure 8.7E–G. Figure 8.7H shows the mean of the angular correlation functions obtained from all of the numbered

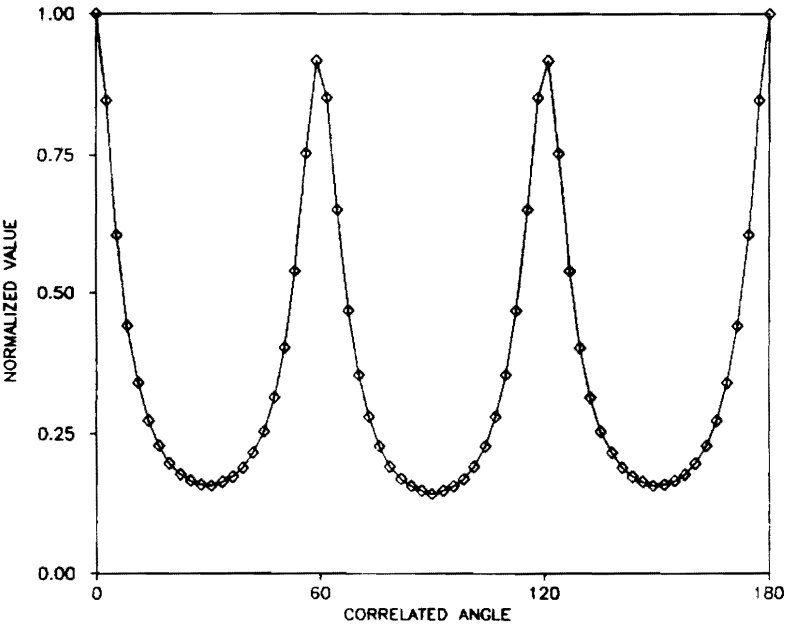

FIGURE 8.5. Plot of the angular correlation function versus angle for the Fourier transform of a close-packed array of perfect hexagons. For hexagonal input patterns, the peaks occur at 0°, 60°, and 120° (180° being the same as 0° for the symmetric patterns).

cells of Figure 8.7A. Note that the peaks and dips are still well defined but are broader and of lower amplitude than those in Figure 8.5. Our measurements confirm that the locations of the peaks and their widths are statistically meaningful parameters representative of shape characteristics of the cells. We hypothesize at this time that they can have clinical diagnostic significance in much the same way that percent-of-hexagons and cell-size coefficient of variation parameters do now.

Perhaps more significant, we have shown that the average *size* of the cells—and therefore cell density—can be inferred from Fourier transform data. The basic idea has its origins in measurements of Fourier spectra such as those of Figure 8.3, which suggest (consistent with property 2, above) that the average diameter of the first bright ring is inversely proportional to the size of the cells themselves. Because the square root of the average cell density is also inversely proportional to the average polygon diameter, we should expect these two parameters—the diameter of the first ring and the square root of the average cell density—to be proportional to one another. In an initial test of this hypothesis we estimated the diameter of the first dark ring using a ruler and plotted the estimates versus the square root of the average cell density, a parameter supplied with the Keeler Instruments endothelial cell tracings. The resultant data points did indeed provide a good fit to a straight line passing through the origin.

To obtain a more quantitative estimate of the diameter of the first bright ring, we worked with the radial projection of the Fourier intensity distribution, given by

$$P_r(r) = \int_0^{2\pi} |F_p(r,\theta)|^2 \, d\theta \qquad (5)$$

In its discretized version, obtained from the computer samples, $P_r(r)$ is represented by a set of 64 numbers R_n calculated by averaging the Fourier transform intensity values within each of 64 semiannular segments, such as those shown in Figure 8.4. To a good approximation, R_n is given by

$$R_n = \frac{1}{M_n} \int_0^{\pi} \int_{(n-1)\Delta r}^{n\Delta r} |F_p(r,\theta)|^2 \, r \, dr \, d\theta,$$

$$1 \leq n \leq 64 \qquad (6)$$

where M_n equals the number of pixels within the nth annular segment. The segment size Δr was adjusted to put the 64 measurements within a diameter slightly greater than twice that of the first bright ring. Plots of R_n versus n are

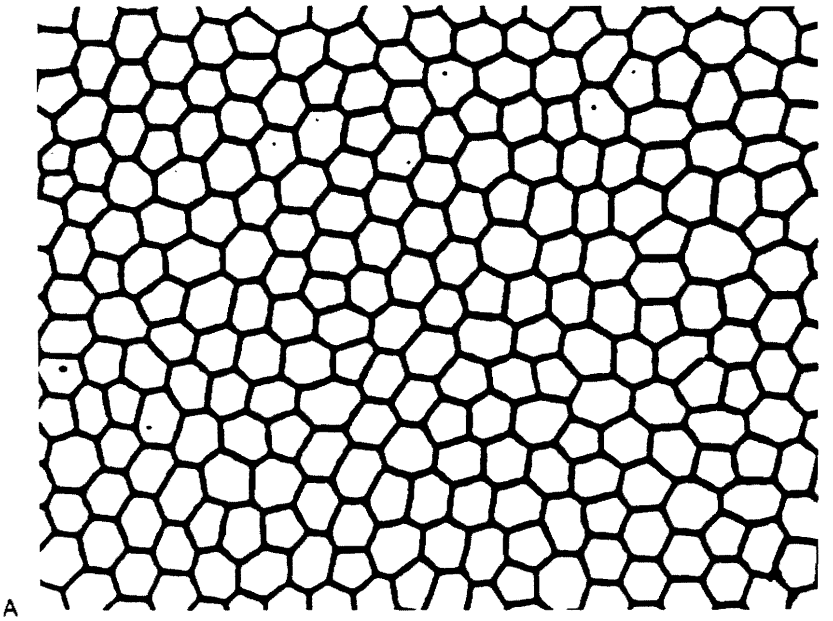

A

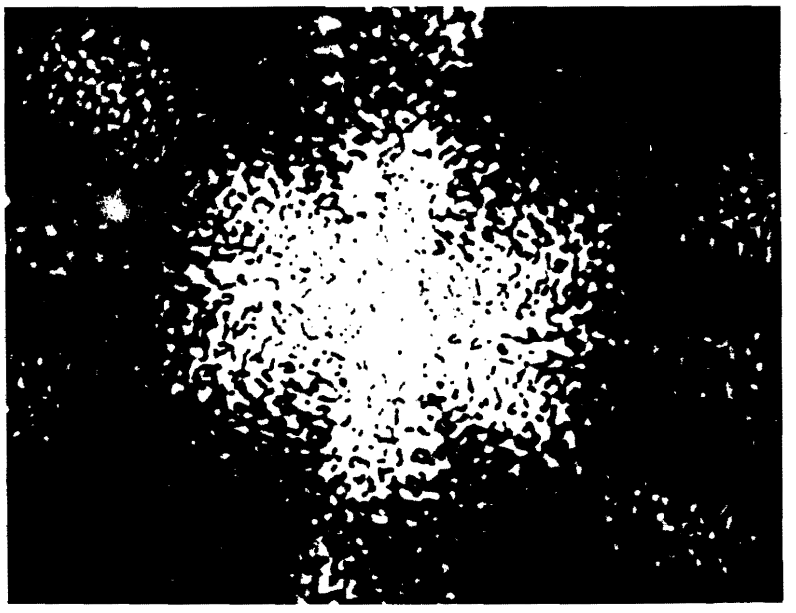

B

FIGURE 8.6. Fourier transform intensity distribution and angular correlation function for an array of endothelial cell (CV 0.2 and density 3000 cells/sq mm) border tracings: (**A**) Input array of cells. (**B**) Fourier transform intensity distribution for circular region of **A** containing roughly 50 cells. (**C**) Angular correlation function obtained from the Fourier intensity distribution. Note the enormous change in vertical scale of the vertical axis of the correlation plot compared to that in Figure 8.5.

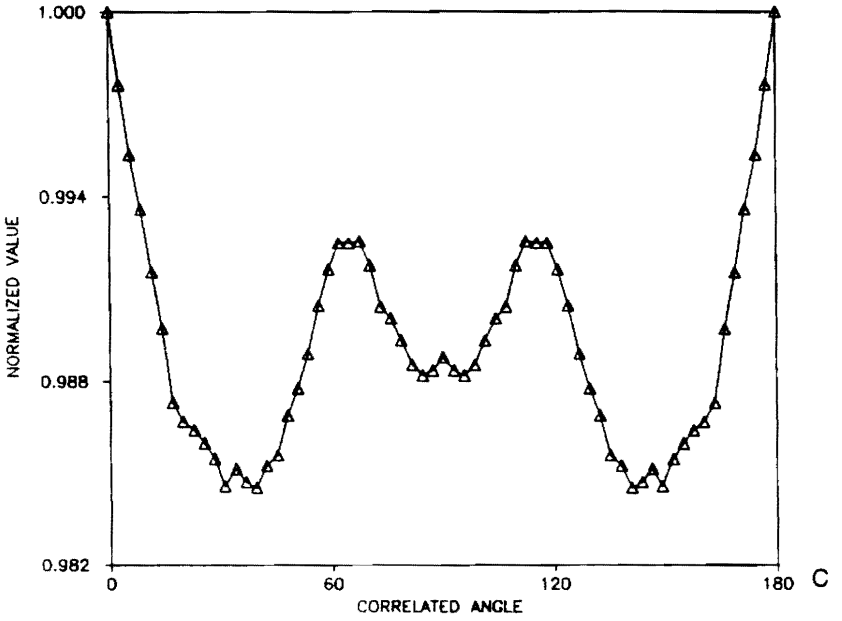

FIGURE 8.6.

shown in Figure 8.8 for endothelial cells with densities of 1000, 1500, 2000, 2500, and 3000/sq mm. The CV was 0.2, implying a high degree of regularity of cell shape and size. When estimating the diameter of the first bright ring, the following procedure was used. We first smoothed the data using a three-point median filter, then fit a fifth-order polynomial to the data points lying between the curve minima on either side of the first peak. The top of the polynomial curve was used to estimate the diameter of the first bright ring. Figure 8.9 shows a plot of these estimates versus the square root of cell density for the five cases of Figure 8.8. The dark line is a least-squared error linear regression of the data. The goodness of this fit and the fact that it passes nearly through the origin strongly support the hypothesis that average cell size can be inferred from Fourier transform data.

Also observed in plots of R_n versus n was a broadening of the first peaks as the CV increased. Currently under investigation is a quantitative evaluation of the relation between the width of this first peak and the CV of the cell samples analyzed.

Discussion

The preliminary investigations described above show the quantitative analysis of the radial projection function can yield information on cell size comparable to the average cell density measured by conventional morphologic methods. Less clear is the relation between the angular correlation functions and cell shape characteristics—percent of hexagons, for example—determined by the conventional methods.

To facilitate further investigation of these relations we think it is essential to reduce by more than an order of magnitude the amount of time needed to go from a collection of cell patterns to a suitable average angular correlation function. Therefore, we are designing an opto-electronic analyzer for cell patterns that consists of the optical Fourier transforming system of Figure 8.1 coupled with a segmented wedge-ring photodetector and simple computational electronics. The wedge-ring photodetector consists of 64 individually wired photodetectors fabricated in a 1.5 cm diameter package. The 64 elements of the detector are

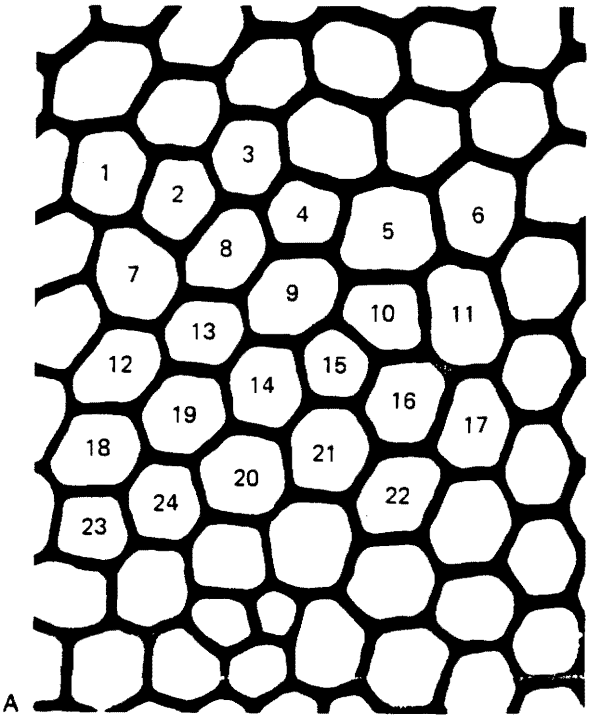

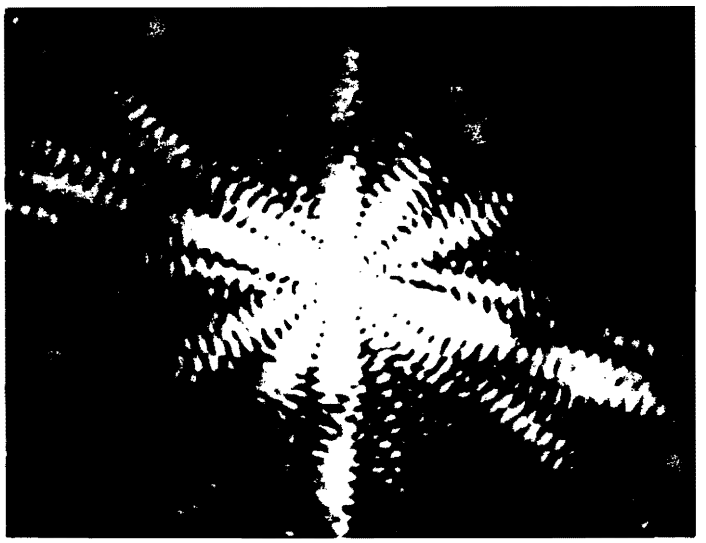

FIGURE 8.7. Effect of Fourier transforming only individual cells. (A) Collection of labeled cells. (B–D) Optical transforms of cells 2, 14, and 15. (continued)

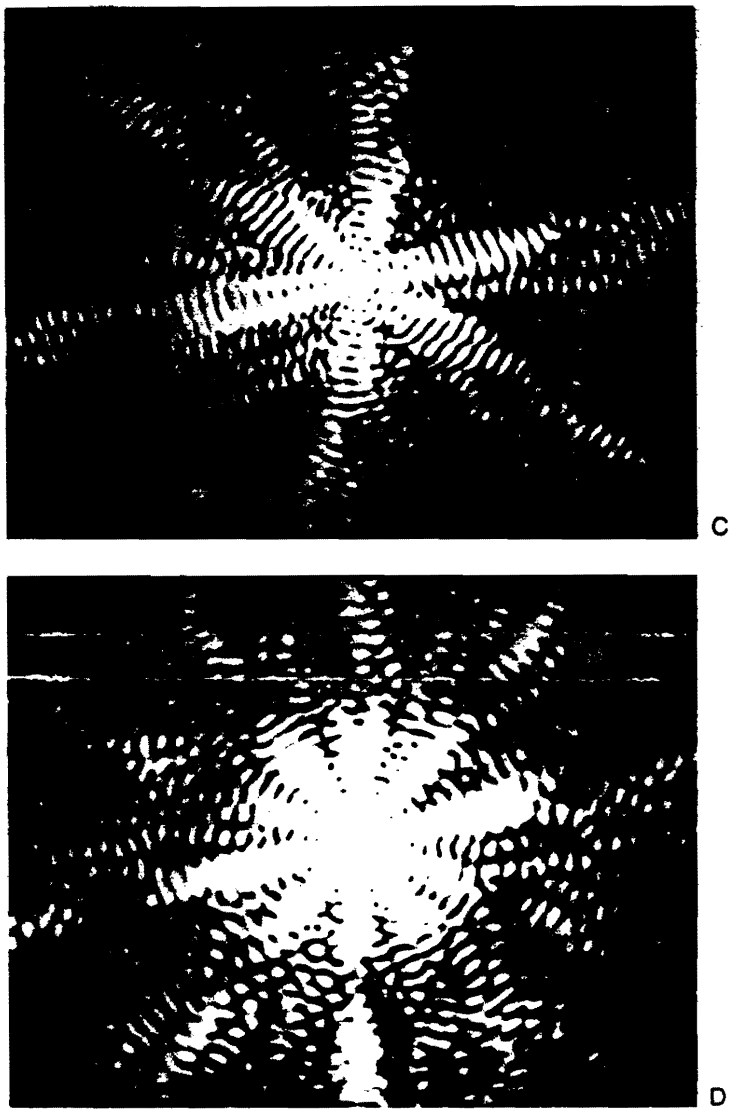

FIGURE 8.7.

laid out in a pattern similar to that of Figure 8.4, with 32 wedges and 32 semiannular segments. Such devices have been successfully applied to other Fourier domain inspection problems.[24] The 64 signals coming from the detector elements will be digitized and computations of the form suggested by Eqs. (3), (4), and (6) performed either by simple digital circuitry or by a desk-top computer that is interfaced to the device. Although our preliminary investigations suggest that 64 wedges and 64 annular segments would perform better, a 128-element device is not manufactured.

The optical Fourier transform, photodetection, and computation of the correlation and projection coefficients C_m and R_n can be performed in a few microseconds. Significantly longer times are required to input the proper cell patterns to the opto-electronic system. One approach we are considering would employ a rapidly scanned laser beam that can be made to address any local region of the input

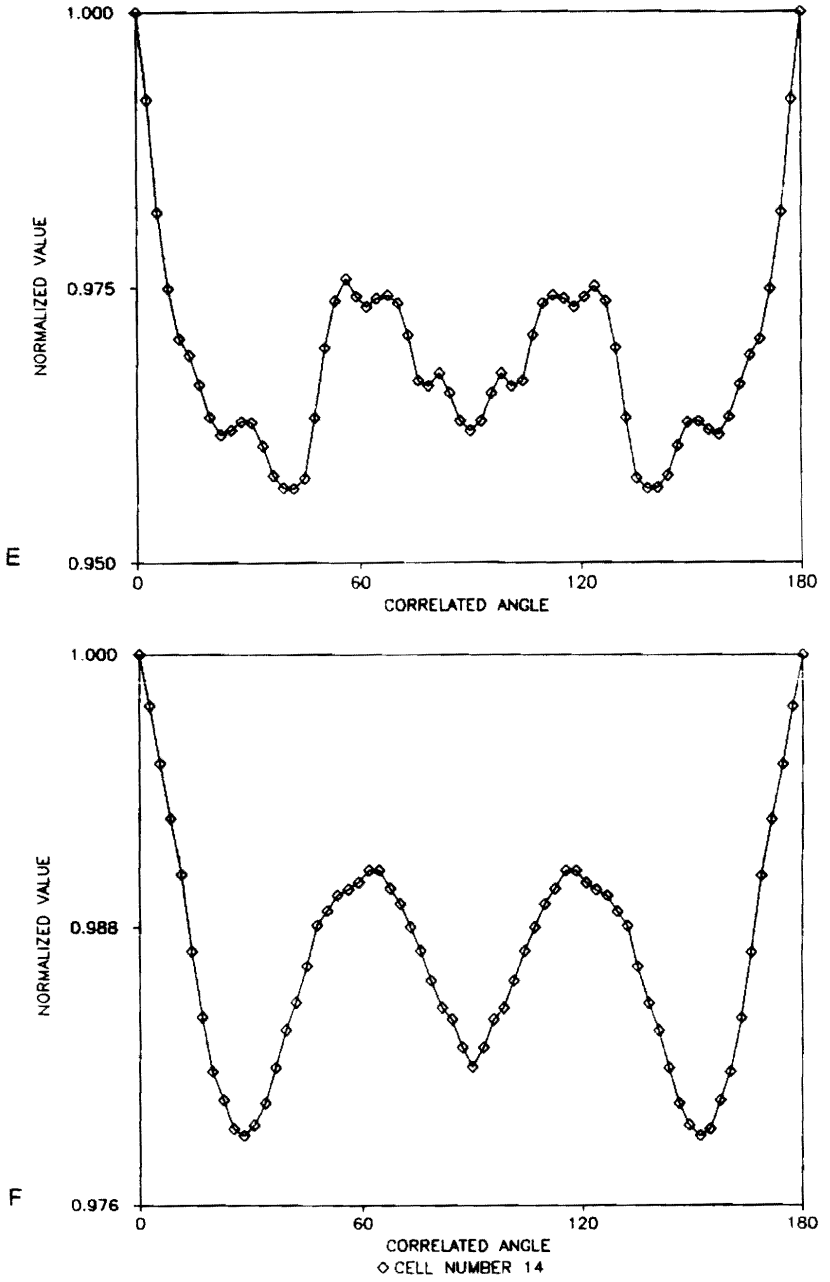

FIGURE 8.7., E–G Respective angular correlation functions. (H) Mean of the angular correlation functions obtained from all of the numbered cells. Again, note the change in the vertical scale.

cell pattern within a fraction of a millisecond. With such a scanner it should be possible to obtain, for example, the angular correlation function averaged over thousands of individual cells within a second or so. The laser beam diameter would be controllable to allow either multiple or individual cell patterns to be Fourier-transformed at a given instant. Thus use of a larger-diameter beam would yield the average cell size, and that information would then be used to fix the beam diameter for scanning individual cells.

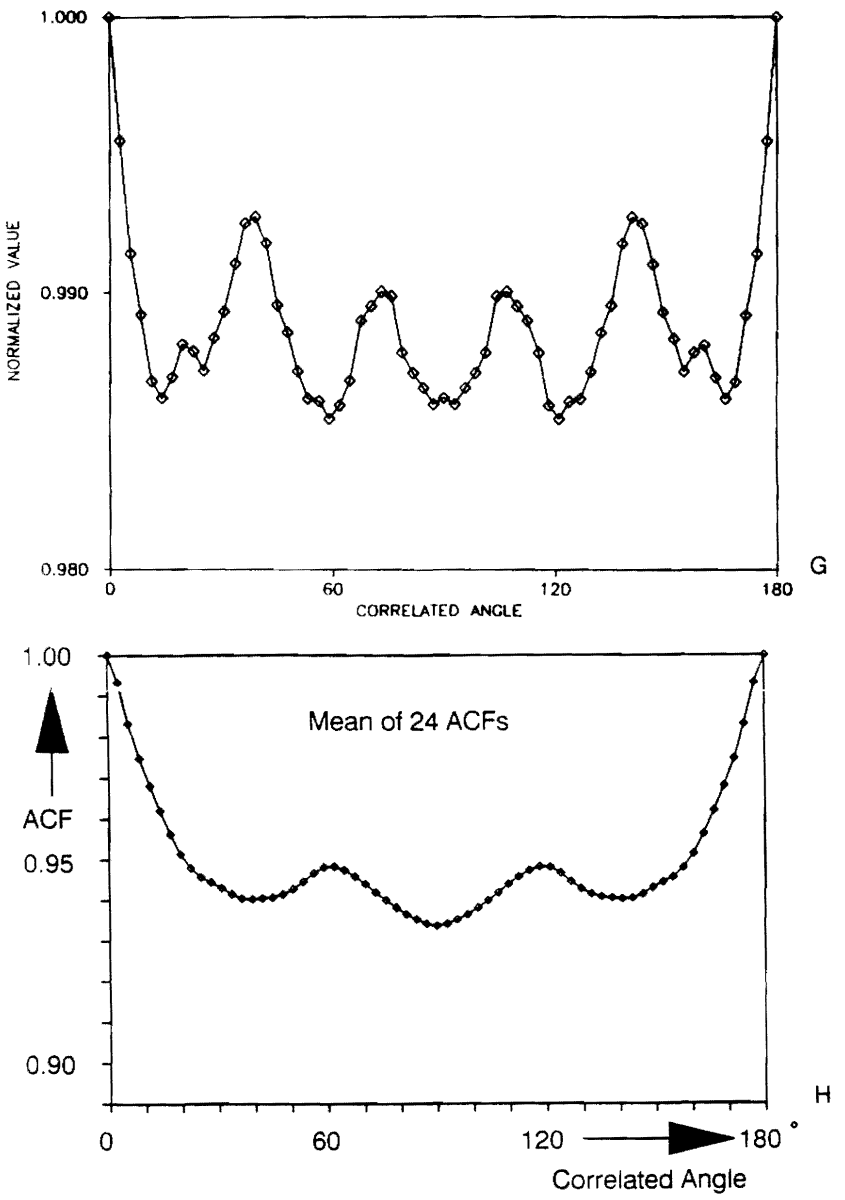

FIGURE 8.7.

One of the most challenging problems to be solved is the rapid conversion of endothelial specular images—which are generally of low contrast and spatially varying quality—to high-contrast (essentially binary, or white-on-back) images that accurately represent the cellular boundaries. Three approaches to solving this problem are suitable for study: digital image processing methods similar to those currently used in computer-aided morphometric analyses; analog processing of the video signals obtained from high-resolution video cameras; and parallel optical processing based on nonlinear filtering concepts.[28] The objective would be a method that is sufficiently fast that it would allow on-line clinical evaluation of endothelial cell patterns. Photographic film is not needed for any of these methods, as the result-

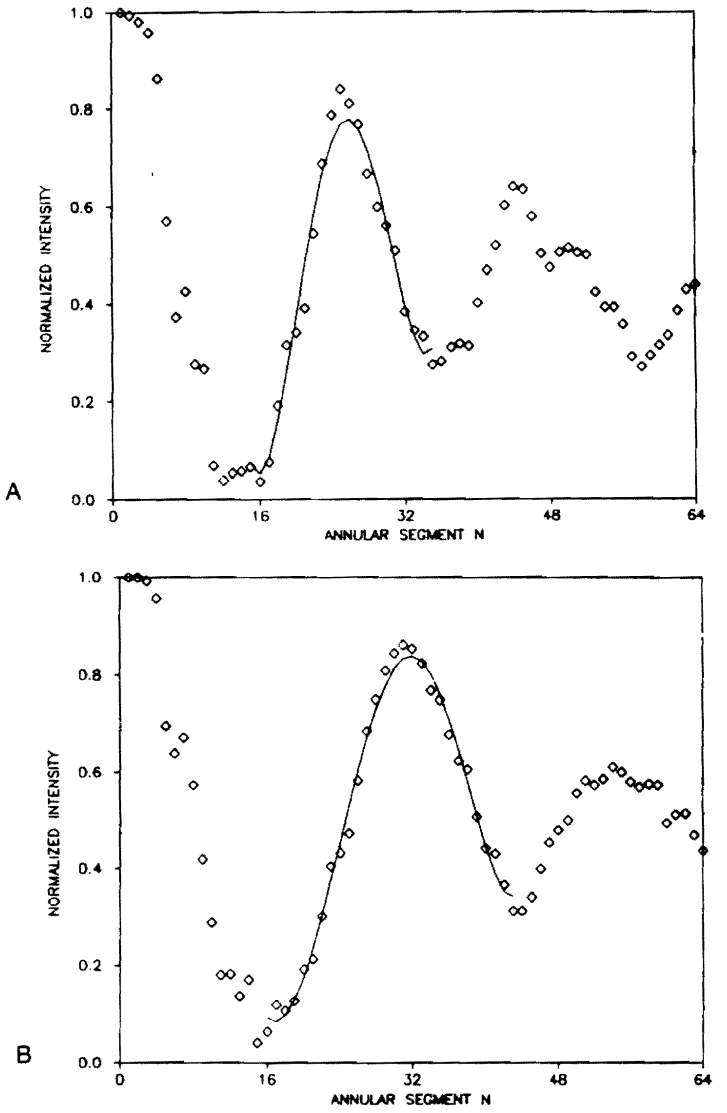

FIGURE 8.8. Plots of R_n versus n For endothelial cells with CV of 0.2 and densities of 1000/sq mm (**A**), 1500/sq mm (**B**), 2000/sq mm (**C**), 2500/sq mm (**D**), and 3000/sq mm (**E**).

ing high-contrast image can be input to the optical Fourier transforming system by means of a real-time spatial light modulator similar to the electronically addressed liquid crystal displays now used in compact television sets.

Concluding Remarks

The Fourier transform of corneal endothelial cell boundary patterns contains information on cell size, shape, and orientation. In the first phase of our investigations we have used cell tracings of human endothelial specular photomicrographs as input images and performed the Fourier transforms both optically and digitally. Our preliminary studies indicate that the Fourier transforms can be analyzed to yield average cell size or density as well as the distribution of sizes. This information, together with the area of the image, yields cell density and the associated coefficient of variation.

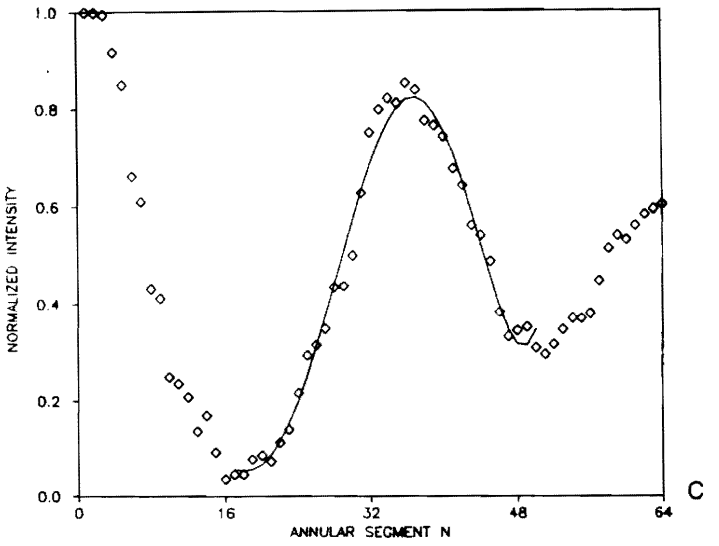
1.0
0.8
0.6
0.4
0.2
0.0
NORMALIZED INTENSITY
0
16
32
48
64
ANNULAR SEGMENT N

C

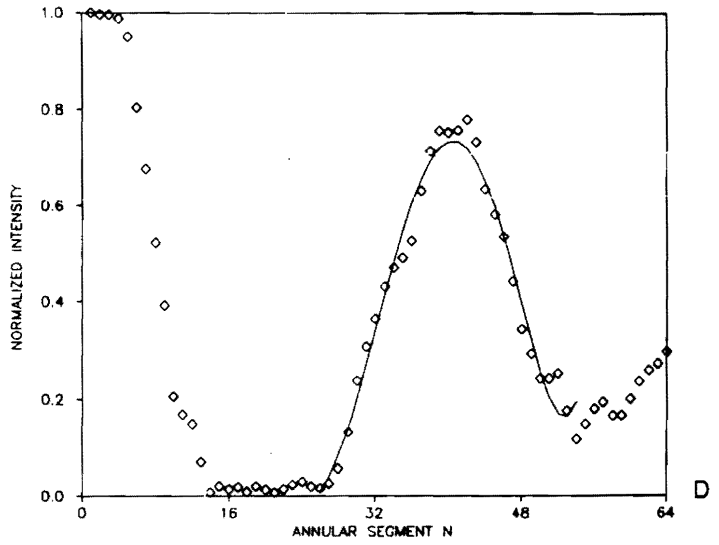
1.0
0.8
0.6
0.4
0.2
0.0
NORMALIZED INTENSITY
0
16
32
48
64
ANNULAR SEGMENT N

D

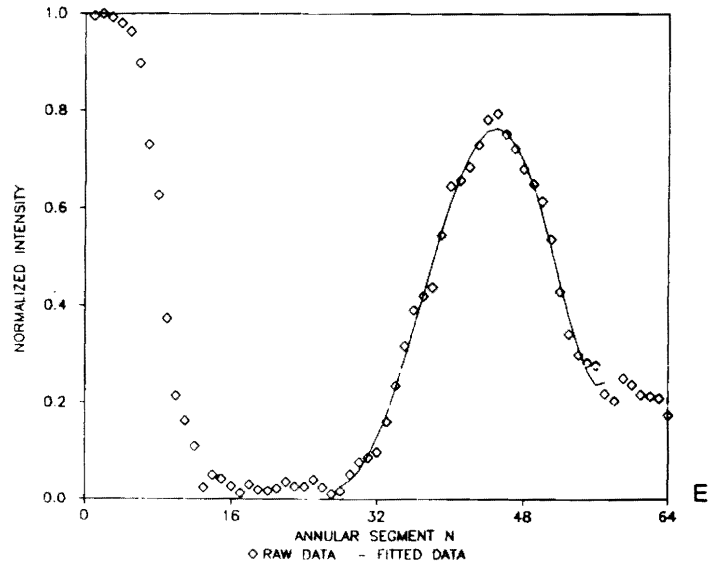
1.0
0.8
0.6
0.4
0.2
0.0
NORMALIZED INTENSITY
0
16
32
48
64
ANNULAR SEGMENT N
◇ RAW DATA - FITTED DATA

E

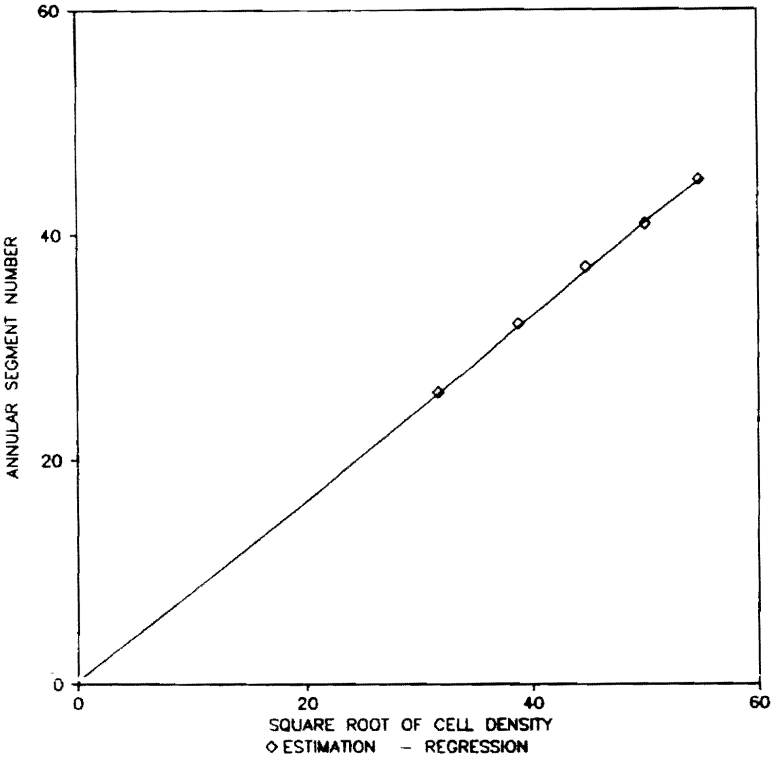

FIGURE 8.9. Plot of estimates of the diameter of the first bright ring in the Fourier intensity distribution versus the square root of cell density for the five cases of Figure 8.8. The dark line shows a least-square error linear regression of the data.

These quantities have major significance in the diagnostic evaluation of the cornea, would healing, pre- and posttransplant surgery, and pre- and postcataract surgery. In addition, the diagnostic evaluation of the clinical course of Fuchs' dystrophy can be monitored by an analysis of endothelial mophology. The current lack of rapid, automated procedures hinders such measurements by clinical ophthalmologists and even hinders the establishment of reliable baselines for proper comparison and evaluation of the endothelium in pathologic states.[29]

The advantage of the Fourier technique for statistical characterization of the cells lies in its applicability to both global and local measurements. The entire collection of cell patterns, which may number several thousand, can be incorporated in the transform in a fully parallel operation, and thus statistical averaging is done automatically. Alternatively, local measurements can be made rapidly to produce other kinds of averages or, if desired, maps of cell characteristics as a function of the local region of the cornea. Furthermore, the Fourier transforms can be evaluated essentially instantaneously using optical techniques.

Our preliminary findings demonstrate the feasibility of the Fourier transform method to characterize and analyze the morphologic structure of the corneal endothelium. We suspect that this methodology can also be applied to the morphologic analysis and pattern recognition of retinal photomicrographs. In addition, the rapid development of real-time confocal scanning microscopes specifically designed for clinical use with an applanating objective would provide wide-field epithelial cell images. The techniques could thus be applied to morphologic analysis of epithelial cell patterns, with possible resultant improvements of the diagnosis of epithelial diseases and dystrophies, e.g., dry eye. Further developments and research are needed to determine the diagnostic utility of the methods.

Acknowledgment. This work was supported in part by NIH grant EY-06958 (B.R.M.) and NIH grant EY-08402 (W.T.R.)

References

1. Speedwell L, Novakovic P, Sherrard ES, Taylor DSI. The infant corneal endothelium. Arch Ophthalmol 1988;106:771–775.
2. Waring GO III, Bourne WM, Edelhauser HF, Kenyon KR. The corneal endothelium, normal and pathological structure and function. Ophthalmology 1982;89:531–590.
3. Yee RW, Matsuda M, Edelhauser HF. Wide-field endothelial counting panels. Am J Ophthalmol 1985;99:596–597.
4. Yee RW, Matsuda M, Schultz RO, Edelhauser HF. Changes in the normal corneal endothelial cellular pattern as a function of age. Curr Eye Res 1985;4:671–678.
5. Bourne WM, Kaufman HE. Specular microscopy of human corneal endothelium in vivo. Am J Ophthalmol 1976;81:319–323.
6. Leibowitz HM, Laing RA. Specular microscopy in corneal disorders. In Leibowitz HM (ed): Corneal Disorders: Clinical Diagnosis and Management. Saunders, Philadelphia, 1984 pp. 123–163.
7. Mayer DJ. Clinical Wide-Field Specular Microscopy. Baillière Tindall, London, 1984.
8. Landshman N, Ben-Hanan I, Assia E, et al. Relationship between morphology and functional ability of regenerated corneal endothelium. Invest Ophthalmol Vis Sci 1988;29:1100–1109.
9. Masters BR. Two-dimensional fluorescent redox imaging of rabbit corneal endothelium. Invest ophthalmol Vis Sci 1988;29(suppl): 285.
10. Collin HB, Grabsch BE. The effect of ophthalmic preservatives on the shape of corneal endothelial cells. Acta Ophthalmol (Copenh) 1982;60:93–105.
11. Fabian E, Mertz M, Koditz W. Endothelmorphometrie durch automatisierte Fernsehbildanalyse. Klin Monatsbt Augenheikd 1983; 182:218–223.
12. Ford GE, Waring, GO. Computer analysis of the corneal endothelial cells. Invest Ophthalmol Vis Sci. 1981;20(suppl):231.
13. Hartmann C, Koditz W. Automated morphometric endothelial analysis combined with video specular microscopy. Cornea 1984/5; 3:155–167.
14. Hirst LW, Sterner RE, Grant DG. Automated analysis of wide-field specular photomicrographs. Cornea 1984;3:83–87.
15. Lester JM, MacFarland JL, Laing RA, et al. Automated morphometric analysis of corneal endothelial cells. Invest Ophthalmol Vis Sci 1981;20:407–410.
16. Serra J. Image Analysis and Mathematical Morphology. Academic Press, New York; 1982.
17. Masters BR. Characterization of corneal specular endothelial photomicrographs by their Fourier transforms. Proc SPIE 1988;938:246–252.
18. Bracewell RN. The Fourier Transform and its Applications. 2nd Ed. McGraw-Hill, New York, 1986.
19. Goodman JW. Introduction to Fourier Optics. McGraw-Hill, New York, 1968.
20. Stark H. Theory and measurement of the optical Fourier transform. In Stark H (ed): Applications of Optical Fourier Transforms. Academic Press, New York, 1982, pp. 2–40.
21. Casasent D, Richards J. Optical Hough and Fourier processors for product inspection. Opt Eng 1988;27:258–265.
22. Harburn G, Taylor CA, Welberry TR. Atlas of Optical Transforms. Cornell University Press, Ithaca, NY, 1975.
23. Horner JL (ed): Optical Signal Processing. Academic Press, New York, 1987.
24. Kasdan HL. Industrial application of diffraction pattern sampling. Opt Eng 1979;18:496–503.
25. Stark H, Lee D. An optical digital approach to the pattern recognition of coal-worker's pneumoconiosis. IEEE Trans Syst Man Cybern 1976;SMC-6:788–793.
26. Almeida SP, Wygant RW, Jearld A Jr, Penttila JA. Optical Fourier transform characterization of fish scale age. Appl. Optics 1987;26:2299–2305.
27. Lipson H. Optical Transforms. Academic Press, London, 1972.
28. Hereford JM, Rhodes WT. Nonlinear optical image filtering by time-sequential threshold decomposition. Opt Eng 1988;27:274–279.
29. Hirst LW, Yamauchi K, Enger C, Vogelpohl W, Whittington V. Quantitative analysis of wide-field specular microscopy. Invest. Ophth. Vis Sci 1989;30:1972–1979.

ATTACHMENT 2

Nonlinear Image Processing and Pattern Analysis by Rotating Kernel Transformation and Optical Fourier Transform, doctoral dissertation by Yim Kul Lee, Georgia Institute of Technology, December 1990.

Contents

SUMMARY

Hybrid opto–electronic procedures are introduced for the automated analysis of polygonal cell boundary patterns obtained from raw endothelial (innermost) layer of the human cornea. Since the raw image used in this research is characterized by low contrast and spatially varying background brightness levels in a noisy background, the entire procedures are implemented by two major operations: image enhancement in a preprocessing step and optical Fourier transformation with post–detection processing. The preprocessing or image enhancement operation investigated is performed by a novel rotating kernel min–max transformation (RKMT), invented by Y. K. Lee and developed through this research program, for enhancing directional features (e.g., straight–line segments). The enhanced image or cell boundary pattern is then input to an optical Fourier transforming system incorporating a wedge–ring detector for diffraction pattern sampling in the Fourier transform plane. The subsequent analysis is performed for size and shape measures of the polygonal cells by illuminating a larger number of cells and then limiting the illuminated area to a small region, approximately the average cell size, respectively.

Major emphasis is placed on developing the RKMT method for the automated enhancement of linear features of an image. For the preprocessing operation, the RKMT method is first introduced, followed by a discussion of the various two–dimensional kernels and mapping functions. Algorithms for linear feature enhancement are then introduced and some numerical results presented, evaluating qualitatively and quantitatively the performance of the RKMT processing under various conditions. It is shown that, while the RKMT processing can be implemented on a digital computer alone, it is a particularly attractive candidate for optical–electronic implementation. Since the kernel is typically real and nonneg-

ative, a hybrid incoherent spatial filtering system is discussed for implementing RKMT processing. The RKMT processing operation is then applied to for the enhancement of cell boundaries (almost all straight–line segments) in the raw image with notable success. Binarization methods for obtaining a binarized cell boundary pattern for subsequent diffraction pattern analysis are also discussed. Comparisons are made with conventional spatial filtering methods. The Basic RKMT processing operations are extended to pattern recognition and edge enhancement. Algorithms for the pattern recognition with rotation and quasi–scale invariance and the edge enhancement are introduced, along with numerical experiments under various conditions. Effects of the kernel dimension and profile on the pattern recognition and edge enhancement capabilities are also discussed.

Finally, the recommendations for future research and other potentional applications, for which the RKMT method might be favorably used, are summarized.

CHAPTER 1

INTRODUCTION

1.1 Research Motivation

The problem originally motivating this research lies in the automated statistical evaluation of size, size variation, and shape of polygonal cells in the endothelial (innermost) layer of the human cornea. These parameters are of importance in the clinical evaluation of corneal tissue [1,2]. Current computer–aided morphometric methods for estimating these parameters require the manual tracing of cell boundary patterns to emphasize morphological features such as the shapes of the cells. Current techniques [3,4] treat the individual cells as discrete and independent entities and do not take into account their relative positions within the cell arrays. Generally speaking, the computer methods are slow, particularly when a large number of cells must be analyzed. Recently, Masters [5] showed that the Fourier transform of manually–traced cell border patterns contains easily interpreted information on average cell size. His work suggested that the optical Fourier transform methods discussed in this thesis proposal can be used to estimate quite rapidly both size and shape parameters for cells ranging in number to several thousand.

Figure 1.1(a) shows a sample of a specular micrograph image of corneal endothelial cells. The raw input image has low contrast and spatially varying local average brightness levels in a noisy background. It does not yield well–defined Fourier signatures suitable for measurement. Figure 1.1(b) shows a cell boundary pattern obtained by manually tracing a raw cell pattern. Note that the cell bound-

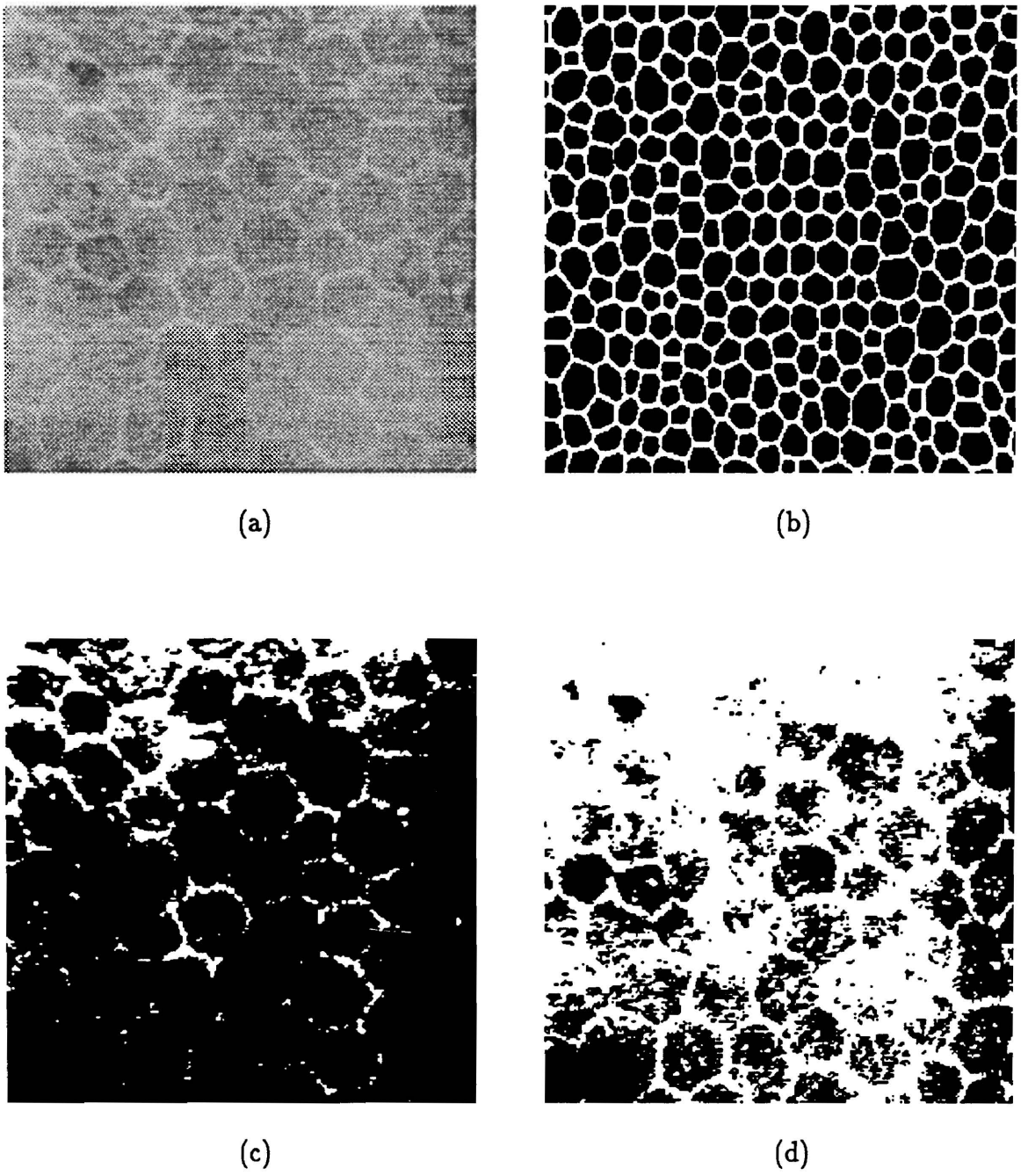

(a) (b)

(c) (d)

Figure 1.1: Human corneal endothelial cell image and their thresholded images at two different gray–levels. (a) Original image. (b) Example of manually–traced binary pattern. (c) and (d) Thresholded versions of (a) at two different gray levels.

aries are almost always straight line segments. Figures 1.1(c) and (d) show examples of the raw imagery of Fig. 1.1(a) subjected to ideal thresholding–hard limiting at two different gray values. It is clear from these latter examples that simple high contrast imaging is not sufficient to delineate or enhance the cell boundaries. Some more sophisticated processing is required. The low contrast and noise of the raw imagery have motivated the development of a method for enhancing automatically cell boundary features. With appropriately enhanced imagery serving as input, an optical Fourier transform system can then indeed be used to obtain rapidly morphometric statistics on the cells.

1.2 Research Objectives

The primary objective of the research is to develop procedures for the automated analysis of polygonal cell boundary patterns obtained from raw endothelial cell imagery. A block diagram of the approach used in the research is shown in Fig. 1.2. The entire system performs two major operations: image enhancement in a preprocessing step and optical Fourier transformation with post–detection processing. It has not been the purpose of this research project to investigate exhaustively the morphometric statistics of corneal endothelial cells but rather to suggest procedures for the extraction of these morphometric statistics using robust opto–electronic methods.

Major emphasis has been placed on developing an opto–electronic method for the automated enhancement of the cell boundary patterns. The preprocessing or image enhancement operation investigated is based on a novel rotating kernel min–max transformation (RKMT) method, invented by Lee [6,7] and developed in this research program, that is particularly useful for enhancing straight–line segments of an image. The transformation method is referred to as RKMT processing throughout the remainder of the thesis. The development of the RKMT method has been

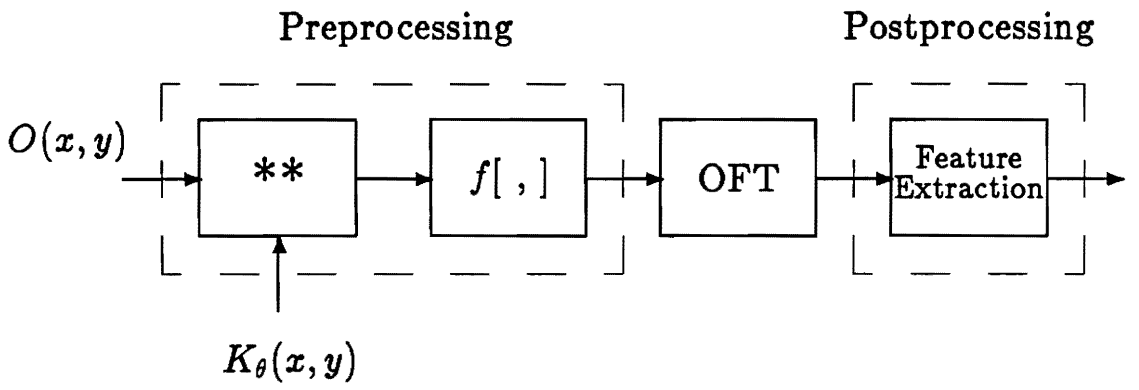

Figure 1.2: A block diagram of the proposed research by nonlinear preprocessing operation and optical Fourier transform (OFT) method, where $O(x,y)$ is a raw input image, $K_\theta(x,y)$ is a 2–D rotating kernel, and $f[\ .\ ]$ is some application–dependent function of the convolution (**) output.

challenging and an important contribution of this research because of its effectiveness: it appears to work better for this kind of processing than any other technique described in the literature [8,9,10,11].

One goal of the research has been to evaluate how well the RKMT method works in preparing the enhanced cell boundary image for subsequent analysis. The development of a hybrid optical electronic system implementing the RKMT processing operation is also important. The RKMT method appears to be a useful and significant technique for general directional image processing operations and pattern recognition. As an offshoot from the primary objectives of the research, RKMT processing is extended to applications such as edge enhancement and pattern recognition with scale and rotation invariance.

1.3 Overview of Related Work

There are several important topics related to the optical Fourier technique and the RKMT processing discussed in this thesis: (1) diffraction pattern analysis; (2) image (or feature) enhancement; (3) pattern recognition; and (4) edge enhancement. The

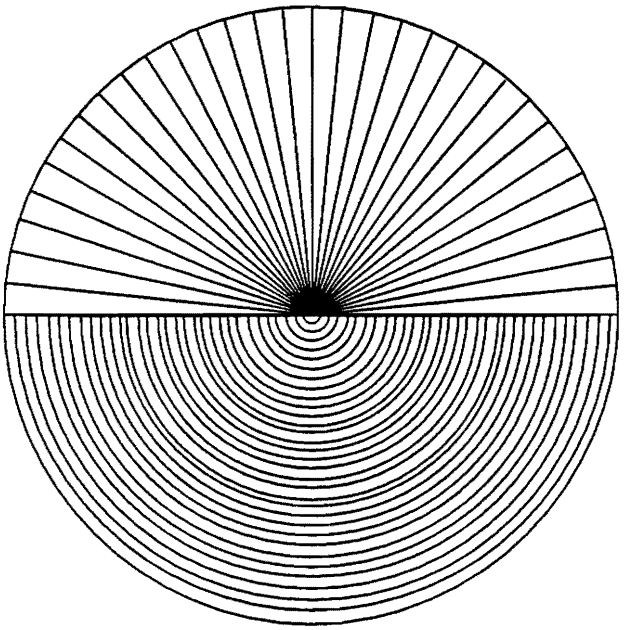

Figure 1.3: A configuration of the wedge–ring detector (WRD) with 32 annular ring and 32 wedge segments. The WRD is a polar–coordinate array of photodetectors coupled to self–ranging electronic amplifiers.

following subsections discuss work done by other researchers in these areas that is particularly relevant to this research.

1.3.1 Diffraction Pattern Analysis

Fourier intensity patterns (diffraction patterns) have been used for many years for analyzing images. In many cases, the intensity pattern is sampled and input to a computer for post–detection processing. Algorithms based on diffraction pattern sampling have been developed for a wide variety of applications, including particle size measurement [12,13,14,15] and pattern recognition and analysis [16,17,18,19,20,21].

An important device in Fourier intensity analysis is the wedge–ring detector (WRD) [18,22,23]. The commercially available WRD, illustrated in Fig. 1.3, is a polar–coordinate array of photodetectors coupled to self–ranging electronic amplifiers. It consists of 32 semiannular ring elements and 32 wedge elements. It produces

discretized projections for both radial and angular coordinates. Equations 1.1 and 1.2 represent mathematically the radial projection R_m and the angular projection A_n:

$$R_m = \frac{1}{S_m} \int_{\rho_m}^{\rho_{m+1}} \int_0^{\pi} I(\rho,\varphi)\rho d\rho d\varphi, \qquad 1 \leq m \leq 32 \tag{1.1}$$

$$A_n = \frac{1}{Q_n} \int_0^{\infty} \int_{\varphi_n}^{\varphi_{n+1}} I(\rho,\varphi)\rho d\rho d\varphi, \qquad 1 \leq n \leq 32 \tag{1.2}$$

where $I(\rho,\varphi)$ is the Fourier intensity distribution in polar coordinates, and S_m and Q_n are the areas corresponding to the m*th* ring and n*th* wedge segments, respectively. The radial projection R_m provides information about the size of the object and is invariant to the orientation of the input object. The angular projection A_n contains shape information on the object and is insensitive to the size of the object. Both R_m and A_n are invariant to horizontal or vertical translation of the object through the invariance of $I(\rho,\varphi)$ to such translation. The WRD exploits the Hermitian symmetry of the Fourier transform pattern of a real input object. Only a half plane is needed for measuring either the radial projection or the angular projection of $I(\rho,\varphi)$; both measurements can be obtained with a single device in a single FT plane. A number of industrial and medical applications of diffraction pattern analysis using the WRD have been investigated [18,21,22,24,25,26,27]. Window functions have been used to improve the accuracy of spectral estimation [28,29,30].

1.3.2 Image and Feature Enhancement

In many cases, an input image or pattern must be preprocessed to provide well-defined Fourier signatures for subsequent pattern recognition and analysis. In this research the enhancement of straight line features (e.g., the boundaries of the endothelial cells) is of special importance. Many digital algorithms have been developed for detecting and enhancing linear features, including those appearing in ocean wave photos [9], roads in military road maps [10], and ridges in fingerprints [11]. The Radon transform [9,31,32] and its inverse have been used for linear feature enhance-

ment, with the enhancement operation being performed in the Radon transform plane. In certain cases, feature enhancement can be performed simply by lowpass or bandpass spatial filtering with an optical system [33], though often with poor results. As discussed later, the RKMT method can be applied to such a problem with good results [6,7].

1.3.3 Invariant Pattern Recognition

In the area of pattern recognition, the conventional matched spatial filter is sensitive to the scale and rotation of an input object [33,34]. The basic method has been improved by many spatial–filter–based invariant pattern recognition schemes developed during the past decade [34,35,36,37,38,39,40,41,42,43]. The Hough transform [44,45] has been used for rotation–invariant recognition of an input object (e.g., airplane) which has highly oriented object features (e.g., straight–line features). Recently, the Hough transform has been used to find vertices from an edge image and to generate rule–based string codes [46] for both scale– and rotation–invariant pattern recognition. Naor and Shamir [47] presented an angular feature mapping method that locates line intersections of the edge image and extracts the information about the intersection angles.

1.3.4 Edge Detection and Enhancement

It is well known that edge enhancement is an important preprocessing operation for pattern recognition and analysis in binary and gray–scale images. Many digital algorithms have been developed for edge enhancement, including gradient techniques [48,49], positions of zero–crossings [50,51], and morphological methods [52]. Recently, specific digital gradient edge operators have been implemented optically. Casasent and Chen [53] implemented Sobel's bipolar digital edge operator using a multiple–exposure matched spatial filter and computer–generated hologram in a coherent optical system. Cherri and Karim [54] implemented Sobel, Prewitt, and

Robert digital edge operators using an optical symbolic substitution technique.

1.4 Overview of The Thesis

The remainder of this thesis is divided into five major chapters. In Chapter 2, the optical Fourier transform methods for extracting statistical cell parameters relating to size and shape are discussed. In one case, a large number of cells are illuminated to extract size information. Once the size information is obtained, individual cells are illuminated to extract shape information. Automated procedures for the quantitative measurement of cell parameters are discussed.

In Chapter 3, the rotating kernel min–max transformation is introduced, followed by a discussion of various two–dimensional kernels and mapping functions. Algorithms for linear feature enhancement are introduced along with numerical experiments, which evaluate qualitatively and quantitatively the performance of the RKMT processing under various conditions. A hybrid optical–electronic system that implements RKMT processing is discussed.

In Chapter 4, the RKMT method is applied to the enhancement of endothelial cell boundaries, which are almost always straight-line segments, in raw input imagery. Comparisons are made with conventional spatial filtering methods.

In Chapter 5, the application of RKMT processing to pattern recognition with scale and rotation invariance is presented. Effects that variations in the kernel length and width have on the discrimination of objects are discussed. A variety of numerical experiments are presented.

In Chapter 6, the application of RKMT processing is extended to edge enhancement. Initial studies indicate that the RKMT method can be used effectively to locate edges (i.e., object contours) in an image. The application to both gray–scale edge imagery and binary edge imagery is discussed.

In the final Chapter, the results of the research and recommendations for future

work are summarized.

The contributions of this research lie in the following areas:

1. Development of hybrid optical–electronic methods for the automated evaluation of size, size variation, and shape of polygonal cells from raw corneal endothelial cell images.

2. Introduction and development of a novel hybrid rotating kernel min–max transformation method for hybrid optical–electronic image processing.

3. Application of the RKMT method to enhancement of linear features.

4. Application of the RKMT method to edge enhancement.

5. Application of the RKMT method to pattern recognition with rotation and quasi–scale invariance.

CHAPTER 2

PATTERN ANALYSIS BY OPTICAL FOURIER TRANSFORM METHOD

This chapter begins with background on polygonal cell boundary patterns in the human corneal endothelial layer and then describes the optical Fourier transform method for the estimation of cell parameters (e.g., size, size variation, and shape). Two different optical Fourier analysis procedures are applied to high contrast cell boundary patterns obtained from specular micrographs of the endothelial layer. In one case, a large number of cell patterns are illuminated to extract average cell size information. Automated procedures for the quantitative estimation of size statistics are discussed. Once the average cell size information has been obtained, individual cells are illuminated to extract shape information.

2.1 Background

The endothelial cell layer consists of some 350,000 to 500,000 polygonal cells. Cells have center–to–center spacings of approximately 20 μm. Their thickness in the longitudinal direction (orthogonal to the plane of observation) is approximately 5 μm. The cells are predominately hexagonal in shape (61~75 %). Cell density decreases with age and disease, as does the degree of hexagonality [55,56]. Under currently–used computer morphometric methods, the polygonal cell boundaries appearing in specular micrographs are traced out by hand or by a computer with strong human intervention. The boundary patterns are then digitized and analyzed by computer.

The statistical estimation of morphological parameters is often based on the spatial analysis of only 50 $\sim$ 100 endothelial cells, since the techniques are so slow. This number is often considered too small for clinical evaluation of the corneal tissue, particularly since there might be wide variation in cell size and shape from one region of the cornea to another.

Preliminary experiments by Masters, Lee, and Rhodes [57] confirmed speculation that the optical Fourier transform obtained from cell boundary patterns could be used to estimate with good accuracy the average cell density over a wide range (1000 to 3000 $cells/mm^2$); further experiments indicated that shape characteristics could be extracted. One important conclusion of the preliminary experiments was that the optical method could be implemented in such a way that large numbers of cells ($>$ 1000) can be easily be analyzed.

2.2 Optical Diffraction Pattern Analysis

2.2.1 Examples: Polygonal Patterns

In the method investigated an input cell boundary pattern is analyzed by a diffraction pattern sampling using a wedge–ring detector (WRD). Equations 1.1 and 1.2 show a mathematical representation of the data reduction operation in the Fourier transform (FT) plane. Figure 2.1 shows a single lens Fourier transforming system with a WRD positioned in the FT plane. With an object $t(x,y)$ illuminated by a converging beam, the output intensity $I(x,y)$ in the FT plane [33,58] is given by

$$I(x,y) = \frac{A}{\lambda^2 d_{of}^4} \left| T\left(\frac{x}{\lambda d_{of}}, \frac{y}{\lambda d_{of}}\right)\right|^2, \tag{2.1}$$

where A is a proportionality factor, λ is the wavelength of the incident quasi–monochromatic light, d_{of} is the distance from the object to the FT plane, and $T(u,v)$ is the FT of $t(x,y)$. In Eq. 2.1, we assume that the object $t(x,y)$ is fully illuminated (i.e., that the pupil function of the lens can be ignored) [33].

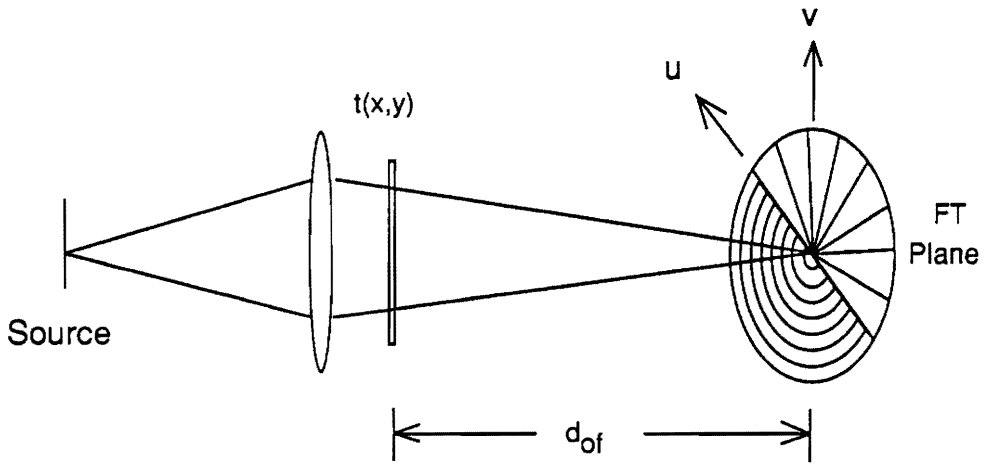

Figure 2.1: A coherent optical system incorporating a wedge–ring detector (WRD) in the Fourier transform (FT) plane, where $t(x,y)$ is the input pattern and d_{of} is the distance to the FT plane.

There are two advantages for using an optical FT system with converging beam illumination [33,58,59] in this research. One advantage is that the scale of the FT pattern can be changed by varying the distance d_{of}. For a cell pattern with cell density CD, the cell diameter or size is inversely proportional to $\sqrt{CD}$ and to the scale of the FT pattern. From the relationship between $\sqrt{CD}$ and the scale of the FT pattern, it can be shown that the scales of the optical Fourier intensity patterns of inputs with $CD = 1000$ and 2000 are the same if the object distances to the FT plane are given in ratio of $\sqrt{2}$ to 1. Alternatively, for the same distance d_{of}, the FT patterns of two cell boundary patterns with different CDs will have scales that are proportional to their $\sqrt{CD}$. The other advantage of the optical system is that an input cell boundary pattern can be scanned both globally and locally with an illuminating beam of chosen size. Global scans are used to estimate size and size variation for a large number of cells; local scans with a smaller diameter illuminating beam size extract the shape statistics of the cells.

Figures 2.2 and 2.3 illustrate how the optical diffraction pattern can be used

for the statistical estimation of morphological parameters of polygonal cells. Figures 2.2(a) and (b) show a single hexagon and its optical Fourier intensity pattern. The distance from the origin to the first bright region in the Fourier intensity pattern is inversely proportional to the diameter of the hexagon. Each spoke in the Fourier intensity pattern results from the corresponding parallel sides of the hexagon. The angles (i.e., 60° for a regular hexagon) between two spokes can be used to infer shape characteristics. Figure 2.2(c) shows the angular projection A_n obtained from the intensity pattern in (b). The locations of the peaks represent the distances in angle of each spoke from a reference angle (e.g., 0°). Figure 2.3(a) shows an array of regular hexagons and Fig. 2.3(b) its Fourier intensity pattern. The radial distance from the origin to the first bright region of the FT pattern remains the same as the number of regular hexagons increases. Spoke patterns acquire a spot–like pattern because of sampling effects. The radial projection R_m of the intensity pattern in Fig. 2.3(b) is shown in Fig. 2.3(c).

For an infinite array of regular hexagons, the hexagonal pattern can be expressed in terms of a convolution:

$$t(x,y) = t_h(x,y) ** s(x,y)$$
$$= t_h(x,y) ** \left[\sum_{m=-\infty}^{\infty} \sum_{n=-\infty}^{\infty} \delta(x + [am + an], y + [bm - bn]) \right] \qquad (2.2)$$

where $t_h(x,y)$ is the basic hexagon function and s(x,y) is a Dirac comb sampling function. The Fourier transform of $t(x,y)$ is given by

$$T(u,v) = T_h(u,v)S(u,v)$$
$$= T_h(u,v) \left[\frac{1}{ab} \sum_{m=-\infty}^{\infty} \sum_{n=-\infty}^{\infty} \delta\left(u + \frac{[m+n]}{2a}, v + \frac{[m-n]}{2b} \right) \right] \qquad (2.3)$$

where $T_h(u,v)$ and $S(u,v)$ are the Fourier transforms of the single hexagon function and the sampling function, respectively [60,58]. Figure 2.4 illustrates pictorially how the hexagonal array pattern $t(x,y)$ and its FT pattern $T(u,v)$ are related. In the figure (p,q) is a spatial sampling vector, (p_f, q_f) is a spatial frequency sampling

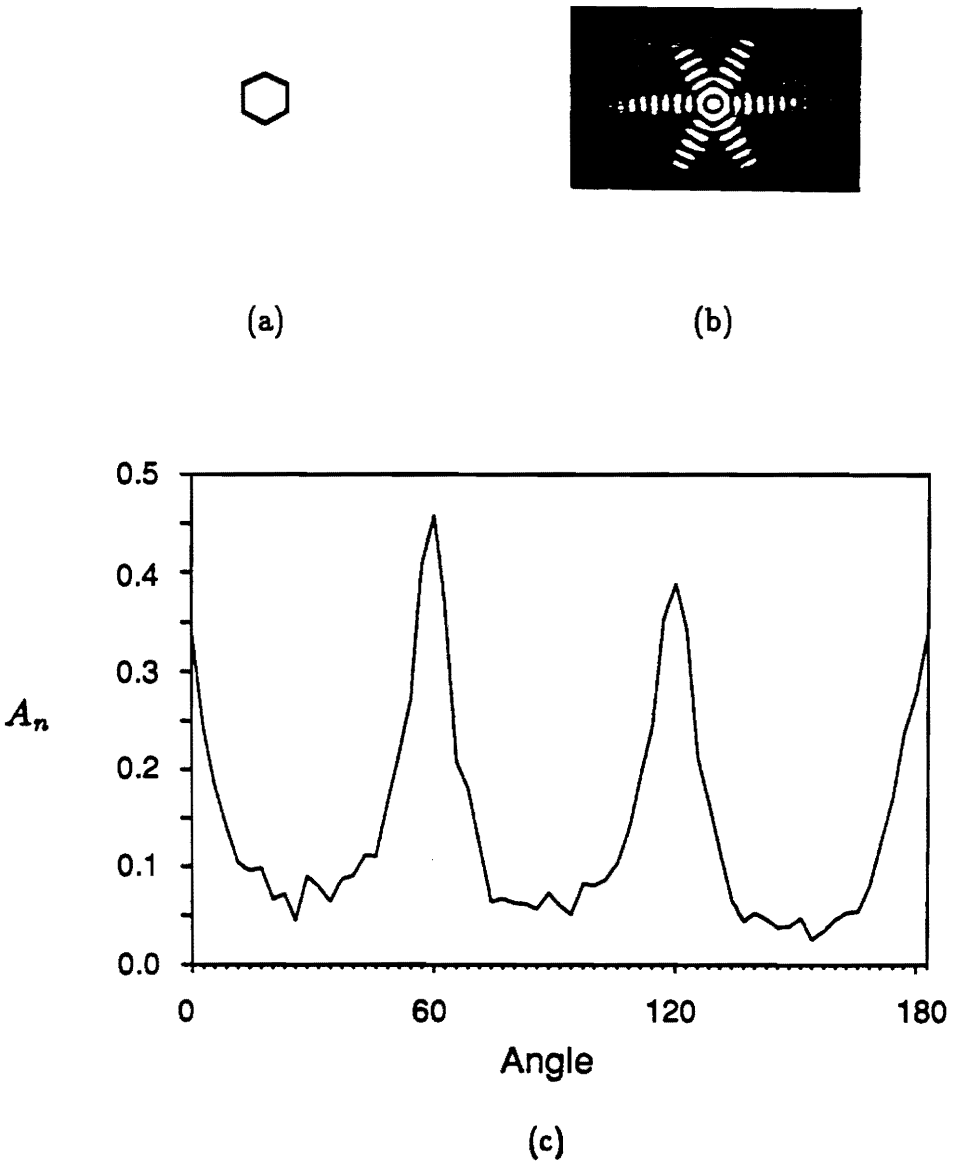

Figure 2.2: A single hexagonal boundary pattern and its Fourier intensity pattern: (a) boundary pattern; (b) Fourier intensity pattern of (a); (c) angular projection A_n obtained from (b).

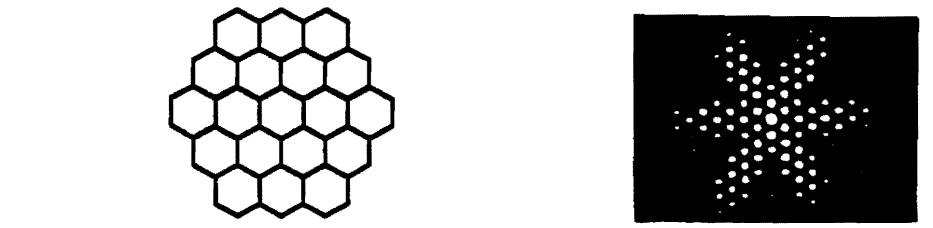

(a) (b)

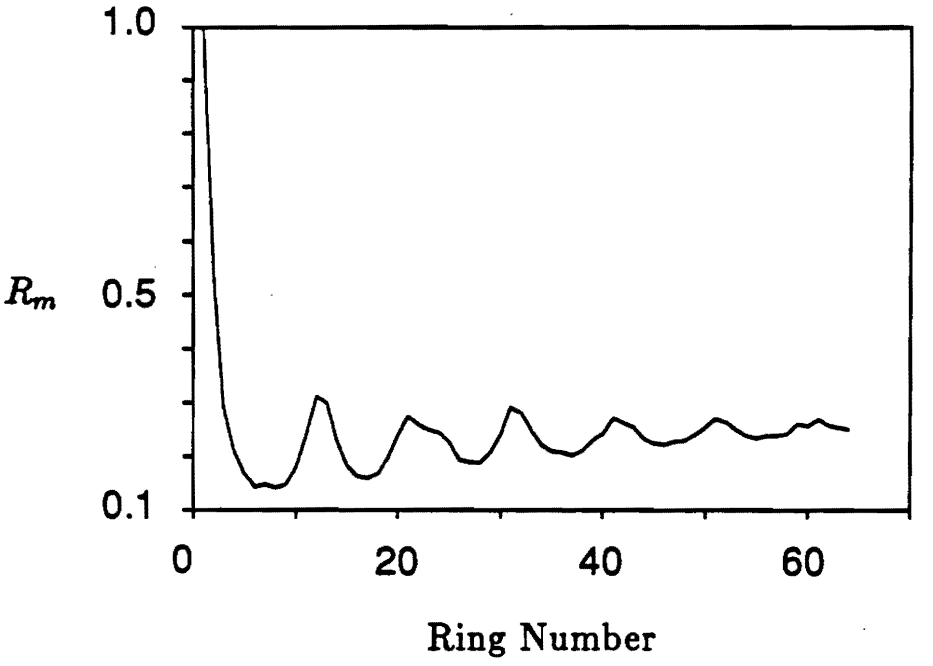

(c)

Figure 2.3: An array of hexagonal boundary patterns: (a) boundary pattern; (b) Fourier intensity pattern of (a); (c) radial projection R_m obtained from (b).

vector, and $b = \sqrt{3}a$. From the figure, it is obvious that the size information can be extracted from a collection of the first six spots of the Fourier transform pattern.

As the regularity of the size and orientation in the input pattern is reduced, for example as the regular hexagonal array changes to the corneal pattern array, a speckle–like pattern arises. However, a bright region still forms in the Fourier intensity pattern. Figures 2.5(a) and (b) show such a cell boundary pattern with random orientation of the cells and variations in size and shape, along with its Fourier intensity pattern. Note in (b) the presence of a central dark ring surrounded by a bright ring. The radial projection of the Fourier intensity pattern is shown in Fig. 2.5(c). The radius of the first bright ring is estimated by measuring the location of the first peak in the plot of the radial projection.

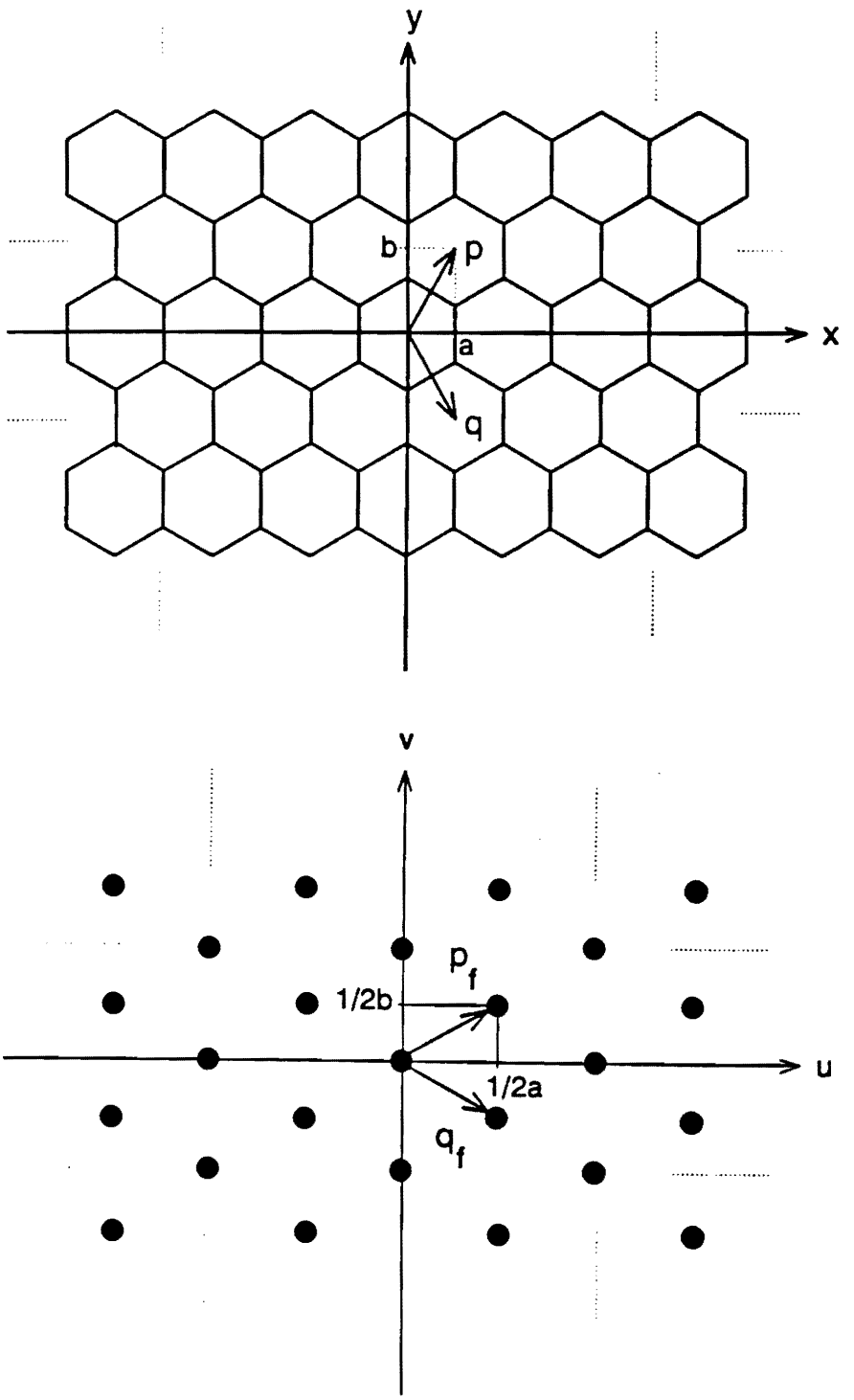

Figure 2.4: Infinite hexagonal array and Fourier transform: (a) Top: hexagonal array pattern with spatial period (p, q): (b) Bottom: Fourier intensity pattern with frequency period (p_f, q_f).

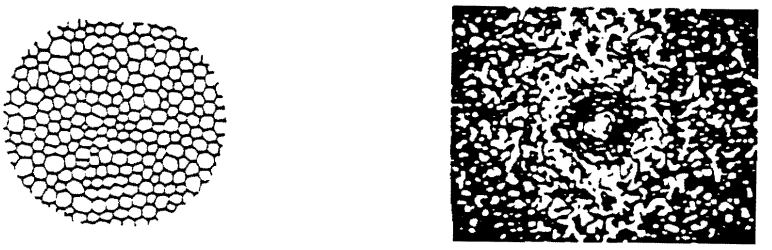

(a) (b)

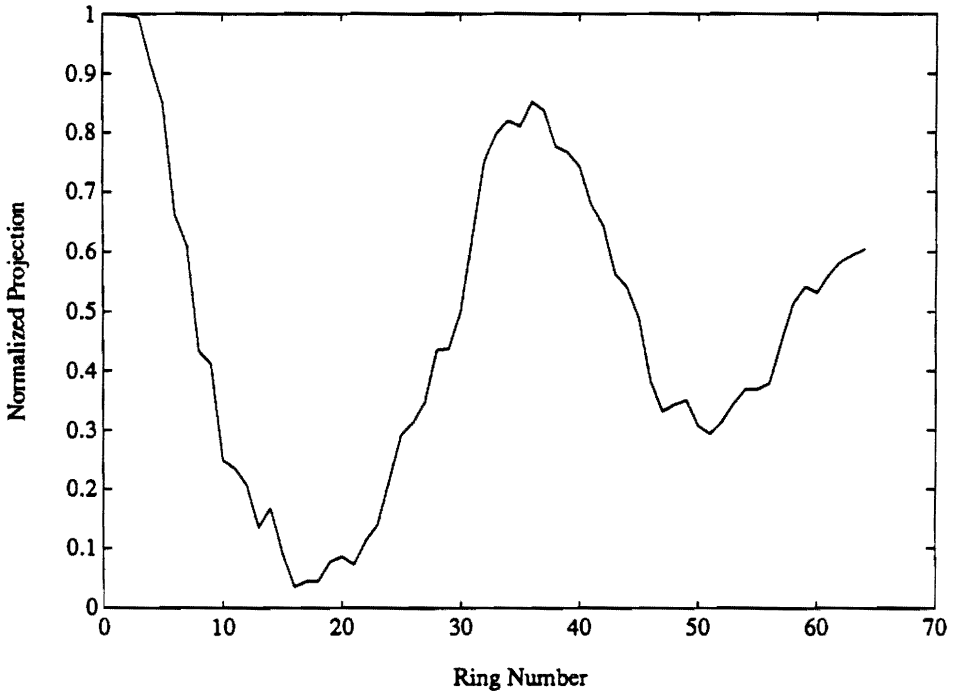

(c)

Figure 2.5: Cell boundary pattern and its Fourier transform: (a) input ($CD = 2000$ and $CV = 0.2$); (b) Fourier intensity pattern of (a); (c) normalized radial projection of (b).

2.2.2 Optical Set–Up and Experiments

Figure 2.6 shows the optical system and associated electronics used for the Fourier analysis of the input cells. This system includes a 2 mW He-Ne laser, a variable beam splitter (VBS) to adjust the laser beam intensity, a 20x microscope objective(MO1), a 25 μm pinhole, and a 2x microscope objective (MO2). MO1 expands the beam (after focusing it through the pinhole to clean the beam) to a suitable diameter. MO2 then focuses the beam to a spot in what is the Fourier plane. In the Fourier transform plane is a CCD TV camera. Since a WRD was not available in our lab, one with 64 annular rings and 64 wedge sections was simulated on a computer. The overall system was used as discussed in the following sections for the estimation of statistical cell parameters.

Figures 2.7 and 2.8 show 15 cell boundary patterns and their optical Fourier intensity patterns used for size statistics measurements. The cell patterns contain cells ranging in number from approximately 100 to 400, depending on cell density. Cell parameters CD and CV are given by the supplier of the patterns, Keeler Instruments, where CD represents the cell density ($1000 \sim 3000/mm^2$) and CV represents the coefficient of size variation ($0.2 \sim 0.5$) with respect to an average cell size. The cell patterns were photographed, and the resulting transparency was input to the optical Fourier transforming system depicted in Fig. 2.6. The optical Fourier intensity pattern was recorded on photographic film and digitized with 512x512 pixels of 256 gray levels for subsequent processing.

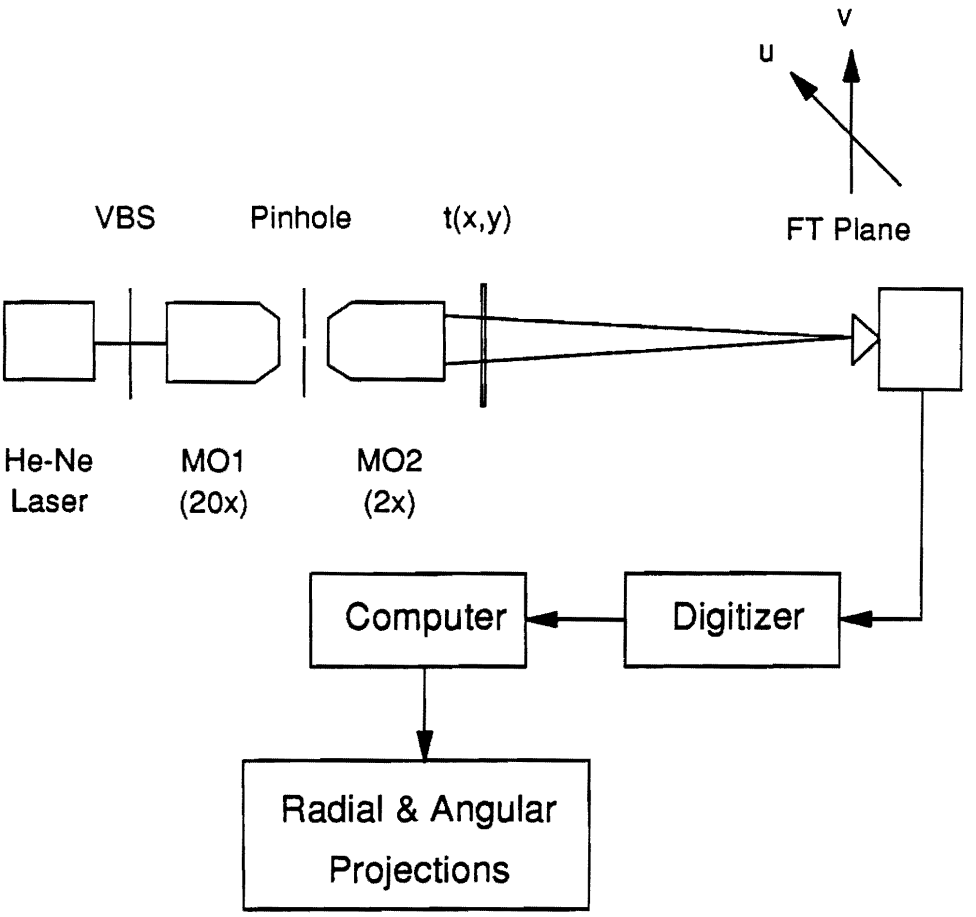

Figure 2.6: Optical setup used for experiments. The diffraction patterns were scanned, digitized, and analyzed on a computer since a wedge–ring detector was not available.

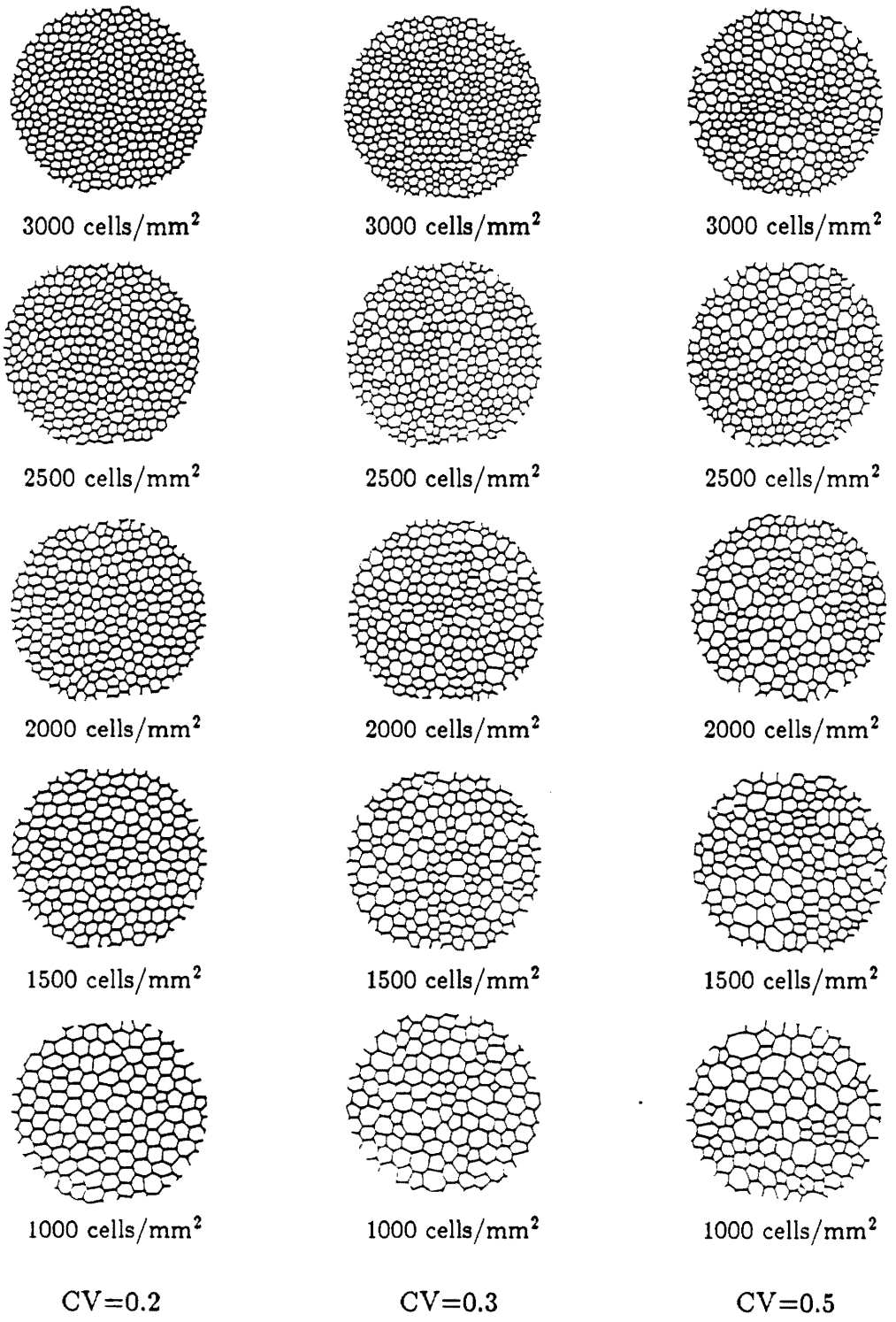

Figure 2.7: 15 cell patterns. The numbers give the cell density CD $(cells/mm^2)$; CV is the coefficient of size variation with respect to the mean cell size.

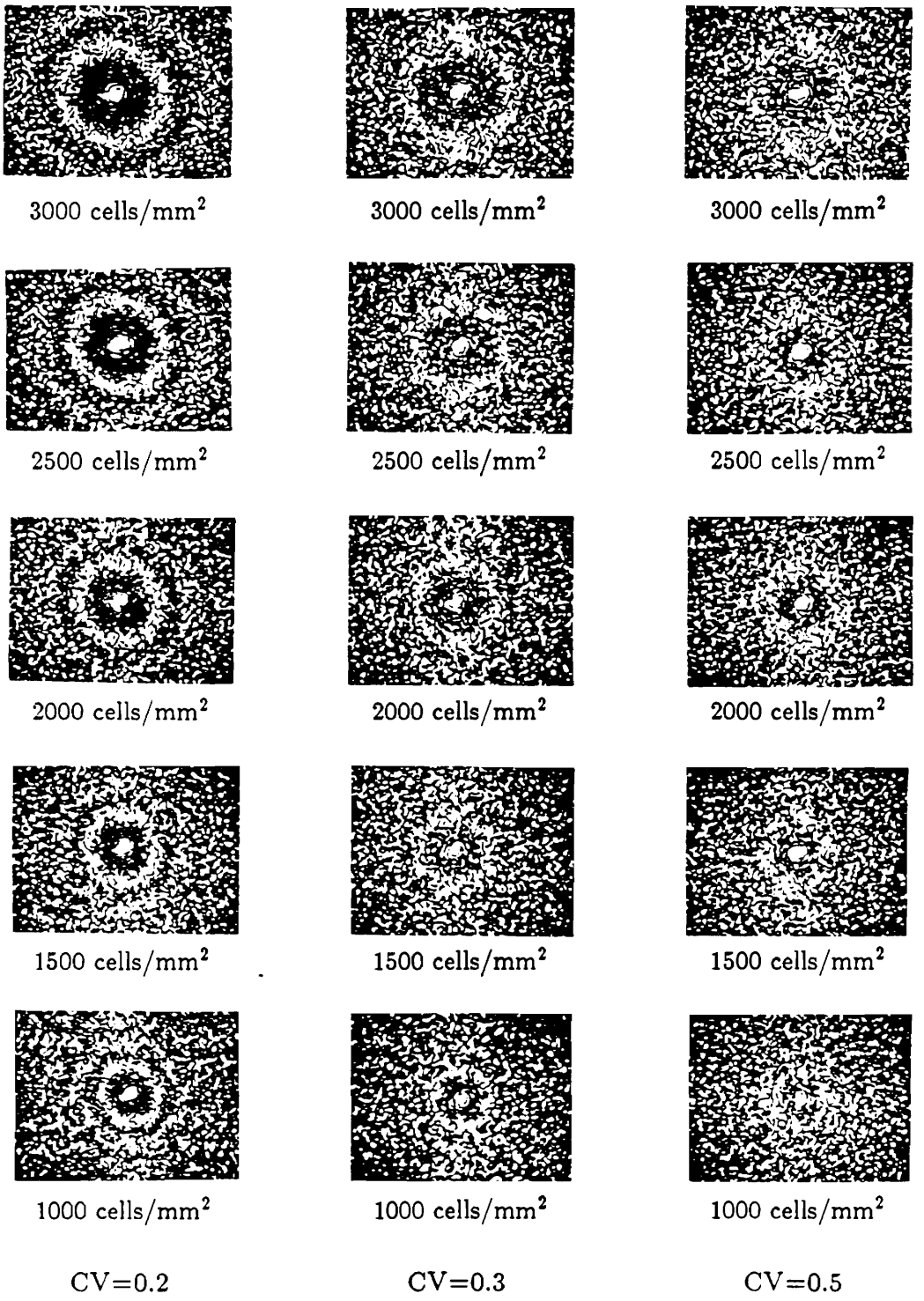

Figure 2.8: Optical Fourier intensity patterns of the cell patterns in Fig. 2.7.

2.3 Size Measures

In this section, methods are described for extracting information on size and size variation. The methods have been designed to be relatively easily automated. Experimental results, obtained optically using high contrast polygonal cell boundary patterns, are presented.

2.3.1 Radial Projection and Curve Fitting

To estimate average cell size (or density) and size variation we used the mean of a polynomial curve fitted to the radial projection R_m. Figure 2.9 shows an example: information is extracted on the average cell size and the size variation for the cell pattern with $CD = 2000$ and $CV = 0.2$. In the figure, the points marked by 'x' represent the raw radial projection R_m. This data is first subjected to 3–point median–filtering to reduce the effects of noise. The resulting points are connected by the dotted line in Fig. 2.9. The mean R_o of the median–filtered radial projection R_m is represented by the dashed line in Fig. 2.9. It is given by

$$R_o = \frac{1}{M_R} \sum_{m=1}^{M_R} R_m, \tag{2.4}$$

where M_R (= 64) is the number of semi–annular rings used in the computer simulation of a WRD. The difference d_{R_m} between R_m and R_o is then calculated:

$$d_{R_m} = R_m - R_o. \tag{2.5}$$

A fifth–order polynomial $p(x)$ is fitted to those points lying between the points labeled p_1 and p_2 in the figure. The variable x of $p(x)$ is the radial distance from the origin of the FT plane, corresponding to the radial spatial frequency. The fitted curve is represented by the solid line. The point $p_1 = 5$ was chosen in such a way that the dc bias and the low spatial frequency components (i.e., first few annular rings) of the Fourier intensity pattern were removed to obtain stable measures. Search was

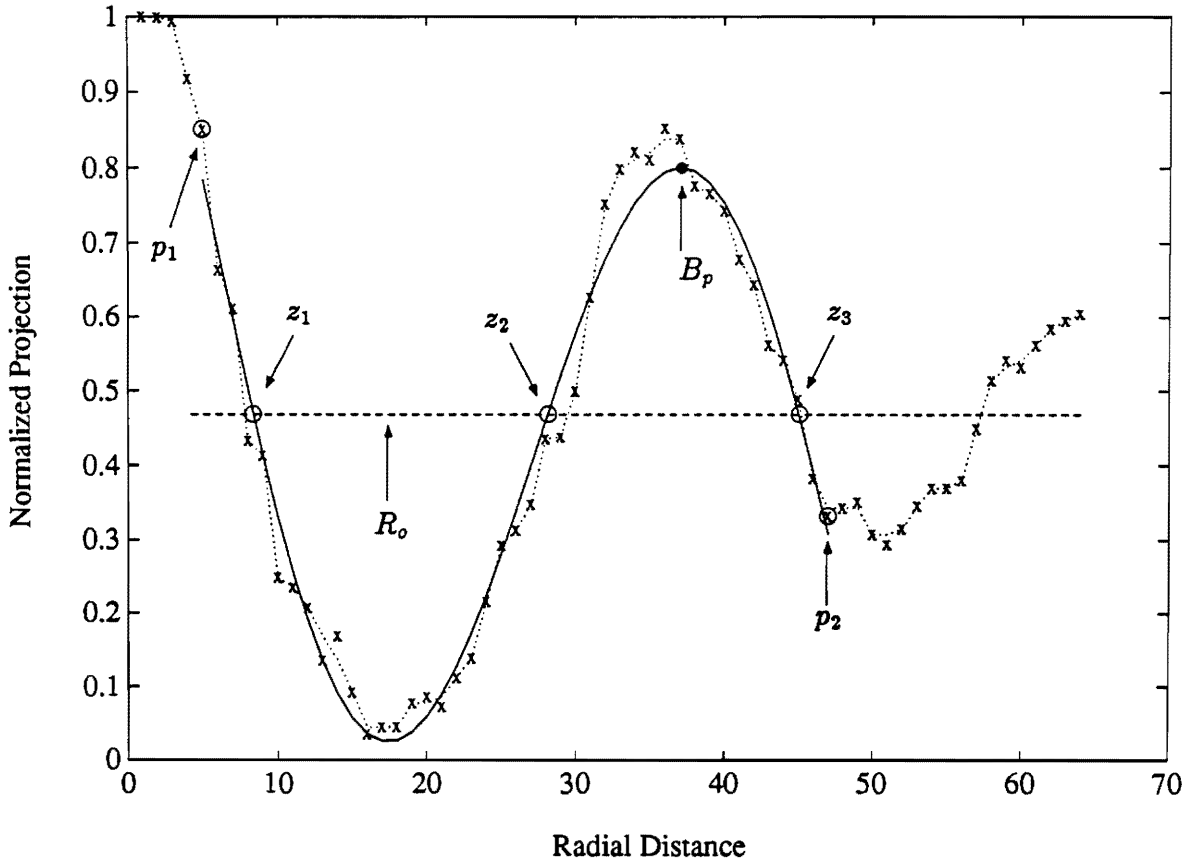

Figure 2.9: Determination of average cell density and size variation from Fourier intensity radial frequency measurements.

conducted among several points in the first lobe of R_m to find a transition point. This was defined as the point at which the difference d_{R_m} of Eq. 2.5 decreases (or increases) monotonically for 3 or more points. The point p_2 was determined by adding two more points to the transition point for the polynomial curve fitting. Three zero crossing points z_1, z_2, and z_3 in the difference $[p(x) - d_{R_m}]$ between the polynomial $p(x)$ and d_{R_m} (Eq. 2.5) were then located for subsequent processing to estimate average size and size variation, where $p(x)$ is the fitted polynomial.

2.3.2 Average Size

The size measure is obtained by locating the maximum point B_p (marked by '•') between z_2 and z_3 in Fig. 2.9. Figure 2.10 shows a plot of B_p versus $\sqrt{CD}$ obtained for the 15 cell patterns in Figs. 2.7 and 2.8. The solid line in Fig. 2.10 represents the linear regression of the 15 data points. It is clear from the high degree of linearity that cell size (or density) can be accurately inferred from measurements of the Fourier intensity patterns. The measurements in Fig. 2.10 were made by illuminating 100 to 400 cells at a time. By scanning the illuminating beam, it is possible to estimate cell density over an entire endothelial pattern, incorporating perhaps several thousand cells in a matter of seconds. That in itself illustrates the power of the hybrid optical method.

2.3.3 Size Variation Measure

For the estimation of size variation, the contrast between the first dark and bright regions of the Fourier intensity pattern is calculated. Note that the contrast decreases as CV increases. (See the cell patterns in Fig. 2.7 and their Fourier intensity patterns in Fig. 2.8.) A possible measure of the size variation can be made by calculating the contrast or normalized mean-square difference (NMSD) measure

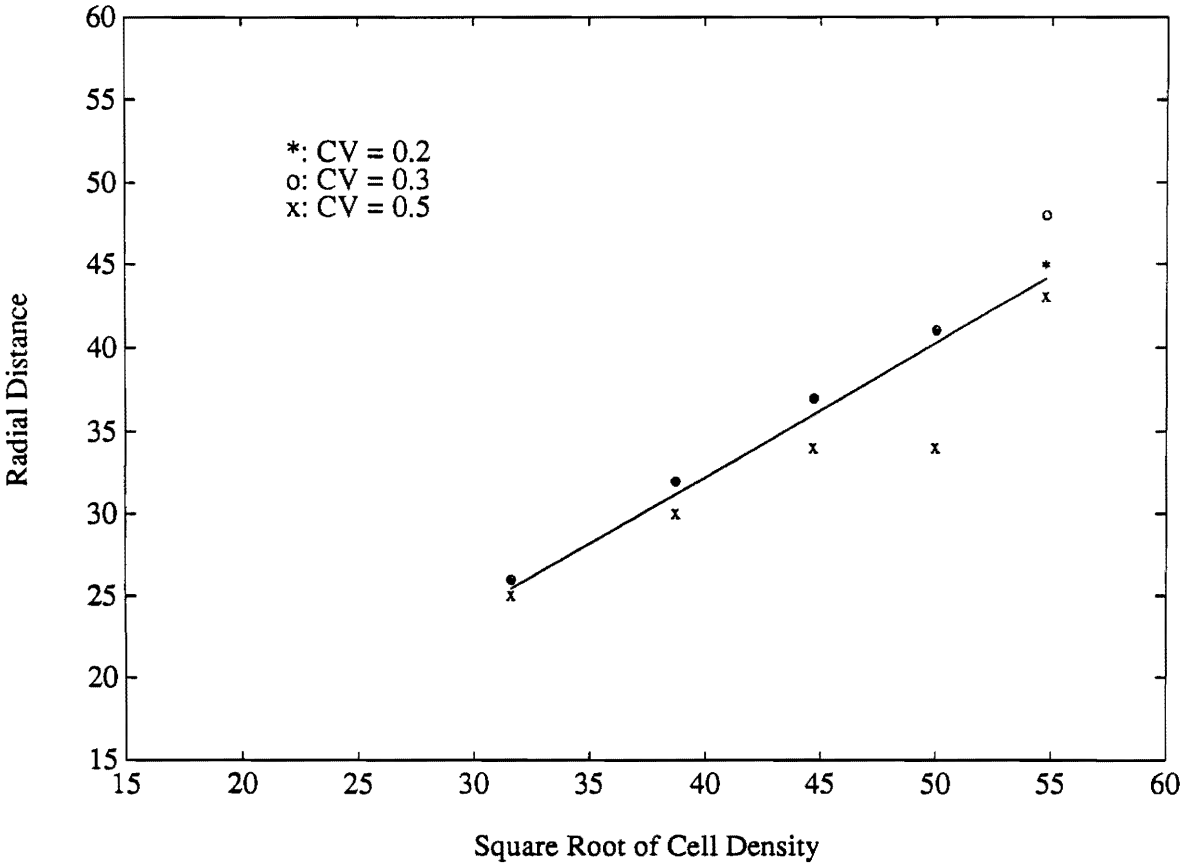

Figure 2.10: Plot of B_p versus $\sqrt{CD}$ for 15 cell patterns. The solid line represents the linear regression of the 15 data points. It is evident from the high degree of linearity of the data that cell size (or density) can be accurately inferred from measurements of the Fourier intensity patterns.

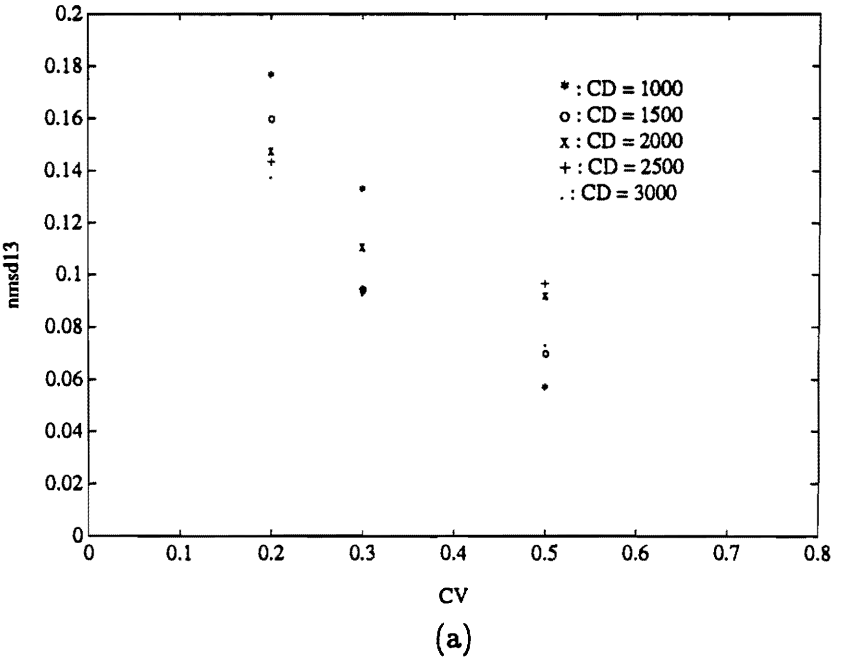

(a)

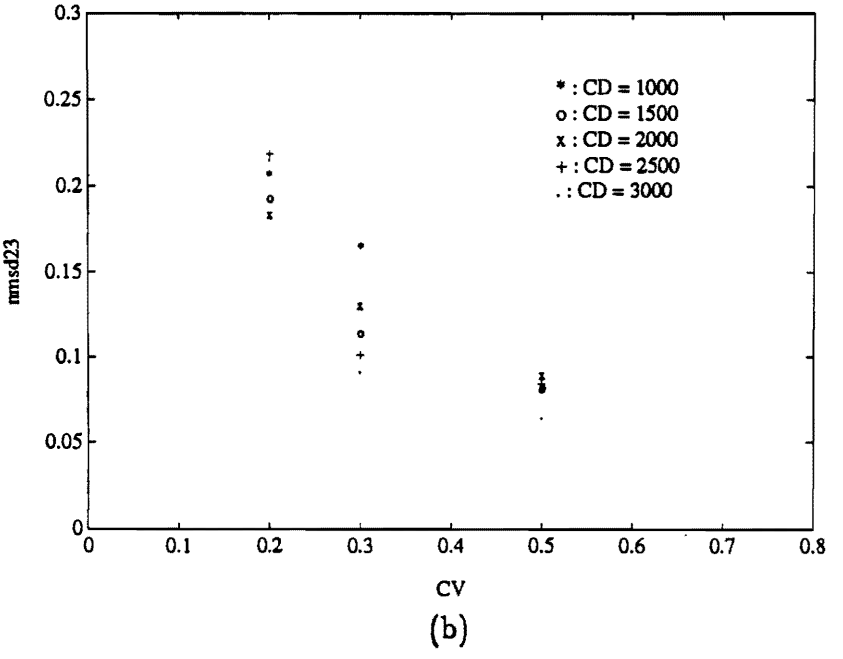

(b)

Figure 2.11: Plot of e_{13} [=nmsd13] in (a) and e_{23} [=nmsd23] in (b) versus CV for 15 cell patterns. The e_{23} measures tend to cluster better than e_{13}.

according to

$$e_{13} = \frac{1}{[z_3 - z_1]} \left\{ \sum_{x=z_1}^{z_3} [p(x) - R_o]^2 \right\}^{1/2} \tag{2.6}$$

where R_o is the mean of median–filtered points and $p(x)$ is the fitted fifth–order polynomial. In Eq. 2.6, the contrast (i.e., NMSD) measure e_{13} is inversely related to CV. Figure 2.11(a) shows the plot of e_{13} versus CV for 15 cell patterns, where nmsd13 = e_{13}. Note how well the data points cluster for each CV. A better clustered measure was obtained by calculating e_{23} between z_2 and z_3 (i.e., the first bright region of the Fourier intensity pattern):

$$e_{23} = \frac{1}{[z_3 - z_2]} \left\{ \sum_{x=z_2}^{z_3} [p(x) - R_o]^2 \right\}^{1/2} \tag{2.7}$$

Figure 2.11(b) shows the values of e_{23} calculated for 15 patterns. Based on the experimental results in Fig. 2.11, e_{23} tends to cluster better than e_{13}.

Figures 2.12 shows the results of polynomial curve fitting after median filtering, along numerical values of B_p, e_{13} [=nmsd13], and e_{23} [=nmsd23] for the cell patterns with $CV = 0.2$. Similarly, Figs. 2.13 and 2.14 show the results obtained from the cell patterns with $CV = 0.3$ and $CV = 0.5$, respectively.

2.3.4 Algorithm

The algorithm for the size measurement of cells is summarized as follows.

- Algorithm:

  1. Obtain the radial projection R_m $(1 \leq m \leq 64)$ for a large group of cells (e.g., 400); subject raw data to median filtering to reduce the effects of noise.
  2. Calculate the mean R_o of the median–filtered value R_m.
  3. Determine p_1 and p_2 in order to fit a polynomial curve. (See text)

4. Fit a fifth–order polynomial $p(x)$ to those points lying between p_1 and p_2.

5. Calculate the difference $[p(x) - R_o]$ and locate the three zero crossing points z_1, z_2, and z_3.

6. For average size or density measure, locate the maximum point B_p between z_2 and z_3.

7. For the size variation measure, calculate the normalized mean–square difference measure e_{13} or e_{23}, in accord with

$$e_{13} = \frac{1}{[z_3 - z_1]} \left\{ \sum_{x=z_1}^{z_3} [p(x) - R_o]^2 \right\}^{1/2} \tag{2.8}$$

or

$$e_{23} = \frac{1}{[z_3 - z_2]} \left\{ \sum_{x=z_2}^{z_3} [p(x) - R_o]^2 \right\}^{1/2} \tag{2.9}$$

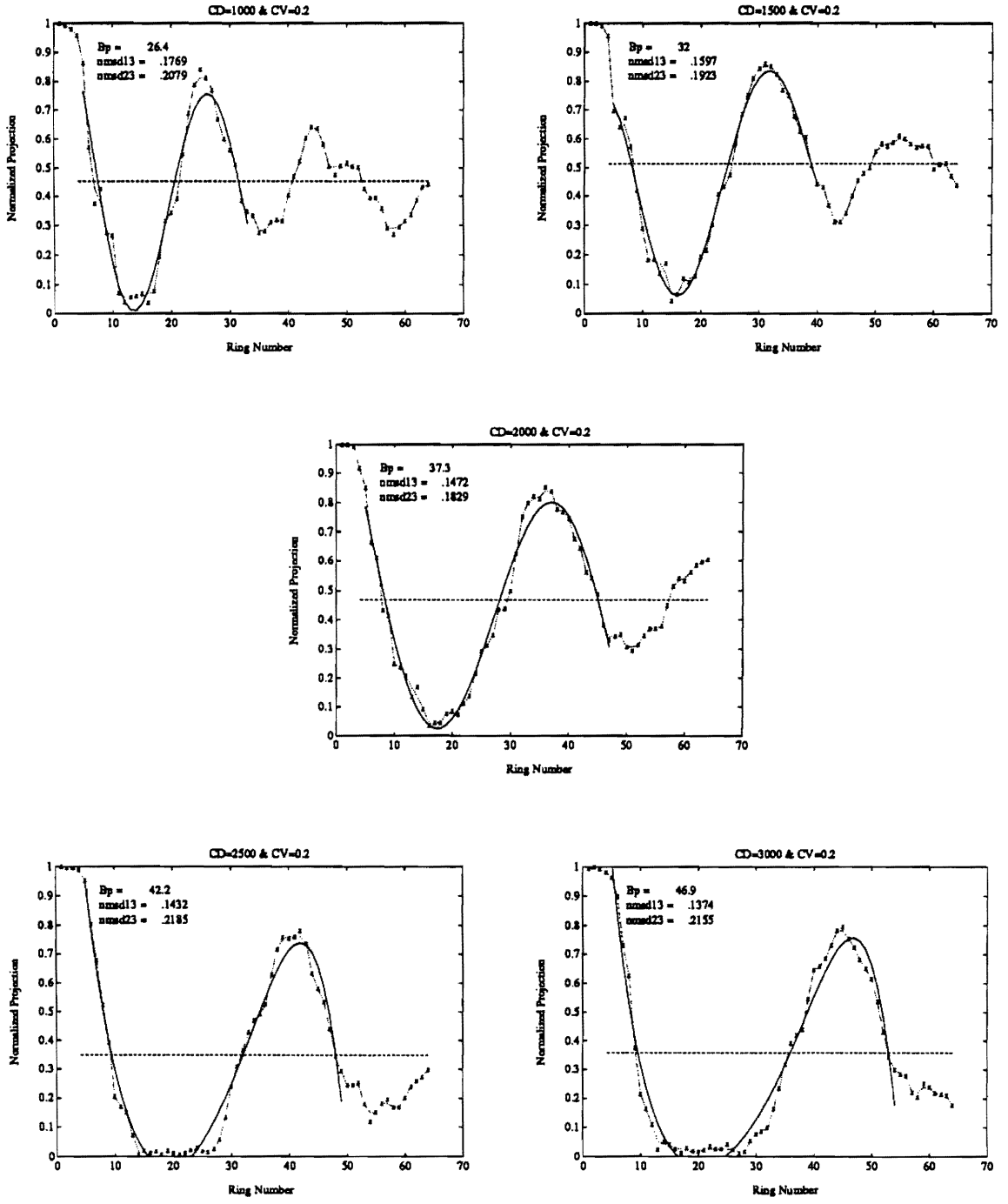

Figure 2.12: Examples of calculating e_{13} [=nmsd13] and e_{23} [=nmsd23] for the patterns with $CV = 0.2$.

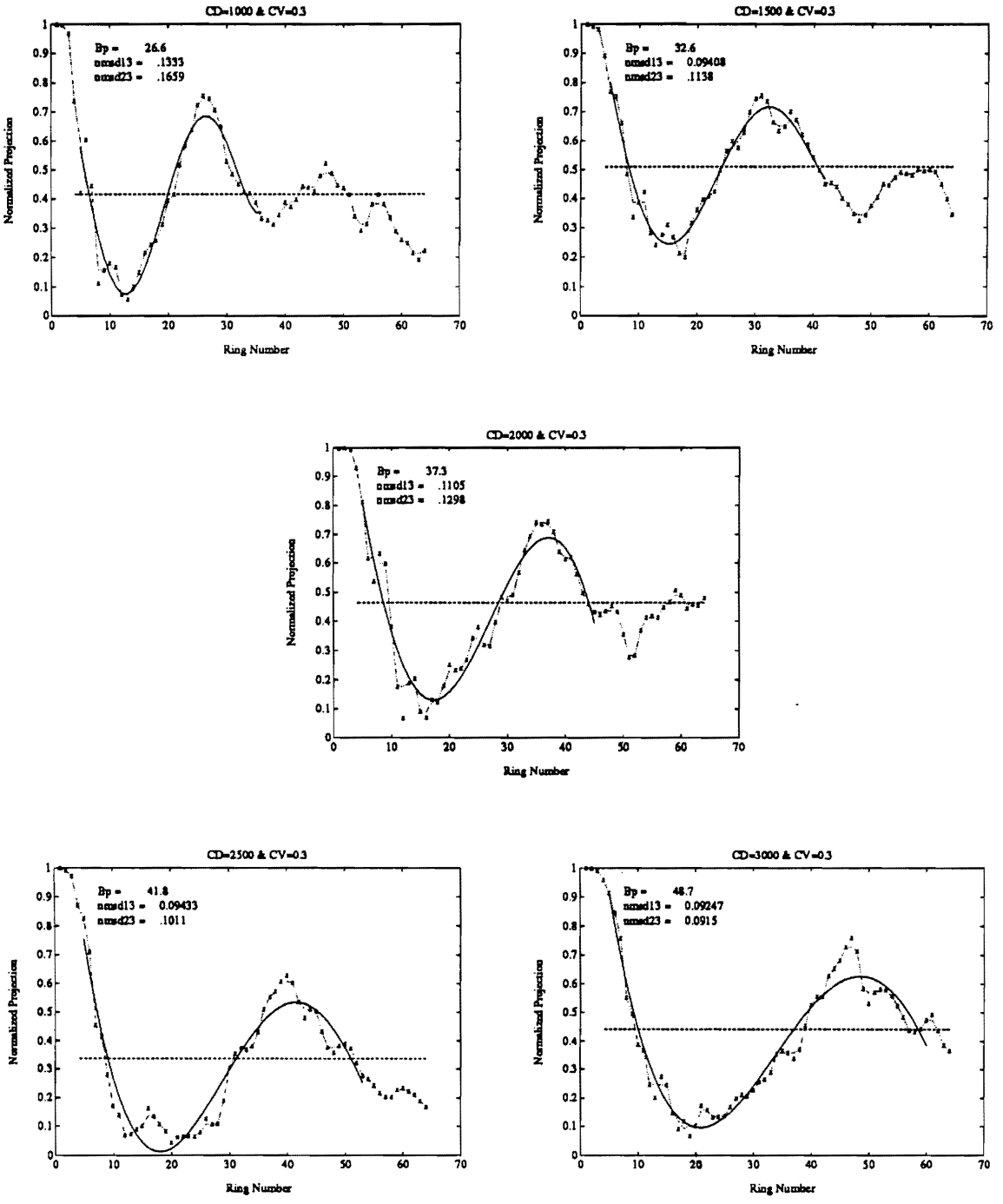

Figure 2.13: Examples of calculating e_{13} [=nmsd13] and e_{23} [=nmsd23] for the patterns with $CV = 0.3$.

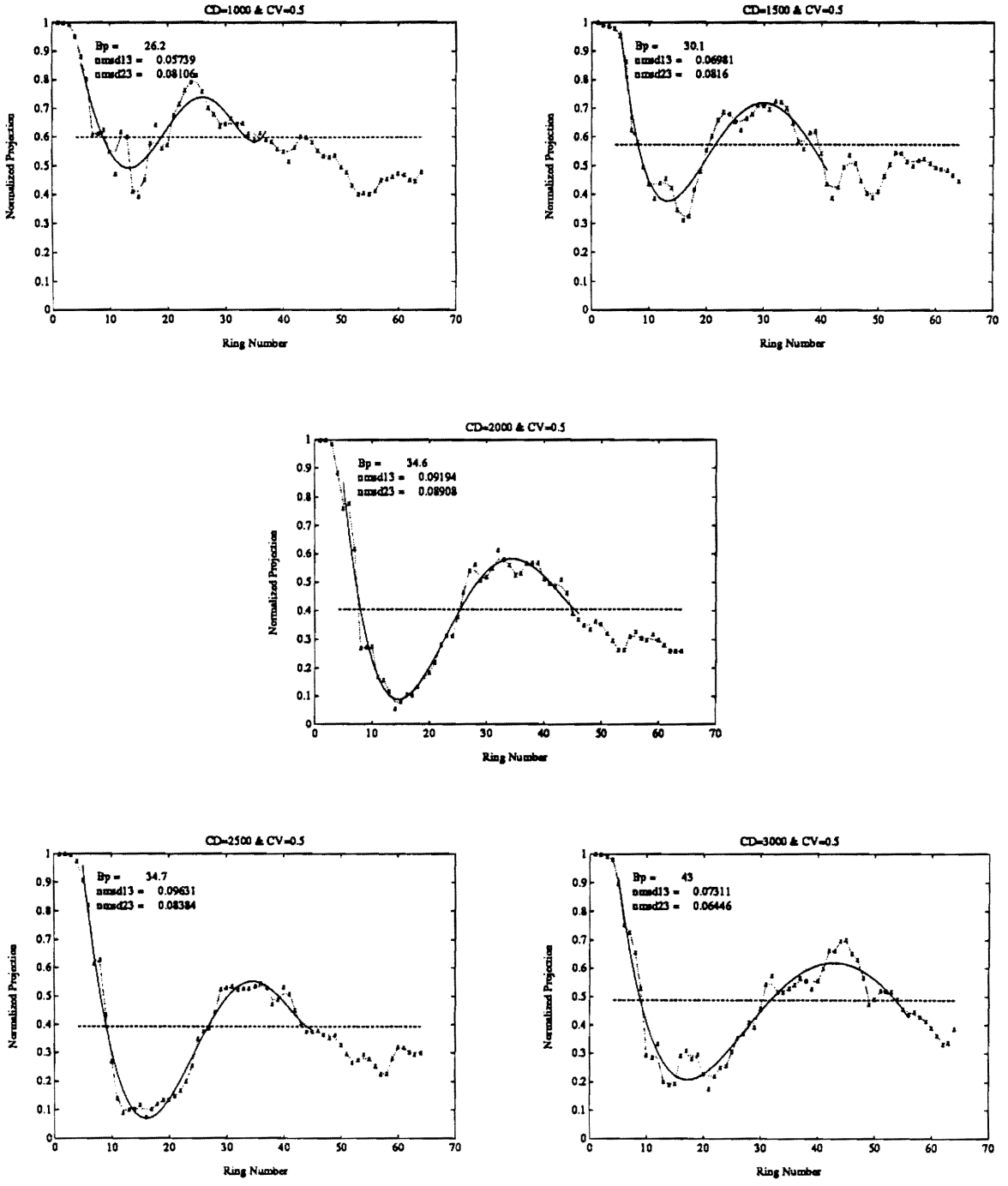

Figure 2.14: Examples of calculating e_{13} [=nmsd13] and e_{23} [=nmsd23] for the patterns with $CV = 0.5$.

2.4 Shape Measures

2.4.1 Algorithm and Optical Experiments

It was relatively straightforward to obtain measures of the size and size variation by scanning a number of cells. However, cell shape cannot be determined directly by scanning a large group of cells at a time, since coherent averaging eliminates shape information on individual cells. This coherent averaging effect can easily be seen in Fig. 2.5 where approximately 200 cells were illuminated. Initial studies [57] indicated that to obtain useful shape information from the FT patterns of cells it is desirable to limit the illuminated area of an input pattern to a small region, i.e., approximately one cell size.

In order to remove the orientational dependence of cells, the angular correlation function, $C(n)$ is calculated from A_n,

$$C(n) = (\sum_{k=1}^{M_W} A_k A_{k+n})/(\sum_{k=1}^{M_W} A_k^2) \qquad 0 \leq n \leq 63 \qquad (2.10)$$

where A_k = the kth component of the angular projection and M_W (= 64) is the number of wedge segments. Figure 2.15 shows $C(n)$ for the single hexagon of Fig. 2.2; two well-defined peaks appear at 60° and 120°. The angular correlation function for a regular hexagonal array pattern has similar appearance, though with sampled version. Examples of the Fourier intensities and associated angular correlations of various polygons are presented by Masters, Lee, and Rhodes in [57].

The algorithm for the shape measurement of cells is summarized as follows.

- Algorithm:

  1. Obtain the angular projection A_n, $1 \leq n \leq M_W$, for each small scanned area, i.e., approximately one cell size.
  2. Compute the angular correlation function $C(n)$ (Eq. 2.10) for each scanned area.

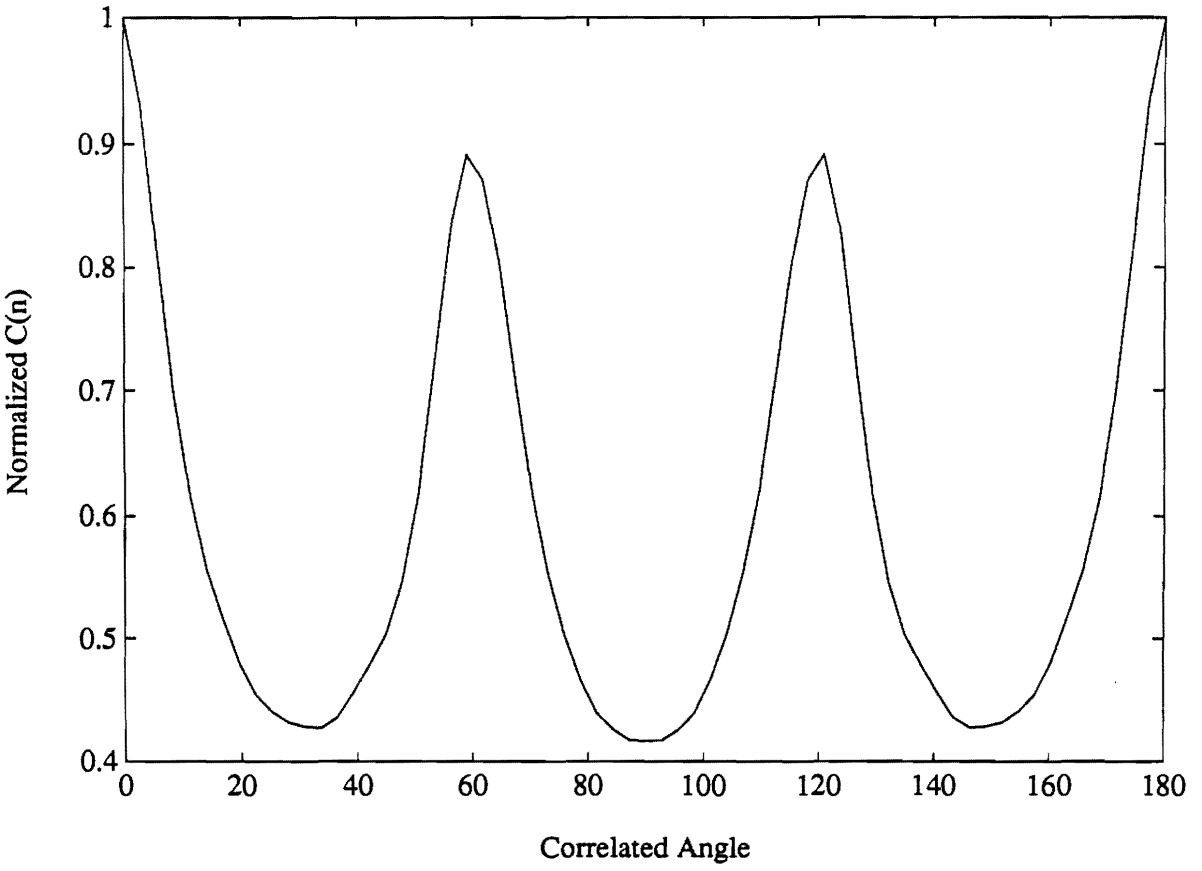

Figure 2.15: Angular correlation $C(n)$ obtained for the single hexagonal boundary pattern in Fig. 2.2.

3. Repeat Steps 1 to 3 N_S times.

4. Sum all $C(n)$'s and find the mean $C_m(n)$:

$$C_m(n) = \frac{1}{N_S} \sum_{i=1}^{N_S} C^i(n), \tag{2.11}$$

   where $C^i(n)$ is $C(n)$ obtained from the ith scanned area.

5. Measure the peak–to–peak distance and the width of the angular lobe around each peak in $C_m(n)$.

In application of this method, the 24 cells shown in Fig. 2.16(a) were manually scanned, one cell at a time, with a beam size slightly larger than the fifth cell. Figure 2.16(b) and (c) show the FT patterns of two cells (Nos. 14 and 15) and their angular correlation functions [= $C(n)$]. The mean $C_m(n)$ of angular correlation functions obtained from 24 numbered cells is shown in Fig. 2.16(d). $C_m(n)$ in (d) still has well–defined peaks and dips as well as angular lobes, but the peaks are broader with much higher amplitude ratio of dip to peak than those of the hexagonal pattern in Fig. 2.15. The peaks are located at approximately 60° and 120°. The shape–related characteristics found with individual cell transforms are lost in the Fourier intensity pattern of a large group of cells, as shown in Fig. 2.5, but preserved, in an average sense, in the mean of the correlation functions associated with these individual cells. It has been observed that the location and width of the peaks in $C_m(n)$ may represent the average shape and the average variation of sides of 24 scanned cells. It is hypothesized that the locations and the widths of the peaks have clinical diagnostic significance in much the same way that percent–of–hexagons and CV do now. For example, pronounced peaks at 60° and 120° on the θ axis suggests a preponderance of hexagonal cells.

2.4.2 Other Effects On Shape Measure

Two factors are noted that affect the mean of the correlation functions, $C_m(n)$.

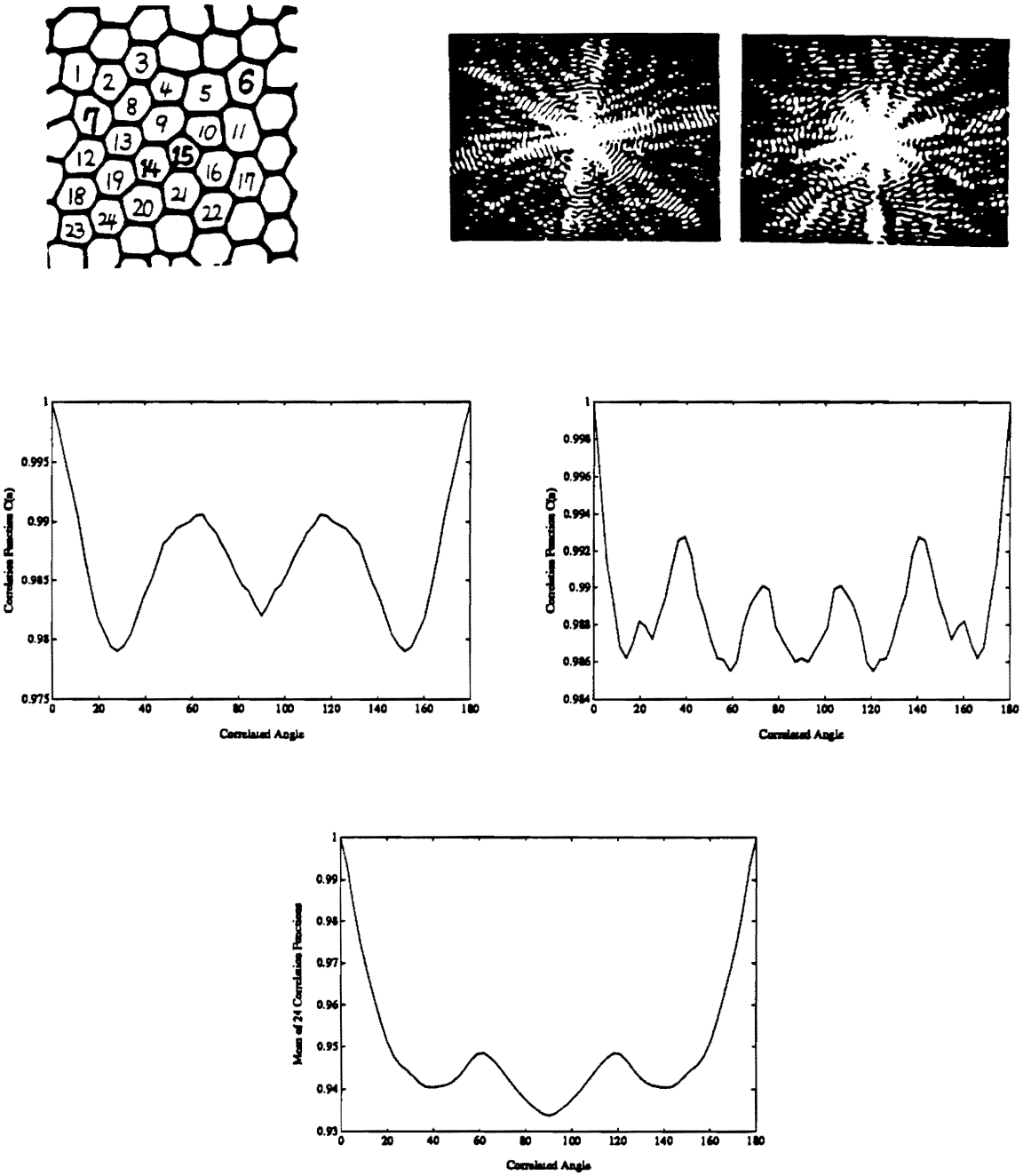

Figure 2.16: Experimental results using local scans for shape measurement. (a) Upper–left: 24 numbered cells. (b) Upper–right: optical Fourier intensity patterns of cells 14 and 15. (c) Middle: angular correlation functions [$= C(n)$] for cells 14 (left) and 15 (right). (d) Bottom: mean of 24 $C(n)$'s obtained from 24 numbered cells in (a).

- Width of line segments.

  To see the effect of line width on the resultant $C_m(n)$, two regular hexagons with thin and thick line segments were Fourier transformed and their $C(n)$ calculated. Figure 2.17 shows the input patterns and their angular correlation functions. It can be seen that a thinning operation on the given input pattern has sharpened the angular correlation function. Thus for a collection of polygons such as pentagons, hexagons, and heptagons, The sharpened angular lobe may reduce the average background value of $C_m(n)$, representing better polygonal characteristics than a wider one.

- Low spatial frequency components on the FT pattern.

  The angular correlation function $C(n)$ in Fig. 2.16(c) is sharpened if the very low spatial frequency components in the FT pattern are removed. In the previous experiment using 24 numbered cells, the low frequency components within a radial distance (16 in pixel number) from the origin of the Fourier intensity pattern with 512x512 pixels were removed to compute $C_m(n)$.

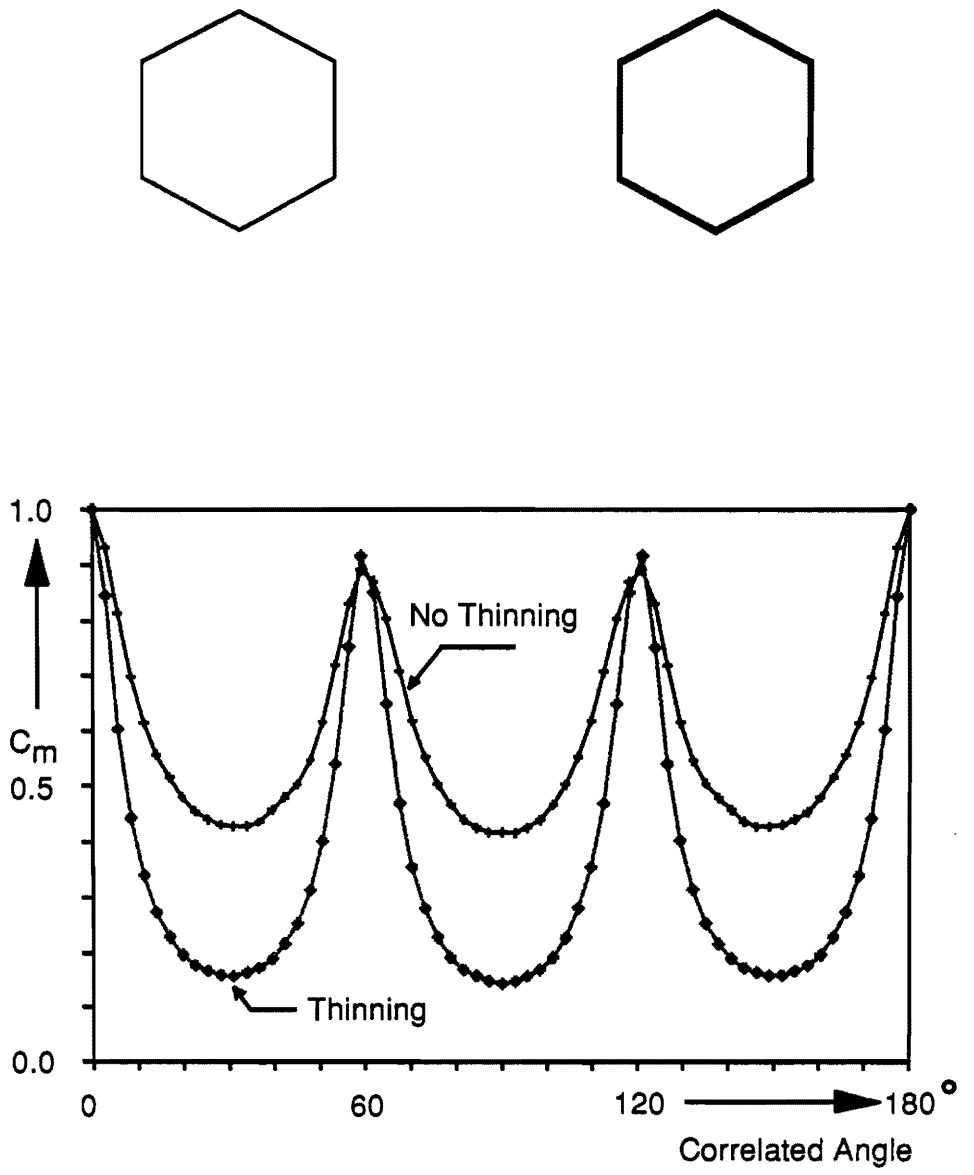

Figure 2.17: Effect of line width on angular correlation function. (a) Top: Two hexagons with thin and thick boundaries. (b) Bottom: Their angular correlation functions.

2.5 Summary and Discussion

Size measures were obtained by applying a median filtering to reduce the effects of noise and then a fifth–order polynomial curve fitting in the first dark and bright region. The size information was then obtained by locating the maximum point B_p between the second and third zero–crossing points (i.e., z_2 and z_3) or spatial frequencies in the fitted fifth–order polynomial. Variations in cell size were extracted by calculating normalized mean–square difference (NMSD) measures in the first dark and bright regions for the fitted fifth–order polynomial. For the size variation measure, two NMSD measures e_{13} and e_{23} were obtained. Based on the experimental results, the latter measure were better clustered.

For shape measure, a local scanning method has been used by illuminating one cell at its center (or equivalently a small region) at a time for 24 cells and then calculating the mean $[= C_m(n)]$ of the resulting angular correlation functions $[= C(n)]$. Other shape measure may be considered other than the method discussed in Sec. 2.4, illuminating vertices of the cell boundaries. At each vertex, the optical Fourier intensity pattern consists of three spokes. If the cells are ideally or predominately hexagonal in shape, vertices of the cells will have three outgoing–lines separated by 60° and then the mean of the angular correlation function in Eq. 2.11 will have two peaks at 60° and 120°. Recently, it was encouraged from a private communication [61] that this information can be useful for a global shape information.

CHAPTER 3

OPTICAL ROTATING KERNEL TRANSFORMATION (RKMT)

This chapter begins with the discussion of techniques for detecting and enhancing linear features (e.g., straight line segments) in an input image, and introduces novel algorithms for linear feature enhancement by a rotating kernel min–max transformation (RKMT) processing. A quantitative evaluation of the RKMT processing is then presented, followed by the introduction of an optical implementation of RKMT processing.

3.1 Introduction

Linear or quasilinear features are observed under many circumstances: straight–line edge segments on outdoor scenes containing man–made objects [62], ocean waves in a SAR image [9], roads in military road maps [10], and a variety of biological structures [63,64,6,7]. Striated–line structures are also of interest in various applications. Such patterns are seen in airport runways, seismic data [65,66], fingerprints [11,67], histologic preparations of the corneal stroma [63], and photographs of the retinal nerve fiber layer [11,64]. To detect or enhance such linear features, digital techniques based on the Hough transform [44,45] and the Radon transform [9,31,32] as well as fan–type filters [67,68,69] and a method [11] based on human visual model [70] have been used in a wide variety of applications. Since these techniques are somewhat related to the RKMT processing, some of these techniques are briefly discussed in

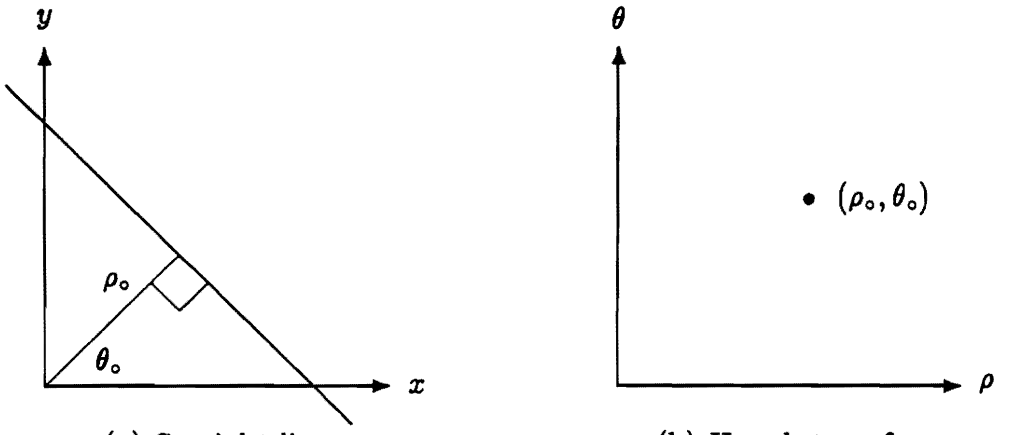

(a) Straight line (b) Hough transform

Figure 3.1: The Hough transform.

this section.

The Hough transform (HT) was initially proposed for detecting lines using the slope–intercept parameters, i.e., (a, b) in the equation $y = -ax + b$. Since the slope and intercept were not bounded, application of the technique was rather complicated. Duda and Hart [45] suggested a modified Hough transform using a different parameter space, (ρ, θ), to overcome the complexity:

$$x\cos\theta + y\sin\theta = \rho, \tag{3.1}$$

where ρ is the normal distance to a straight–line and θ is the angle between the normal direction and the horizontal axis in the Cartesian coordinate system. Figure 3.1 shows an example of the HT of a single straight line in an input image. Each point on the line in (a) maps into a sinusoidal curve in the HT plane. All the mapped points have a common point (ρ_o, θ_o) in the HT plane (ρ, θ) as shown in (b), and contribute to producing a high peak at that point. Extensions of the approach have been described for the detection of circles [71], parabolas [72], ellipses [73], and other arbitrarily shaped curves [74,75]. The HT can be applied to binary–valued images [45] or, in extended form, to multiple–valued images [76,77]. The HT may also be applied to the detection of lines in noisy images. If the points in input im-

age are approximately collinear in noisy background, for example, the HT of these points tends to show clustering rather than producing an ideal common point with high peak.

Closely related to the HT is the Radon transform (RT) [31,32]. The RT may be applicable to the enhancement of linear features (e.g., straight line segments) because it has an inverse. Deans [78] has pointed out that the HT can be interpreted in terms of the RT. The special case of the RT in 2–D image space can be expressed as

$$f_R(\rho,\theta) = \int\int_D f(x,y)\delta(\rho - x\cos\theta - y\sin\theta)dx\,dy \tag{3.2}$$

where $f(x,y)$ and $\delta(*)$ are a two dimensional input image and a line–delta function, respectively. In Eq. 3.2, $f_R(\rho,\theta)$ represents a line integral of $f(x,y)$ along the line, $x\cos\theta + y\sin\theta = \rho$. Equation 3.2 can be written in 2–D convolution form using the rotation operator $\mathcal{R}_\theta\{\ \}$:

$$f_R(\rho,\theta) = f(x,y) ** \mathcal{R}_\theta\{1(x)\,\delta(y)\}, \tag{3.3}$$

where $**$ represents the 2–D convolution operation and $\mathcal{R}_\theta\{\ \}$ represents a rotation of the 2–D function serving as an argument through an angle θ. The 2-D Fourier transform of $f_R(\rho,\theta)$ is given by

$$F_R(\rho,\theta) = F(u,v)\,\mathcal{R}_\theta\{\delta(u)\,1(v)\}, \tag{3.4}$$

where $F_R(\rho,\theta)$ and $F(u,v)$ are the 2–D Fourier transforms of the RT and the input image, u and v being the horizontal and vertical frequency coordinates, respectively. From Eqs. 3.3 and 3.4, it can be seen that the RT is a 1–D projection along the straight line at angle θ in the frequency domain whose direction is orthogonal to that of the line feature itself in the space domain. Therefore, the RT performs well detecting and enhancing such linear features extended over the entire input plane, by incorporating an enhancement operator in the RT plane with the inverse RT.

Various methods have been proposed for the optical implementation of the HT and the RT, including use of an input rotator and a linear detector array [79], a

pair of spherical and cylindrical lenses with a linear detector array [80], a matrix of space variant holographic filters [81], and parallel holographic generation of multiple Hough transform slices [82].

Two digital techniques [9,11] to enhance linear features in noisy background are briefly discussed using the RT and human fan–type filter based on human visual model. Some distinctions between these techniques and RKMT processing are made for automated enhancement of linear features with random orientations and varying dimensions. Murphy [9] has successively applied the RT for enhancing the linear features of ocean waves seen in a noisy SAR image. However, there are two major deficiencies of using the RT for line detection and enhancement in certain situations:

1. Linear features are embedded in noisy background with spatially varying average intensity from one region to another.

2. Dimensions of linear features have a wide variation, certain dimensions being much less than those of the input image itself.

3. Mixture of cases 1 and 2.

In case (1), high peaks may not represent the existence of linear features since these peaks may result from some local bright regions with no linear features. A highpass spatial filtering operation may be used to reduce the effect of such slowly varying characteristics. However, the highpass filtering operation emphasizes noise structures. In case (2), specific peaks obtained from noise structures in the RT plane may achieve higher magnitudes than those obtained from linear features with small dimensions.

A method alternatively described by Peli [11] for enhancing striated–line features in fingerprint imagery is based on a visual model of the cortical cells' response [70]. The latter method may be used to overcome the deficiency encountered in case (2). In the method, a small block or local region of the input image is filtered by a small window (i.e., filtering mask) one at a time, where striated–line

features (i.e., ridge structrues) have a predominant orientation (perhaps only one orientation). However, this method requires intensive human intervention to select an appropriate window size and is difficult to place automatically the selected window in the input image, avoiding multiple orientations of linear features within the window. Furthermore, such block processing approach may loose information about boundaries between two windows containing linear features and noise background. To overcome the aforementioned difficulties encountered in automated linear feature enhancement operation, the RKMT processing operation, discussed for the remainder of this thesis, has been proposed [6,7].

3.2 Rotating Kernel Min–Max Transformation

In this section, the rotating kernel min–max transformation (RKMT) is defined along with various types of 2–D kernels and transform functions used in its applications.

3.2.1 Definitions

The RKMT method utilizes directional information in a local–circular region about each point in an input image. It can be used to extract information on particular locally directional features (e.g., linear features) to be detected. The theory for the RKMT is easily described in terms of space–domain operations. Figure 3.2 shows a block diagram of the basic operation. The input image is convolved with a long, narrow 2–D kernel of noncircular symmetric or asymmetric profile, which is rotated through 360 degrees, either continuously or discretely in a large number of steps. The convolution output $S_\theta(x,y)$ is described by

$$S_\theta(x,y) = \int_{-\infty}^{\infty}\int_{-\infty}^{\infty} O(x-p, y-q)\, K_\theta(p,q)\; dp\, dq \tag{3.5}$$

where $O(x,y)$ is the input image and $K_\theta(x,y)$ is the 2–D kernel, rotated through the angle θ. As the kernel rotates, the convolution output $S_\theta(x,y)$ is monitored and the maximum [= Max(x,y)] and minimum [= Min(x,y)] values of $S_\theta(x,y)$ at each point (x,y) are stored. The Max(x,y) and Min(x,y) values are defined in accord with

$$Max(x,y) = \text{maximum}\{S_\theta(x,y) : 0 \le \theta < 360°\}, \tag{3.6}$$

$$Min(x,y) = \text{minimum}\{S_\theta(x,y) : 0 \le \theta < 360°\}. \tag{3.7}$$

The output image $I_{out}(x,y)$ is given by an application–dependent function $f[\ ,\ ]$ of $Max(x,y)$ and $Min(x,y)$ values:

$$I_{out}(x,y) = f[Max(x,y), Min(x,y)]. \tag{3.8}$$

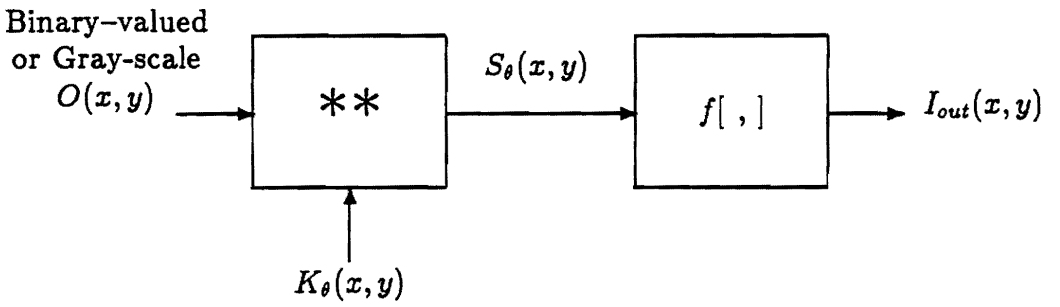

Figure 3.2: A block diagram of the RKMT operation. $O(x,y)$ and $K_\theta(x,y)$ are the input and rotating kernel oriented at an angle θ. $S_\theta(x,y)$ is the convolution output. The output $I_{out}(x,y)$ is given by an application–dependent function $f[\ .\ ]$ of Max(x,y) and Min(x,y) values.

3.2.2 Symmetric and Asymmetric 2–D Kernels

A variety of 2–D kernels with high directionality (large aspect ratio) can be used for RKMT processing [6,7,83,84]. These can be classified into two groups: symmetric profiles and asymmetric profiles. The symmetric kernels include 2–D rectangular, parabolic, triangular, exponential, and more generally Gaussian profiles, as presented in Tab. 3.1. L and W are the length and width of the kernels. Because of the symmetry of these kernels, it is only necessary to consider the convolution outputs for θ ranging from 0° to 180°, since the convolution outputs for the remaining angles are the duplication of those for the first 180 degrees. Figures 3.3(a) and (b) show side views of the symmetric rectangular and triangular profile kernels. Figure 3.3(c) and (d) show corresponding asymmetric kernels. Figure 3.4 shows perspective views of various kernels and their Fourier transform amplitudes, including rectangular, triangular, parabola, and Gausslan (a=7) profiles in Table 3.1. The kernel dimension used is $L = 21$ and $W = 3$. The kernel profile in the y direction (see Fig. 3.4) is not critical, though somewhat better performance is expected to result with a Gaussian profile. A variation of the rectangular profile kernel can be considered as a kernel with a + (plus) mark profile or the sum of two symmetric

1–D Profile	$K_\theta(x,y)$	Note
Rectangular	$\mathcal{R}_\theta\{\text{Arect}(\frac{x}{L},\frac{y}{W})\}$	$W \ll L$
Parabolic	$\mathcal{R}_\theta\{\text{A}[\text{rect}(\frac{x}{L},\frac{y}{W})][1-(\frac{x}{L})^2]\}$	$W \ll L$
Triangular	$\mathcal{R}_\theta\{\text{Atri}(\frac{x}{L/2})\text{rect}(\frac{y}{W})\}$	$W \ll L$
Exponential	$\mathcal{R}_\theta\{\text{Arect}(\frac{x}{L},\frac{y}{W})\exp(-\frac{x}{a})\}$	$W \ll L$
Gaussian	$\mathcal{R}_\theta\{\text{Arect}(\frac{x}{L},\frac{y}{W})\exp(-\frac{x^2}{a^2})\}$	$W \ll L$

Table 3.1: Various 2–D kernels in which rect and tri represent rectangular and triangular functions, respectively. In each kernel, L and W are the length and width of 2–D kernels, respectively, and A and a are constants.

rectangular profiles which are orthogonal to each other.

The rectangular profile kernel in Tab. 3.1 has uniform weight for all points. Application of the rectangular profile kernel to linear feature enhancement may cause certain features (e.g., line segments) to be thickened and some image detail to be lost. A rectangular profile kernel with an impulse in the center will in some cases reduce this thickening and smoothing effect.

With the various nonrectangular profile kernels shown Tab. 3.1, input image points away from the center of the kernel contribute less to the convolution output compared to those points near the center, and thickening of line segments is reduced. This property is illustrated by a Min operation followed by an ideal thresholding–hard limiting. Figure 3.5 illustrates this operation, in a numerical simulation, with a symmetric triangular profile kernel of length $L = 23$ and width $W = 1$. Min values are found when the kernel orientation is orthogonal to the line segments. A binary input in Fig. 3.5(a) is subjected to the Min operation, where the width of a typical line segment is approximately 9 pixels. The result of applying the Min operation is shown in (b). Figure 3.5(b) demonstrates enhancement of the center portions of the line segments. Thus, a thin line segment can be obtained by thresholding

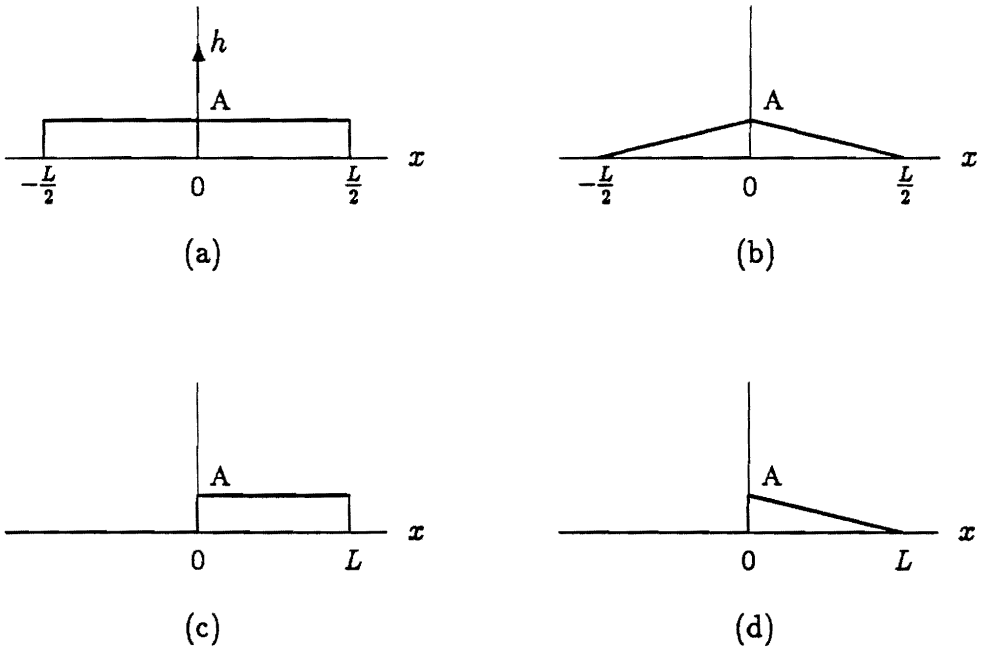

Figure 3.3: 1–D representation (broad side view) of 2–D kernels: (a) symmetric rectangular profile (impulse at center may be excluded); (b) symmetric triangular profile; (c) aymmetric rectangular profile; (d) asymmetric triangular profile.

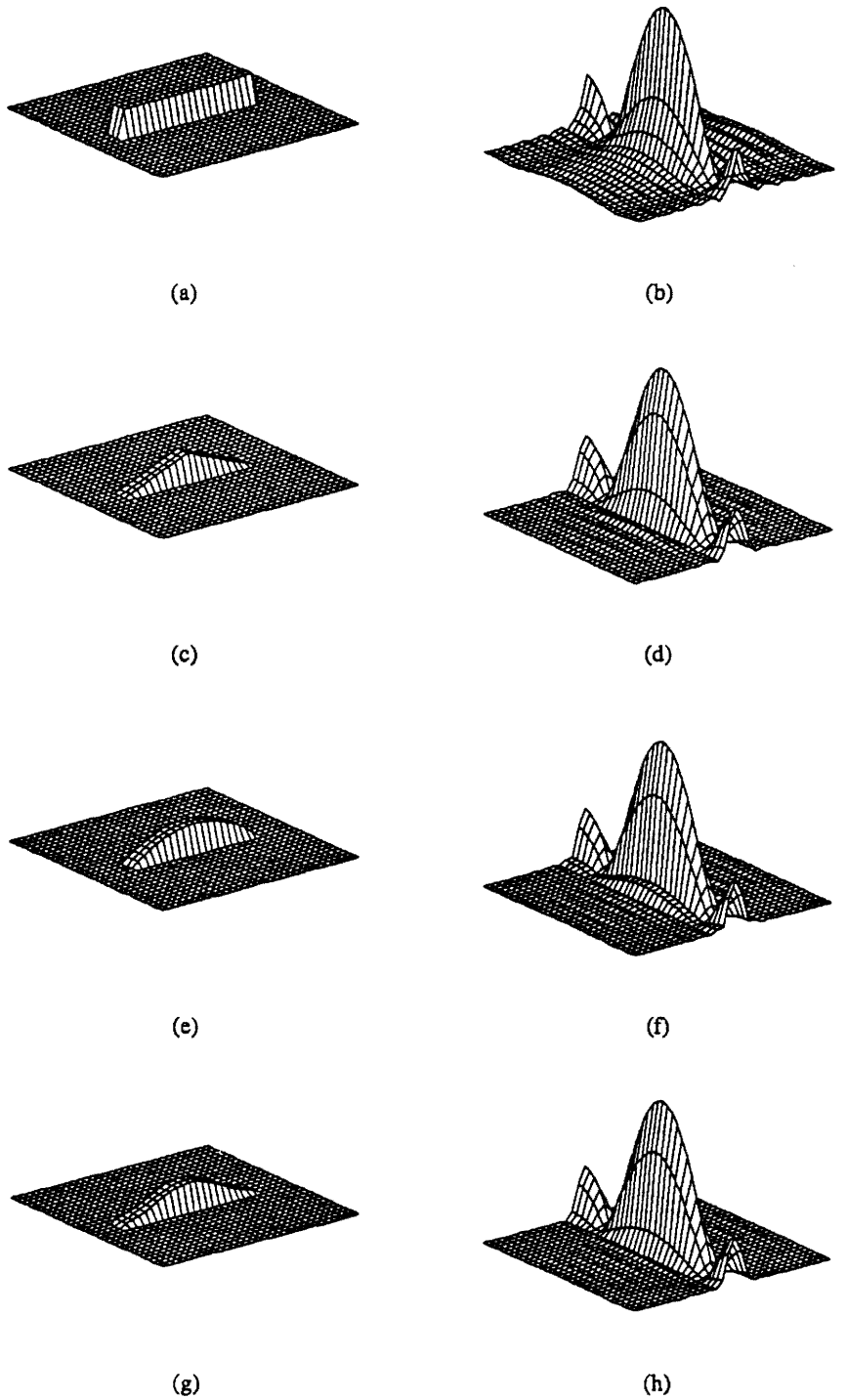

Figure 3.4: Perspective views of symmetric kernels (left) and their Fourier transform amplitudes (right): rectangular (a,b), triangular (c,d), parabolic (e,f), and Gaussian (g,h) profiles. The kernel dimension used is $L = 21$ and $W = 3$.

at a certain gray level. It is seen that the enhancement characteristics obtained from the nonuniform weight of the nonrectangular kernels may be incorporated into a method to enhance the center of lines or line intersections of 3 lines or more. Figures 3.5(c) and (d) show such an application of detecting the intersections of linear features, for which the gray–scale image in (b) was processed by the Min operation once more. In Fig. 3.5(c), vertices are much brighter than other portions. Note that these vertices tend to obtain larger Min values than those obtained at other portions of linear features in (c). A thresholded version of Fig. 3.5(c) is shown in Fig. 3.5(d), yielding only vertices.

As a numerical example of the Min operation, suppose that a binary input image with a line segment (5 pixels wide) is convolved with the symmetric triangular profile kernel ($L = 11$, $W = 1$, and A=5) in Fig. 3.3(b). The convolution output is 19, 17, 15, 10, 6, 3, 1, and 0 measured from the center of the line segment. A binary output image with a thin line segment is obtained by thresholding at 18 (16) for the line segment of 1 (3) pixel width. The nonuniformity of the nonrectangular kernel allows one to use a longer kernel with less thickening of line segments for the enhancement operation, preserving greater output line connectivity. A rectangular kernel with a large L results in thickening of the line segments. For this reason, the nonrectangular profile kernels are preferable to the rectangular profile kernel in some applications.

The kernels discussed can be used in a variety of applications: image enhancement including linear feature enhancement and edge enhancement, and pattern recognition with various kernel profiles. A long, narrow kernel is particularly useful for the enhancement of line segments in noisy background and for reducing noise in an image while preserving edges or other directional features. These applications are discussed in the following chapters.

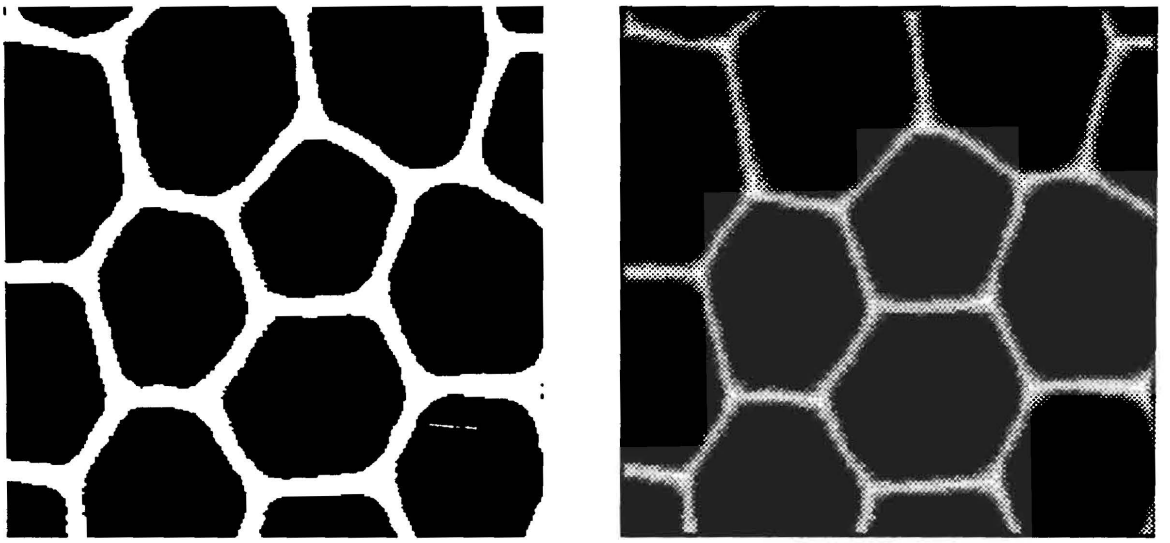

(a) (b)

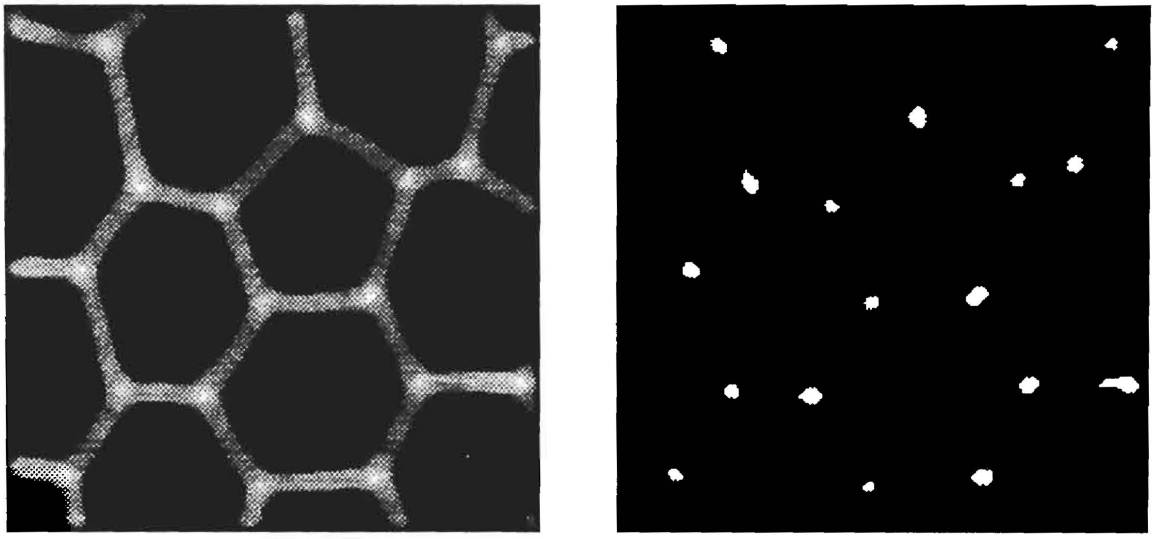

(c) (d)

Figure 3.5: Min operation with a triangular profile kernel. (a) Original image. (b) Result of applying the Min operation to (a). (c) Result of applying the Min operation to (b). (d) Thresholded version of (c).

3.2.3 Transform Functions

Various forms of transform function were investigated, including the following:

$$f_1[Max, Min] = Max(x, y) \tag{3.9}$$

$$f_2[Max, Min] = Min(x, y) \tag{3.10}$$

$$f_3[Max, Min] = Max(x, y) - Min(x, y) \tag{3.11}$$

$$f_4[Max, Min] = Max(x, y) \cdot Min(x, y) \tag{3.12}$$

$$f_5[Max, Min] = 1 - \rho^m \tag{3.13}$$

$$f_6[Max, Min] = (1 - \rho^m)e^{\rho^m} \tag{3.14}$$

$$f_7[Max, Min] = \frac{1 - \rho^m}{1 + \rho^m} \tag{3.15}$$

where

$$\rho(x, y) = Min(x, y)/Max(x, y). \tag{3.16}$$

As defined in Eq. 3.16, ρ possesses a value between 0 and 1, having the maximum value (=1) when Min(x,y) = Max(x,y). A small value of ρ represents a significant variation in intensity at a particular point, whereas a large value indicates that there is no significant variation in intensity. In other words, $(1 - \rho)$ measures the amount of directional intensity variation at a point. Figure 3.6 shows the functions $(1 - \rho^m)$ (Eq. 3.13) for $m = 1, 2$, and 3. A high value of m leads to greater sensitivity to a small variation in directional intensity for a large value of ρ. Thus, a low contrast image would be processed to enhance some directional feature using the function $(1 - \rho^m)$ with a high value of m rather than a low value. Similar effects are observed with the mappings represented by Eqs. 3.14 and 3.15.

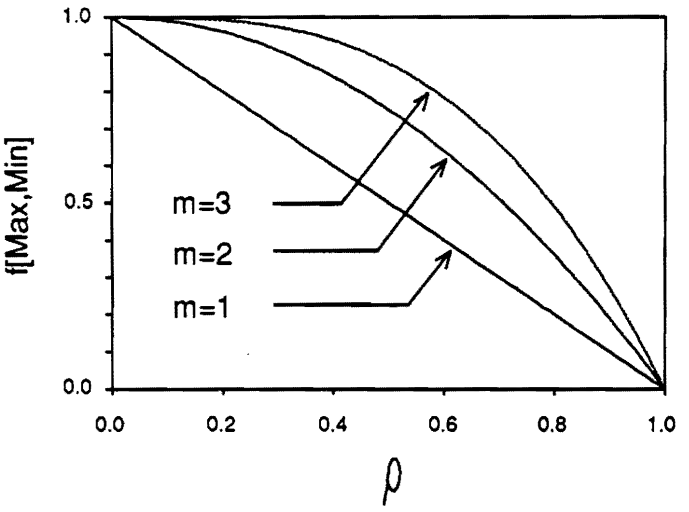

Figure 3.6: The RKMT function $f[Max, Min] = 1 - \rho^m$ for $m = 1, 2$, and 3 from bottom to top. It is shown that, for a large value of ρ, a higher order m provides greater sensitivity to small variations in gray–level than a lower one.

3.3 Algorithms for Linear Feature Enhancement by RKMT

In this section, algorithms for the RKMT enhancement of linear features are introduced. A simple [Max - Min] operation is first described by calculating $I_{out}(x,y) = Max(x,y) - Min(x,y)$ at each input point, followed by further general multipass operation obtained by cascading a Max operation with the [Max - Min] operation. The algorithms are simulated for each operation on a computer with a synthetic image containing linear features which are of four orientations: 0°, 45°, 90°, and 135°. In each numerical simulation, the kernel was thus rotated through these four discrete angles.

3.3.1 Direct [Max - Min] operation

A block diagram of [Max - Min] operation is shown in Fig. 3.7. The solid box in Fig. 3.7(a) includes both the convolution operation of the input with the kernel $K_\theta(x,y)$ and the operation to calculate $I_{out}(x,y) = Max(x,y) - Min(x,y)$. A simplified version shown in (b) is used throughout the remainder of the thesis. An example of the [Max - Min] operation is suggested by Fig. 3.8. A noiseless input image is shown in Fig. 3.8(a) which consists of only straight-line segments. A noisy image is generated by adding short line segments, curved line segments, and impulsive noise to the noiseless image. The resulting noisy image $O(x,y)$, shown in Fig. 3.8(b), is subjected to the [Max - Min] operation to enhance straight-line features relative to the other features and noisy background. As the kernel $K_\theta(x,y)$ rotates, the input is convolved with the kernel, which is long and narrow in profile, and both Max(x,y) and Min(x,y) values from the convolution outputs are obtained. The difference [Max(x,y) - Min(x,y)] is large at points that lie along the straight-line segments. Along short line segments, curved lines, and at impulsive noise, [Max(x,y) - Min(x,y)] will be comparatively smaller. The result is an enhancement

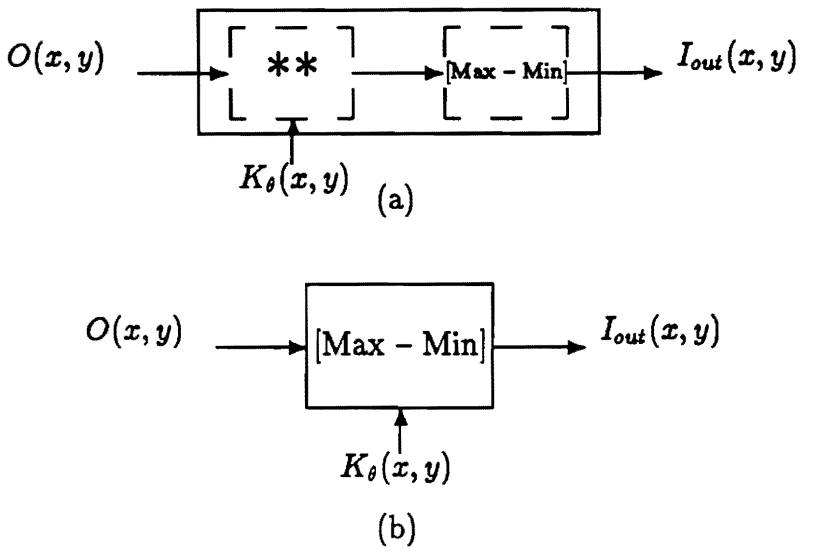

Figure 3.7: A block diagram of the direct [Max - Min] operation where $O(x,y)$ and $K_\theta(x,y)$ are the input and 2–D rotating kernel, respectively: (a) [Max – Min] operation; (b) simplified version of (a).

of the straight–line segments relative to the other features.

Figure 3.8(c) shows the result of applying the [Max(x,y) - Min(x,y)] operation in a numerical simulation. A typical line width is 5 pixels wide. The kernel $K_\theta(x,y)$ used is rectangular in profile with $L = 19$ and $W = 1$. Some enhancement of the straight–line segments relative to the background is evident. This operation also fills in gaps in a broken line segment. Figure 3.8(d) shows an image thresholded at a gray value (i.e., 128 for 8 bit gray levels) that corresponds to approximately half the length of the kernel. Asymmetric kernels can be used in much the same way.

3.3.2 Cascade Max and [Max - Min] Operations

Greatly enhanced line segments can be obtained if, in a pre–processing step, an intermediate image [$= I_{int}(x,y)$] is calculated in accord with $I_{int}(x,y) = Max(x,y)$ [i.e., Max operation], and then processed by the [Max - Min] operation. Figure 3.9 shows a block diagram of such a cascade system. The kernel $K_\theta(x,y)$ may be different in the Max and [Max – Min] operations.

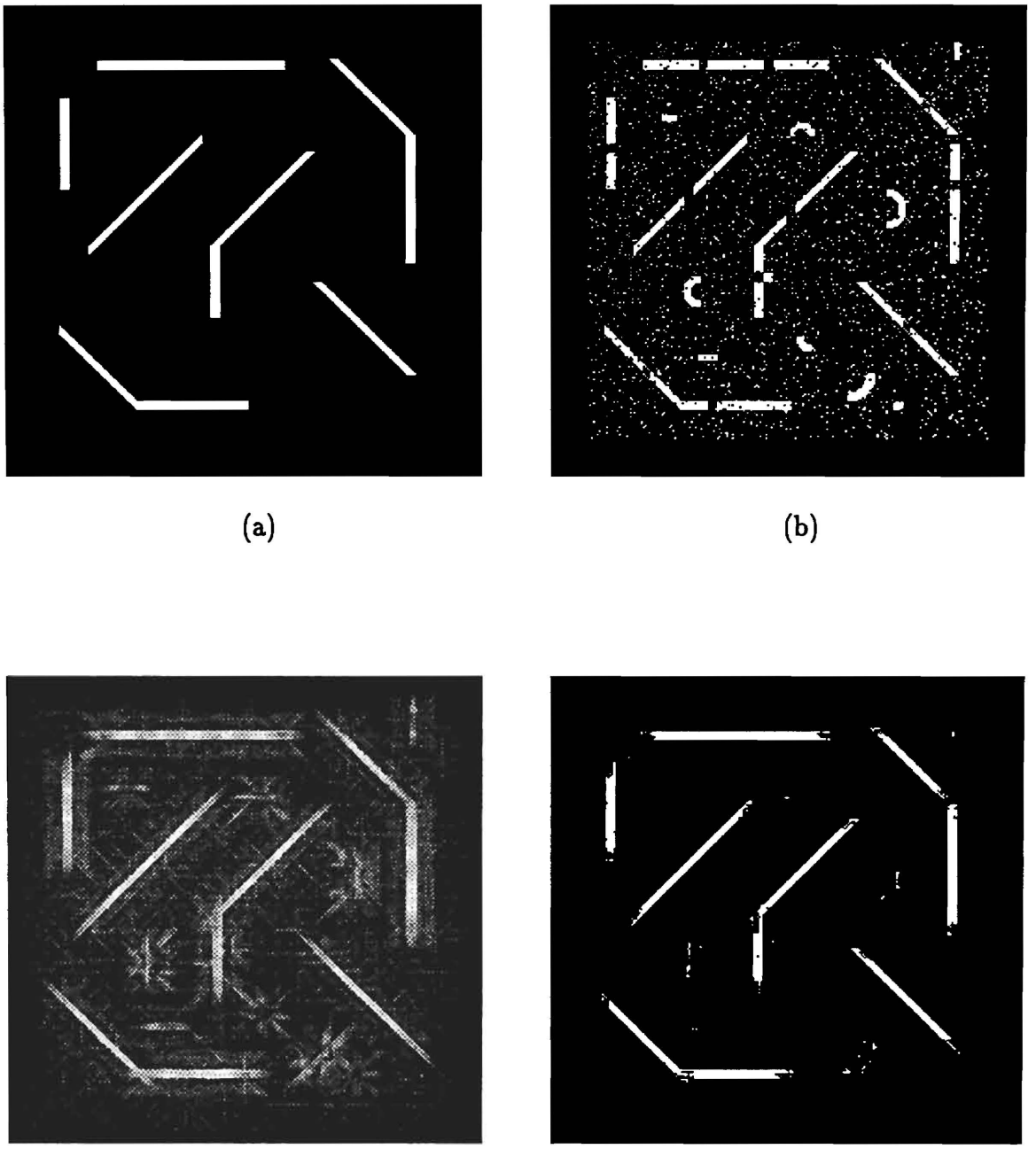

(a) (b)

(c) (d)

Figure 3.8: Direct [Max - Min] operation numerically performed: (a) noiseless image; (b) noisy input image; (c) result of applying [Max - Min] operation (with rectangular kernel) to the noisy image in (b); (d) thresholed image of (c) at a gray level.

o

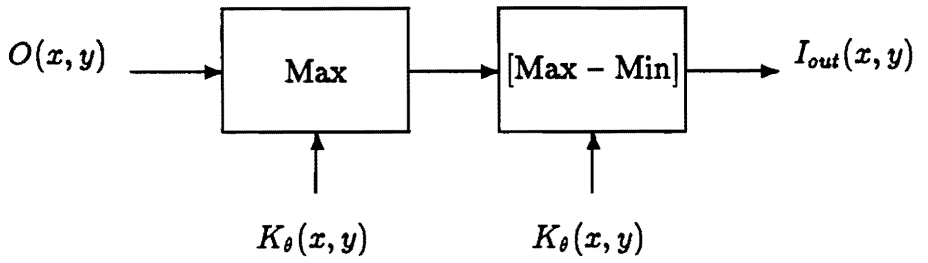

Figure 3.9: Cascade system combining a Max operation with [Max - Min] operation. In the cascade system, the kernel $K_\theta(x,y)$ may be different in each operation.

In the cascade system, the Max operation pre–enhances line segments somewhat with some smoothing and noise reduction. Figure 3.10 illustrates these characteristics using a binary input containing a broken line segment with two holes and a binary kernel oriented at 0°. As the kernel ($L = 5$) rotates, the binary input is convolved with the kernel. The output $I_{out}(x,y)$ is shown only at $y = 0$ for convenience in (b). Those points within a small region near the x axis ($-8 \leq x \leq 8$ and $-2 \leq y \leq 2$) achieve $I_{out}(x,y) = 1$; for other background points away from the x axis $I_{out}(x,y) = 0$. The broken line segment is filled in, and the ends of the line segment are smoothed. If desired, a binary output can be obtained by thresholding–hard limiting. Figures 3.10 (c) and (d) show two completely filled binary outputs obtained by thresholding at $Th = 2.5$ and $Th = 1.5$. These thresholding values are equal to the gray values, $Th = L/2$ and $Th = L/2 - 1$. Similarly, the pre–enhancing operation can be effected in a gray–scale image in such a way that the points with low gray values on a line segment will be enhanced relatively to background intensity.

To reduce smoothing at the ends of line segments, a modified kernel with an impulse at its center may be used. Figure 3.11 illustrates this effect for $I_{out}(x,y) = Max(x,y)$ in the same way as in Fig. 3.10. In Fig. 3.11(a), the input has a broken line segment with a gap at $x = 0$; the kernel has an impulse of height h at its center. The output $I_{out}(x,y)$ for a Max operation is seen only for $y = 0$ in (b). Those points within a finite region near the x axis ($-5 \leq x \leq 5$ and $-2 \leq y \leq 2$)

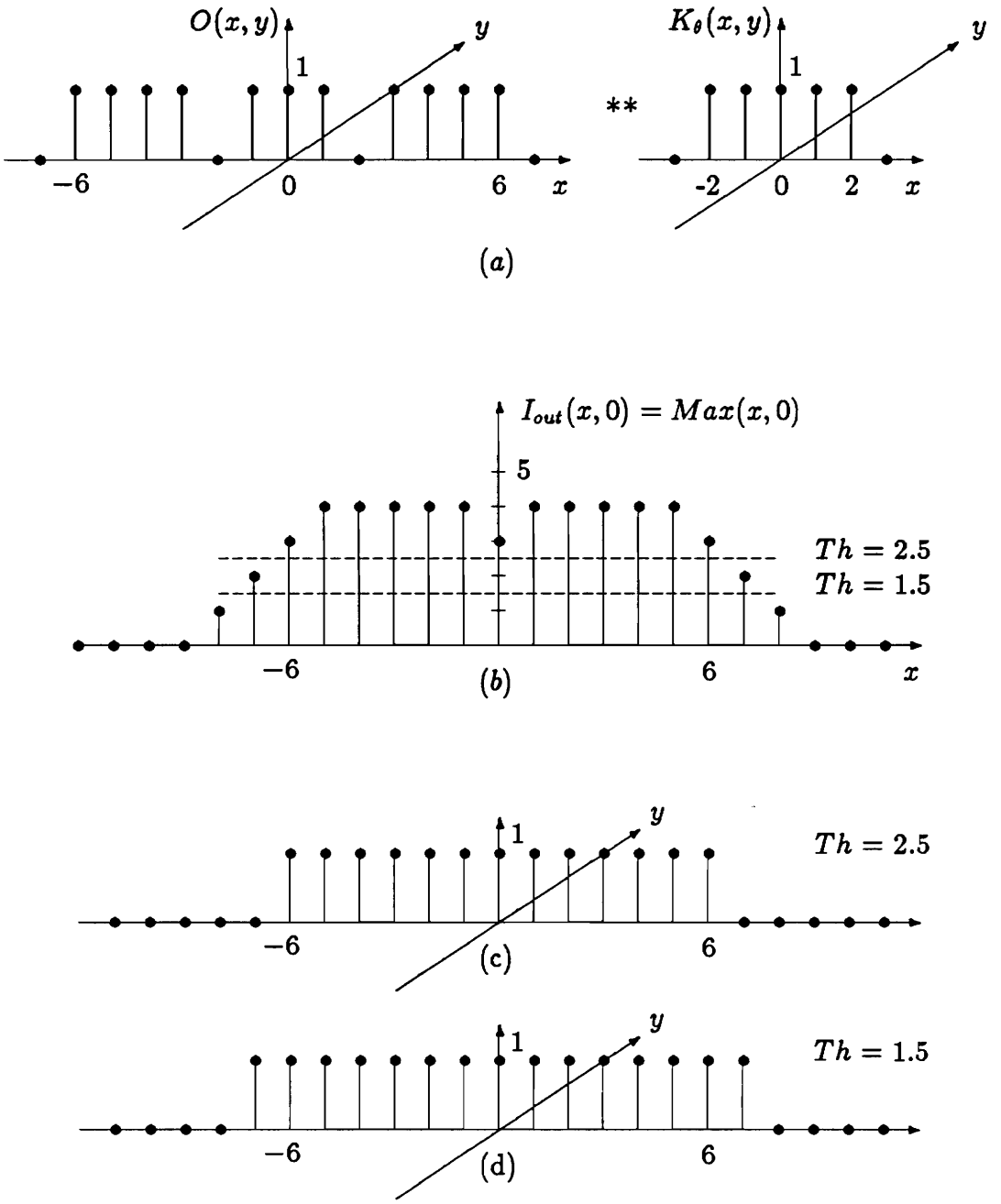

Figure 3.10: Max operation on a binary input with a binary kernel oriented at 0°. (a) Binary input and kernel. (b) $I_{out}(x,y) = Max(x,y)$ for $y = 0$. (c) Thresholded output at $Th = 2.5$ $(= L/2)$. (d) Thresholded output at $Th = 1.5$ $(= L/2 - 1)$.

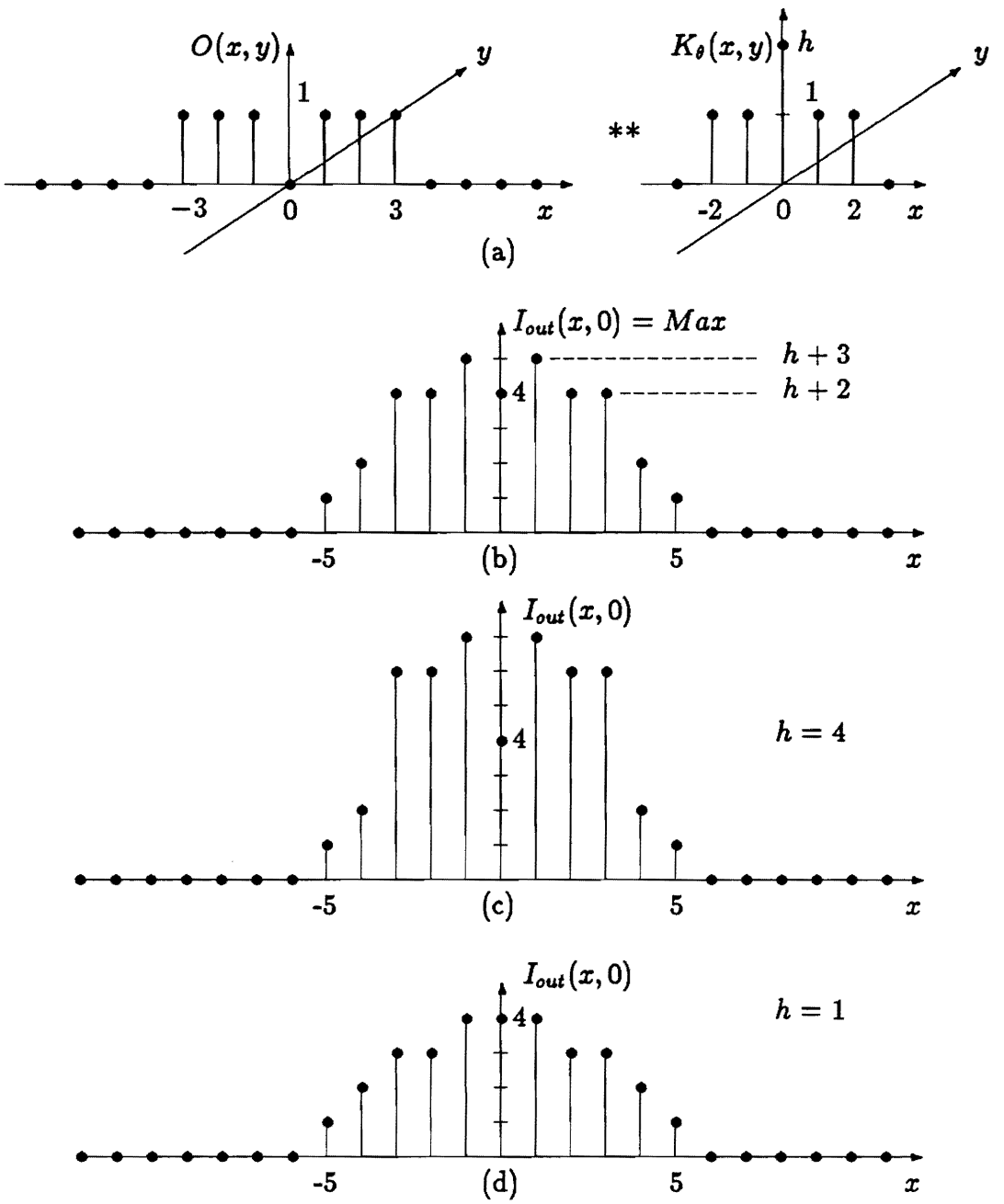

Figure 3.11: Max operation using a kernel with an impulse. The output is shown only at $y = 0$. Smoothing at the ends of the line segment is reduced as compared with Fig. 3.11. (a) Input and kernel. (b) $I_{out}(x,y) = Max(x,y)$ for $y = 0$. (c) $I_{out}(x,0)$ with $h = 4$. (d) $I_{out}(x,0)$ with $h = 1$.

have $I_{out}(x, y) = 1$. For other background points away from the x axis $I_{out}(x, y) = 0$. As h increases from $h = 0$, the output tends to show steeper ends of the line segment and thus to reduce the smoothing effect. In (c) and (d), the convolution output is shown for $h = 1$ and $h = 4$. From (c) and (d), a completely filled binary line segment, as shown in Fig. 3.10, can also be obtained by thresholding the output $I_{out}(x, y)$ at $Th = 2.5$ $(= L/2)$. Note that an impulse at the center of kernel affects the Max operation but not the [Max - Min] operation, since the impulse contributes equally to both Max and Min operations.

Figure 3.12 shows the results of applying the Max operation with the [Max - Min] operation using the same noisy image as used for the direct [Max - Min] operation. The kernel used is of rectangular profile ($L = 21$ and $W = 1$). Figure 3.12(a) shows an image processed by the cascade system using the rectangular profile kernel. A thresholded image is shown in Fig. 3.12(b). Figures 3.12(c) and (d) show the results of conventional median filtering with 3x3 and 7x7 filtering mask. It is easily seen that the RKMT processing outperforms the median filtering, since the median filtering does not take into account directionality of certain features and works well only for impulsive noise. It is seen in Fig. 3.8(d) and Fig. 3.12(b) that the Max operation preenhances the straight–line segments, with noise reduction but some smoothing. Then, calculating $I_{out}(x, y) = Max(x, y) - Min(x, y)$ tends to remove the effects of variations in background intensity and to remove any uniform bias, resulting in greatly enhanced linear features.

3.3.3 Multipass Operation with Cascade System

The cascade system combining a Max operation with a [Max-Min] operation may be continued iteratively (e.g., two iterations) in the form of multipass operation. Figure 3.13 shows a block diagram for the multipass operation in which the image obtained in the first iteration is passed through the cascade system again. The output image $I_{out}(x, y)$ can be obtained either by the Max operation or by the [Max

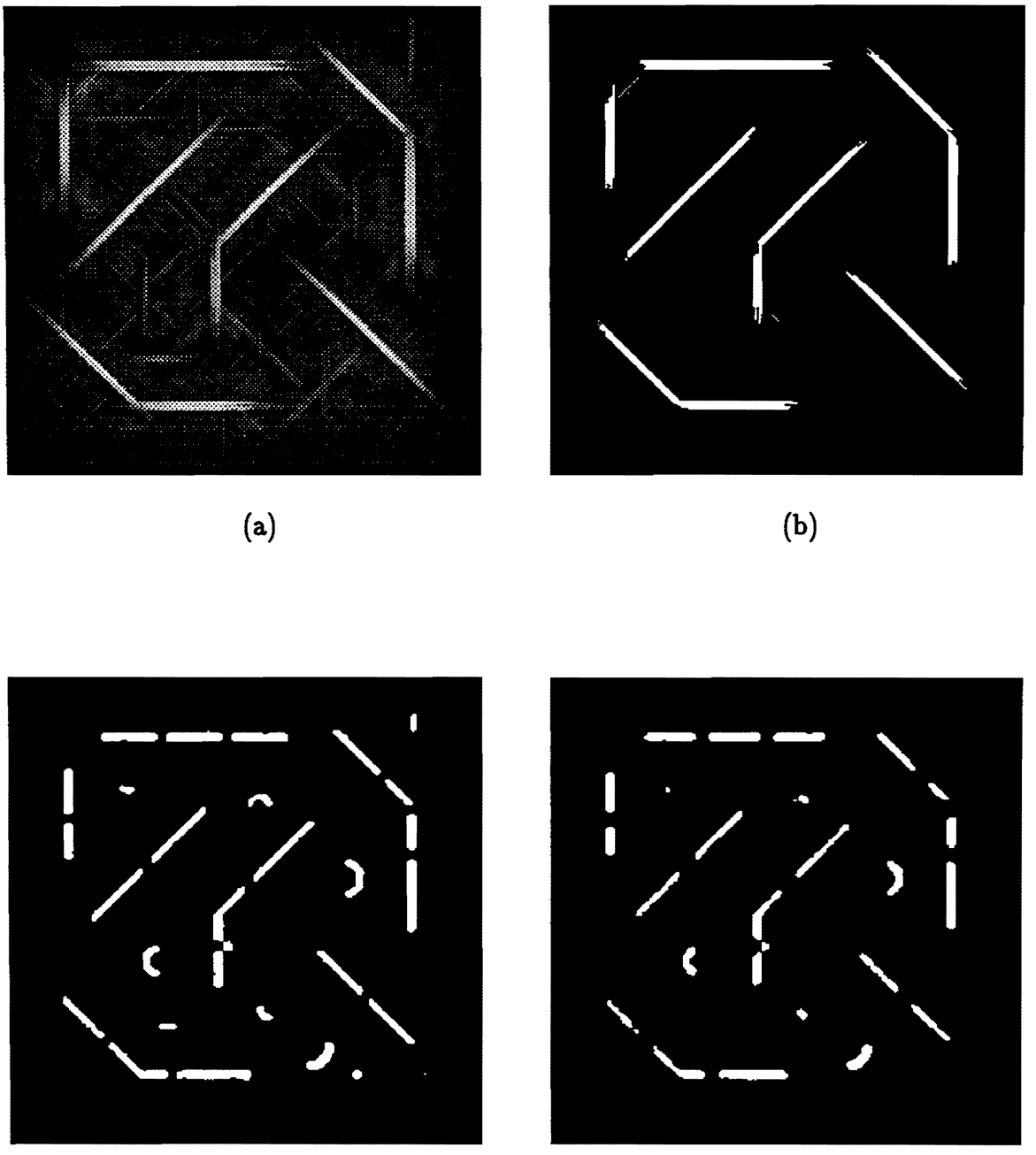

Figure 3.12: Cascade operation: (a) result of using the rectangular kernel with $L = 25$ and $W = 1$; (b) result of thresholding the result in (a); (c) and (d) results of median filtering operations with 3x3 and 5x5 masks, respectively.

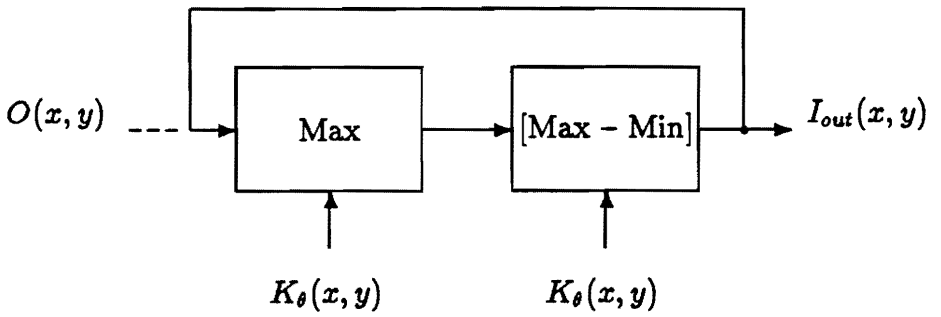

Figure 3.13: Multipass operation for which the output from the first cascade operation (i.e., first iteration) is used as the input to the entire cascade system.

- Min] operation. In the multipass operation, one or two iterations are sufficient for the enhancement of linear features in noisy background. For example, one iteration was sufficient for the image without the spatially varying characteristics of background intensity as shown in Figs. 3.8(b) and (d) and Fig. 3.12(b).

Figures 3.14 shows the results of applying the second Max/[Max - Min] operation to the image of Fig. 3.12(a) obtained in the first iteration of the multipass operation. The result of applying the Max operation in the second iteration is shown in Fig. 3.14(a). A thresholded version of the image in Fig. 3.14(a) is shown in Fig. 3.14(b). Similarly, the result of applying the [Max - Min] operation to Fig. 3.14(a) is shown in Fig. 3.14(c). A thresholded version of Fig. 3.14(c) is also shown in Fig. 3.14(d). No improvement in the enhancement capability is observed by the second iteration, as seen in Fig. 3.12(b) and Figs. 3.14(b) and (d), since the noisy input in Fig. 3.8(b) does not have the spatially varying characteristics of background intensity. As this cascade operation continues iteratively, smoothing increases and some image details such as line intersections may be deemphasized or lost.

3.3.4 Effect of the Kernel Length and Width

It is important to choose the kernel length relative to features (e.g., line segments) to be enhanced, even though the basic RKMT processing performs well for a wide

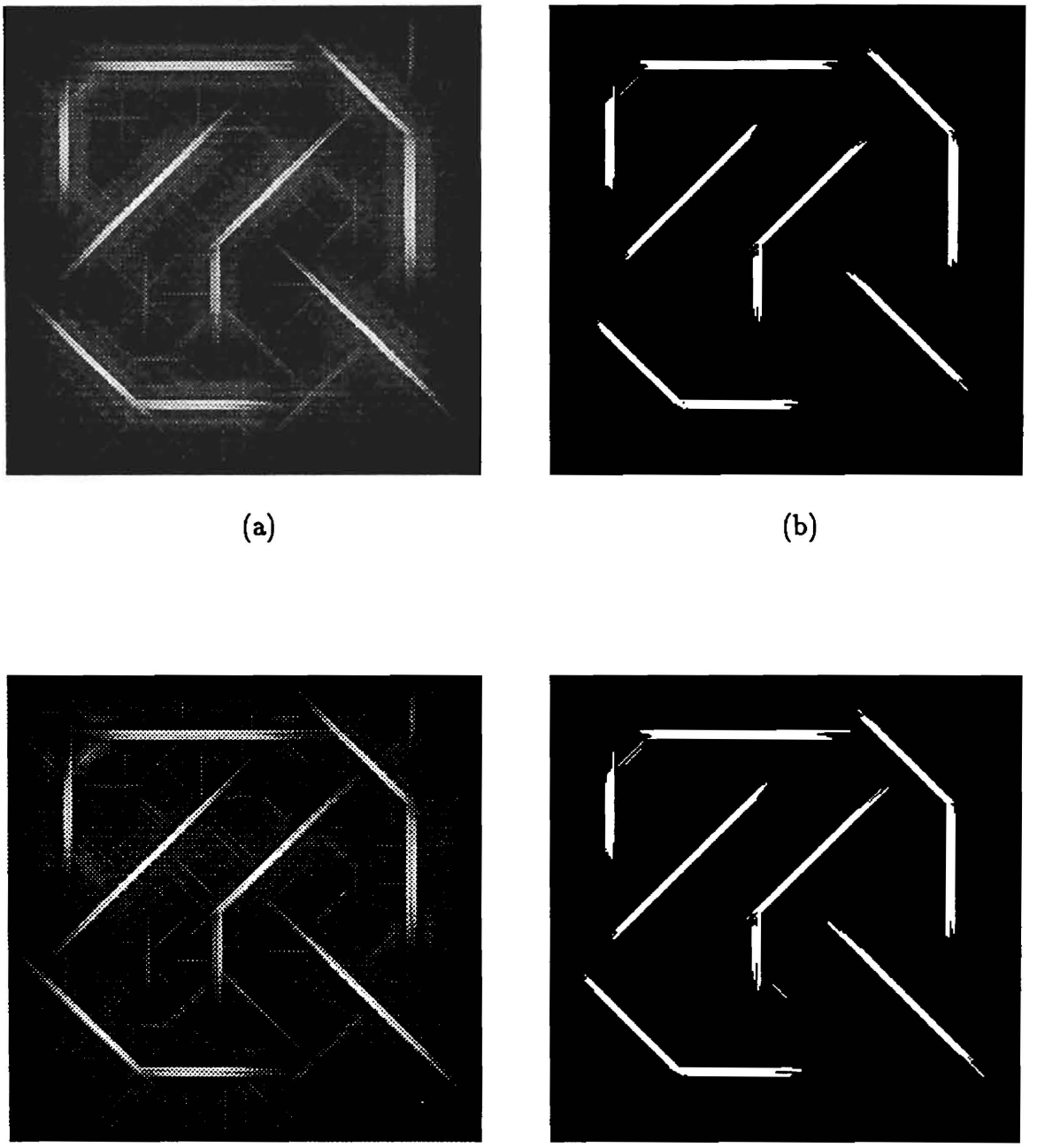

(a) (b)

(c) (d)

Figure 3.14: Second iteration with cascade system using a rectangular kernel (L=25 and W=1): (a) result of applying a Max operation to (a) in Fig. 3.12; (b) thresholded version of (a); (c) result of applying a [Max - Min] operation to (a); (d) thresholded version of (c);

range of the kernel length. If the kernel is too long, such features will be smoothed or smeared out during the enhancement operation. As a result, certain desirable features with small scale may be lost. On the other hand, the operation may be sensitive to noise and thus lose the enhancement capability as the kernel is made too shorten or shorter. It was shown in Fig. 3.11 that the smoothing effect could be reduced by using a kernel with an impulse at its origin. Similar effects to reduce smoothing can be achieved by using other nonrectangular profile kernels. In general, lengthening a long, narrow kernel results in greater output line segment connectivity, but with a smoothing of image details such as line intersections. Figure 3.15(a) shows an image processed by a cascade system with a rectangular kernel ($L = 15$ and $W = 1$) followed by thresholding. The enhancement effect is somewhat poor. A significantly enhanced image can be obtained using a longer kernel. Figures 3.15(b), (c), and (d) show the results of applying the cascade system with a longer kernel of $L = 25$, 37, and 49.

It is also important to consider the width of the kernel ($= W$). Consider the case of an infinitely–long line segment with width W' and rectangular kernel of length L ($L >> W$ and $L >> W'$). Figure 3.16 shows the result for three different cases: (a) $W = W'$; (b) $W < W'$; and (c) $W > W'$. Max values are found when the kernel is oriented with the line segment. The line segment and kernel are shown on the left of Fig. 3.16 for each case while 1–D profiles of Max values along the x axis are shown on the right. (The z axis is orthogonal to the image plane.) For $W = W'$, the Max value decreases monotonically on both sides of the line segment as shown in (a). This effect can be demonstrated numerically as follows. If $W = 5$, $W' = 5$, and $L = 15$, Max values at points along the line segment are $\cdots$ 45, 60, 75, 60, and 45 $\cdots$, going from one side of the line segment to the other. The largest value (=75) among these Max values is obtained at the center of the line segment. The result is an enhancement at the center. If the processed image is thresholded at a gray value, a thinner line segment is produced. Thus, incorporating this effect

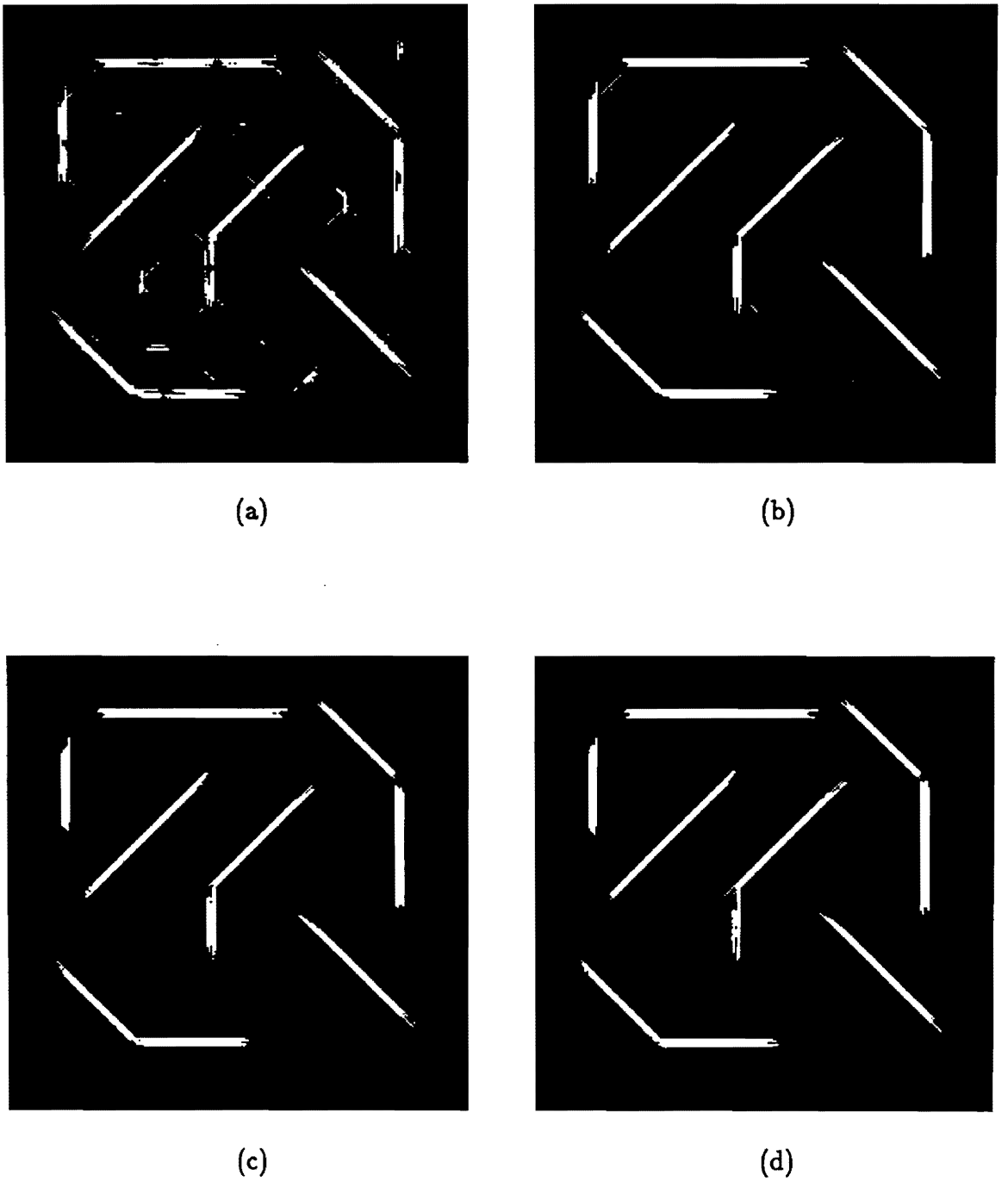

(a) (b)

(c) (d)

Figure 3.15: Effect of varying the kernel length ($= L$) for a cascade system using a rectangular kernel ($W = 1$): (a) $L = 13$; (b) $L = 25$; (c) $L = 37$; (d) $L = 49$.

into the [Max - Min] operation results in a thinning of the line segments as well as an enhancement at their centers. In (b) and (c), the Max values form a plateau around the center of the line segment and decrease monotonically to either side of the line segment.

Figures 3.17(a), (b), and (c) show the numerical results of varying W from 1 to 5 for the cascade system (i.e., first iteration). The kernels used are rectangular in profile and of length $L = 25$. Similarly, the same effect of varying the kernel width on the enhancement of line segments can be demonstrated by using a triangular profile kernel. The result of using the triangular kernel with $L = 37$ and $W = 3$ is shown in Fig. 3.17(d). As the input image is more noisy, the longer and wider kernel needs to be used. Figure 3.18 shows such example. The noisy input is shown in (a). Figures 3.18(b) and (c) show the images obtained in the first iteration using the rectangular kernel of $L = 25$, followed by thresholding, for $W = 3$ and $W = 5$, respectively. As comparison, the result of applying the median filtering operation with 5x5 mask is shown in Fig. 3.18(d).

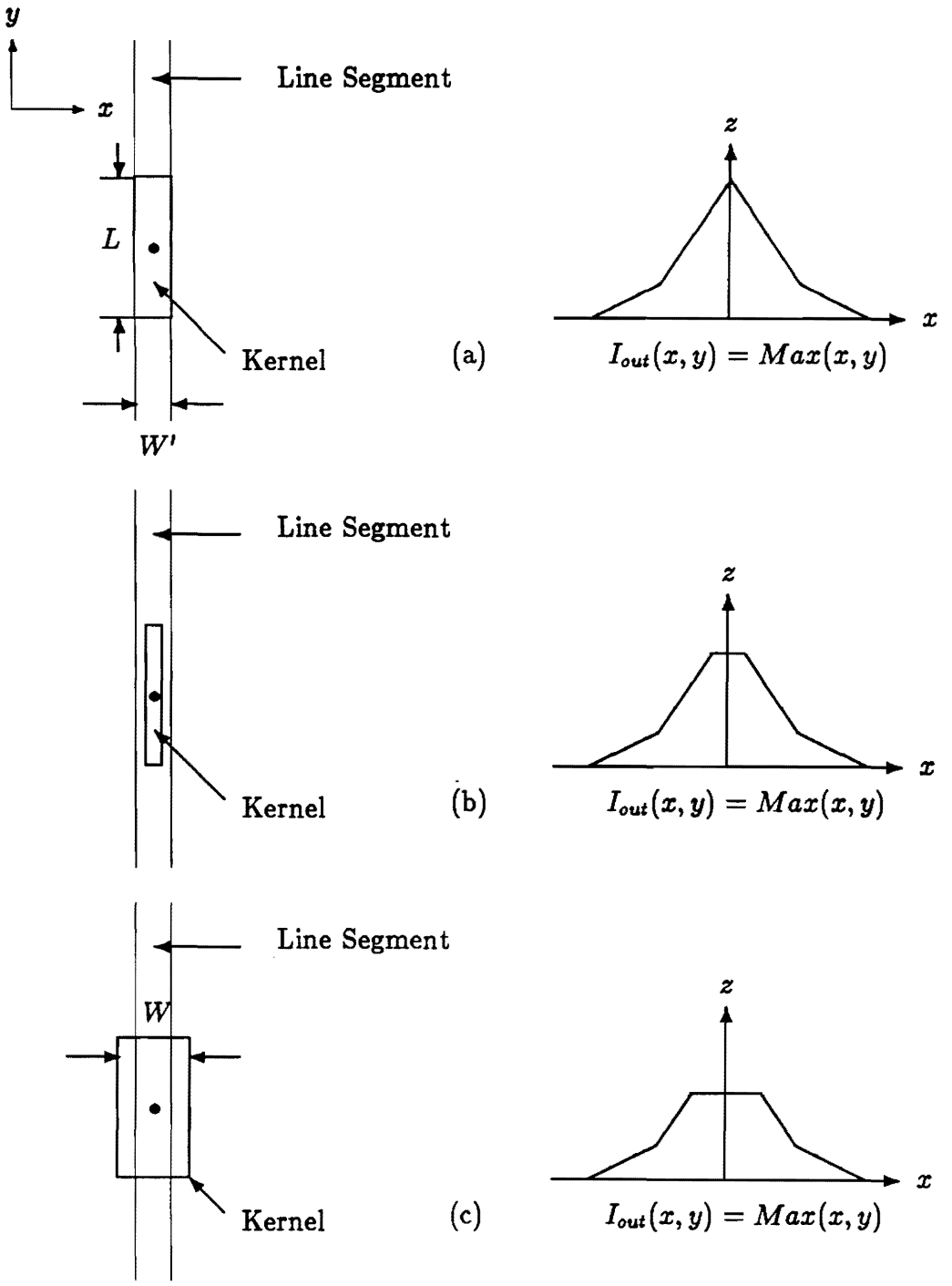

Figure 3.16: Effect of the kernel width W: (a) $W = W'$: (b) $W < W'$: and (c) $W > W'$ where W' is the width of the line segment. In each case, $L \gg W$, $L \gg W'$, and $L \gg WW'$ where L is the kernel length.

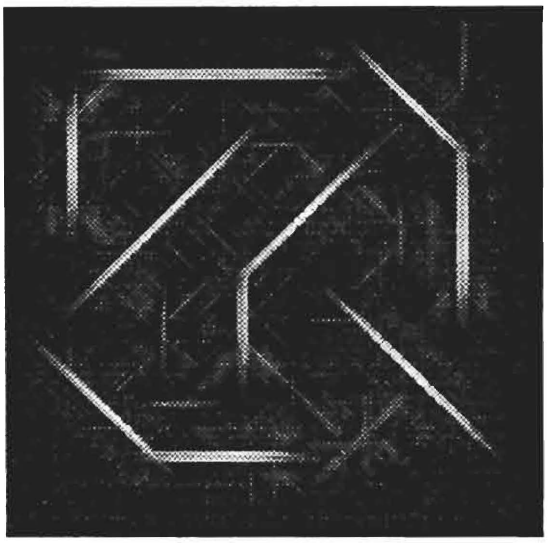

(a)

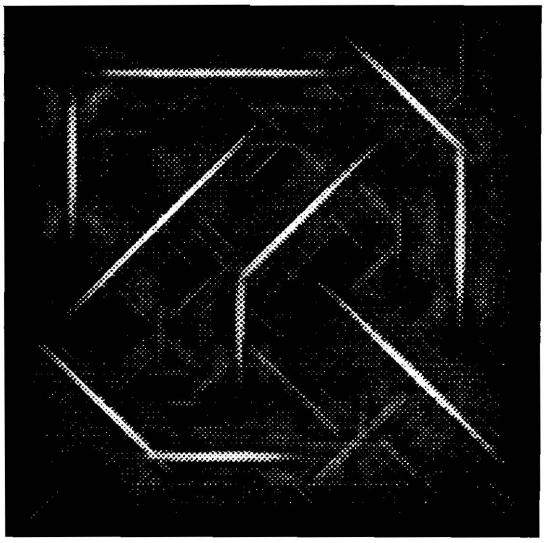

(b)

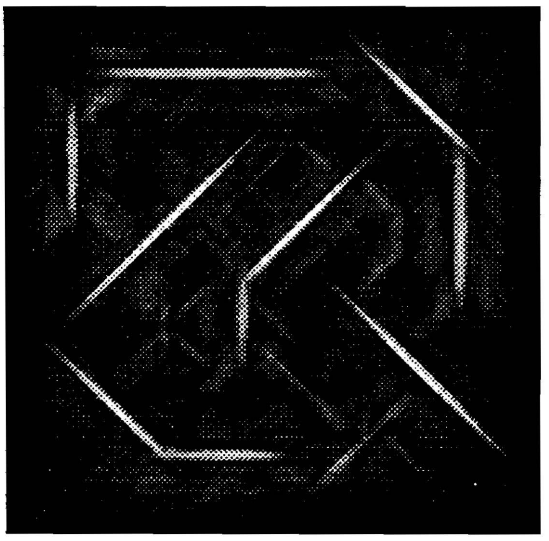

(c)

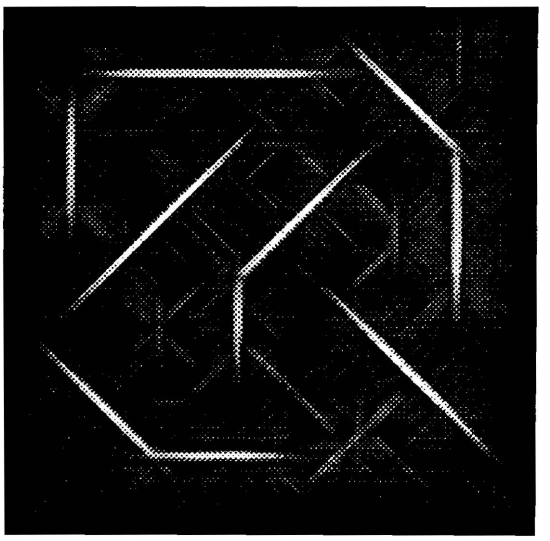

(d)

Figure 3.17: Effect of varying the kernel width ($= W$) for a cascade system where a rectangular kernel with $L = 25$ was used for (a), (b), and (c): (a) result for $W = 1$; (b) result for $W = 3$; (c) result for $W = 5$; (d) result using a triangular kernel with $L = 37$ and $W = 3$.

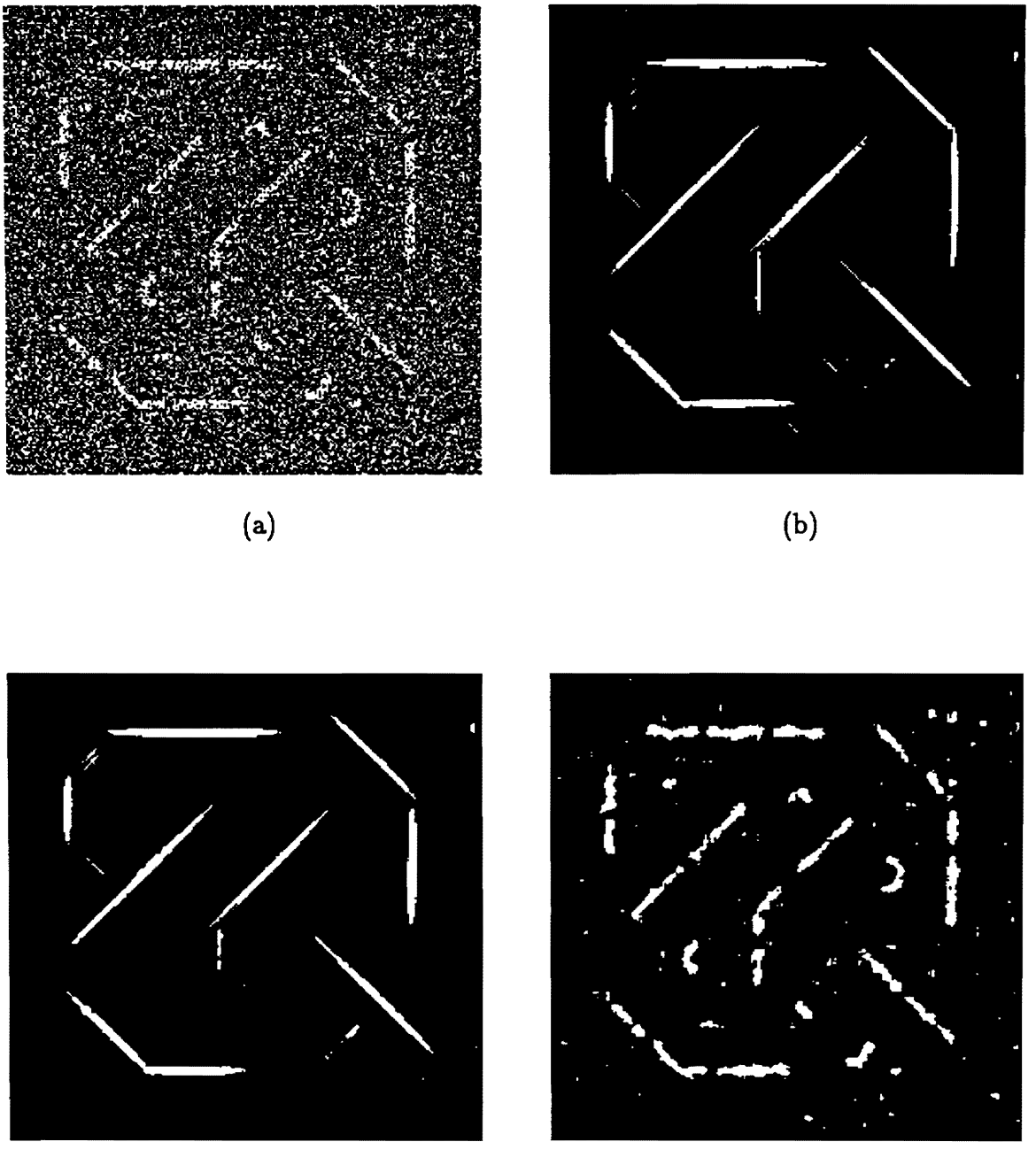

(a) (b)

(c) (d)

Figure 3.18: Noisy input image and its processed images with the cascade system for varying the kernel width ($= W$). (a) noisy input image; (b) result for $W = 3$; (c) result for $W = 5$; (d) median filtering with 5x5 mask.

3.4 Quantitative Performance Measure of Image Enhancement by the RKMT Method

3.4.1 Analysis Method

RKMT processing has been shown to be particularly useful for the enhancement of linear features (e.g., straight line segments). Although RKMT processing clearly performs well qualitatively, it is worth analyzing quantitatively its effectiveness under various conditions. One of the reasons for performing a quantitative analysis is to understand how effectively RKMT processing can serve as a preprocessor for the cell boundary patterns.

An important question is what quantitative performance measure correlates well with the visual inspection of the processed images. There are various methods commonly used for quantitative measure of image quality, including normalized mean–square error measure and normalized peak mean–square error measure [85]. These methods yield an error measure between a raw input and a processed image that correlates well with visual inspection. The normalized mean–square error measure ($\hat{e_r}$) is defined in the discrete case by

$$\hat{e_r} = \frac{\sum_{i=1}^{D_i}\sum_{j=1}^{D_j}[O_r(i,j) - O_p(i,j)]^2}{\sum_{i=1}^{D_i}\sum_{j=1}^{D_j}[O_r(i,j)]^2}, \tag{3.17}$$

where D_ixD_j is the dimension of image in rows by columns and $O_r(i,j)$ and $O_p(i,j)$ are the raw input and processed image, respectively. Similarly, the normalized peak mean–square error measure ($\hat{e_p}$) is defined by

$$\hat{e}_p = \frac{(1/D_iD_j)\sum_{i=1}^{D_i}\sum_{j=1}^{D_j}[O(i,j) - O_p(i,j)]^2}{p^2}, \tag{3.18}$$

where p represents the peak gray value in the image $O_r(x,y)$ (e.g., $p = 255$ for 8 bit

digitization).

The peak mean–square error measure for the performance measure (i.e., similarity measure) has been chosen, used in this research, and expressed in decibel form as an equivalent signal–to–noise ratio (SNR):

$$\text{SNR} = -10\log_{10}[\hat{e}_p]. \tag{3.19}$$

Equivalently,

$$\text{SNR} = 10\log_{10}\left[\frac{p^2}{(1/D_iD_j)\sum_{i=1}^{D_i}\sum_{j=1}^{D_j}[O_r(i,j) - O_p(i,j)]^2}\right]. \tag{3.20}$$

Note that the noiseless and noisy input images used for the enhancement of linear features in Sec. 3.3 were binary images. Since the processed image obtained by RKMT processing was a gray–scale image, a global thresholding operation is used to obtain a binary output image. A thresholding value was chosen at that gray value for which the maximum SNR was obtained. In certain situations, choice of the thresholding value may depend on the volume of the kernel dimension, by considering points on a binary line segment for [Max -Min] operation. Consider the case shown in Fig. 3.16(b) ($W < W'$). In that case, the Max and Min orientations for those points on the line segment are parallel and perpendicular to the line segment, respectively. Then the thresholding value I_{th} is obtained by calculating $[V - V_o]$, where V is the total volume of the kernel and V_o the overlapped volume between the kernel and line segment in both orientations:

$$I_{th} = \frac{p}{2}\left(1 - \frac{V_o}{V}\right) = \frac{p}{2}\left(1 - \frac{W'}{L}\right) \tag{3.21}$$

for a rectangular kernel and

$$I_{th} = \frac{p}{2}\left(1 - \frac{V_o}{V}\right) = \frac{p}{2}\left[1 - \frac{2W}{L}(1 - \frac{W}{2L})\right] \tag{3.22}$$

for a triangular kernel. Although these values worked well to binarze the processed gray–scale image, they did not yield a maximum SNR for the quantitative analysis.

This problem occurs since negative–going noise on the line segment may reduce the Max value. The processed images were therefore thresholded at slightly different gray values to obtain the maximum SNR.

3.4.2 Experimental Results

The peak mean–square error (PMSE) analysis method has been applied to investigate how effectively RKMT processing works for the enhancement of linear features in a noisy environment. To understand better how the RKMT processing behaves under certain situations, three different cases are considered. The first investigates how the processing behaves as the kernel length changes. The second involves a quantitative comparison of the enhancement of linear features using the direct [Max - Min] operation and the cascade system, which combines a Max operation with a [Max - Min] operation. The third compares the performance of RKMT processing for various rectangular and nonrectangular (e.g., triangular) kernel profiles. For this analysis, the raw input in Fig. 3.7(a) is used as $O_r(i,j)$ in Eq. 3.20; the processed image is subjected to a global thresholding operation [$O_p(i,j)$ in Eq. 3.20].

Figure 3.19 shows the experimental results obtained calculating $I_{out}(x,y) = Max(x,y) - Min(x,y)$ subject to an ideal thresholding at a gray value that maximizes SNR for each kernel length. The length L increases from $L = 5$ to $L = 77$. The kernel ($W = 1$) used is rectangular in profile with the width $W = 1$ pixel. The width of the line segments is W' (=5) pixels. As shown qualitatively in Fig. 3.15, lengthening the kernel improves the SNR. The SNR increases monotonically up to approximately 22 dB for $L = 29(= L_{max})$. Note that $L_{max} \simeq 5.8W'$ (= 29) where $W' = 5$ is the width of line segments in the raw image. As L exceeds the length L_{max}, the SNR becomes nearly constant ($\simeq$ 21.7 dB) and then falls off slightly. Lengthening the kernel further tends to decrease the SNR slightly, but not significantly.

Figure 3.20 shows experimental results for the direct method and cascade sys-

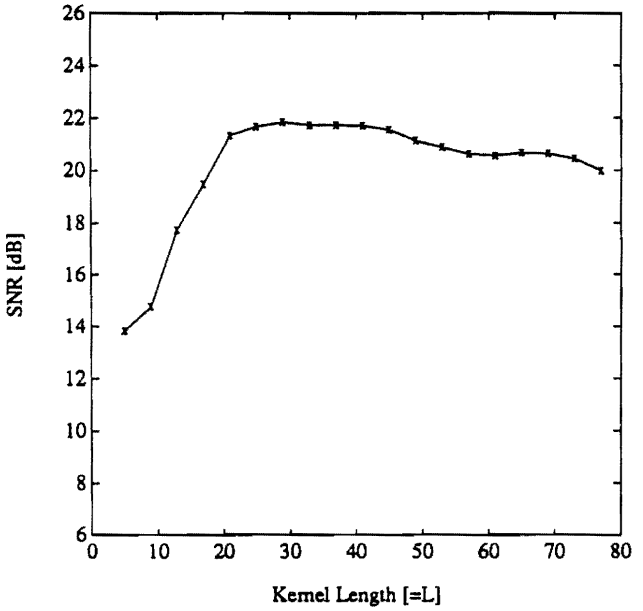

Figure 3.19: Signal–to–noise ratios (SNR) for different kernel lengths (= L). The kernel used is rectangular in profile width $W = 1$.

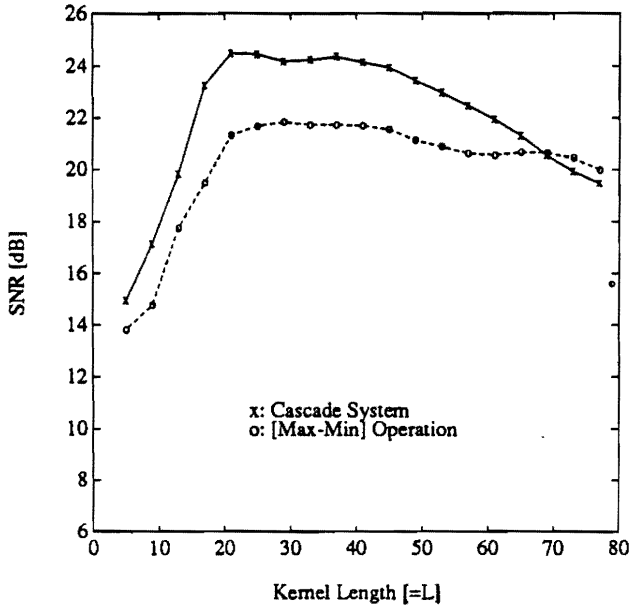

Figure 3.20: Performance measures for direct method ([Max - Min] opertion) and cascade system. Higher signal–to–noise ratios (SNR) are obtained from the cascade system.

tem as the kernel length L increases from $L = 5$ to $L = 77$. The SNR for the direct method is represented by a dashed line, whereas the solid line represents the SNR for the cascade system. The SNR for the cascade system increases monotonically up to 24.5 dB at $L = 21$ ($L_{max} = 4.2W'$) as does the SNR for the direct method. There is an increase of 2.5 dB in the SNR obtained by combining a Max operation with [Max - Min] operation. This increase is consistent with visual inspection of the processed images, as noted in Sec. 3.3. As L increases further, the SNR tends to decreases more rapidly for the cascade system than for the direct method does. The reason for this tendency is that lengthening the kernel in the cascade system affects more rapidly other input features placed in different regions. In general, the RKMT processing using the cascade system tends to reach the maximum SNR for a shorter kernel length (i.e., L_{max}).

The other important quantitative analysis is to investigate how RKMT processing behaves over different kernel shapes, e.g., rectangular and nonrectangular profiles. Figure 3.21 shows the experimental results obtained with rectangular and triangular kernels. The SNRs for the direct method and cascade system are shown in (a) and (b), respectively. In (a), the triangular kernel yields slightly higher SNRs (e.g., 2.65 dB) for large kernel lengths (e.g., $L = 49$) than the rectangular kernel does. In (b), the triangular kernel still produces higher SNRs (e.g., 1.23 dB at $L = 57$) for large kernel lengths. In both cases, RKMT processing using the rectangular kernel tends to reach the maximum SNR and then fall off for a shorter kernel length (note L_{max} both for the direct method and for the cascade system) than is the case using the triangular kernel. Table 3.2 shows the numerical results obtained for the direct method and cascade system for the rectangular and triangular profile kernels. As a comparison, the PMSE method has been applied to the image processed by a digital median filtering operation. The SNRs obtained by using 3x3, 5x5, and 7x7 filtering masks are 18.6 dB, 18.3 dB, and 17.6 dB, respectively. Note that the SNR for the cascade system is approximately 6 dB higher than obtained

with the median filtering for the particular image shown in Fig. 3.7(b). As more undesirable features such as short line segments and curved line segments are added to the noisy image, RKMT processing will achieve more significant improvement in SNR than the median filtering operation. Table 3.2 shows the numerical results obtained for the direct method and cascade system for the rectangular and triangular profile kernels.

3.4.3 Discussion

The quantitative performance measures of RKMT processing correlate well with the visual inspection of the RKMT enhanced images. The cascade system certainly performs better than a simple direct method. From this result, it can be expected that the general multipass operation discussed in Sec. 3.3 can yield well enhanced linear features using either a rectangular kernel or a nonrectangular kernel.

In the next section, a possible optical system for implementing RKMT processing is discussed.

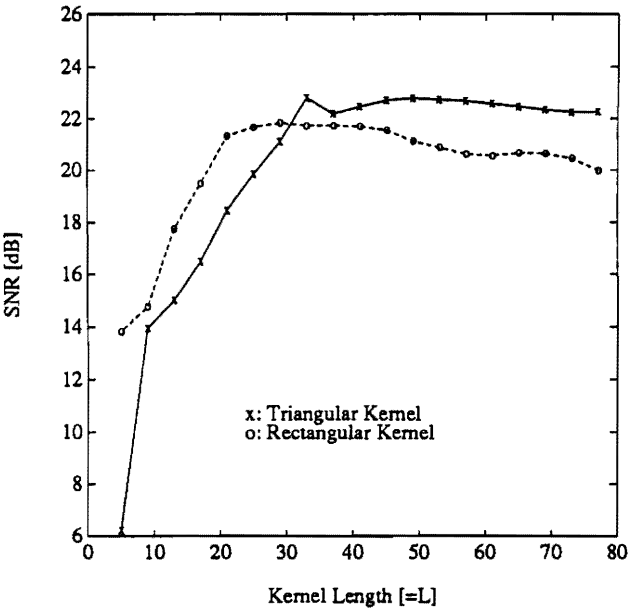

(a) [Max - Min] Operation

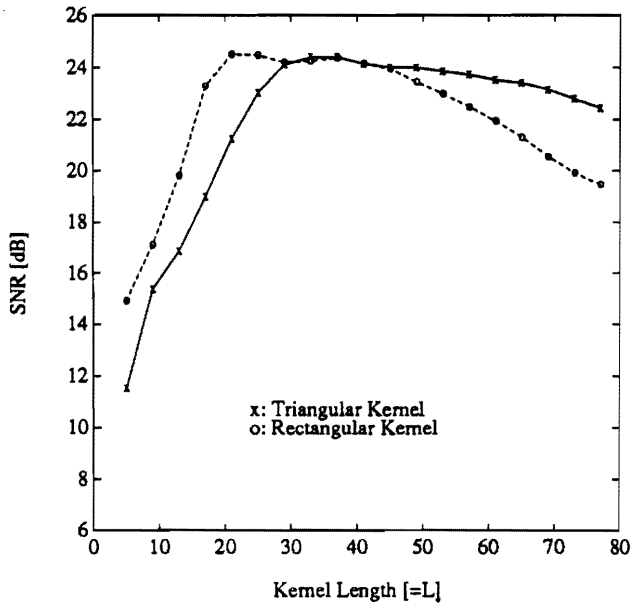

(b) Cascade System

Figure 3.21: SNR obtained for rectangular and triangular kernels.

Signal–To–Noise Ratios (SNR) dB				
Kernel Length	Direct [Max - Min] Operation		Cascade System	
L	Rectangular	Triangular	Rectangular	Triangular
5	13.8208	6.2114	14.9303	11.5156
9	14.7545	13.9324	17.1234	15.3659
13	17.7352	15.0094	19.8334	16.8680
17	19.4902	16.4740	23.2793	19.0003
21	21.3434	18.4521	24.5099	21.2540
25	21.6910	19.8641	24.4726	23.0326
29	21.8504	21.1233	24.2028	24.1165
33	21.7402	22.8100	24.2554	24.3990
37	21.7402	22.1879	24.3808	24.3990
41	21.7106	22.4594	24.1681	24.1508
45	21.5562	22.7117	23.9488	23.9984
49	20.1405	22.7866	23.4519	23.9984
53	20.8976	22.7366	22.9929	23.8512
57	20.6290	22.6748	22.4946	23.7244
61	20.5757	22.5777	21.9531	23.5257
65	20.6752	22.4711	21.3254	23.4081
69	20.6520	22.3442	20.5606	23.1542
73	20.4563	22.2542	19.9236	22.7992
77	19.9892	22.2653	19.4784	22.4361

Table 3.2: Numerical results obtained for direct method and cascade system over different kernel shapes ($W = 1$) where the kernel length L changes from $L = 5$ to $L = 77$.

3.5 Optical Implementation

3.5.1 General Principle

RKMT processing can be implemented using a computer or specialized digital–electronic image processing hardware. The method is computationally expensive on a digital computer, since a large number of convolutions and rotations (perhaps with a large kernel) must be evaluated. Suppose that an input image with DxD pixels is convolved with a rotating kernel of dimension LxW. For a Max operation using M discrete kernel orientations, the number of multiplications and additions required is given by approximately $2LWMD^2$ for serial processing and $2LWM$ for parallel processing (using specialized digital–electronic hardware) on the computer. In either case, the number of computations increases greatly as L, W, M, and D increase. However, the RKMT method lends itself to hybrid optical electronic implementation [22], where the computationally–intensive convolution and rotation operations are performed optically and optomechanically, respectively, and the Min–Max operations are performed electronically.

A coherent optical system may be used to implement the convolution. As given in Eq. 3.5,

$$S_\theta(x,y) = O(x,y) ** K_\theta(x,y), \tag{3.23}$$

or, in the spatial frequency domain,

$$\hat{S}_\theta(u,v) = \hat{O}(u,v)\,\hat{K}_\theta(u,v), \tag{3.24}$$

where $\hat{S}_\theta(u,v)$, $\hat{O}(x,y)$, and $\hat{K}_\theta(x,y)$ are the 2–D Fourier transforms of $S_\theta(x,y)$, $O(x,y)$, and $K_\theta(x,y)$, respectively, and u and v are the horizontal and vertical spatial frequency coordinates in the Fourier transform plane. There are certain drawbacks to coherent optical implementation of RKMT processing, particularly when including general multipass operations or when combining a Max operation with a [Max - Min] operation. To begin with, the input distribution in the coherent

optical system must be in the form of a complex wave amplitude distribution. Thus, a high definition TV monitor or LED array cannot be used directly for input to a coherent spatial filtering system, but somehow must be converted to wave amplitude form using an incoherent–to–coherent converter. Photographic film may be used to record an intermediate output image, but it generally requires time–consuming chemical processing. Other serious problems with coherent spatial filtering systems include coherent noise and dynamic range. Any speck on an optical element, e.g., a lens, can scatter light that ultimately manifests itself as an undesired diffraction pattern in the output image. The dynamic range problem applies at the output plane because of the square–law relationship between wave amplitude and intensity. For example, in order to measure a wave amplitude distribution with dynamic range of three orders of magnitude, a detector must be used whose intensity response can vary over six orders of magnitude.

These problems are not found in incoherent spatial filtering systems [86,87,88]. Since the kernels shown in Fig. 3.3 are typically real and non–negative, an incoherent spatial filtering can be used to implement RKMT processing, incorporating additional hybrid components [22] for general multipass operation. Figure 3.22 shows one possible incoherent system implementation. A holographically–recorded pupil transparency or computer–generated hologram [89], placed in the pupil plane, is used to determine the convolution kernel. In the optical implementation, it is necessary to physically rotate the pupil transparency (thereby rotating the convolution kernel) in the optical system. This is much faster than effecting an equivalent kernel–rotation operation on a digital computer, particularly when the input image has a high space–bandwidth product (high definition image) [22], since the convolution operation can be done instantaneously regardless of the kernel size (e.g., 41x5 pixels) and the dimension of the input image (e.g., 1024x1024 pixels). Normally the holographically–reconstructed kernel would be diffracted off–axis, and the convolution output would therefore swing in an arc around the optical axis. Use of a

compensating prism prevents this by bring the convolution on axis. Details of the incoherent system implementation are described in the following sections.

3.5.2 Holographical Spatial Filter

Figure 3.23 shows an interferometric system [33] for recording the desired pupil mask on a photographic film or holographic plate [33]. A positive lens is represented by two arrows vertically positioned. Suppose that the convolution kernel to be recorded is given by $h(x,y)$. The distribution, perhaps recorded on film, is illuminated by a collimated beam of laser light. The lens Fourier transforms $h(x,y)$, yielding in the Fourier transform plane the amplitude distribution

$$\frac{1}{\lambda f}\widehat{H}\left(\frac{x'}{\lambda f},\frac{y'}{\lambda f}\right), \tag{3.25}$$

where $\widehat{H}(\ ,\ )$ represents the Fourier transform of $h(x,y)$. A portion of the collimated light passes through a prism, is deflected down, and is incident on the Fourier transform plane at angle θ. This reference beam has field distribution

$$U_r(x',y') = R\exp(-j2\pi\alpha y'), \tag{3.26}$$

where R is the amplitude of the reference beam and the spatial frequency carrier is given by

$$\alpha = \frac{\sin\theta}{\lambda}, \tag{3.27}$$

where λ is the wavelength of a quasi–monocromatic laser beam. Assume that a positive–working film with $|\gamma| = 2$ is used to record the interference pattern produced by the two incident waves in the Fourier transform plane. Then, the amplitude transmittance of the resulting photographic transparency is represented by

$$\begin{aligned} t(x',y') &= \left|R\exp(-j2\pi\alpha y') + \left(\frac{1}{\lambda f}\right)\widehat{H}\left(\frac{x'}{\lambda f},\frac{y'}{\lambda f}\right)\right|^2 \\ &= R^2 + \frac{1}{\lambda^2 f^2}\left|\widehat{H}\left(\frac{x'}{\lambda f},\frac{y'}{\lambda f}\right)\right|^2 + \frac{R}{\lambda f}\widehat{H}\left(\frac{x'}{\lambda f},\frac{y'}{\lambda f}\right)\exp(j2\pi\alpha y') \end{aligned}$$

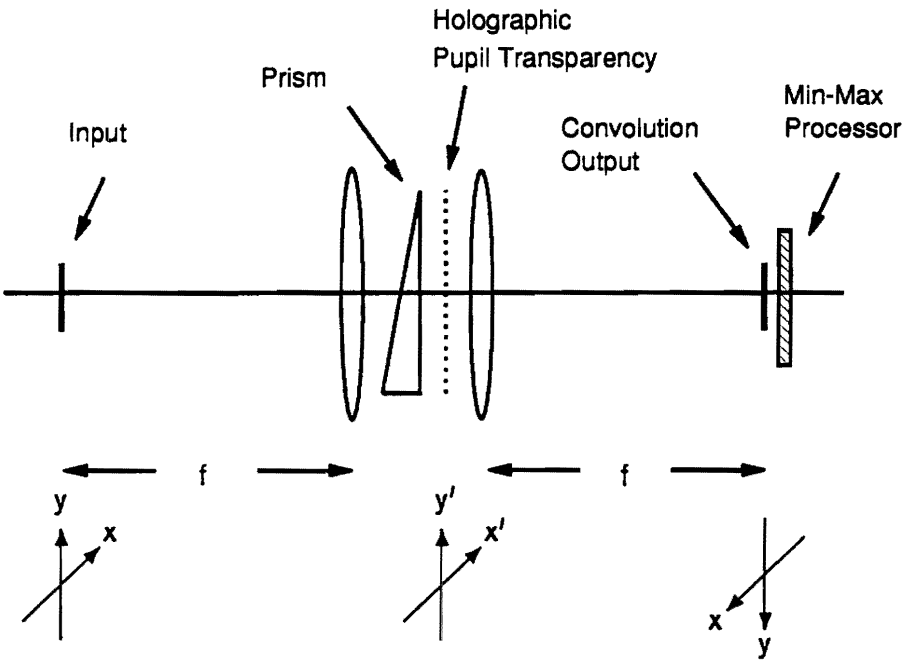

Figure 3.22: One possible hybrid optical implementation. Incoherent optical convolver with electronic min–max processor in output plane. The prism compensates for holographic carrier. Prism and hologram trun as a pair to rotate on–axis convolution kernel. Min–Max processor performs Min–Max calculations.

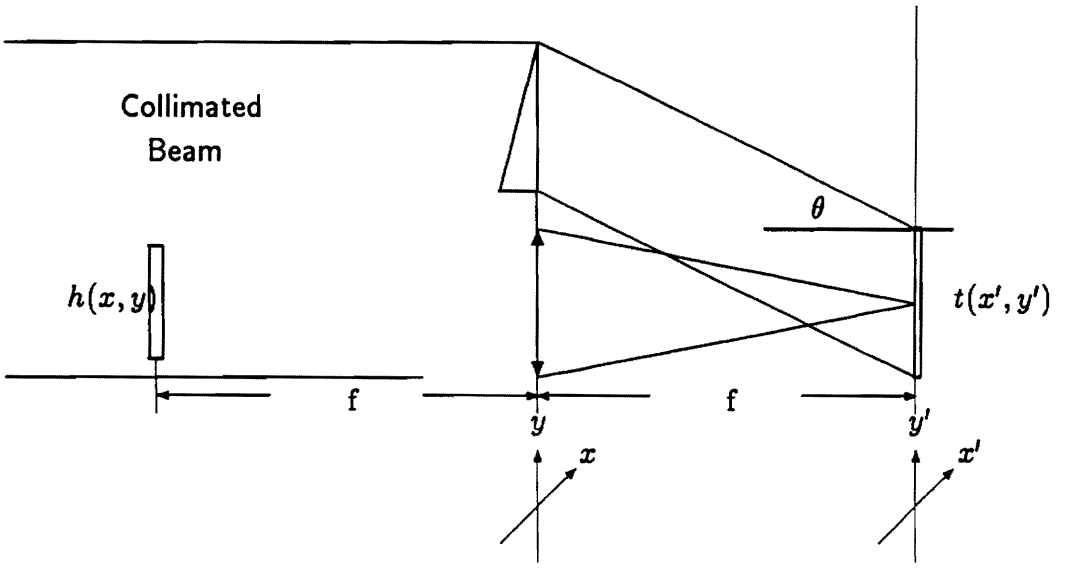

Figure 3.23: An interferometric setup for recording a kernel $h(x,y)$ where a positive lens is represented by double arrows and photographic film is used to record the interference pattern.

$$+\frac{R}{\lambda f}\widehat{H}^{*}\left(\frac{x'}{\lambda f},\frac{y'}{\lambda f}\right)\exp(-j2\pi\alpha y'). \tag{3.28}$$

3.5.3 Incoherent Spatial Filtering

The pupil transparency with amplitude transmittance $t(x',y')$, given above, is inserted in the pupil plane of the incoherent spatial filtering system of Fig. 3.22. With no prism in the pupil plane, the output image $I_{im}(x,y)$ is given by the convolution:

$$\begin{aligned} I_{im}(x,y) &= \kappa\, I_g(x,y) ** f_g(x,y) \\ &= \kappa\, |O(x,y)|^2 ** \left|\left(\frac{1}{\lambda f}\right)\widehat{T}\left(\frac{x}{\lambda f},\frac{y}{\lambda f}\right)\right|^2 \end{aligned} \tag{3.29}$$

where $I_g(x,y)$ and $f_g(x,y)$ are the intensities of input image and the system point spread function, respectively, $\widehat{T}(,\,)$ is the Fourier transform of $t(x,y)$, and κ is a proportionality constant. Equation 3.29 can be Fourier transformed to obtain

$$\widehat{I}_{im}(x',y') = \kappa\, \widehat{I}_g(x',y')\,\widehat{F}_g(x',y'), \tag{3.30}$$

where $\widehat{I}_g(x',y')$ and $\widehat{F}_g(x',y')$ are the Fourier transforms of $I_g(x,y)$ and $f_g(x,y)$, respectively. With the same prism used for recording the convolution kernel $h(x,y)$ in the pupil plane, Eq. 3.30 is modified as follows:

$$\widehat{I}_{im}(x',y') = \kappa\, \widehat{I}_g(x',y')\,[\widehat{F}_g(x',y')\exp(-j2\pi\alpha y')], \tag{3.31}$$

or in the space domain,

$$I_{im}(x,y) = \kappa\, I_g(x,y) ** [f_g(x,y) ** \delta(x,y-\lambda f\alpha)]\,. \tag{3.32}$$

The result shown in Eq. 3.32 indicates that the holographically reconstructed images are shifted by $\lambda f\alpha$ along the y direction in the output plane.

Normally, the holographically reconstructed kernel is diffracted off axis, and the reconstructed images consist of four components at three different locations: convolution, crosscorrelation, and combination of the input function and kernel. Use

of a compensating prism brings the convolution on axis as shown in the following simple analysis. From Eq. 3.29 and Eq. 3.32,

$$f_g(x,y)**\delta(x,y-\lambda f\alpha) = \left(\frac{1}{\lambda f}\right)^2 \left|\hat{T}\left(\frac{x'}{\lambda f},\frac{y'}{\lambda f}\right)\right|^2 **\delta(x,y-\lambda f\alpha)$$

$$= \left(\frac{1}{\lambda f}\right)^2 \left|\mathcal{F}\left\{\left|R\exp(-j2\pi\alpha y') + \left(\frac{1}{\lambda f}\right)\widehat{H}\left(\frac{x'}{\lambda f},\frac{y'}{\lambda f}\right)\right|^2\right\}\right|^2 **\delta(x,y-\lambda f\alpha)$$

$$= \left(\frac{1}{\lambda f}\right)^2 \left|\mathcal{F}\left\{R^2 + \frac{1}{\lambda^2 f^2}\left|\widehat{H}\left(\frac{x'}{\lambda f},\frac{y'}{\lambda f}\right)\right|^2 + \frac{R}{\lambda f}\widehat{H}^*\left(\frac{x'}{\lambda f},\frac{y'}{\lambda f}\right)\exp(-j2\pi\alpha y')\right.\right.$$

$$\left.\left. + \frac{R}{\lambda f}\widehat{H}(\frac{x'}{\lambda f},\frac{y'}{\lambda f})\exp(+j2\pi\alpha y')\right\}\right|^2 **\delta(x,y-\lambda f\alpha)$$

$$= \left(\frac{1}{\lambda f}\right)^2 |R^2\delta(x,y) + h(x,y)**h(-x,-y) + Rh(-x,-y)**\delta(x,y-\lambda f\alpha)$$

$$+ Rh(x,y)**\delta(x,y+\lambda f\alpha)|^2 **\delta(x,y-\lambda f\alpha). \qquad (3.33)$$

With the substitution of Eq. 3.33 into Eq. 3.32, the expression for the output image assumes the form

$$I_{im}(x,y) = \frac{\kappa}{\lambda^2 f^2} I_g(x,y) ** \left|R^2\delta(x,y) + h(x,y)**h(-x,-y)\right.$$

$$+ Rh(-x,-y)**\delta(x,y-\lambda f\alpha)$$

$$\left. + Rh(x,y)**\delta(x,y+\lambda f\alpha)\right|^2 **\delta(x,y-\lambda f\alpha). \qquad (3.34)$$

Equation 3.34 can be simplified into

$$I_{im}(x,y) = \frac{\kappa}{\lambda^2 f^2}\left[\{R^4 I_g(x,y) + |h(x,y)**h(-x,-y)|^2\}**\delta(x,y-\lambda f\alpha)\right.$$

$$+ R^2 I_g(x,y)**|h(-x,-y)|^2**\delta(x,y-2\lambda f\alpha)$$

$$\left. + R^2 I_g(x,y)**|h(x,y)|^2\right]$$

$$= A + B + C + D. \qquad (3.35)$$

In Eq. 3.35, the first [=A] and second [=B] terms correspond to the input itself and the intensity of the autocorrelation of the kernel $h(x,y)$ located at $y = \lambda f\alpha$,

respectively. The third [=C] and fourth [=D] terms are the correlation and convolution of the input with the kernel located at $y = 2\lambda f\alpha$ and on axis, respectively. The desired convolution output [=D] as given in Eq. 3.35 can be obtained on axis if $I_g(x,y)$ and $h(x,y)$ are replaced by $O(x,y)$ and $\sqrt{K_\theta(x,y)}$, respectively.

Figure 3.24 shows the reconstructed images (a) without and (b) with a compensating prism combined with the pupil transparency in the pupil plane. As shown in that figure, the incident angle of the reference beam for recording the kernel $h(x,y)$ should be large enough to avoid overlap of the convolution output and the reconstructed images located at $y = \lambda f\alpha$. Figure 3.25 illustrates how the reconstructed images without the prism appear in the output plane. Without the kernel rotation, the convolution output is located at upper–plane. As the kernel rotates, however, the convolution output D swings around the optical axis. Similarly, Fig. 3.25 shows the reconstructed images with the prism–pupil combination in the pupil plane. Thus, rotation of the prism–hologram combination results in the desired rotation of the kernel $K_\theta(x,y)$.

3.5.4 Min–Max Processor

Determination of Max(x,y) and Min(x,y) requires that the convolution output $S_\theta(x,y)$ in Eq. 3.5 be measured for a large number of orientation angles θ, e.g., between 8 and 300 for typical processing operations. Use of the TV camera in the output plane would in such cases require approximately 0.26 – 10 seconds for an asymmetric kernel or 0.13 – 5.0 seconds for a symmetric kernel to process a given input image, assuming 30 frames per second. Thus, if a digitizing TV camera is used as a detecting device in the output plane, the speed is limited to TV frame rate. Much greater speed can be achieved if a detector array is integrated electronically with simple peak-detection circuitry to produce the desired Max(x,y) and Min(x,y) outputs directly. Alternatively, a smart spatial light modulator may also be considered to detect Max and Min values and to perform a simple arithmetic operation

using these values, although such light modulator is not commercially available at present.

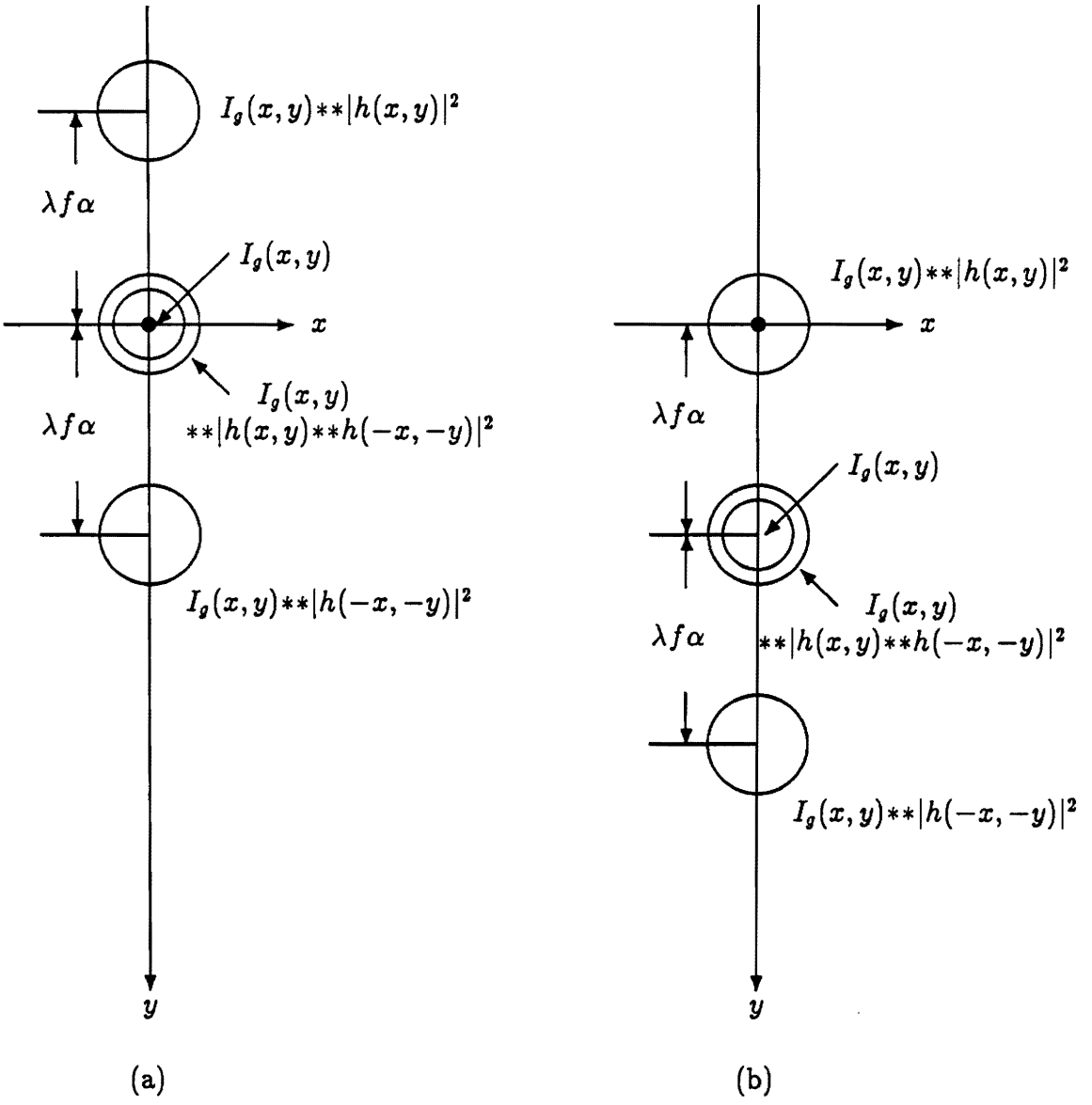

Figure 3.24: Reconstructed images without kernel rotation: (a) result without the prism; (b) result with the prism. Thus, the prism–pupil combination yields the desired convolution output on axis. (•) is the center of the axis.

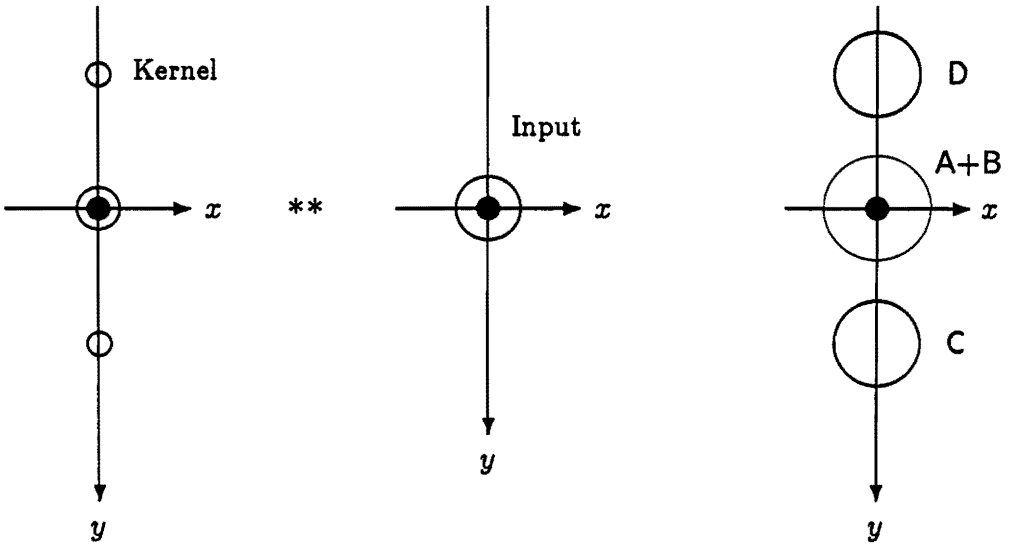

(a) Without kernel rotation

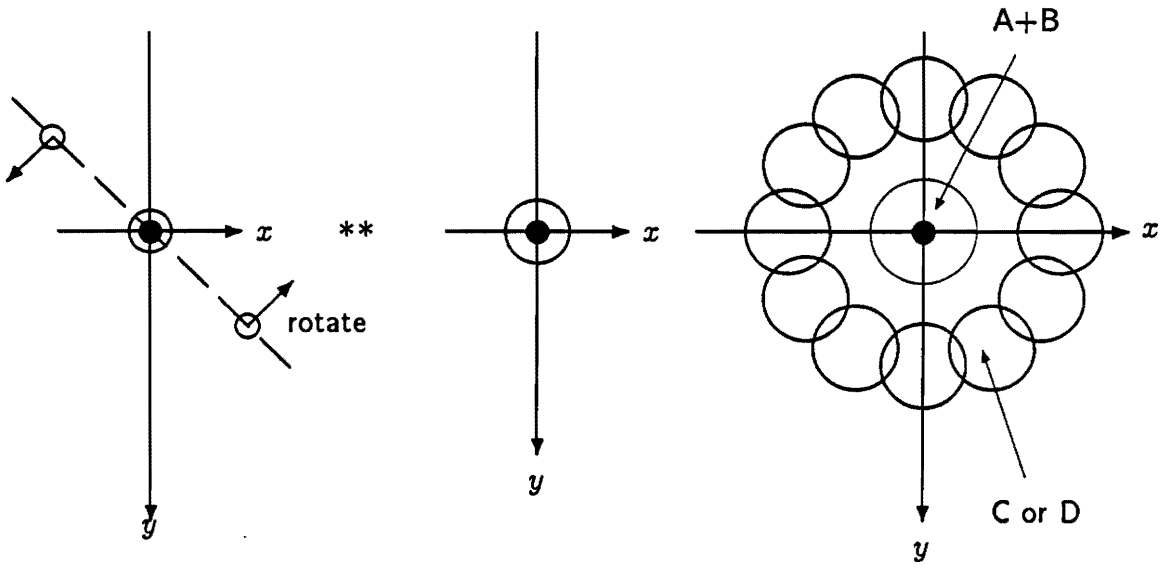

(b) With kernel rotation

Figure 3.25: Reconstructed images (third column) without a prism. The reconstructed kernel $|h(x,y)|^2$ with a point source is located in the upper–plane of the first column of (a). As the kernel rotates, the desired convolution output [=D] is completely lost as shown in (b). (•) is the center of the axis.

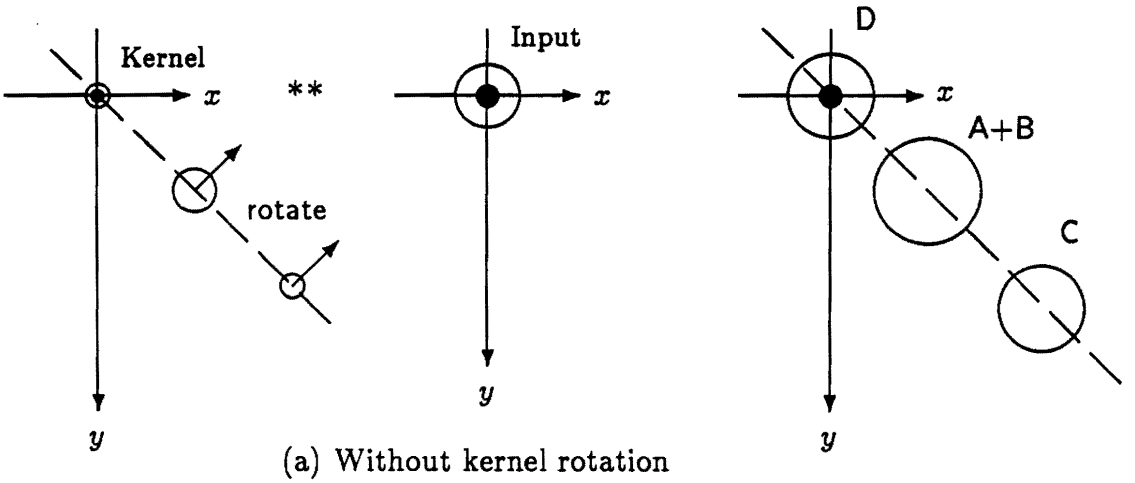

(a) Without kernel rotation

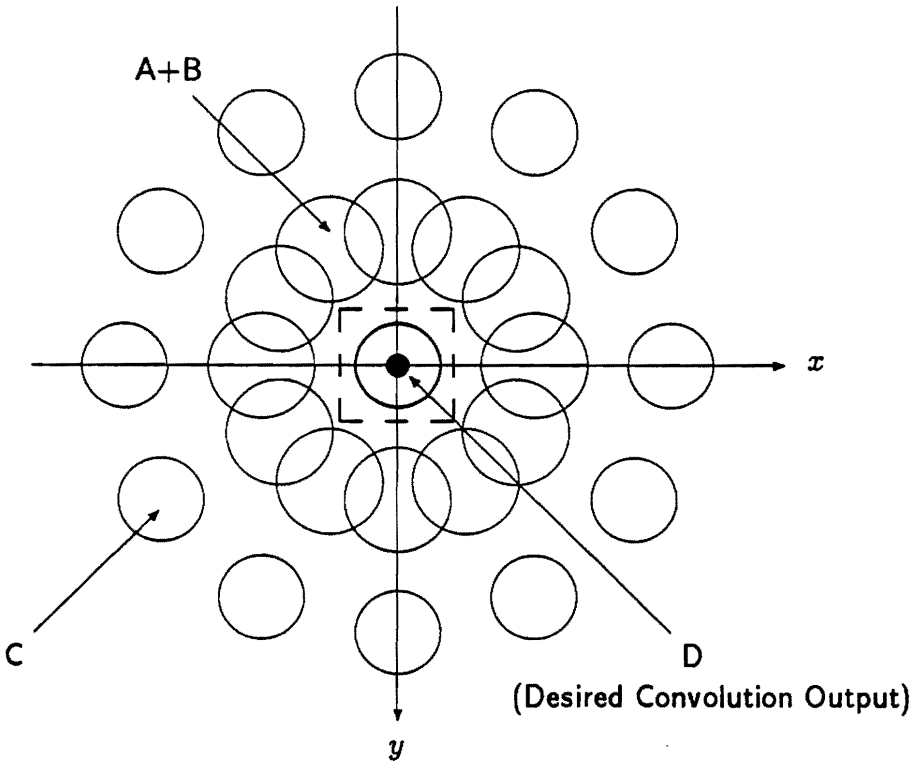

(b) With kernel rotation

Figure 3.26: Reconstructed images with a prism. The reconstructed kernel (i.e., $|h(x,y)|^2$) with a point source is on axis in (a). As the kernel rotates, the desired convolution output [=D] is obtained on the optical axis as shown in (b) (inside dashed box). (•) is the center of the axis.

CHAPTER 4

NONLINEAR IMAGE PROCESSING: PREPROCESSING

4.1 Introduction

In Chapter 2, the estimation of cell parameters was performed using high contrast cell boundary patterns. In this chapter, the rotating kernel min–max transformation (RKMT) discussed in Sec. 3 is applied to raw gray–scale imagery to obtain such high contrast image patterns. The raw imagery is processed either by the direct [Max – Min] operation or by the multipass operation combining a Max operation with the [Max – Min] operation. Both rectangular and triangular kernels are used. Numerical experiments performed on a computer are presented. The effects of using the function $f[\ ,\ ] = [1 - \rho][Max - Min]$ to reduce variations in the brightness of the enhanced line segments are also discussed. The processed image is subjected to a thresholding operation to obtain a binarized image. Three thresholding methods are discussed. The results of the RKMT processing are then compared with results of conventional spatial filtering methods. The application of the RKMT processing operation to the enhancement of linear features is then summarized.

4.2 Application of RKMT to Raw Endothelial Cell Imagery

4.2.1 Basic Max and [Max – Min] Experiments

The polygonal cell boundaries shown in Fig. 4.1(a) are fairly easy to see by eye, since simple cells in the human visual cortex respond strongly to specifically oriented features (e.g., lines or edges) positioned in their receptive fields [70]. However, because of relatively low contrast, noise, and spatially varying average intensity, the cell boundaries are difficult to locate and enhance automatically. Furthermore, they are randomly oriented and have varying lengths and thicknesses. These characteristics of the raw image hinder such techniques as the Radon transform [31] method and a method based on the human visual model [11] from being used for the automated enhancement operation. However, the RKMT processing operation implemented using an appropriately chosen kernel can overcome these difficulties.

Figure 4.1 shows the results of applying the RKMT processing operation in a numerical simulation. The input is shown in (a). A typical cell boundry in this input is approximately 22 pixels long and 4 pixels wide. Note in (a) that the upper–center region is brighter than the lower–right region. This spatially varying brightness characteristics is much more noticeable in a wide field image, which consists of many more cells. The result of applying the [Max - Min] operation with a symmetric triangular kernel ($L = 11$ and $W = 1$) is shown in Fig. 4.1(b). Lengthening the kernel results in greater connectivity for output line segments, but also in some smoothing, particularly at the cell vertices. Figure 4.1(c) shows the result of applying the [Max - Min] operation to (a) with a longer symmetric triangular kernel ($L = 19$ and $W = 1$). Calculating [Max - Min] tends to reduce the effects of slowly varying changes in background intensity and to remove any uniform bias. Thus, the result is an enhancement of the cell boundaries relative

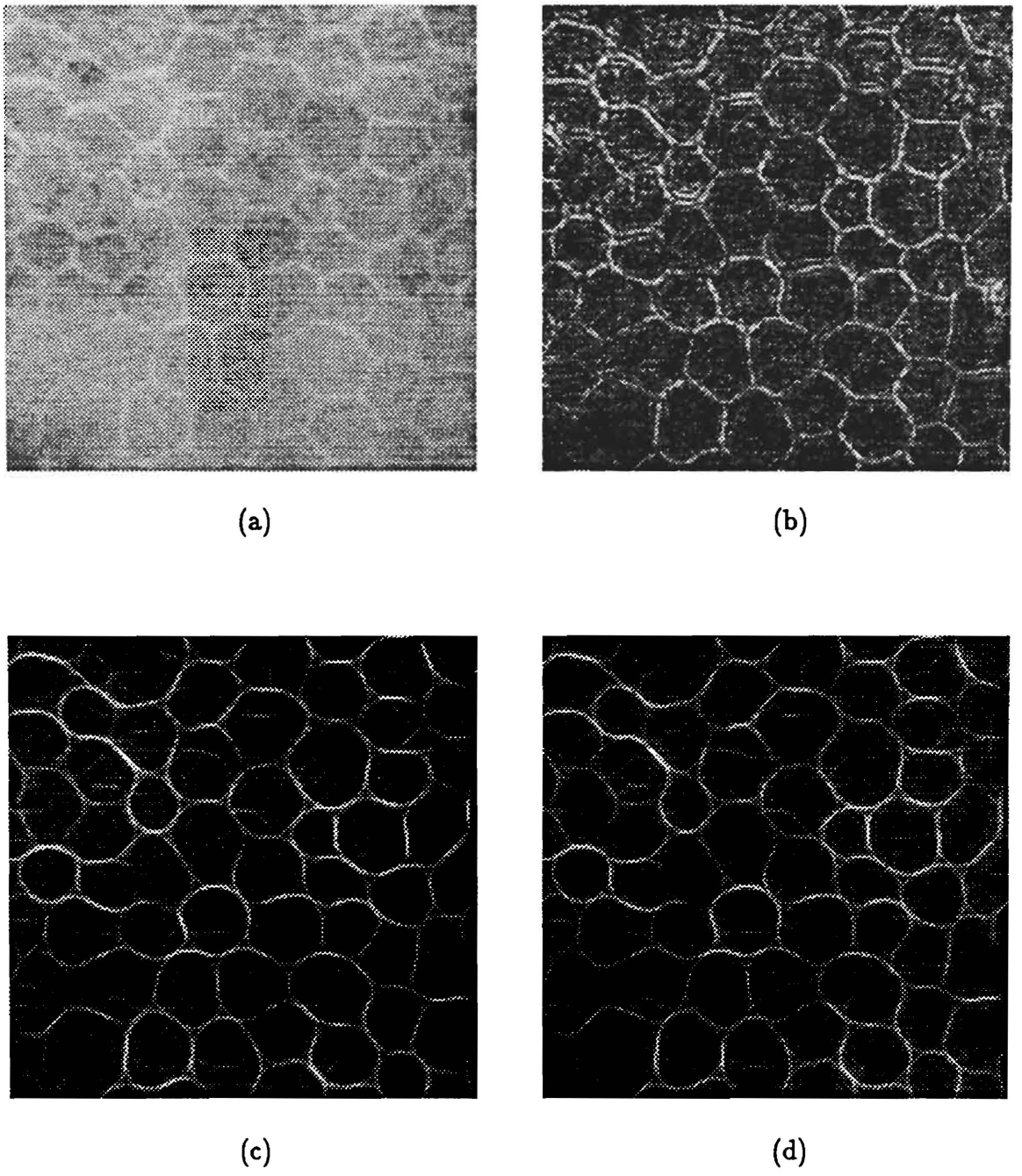

Figure 4.1: Results of applying [Max - Min] operation numerically using different kernels: (a) input image; (b) triangular kernel ($L = 11$ and $W = 1$); (c) triangular kernel ($L = 19$ and $W = 1$); (d) rectangular kernel ($L = 11$ and $W = 1$).

to the background. Similar thickening and smoothing effects result from using a rectangular kernel instead of a triangular kernel. Figure 4.1(d) shows the result of using a symmetric rectangular kernel with $L = 11$ and $W = 1$. In the simulation, the kernel used was rotated through 12 discrete angles separated by approximately 15° in angle. Detection or delineation capability of linear features (e.g., cell boundaries) can be improved by increasing the number of rotation angles. Figure 4.2 shows the kernel and rotating angles used for the simulation.

Better results were obtained by multipass operation (e.g., cascade system) that combines a Max operation with a [Max - Min] operation. Figure 4.3 shows the results of applying the multipass operation to the input image in Fig. 4.1(a) with a symmetric triangular kernel ($L = 11$ and $W = 1$). The intermediate image obtained from the Max operation is shown in Fig. 4.3(a). This image is subjected to a [Max - Min] operation. The result of the [Max - Min] operation is shown in Fig. 4.3(b). Some enhancement of the cell boundaries relative to background is evident. The image obtained at the cascade system (i.e., first iteration) is further processed by a Max operation. The result of applying the Max operation in the second iteration is shown in Fig. 4.3(c). Figure 4.3(d) shows the result of applying the [Max - Min] operation to the image in Fig. 4.3(c). Note in (b) and (d) that background variations have been effectively removed and the contrast is greatly enhanced. If this multipass operation is repeated over and over, smoothing begins to increase and some image details such as vertices may be deemphasized or even fully lost. Figure 4.4 shows the results of using different kernel dimensions and profiles for the cascade system (i.e., first iteration). Figures 4.4(a) and (b) show the output images obtained using a triangular kernel with $L = 19$ and $W = 1$. The result of applying a Max operation is shown in (a). This image is subjected to the [Max - Min] operation, yielding the image in (b). Figs. 4.4(c) and (d) show the results of using a rectangular profile kernel ($L = 11$ and $W = 1$). The result of applying the Max operation is shown in (c). Figure 4.4(d) shows the result of

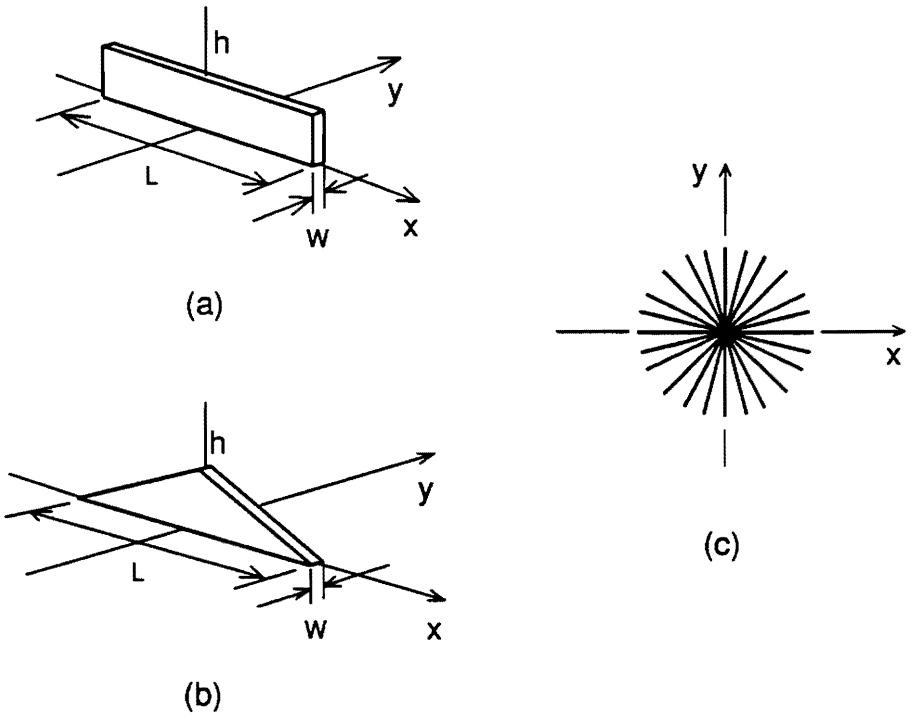

Figure 4.2: Two kernels and rotating angles used for numerical experiments ($h = 1$): (a) long, narrow rectangular profile; (b) long, narrow triangular profile; (c) 12 discrete kernel orientations used for numerical experiments.

applying the [Max – Min] operation to Fig. 4.4(c). As seen in the processed images of Figs. 4.1, 4.3, and 4.4 lengthening the kernel increases output line connectivity and smoothing. It is also clear from the figures that a nonrectangular kernel yields less smoothing than a rectangular kernel.

It can be seen in Figs. 4.3 and 4.4 that vertices are typically darker than other portions of the cell boundaries (e.g., the centers of line segments). Note that the kernel used ($L = 11$) is approximately half the length of a typical cell boundary (22 pixels long). Consider only those points along a typical cell boundary or line segment. The Max value at the center of the cell boundaries is comparatively larger than that at or near the vertices (or line intersections). (Recall from Fig. 3.5 that the Min value at the centers of these vertices tends to be larger than that at the centers of the line segments in a binary image.) Then, the difference [Max - Min] value at points at or near these vertices will be smaller than that at or near the center of the cell boundary.

4.2.2 Nonuniform Brightness of Enhanced Line Segments

Operations similar to [Max - Min] may be performed by other transform functions as discussed in Sec. 3.2.3. For example, $f[Max(x,y), Min(x,y)] = [1-\rho^m(x,y)]$ and $f[Max(x,y), Min(x,y)] = [1-\rho^m(x,y)]/[1+\rho^m(x,y)]$ produce good results in certain situations (e.g., low contrast imagery), where $\rho = Min(x,y)/Max(x,y)$. Note that, for $m = 1$, $[1-\rho(x,y)]/[1+\rho(x,y)] = [Max(x,y) - Min(x,y)]/[Max(x,y) + Min(x,y)]$, commonly referred to as a visibility measure of an image. In some cases, certain line segments representing cell boundaries are brighter than others. Two different methods can be considered for compensating for this nonuniform brightness. Recall first that the kernel used in the simulation was rotated through only the 12 discrete angles. Those boundary segments actually aligned with the rotation angles received the greatest enhancement. As the number of rotation angles increases, the results can be expected to improve. Second, note that the difference

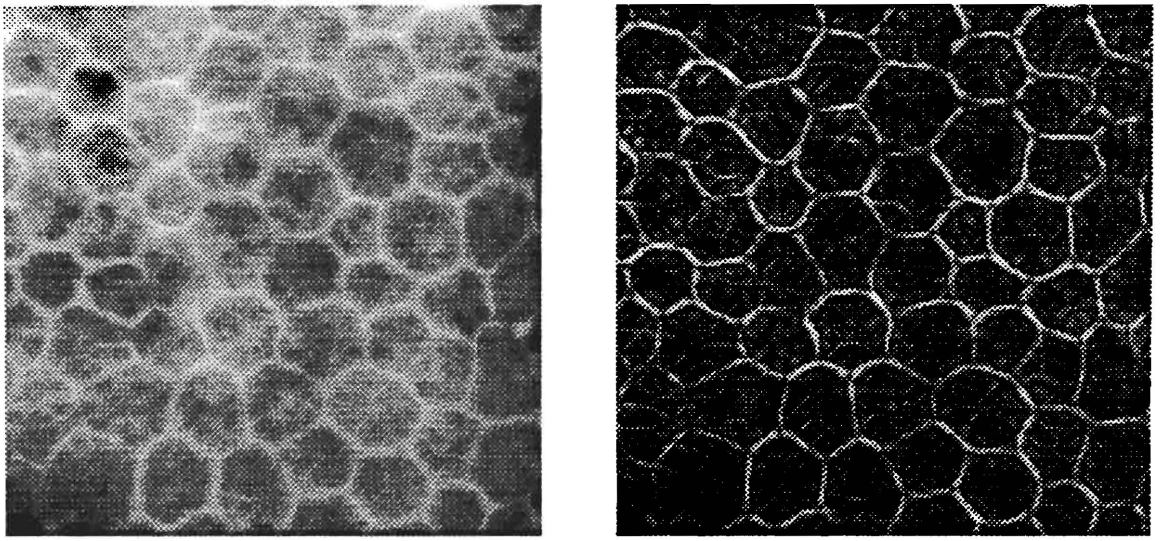

(a) (b)

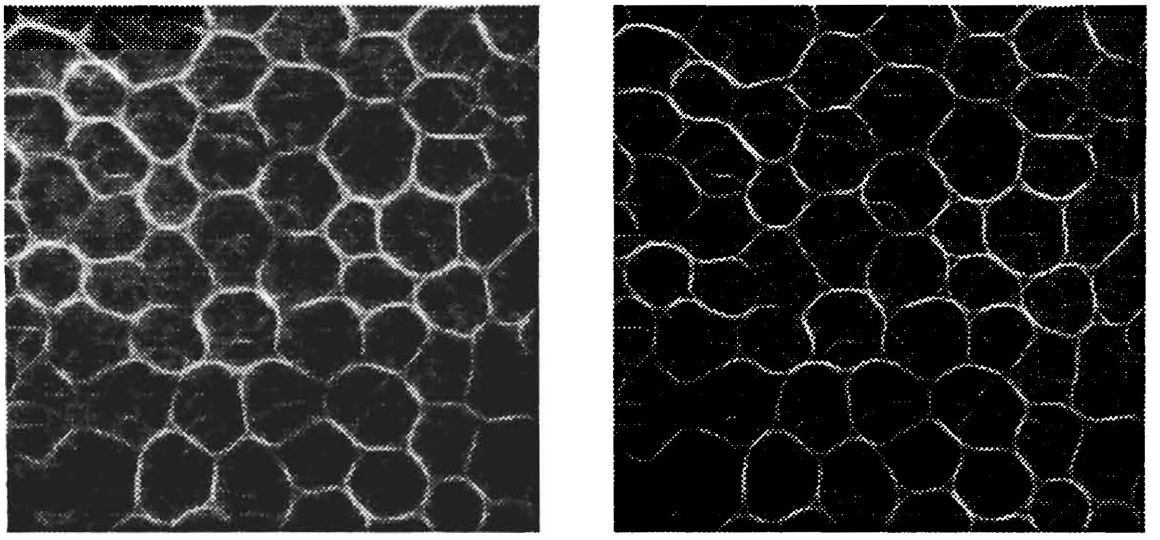

(c) (d)

Figure 4.3: Multipass operations numerically performed using a triangular kernel with $L = 11$ and $W = 1$: (a) result of Max operation applied to the image in Fig. 4.1(a); (b) result of [Max - Min] operation applied to (a); (c) result of Max operation applied to (b); (d) result of [Max - Min] operation applied to (c).

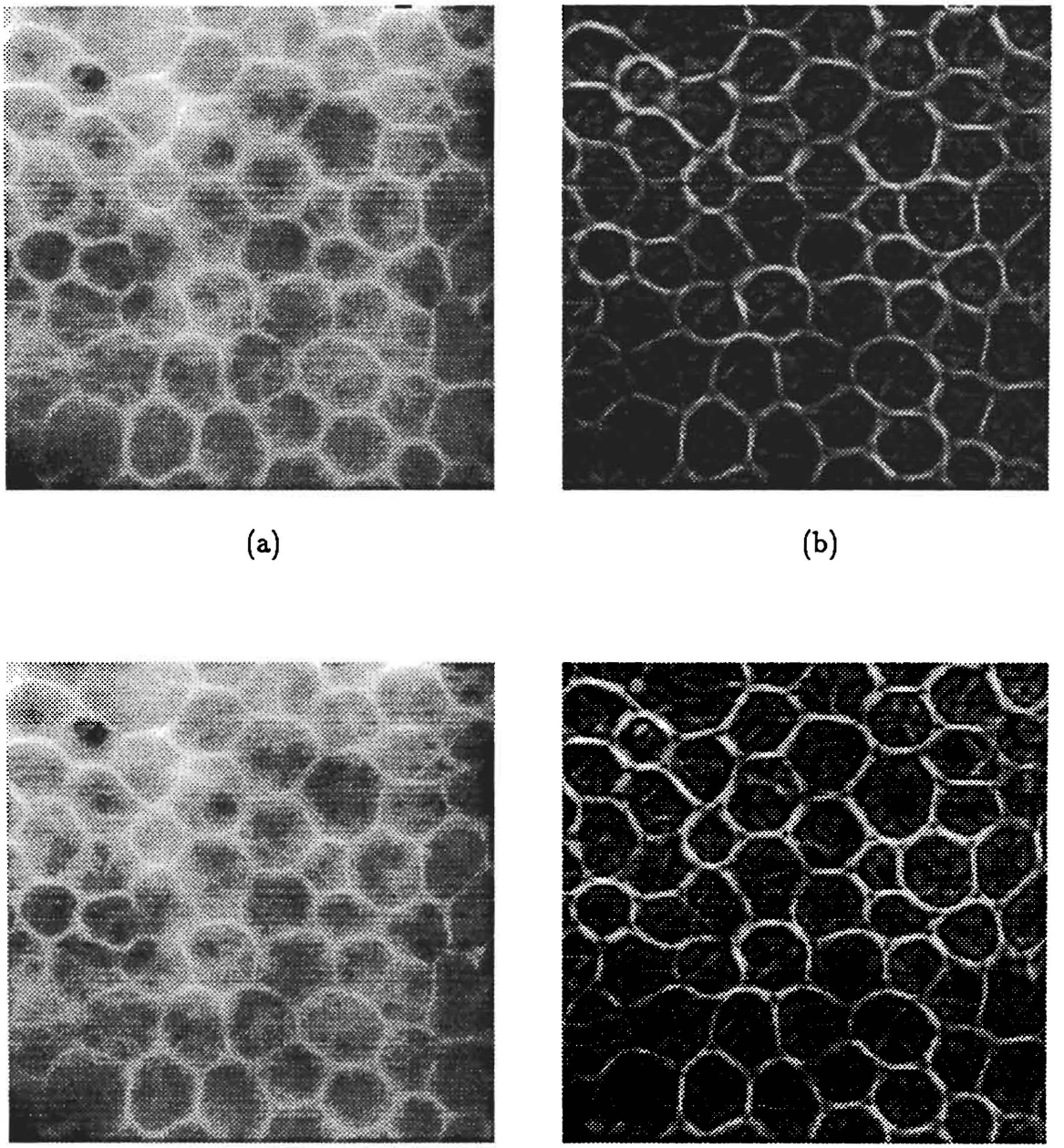

(a) (b)

(c) (d)

Figure 4.4: First iterations using different kernel shapes. (a) and (b): results of Max and [Max - Min] operations using a triangular kernel ($L = 19$ and $W = 1$). (c) and (d): results of Max and [Max - Min] operations using a rectangular kernel ($L = 11$ and $W = 1$).

[Max(x,y) – Min(x,y)] along the cell boundaries may vary spatially from one region to the other, even though the enhanced line segments are brighter than their backgrounds. In certain situations, this nonuniform brightness may be compensated by using the function $f[Max, Min] = [1 - \rho^m(x,y)][Max(x,y) - Min(x,y)]$ rather than simply [Max(x,y) – Min(x,y)]. As discussed in Sec. 3.2.3 (also see Fig. 3.6), the function $[1 - \rho^m(x,y)]$ is sensitive to small variations in background intensity of a low contrast region, where $[1 - \rho(x,y)] = [Max(x,y) - Min(x,y)]/Max(x,y)$ for $m = 1$. It has the effect of normalizing [Max - Min] by the Max value, The difference [Max(x,y) - Min(x,y)] at each point represents the brightness of line segments relative to their backgrounds regardless of their locations. Thus, by incorporating [Max(x,y) – Min(x,y)] with $[1 - \rho^m(x,y)]$, the former term detects the brightness of line segments relative to their backgrounds and the latter term compensates, to some extent, for the spatially varying characteristics of the contrast.

Consider two input points which lie on two different line segments. One line segment is located in a bright region whereas the other line segment is located in a dark region. Assume that one point in the bright region achieves Max = 200 and Min = 140 as the kernel rotates, and the other point in the dark region achieves Max = 30 and Min = 8. The differences [Max - Min] at these points are 60 and 22, respectively, differing by 38, even though these input points both lie on line segments. The function $[1 - \rho][Max - Min]$ for $m = 1$ can reduce these intenisty variations of the enhanced line segments, yielding 18 and 16.1 at each point. Table 4.1 shows numerically, for eight different input points (P_1 to P_8), the effect of using the function $[1 - \rho^m][Max - Min]$ for m=1/2, 1, 2, and 3. Those points (e.g., P_1 to P_3) in a region with comparatively low gray levels may have the smaller difference [Max - Min] than other points (e.g., P_6 to P_8) in a region with high gray levels, even though all these points lie on certain line segments. With only the [Max - Min] operation, the difference [Max - Min] varies from 22 to 60: normalized deviation $\sigma_N \simeq 0.30$. With the function $f[\ ,\ ] = [1 - \rho^m][Max - Min]$,

the variation in [Max - Min] is well reduced: normalized deviation $\sigma_N = 0.05$ (or 0.18) for $m = 1$ (or $m = 3$). It is seen from Tab. 4.1 that the function $f[\ ,\ ] = [1 - \rho^m][Max - Min]$ tends to work best for $m = 1$ to reduce the nonuniformity of the brightness of enhanced line segments.

Operations	P_1	P_2	P_3	P_4	P_5	P_6	P_7	P_8	m_o	σ	σ_N
Max(x,y)	30	50	70	100	140	160	180	200			
Min(x,y)	8	22	37	60	92	108	125	140			
[Max - Min]	22	28	33	40	48	52	55	60	42.25	12.79	0.30
$m = \frac{1}{2}$: $f[\ ,\ ]$	10.6	9.4	9.0	9.0	9.1	9.3	9.2	9.8	9.43	0.51	0.05
$m = 1$: $f[\ ,\ ]$	16.1	15.7	15.6	16.0	16.45	16.9	16.8	18.0	16.5	0.74	0.04
$m = 2$: $f[\ ,\ ]$	20.4	24.1	23.8	25.6	27.3	28.3	28.5	30.6	26.08	3.05	0.12
$m = 3$: $f[\ ,\ ]$	21.6	25.6	28.1	31.4	34.4	36	36.6	39.4	31.64	5.72	0.18

Values under each input point P_i represent gray-levels.

m_o = Mean

σ = Standard Deviation

$\sigma_N = \sigma/m_o$ (= Normalized Deviation)

Table 4.1: Effect of the function $f[Max, Min] = [1-\rho^m][Max--Min]$ for $m = 1/2$, 1, 2, and 3 on nonuniform brightness of enhanced line segments where ρ = Min/Max. The function tends to work best for $m = 1$ among these values of m to reduce the nonuniformity in the brightness of enhanced line segments.

4.3 Binarization of Enhanced Gray–Scale Image

In the application of RKMT processing to linear feature enhancement, the enhanced image is typically binarized for the subsequent postprocessing. A global thresholding–hard limiting operation can be used to binarize the image processed by the RKMT method. Figures 4.5(a) and (b) show the binarized results obtained by thresholding the images obtained at the first and second iterations in Figs. 4.3(b) and (d), respectively. Most cell boundaries in Fig. 4.5 were well extracted by such a global thresholding.

In many situations, it is difficult to choose an appropriate threshold value for automated enhancement operation in a global thresholding operation, since the enhanced line segments may have spatial variations in brightness from one region to the other. A threshold value that is too high may lose line segments with relatively low gray levels, even though these line segments were greatly enhanced relative to their backgrounds. Two methods, discussed below, have been considered for compensating the nonuniform brightness characteristics in automatic binarization of the processed gray–scale images resulting from by the RKMT method: (1) Min–Max deviation measure and (2) angular variance measure.

4.3.1 Method 1: Min–Max Deviation Measure

The Min–Max deviation measure (MDM) extracts the deviations of the Max and Min values from the mean value $[= S_o(x,y)]$ of the convolution output $S_\theta(x,y)$ obtained at each point over the range of rotation angles.

The Min–Max deviation measure is calculated as follows:

$$D(x,y) = \sqrt{\frac{[Max(x,y) - S_o(x,y)]^2 + [Min(x,y) - S_o(x,y)]^2}{2S_o(x,y)}} \qquad (4.1)$$

where $S_o(x,y)$ is given by in continuous case with the angular period T for one or

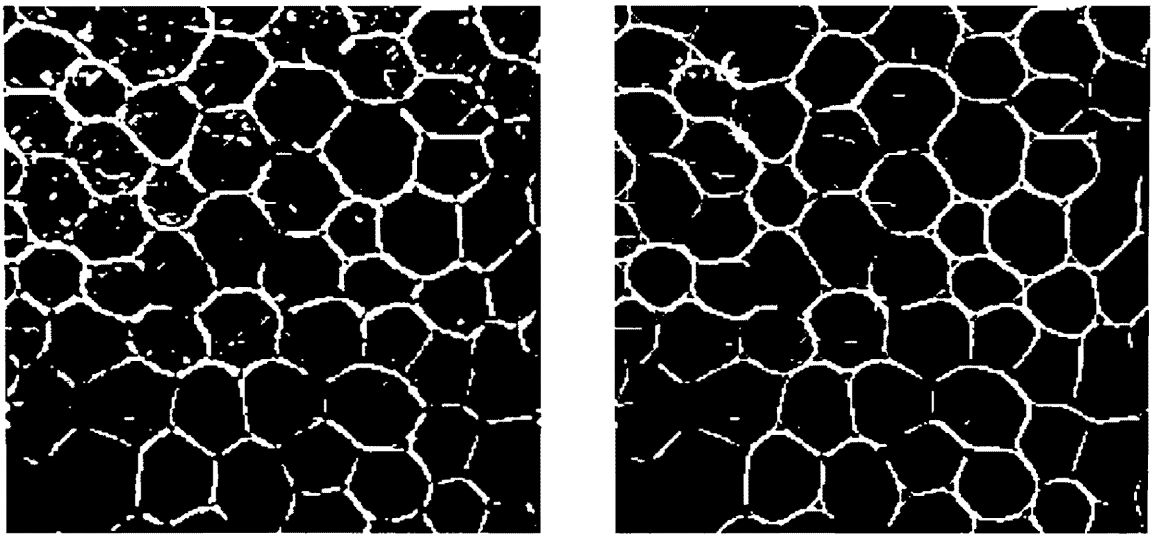

(a) (b)

Figure 4.5: Results of applying a global thresholding operation to the images (Fig. 4.3) obtained in multipass operation combining a Max operation with a [Max - Min] operation: (a) first iteration; (b) second iteration.

half revolution of the convolution kernel,

$$S_o(x,y) = \frac{1}{T}\int_{\theta=0}^{T} S_\theta(x,y)\, d\theta,$$

where $T = \pi$ or 2π, depending on whether the kernel rotates through 180° or 360°. In the discrete case with M discrete rotation angles,

$$S_o(x,y) = \frac{1}{M}\sum_{i=1}^{M} S_i(x,y).$$

The decision procedure for the binarization of the RKMT enhanced image is given by

$$\begin{aligned} I_{out}(x,y) &= 1 \qquad \text{if } D(x,y) \geq D_{th}, \\ I_{out}(x,y) &= 0 \qquad \text{otherwise,} \end{aligned} \tag{4.2}$$

where D_{th} is the particular threshold value chosen. In a region with nearly uniform brightness, the numerator in Eq. 4.1 becomes small (e.g., < 1.0) and approaches 0. In regions where the enhanced line segments (i.e., cell boundaries) are located, $D(x,y)$ becomes large (e.g., 5.0) since each term in the numerator in Eq. 4.1 is large. Figure 4.6(a) shows the result of binarizing the same image used for Fig. 4.5(b) with $D_{th} = 4.5$. It can be seen that line segments located in the lower–right side in Fig. 4.6(c) were better extracted than those in Fig. 4.5(b). Thus, the MDM method is comparatively less sensitive to spatial variations in brightness of the enhanced line segments than a global thresholding operation.

For the enhanced endothelial cell images used, it was not difficult to determine a suitable value of D_{th}. A certain range of D_{th} (e.g., $4.0 \leq D_{th} \leq 4.5$ for the second iteration) yielded good results, even though D_{th} may depend on, to a small degree, each RKMT enhanced image for the automatic binarization. If D_{th} is too large, however, some line segments may be lost. If D_{th} is too low, background noise will appear. A modified deviation measure $D'(x,y)$ can also be used:

$$D'(x,y) = \left[\frac{[Max(x,y) - S_o(x,y)]^2 + [Min(x,y) - S_o(x,y)]^2}{2S_o(x,y)}\right]. \tag{4.3}$$

The MDM method is simple to determine D_{th} for the binarization, and may be performed in an optical implementation if a smart focal plane array processor is used by detecting only Max, Min, and Mean values from the convolution output $S_\theta(x, y)$.

4.3.2 Method 2: Angular Variance Measure

The angular variance measure (AVM) utilizes the directional convolution outputs or local energies obtained at each point (x, y). Suppose that the convolution kernel $K_\theta(x, y)$ is rotated through M discrete angles. In the discrete case, the normalized standard variation $\sigma_M(x, y)$ of the convolution outputs at each point is first calculated as follows:

$$\sigma_M(x, y) = \sqrt{\frac{\sum_{i=1}^{M}[S_i(x, y) - S_o(x, y)]^2}{M \cdot S_o(x, y)}}. \tag{4.4}$$

Then, the binarization operation is performed in accord with

$$\begin{aligned} I_{out}(x, y) &= 1 \qquad \text{if } \sigma_M(x, y) \geq \sigma_{th}, \\ I_{out}(x, y) &= 0 \qquad \text{otherwise,} \end{aligned} \tag{4.5}$$

In uniform regions, σ_M approaches 0 as does $D(x, y)$ in Eq. 4.1. However, if there is a prominent line segment or linear feature, σ_M becomes large. Thus, a certain range of values for σ_{th} (e.g., $2.0 \leq \sigma_{th} \leq 2.5$ for the image obtained in the second iteration in Fig. 4.3) yielded good results for the binarization of the enhanced gray–scale image. Figure 4.6(b) shows the result of binarizing with $\sigma_{th} = 2.2$ the image used for Fig. 4.5(b).

Table 4.2 compares numerically the MDM and AVM methods for the binarization of RKMT enhanced image. Suppose that eight points (P_1 to P_8) are located in different regions with high and low gray levels (e.g., P_1 to P_4 for low gray levels and P_5 to P_8 for high gray levels). If D_{th} (σ_{th}) is chosen as 3.0 (2.0), the points P_4, P_6, P_7, and P_8 will then be extracted. The AVM method is computationally intensive,

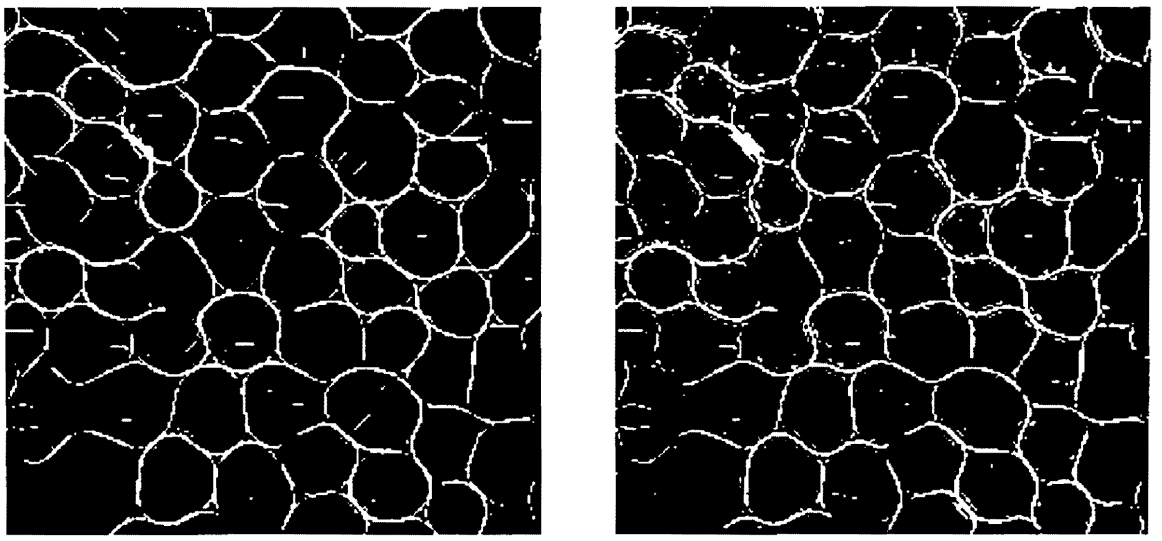

(a) (b)

Figure 4.6: Binarization of the image obtained at the second iteration in Fig. 4.3(d): (a) Min-Max deviation measure ($D_{th} = 4.5$); (b) angular variance measure ($\sigma_{th} = 2.2$).

even though the method can be implemented on a computer, yielding a good result. In contrast to the AVM method, the MDM method is simple and preferable to an optical implementation of the binarization of RKMT enhanced images.

Binarization by MDM and AVM							
Input Points	θ_1	θ_2	θ_3	θ_4	θ_5	D	σ_M
$P_1(x,y)$	1	1.1	1.2	0.8	1	0.20	0.13
$P_2(x,y)$	1	2	2	0	5	1.80	0.83
$P_3(x,y)$	1	2	2	0	4	1.50	0.99
$P_4(x,y)$	1	1	1	1	10	3.14	2.50
$P_5(x,y)$	10	11	12	8	10	0.63	0.41
$P_6(x,y)$	10	20	20	0	40	4.74	3.13
$P_7(x,y)$	10	10	10	10	50	5.50	3.77
$P_8(x,y)$	10	10	10	10	100	9.92	6.80
$D(x,y)$: Min–Max deviation measure [MDM] σ_M: angular deviation measure [AVM]							

Table 4.2: Comparison of Min–Max deviation measure and angular variance measure for eight input points located in different regions and five kernel rotation angles θ_i. If D_{th} (σ_{th}) is chosen as 3.0 (2.0), the points P_4, P_6, P_7, and P_8 will then be extracted.

4.4 Comparisons of RKMT Method with Other Methods

RKMT method of image enhancement is highly nonlinear, depending upon the measurements of Max and Min values obtained at each point. It is appropriate to compare this nonlinear processing operation with results that can be achieved using other linear and nonlinear filtering methods. Two methods are evaluated for purposes of comparison: (1) convolution with the circular Mexican hat kernel and (2) nonlinear spatial filtering using wedge–shaped filters. The input image used is that shown in Fig. 4.1(a). Note that this input image has nearly uniformly spaced cell boundaries: the cell to cell distance is relatively uniform. Such characteristics of the cell boundaries suggest the use of the filter with bandpass characteristics to enhance frequency components corresponding to uniformly spaced distribution of cell boundaries. Appropriate kernel to be used in such cases is so–called Mexican hat kernel [50] given by the expression $k(r) = [1 - c(r^2/\sigma^2)]\exp(-r^2/2\sigma^2)$ where r is a radial distance, $\sigma(= 1.5)$ determines the diameter of the kernel, and $c(= 1.027)$ is a scaling factor for integer arithmetic [51]. The corresponding filter is circularly symmetric with no directional filtering capability, bandpass in nature with a passband centered at $1/\sqrt{2}\pi\sigma$ in the frequency domain. Figure 4.7(a) shows the result of applying the filtering operation to the image in Fig. 4.1(a), for which the parameter σ was chosen to optimize the result in (a). The internal noise–like structures in (a) have also been emphasized. Figure 4.7(b) shows the result of thresholding the image in Fig. 4.7(a), for which threshold value was visually chosen to obtain a good result.

Another comparison can be obtained using wedge–shaped filters with directional filtering capability. The comparison using the eight wedge–shaped filters was provided by Bamberger [67] using his method, originally developed for the enhancement of linear features (i.e., ridge structures) in fingerprints. His methodology is

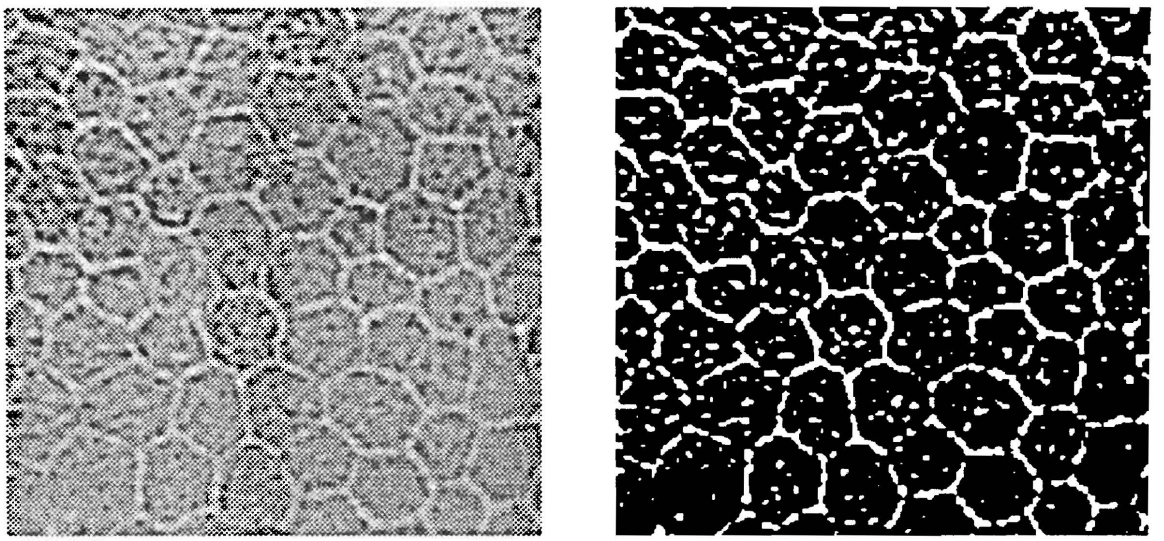

(a) (b)

Figure 4.7: Comparison with RKMT processing: (a) result of linear spatial filtering using a Mexican hat kernel which is bandpass in nature ($\sigma = 1.5$): (b) result of thresholding the image in (a).

summarized as follows, the remainder of this section being based on a private communication with him:

1. Eight wedge–shaped filters were generated. Figure 4.8(a) shows the eight wedge–shaped filters used for comparison.

2. The input image in Fig. 4.1(a) was Fourier transformed. Low spatial frequency components in the Fourier transform were removed to avoid some noise structure (i.e., slowly varying background intensity in the input image).

3. The resulting Fourier transform is multiplied by each wedge–shaped filter, yielding eight filtered images through the inverse Fourier transform.

4. The maximum value at each input point (x,y) is searched for the eight angularly filtered images obtained in Step 3. The output image is then given the maximum value.

5. In Step 4, a certain situation was considered, because the resulting maximum value could result from some noise structure rather than line segments (i.e., cell boundaries). The mean and variance of eight values obtained at each point were thus calculated to exclude such undesirable maximum values. As the variance was smaller than a certain threshold value, the mean value was then assigned to the particular point. Otherwise, the maximum value was given the desired output value.

Figures 4.8(b), (c), and (d) show the processed images provided by Bamberger [90] using the eight wedge–shaped filters shown in (a). The highpass–filtered image as described in Step 2 is shown in (b). The result of applying Steps 3, 4, and 5 to the image in (b) is shown in (c). The thresholded version of (c) is shown in (d). Most line segments (i.e., cell boundaries) were extracted well, but still noisy. Thus, it is evident that the RKMT method works best among these methods used for comparison, yielding excellent results.

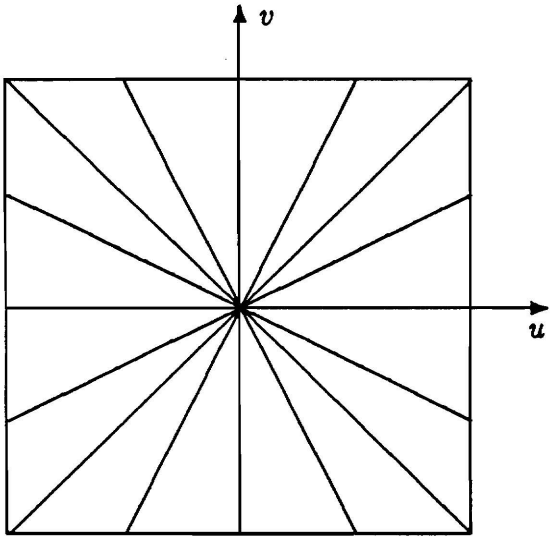

(a)

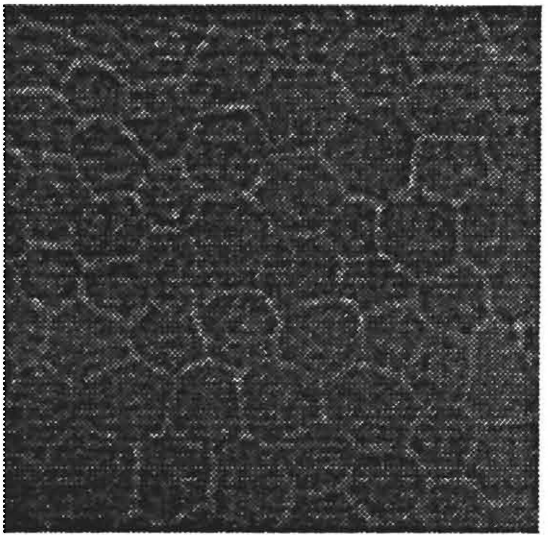

(b)

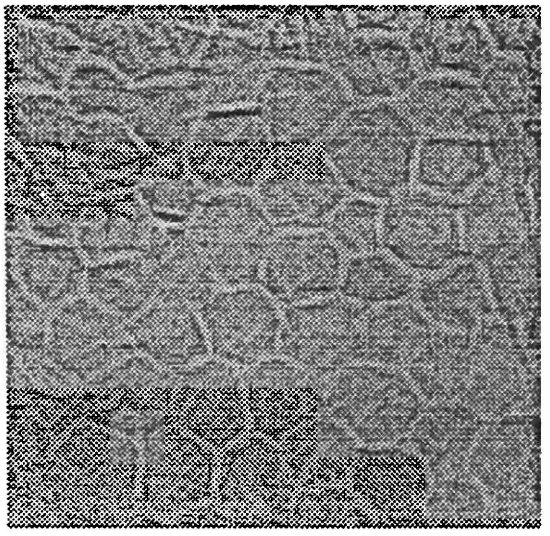

(c)

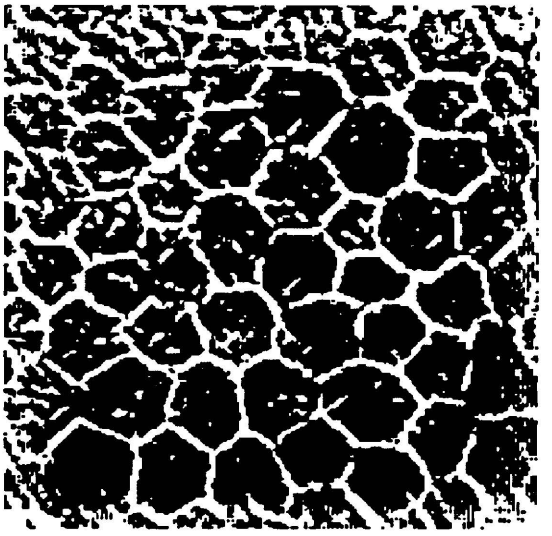

(d)

Figure 4.8: Wedge–shaped filtering: (a) eight wedge–shaped filters where (u, v) is the frequency coordinate; (b) result of highpass filtering; (c) result of using the wedge–shaped filters in (a); (d) result of thresholding the image in (c).

4.5 Summary and Discussion

In the application of the RKMT method to the enhancement of linear features, the basic Max and [Max - Min] operations have proven particularly useful and powerful. Because the RKMT method extracts orientational information from an image, it is not surprising that kernels with a high degree of orientation perform best.

The RKMT processing operation tends to be insensitive to variations in brightness as compared to other methods associated with linear spatial filtering and ideal wedge–shaped filtering methods. The insensitivity to changes in brightness is one of the advantages by which the RKMT method may be quite attractive for image processing (e.g., biomedical or industrial image processing) under poor illuminating conditions. Figure 4.9 shows a typical wide–field image which is noisy and very low contrast. The spatially varying background intensity is evident; most regions except the upper–left region are difficult to see by eye. The cell density of the image in Fig. 4.9 is approximately four times that of the image shown in Fig. 4.1(a). The wide–field image was processed by the multipass operation using a symmetric triangular kernel with $L = 11$ and $W = 1$. The result of the second iteration is shown in Fig. 4.10. As can be seen, the cell boundaries are greatly enhanced. Note that the cell boundaries in the lower–left region are not well delineated whereas those in the lower–right region are relatively well enhanced. The RKMT processed image was binarized by the MDM method ($D_{th} = 3.5$). The result is shown in Fig. 4.11. Similarly, the binarized image obtained by the AVM method ($\sigma_{th} = 1.9$) is shown in Fig. 4.12. The binarization operation can also be applied to the image obtained in the first iteration or the intermediate image obtained by a Max operation in the second iteration.

In summary, the multipass operation (e.g., first or second iteration) based on the basic Max and [Max - Min] operations is useful for the enhancement of raw endothelial cell imagery. A triangular profile kernel is preferable to a rectangular kernel for reducing noise and thickening of line segments. Alternatively, a Gaussian

profile kernel can also be used, yielding a good result. With an optical implementation discussed Sec. 3.5, the enhancement operation and binarization of line segments by the RKMT method can be performed by two steps: (1) the enhancement of line segments by the simple [Max – Min] or the iterative operation; then, (2) the binarization of the enhanced image by the MDM method. The MDM method is easy to use for the binarization and simple to implement in the optical implementation since it requires only Max, Min, and Mean values of the convolution output.

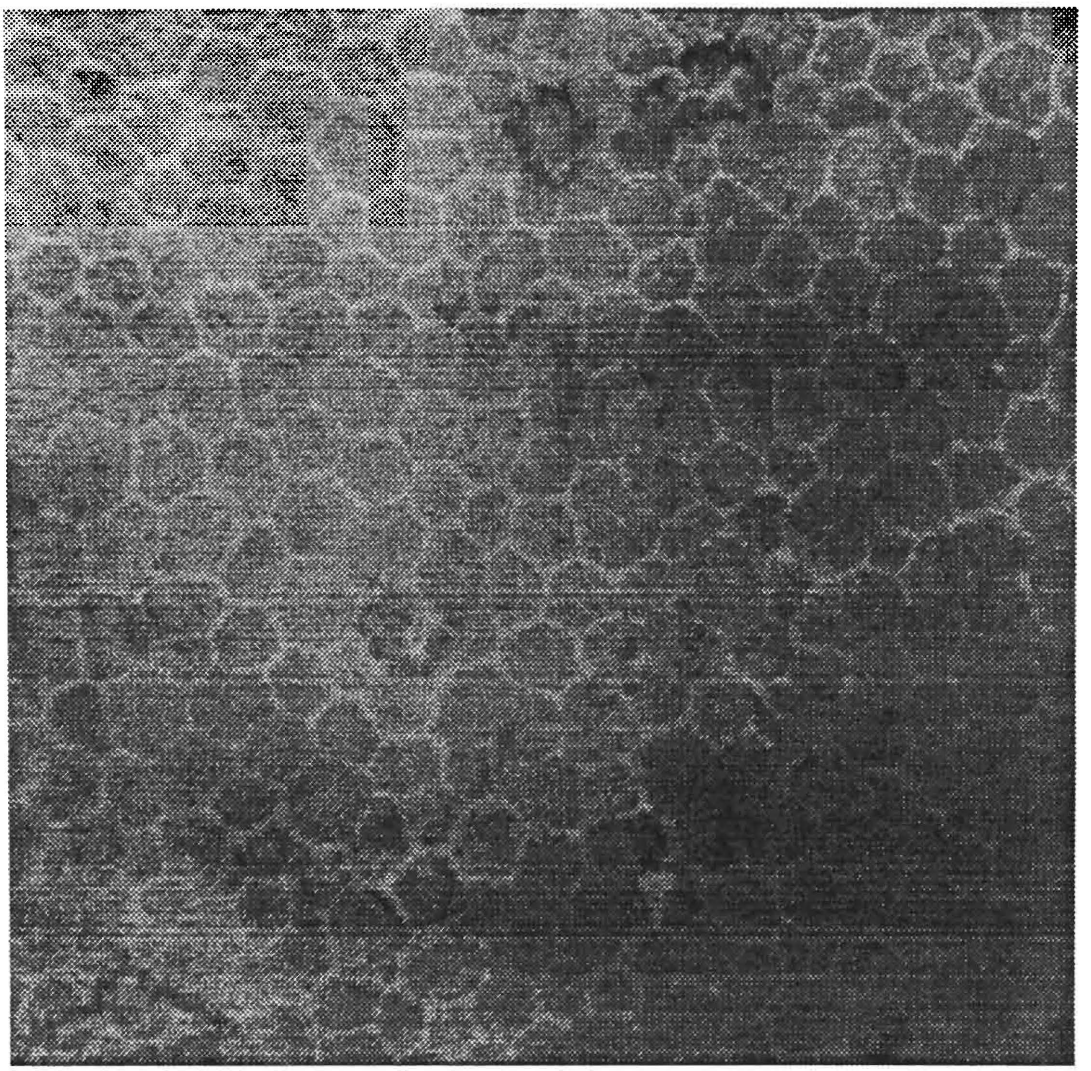

Figure 4.9: A wide–field raw image in which a spatially varying characteristic in average background intensity from one region to the other is evident.

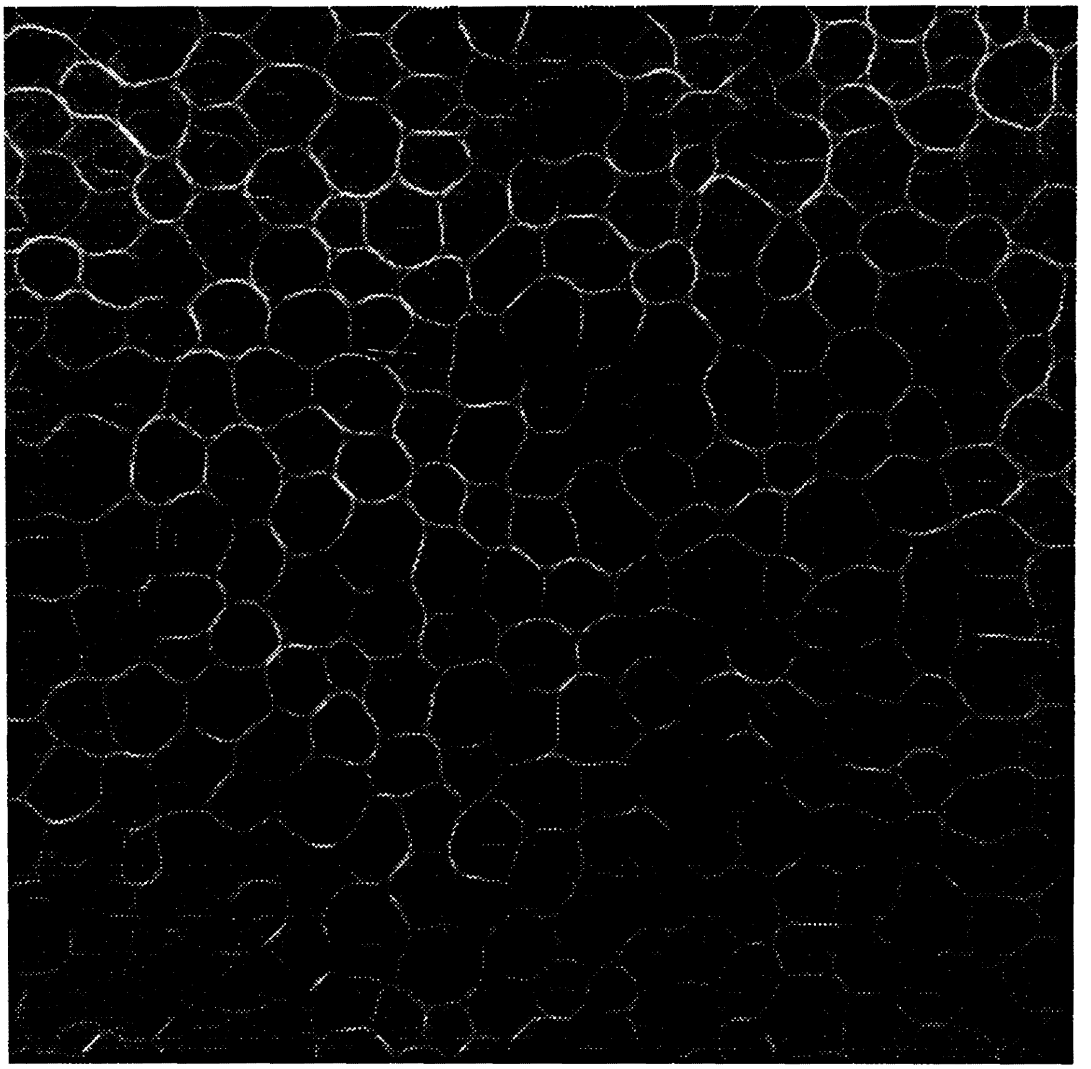

Figure 4.10: Result of applying the second iteration to the image in Fig. 4.9: a symmetrical kernel used is triangular in profile ($L = 11$ and $W = 1$).

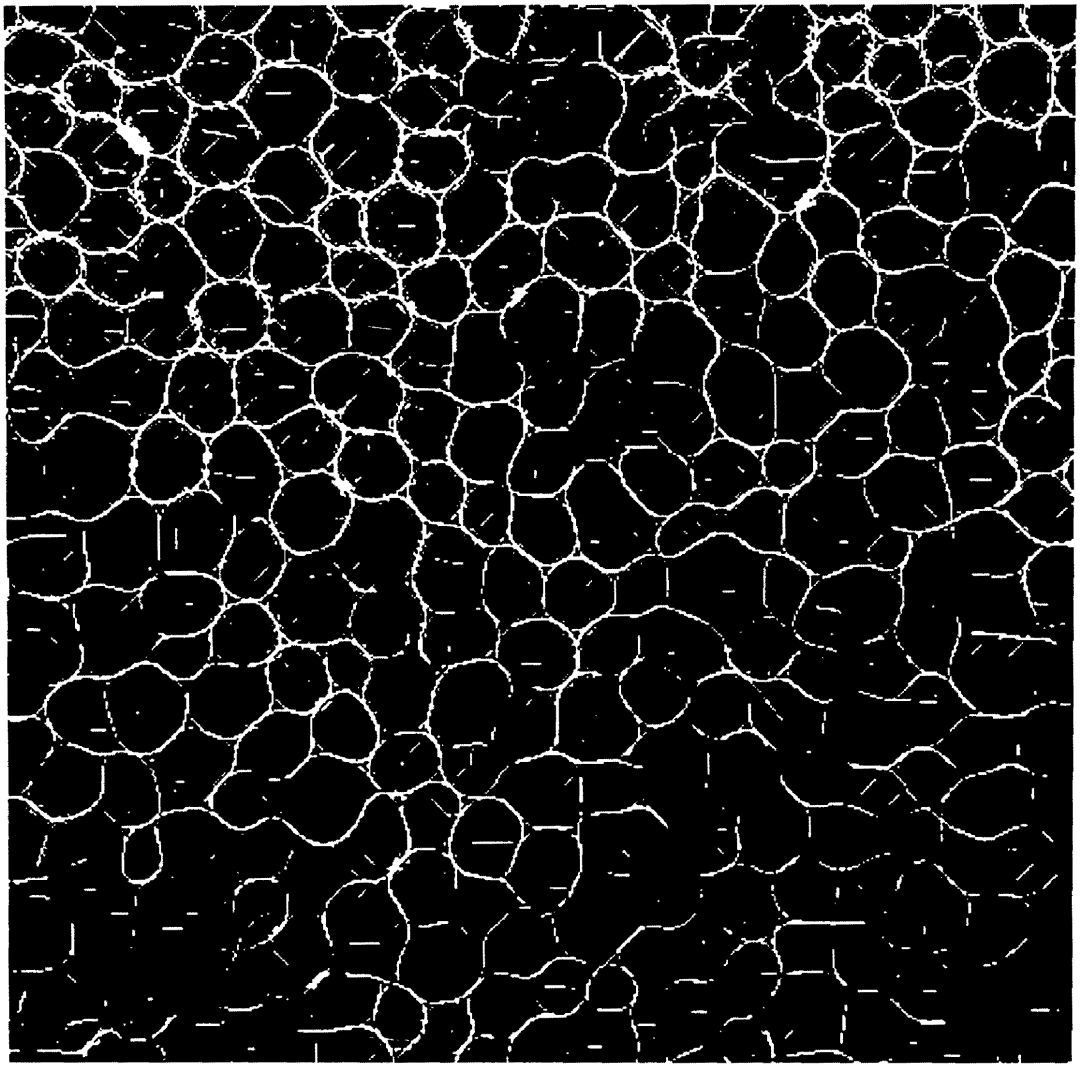

Figure 4.11: Result of binarizing the image in Fig. 4.10 by the Min–Max deviation measure ($D_{th} = 3.5$).

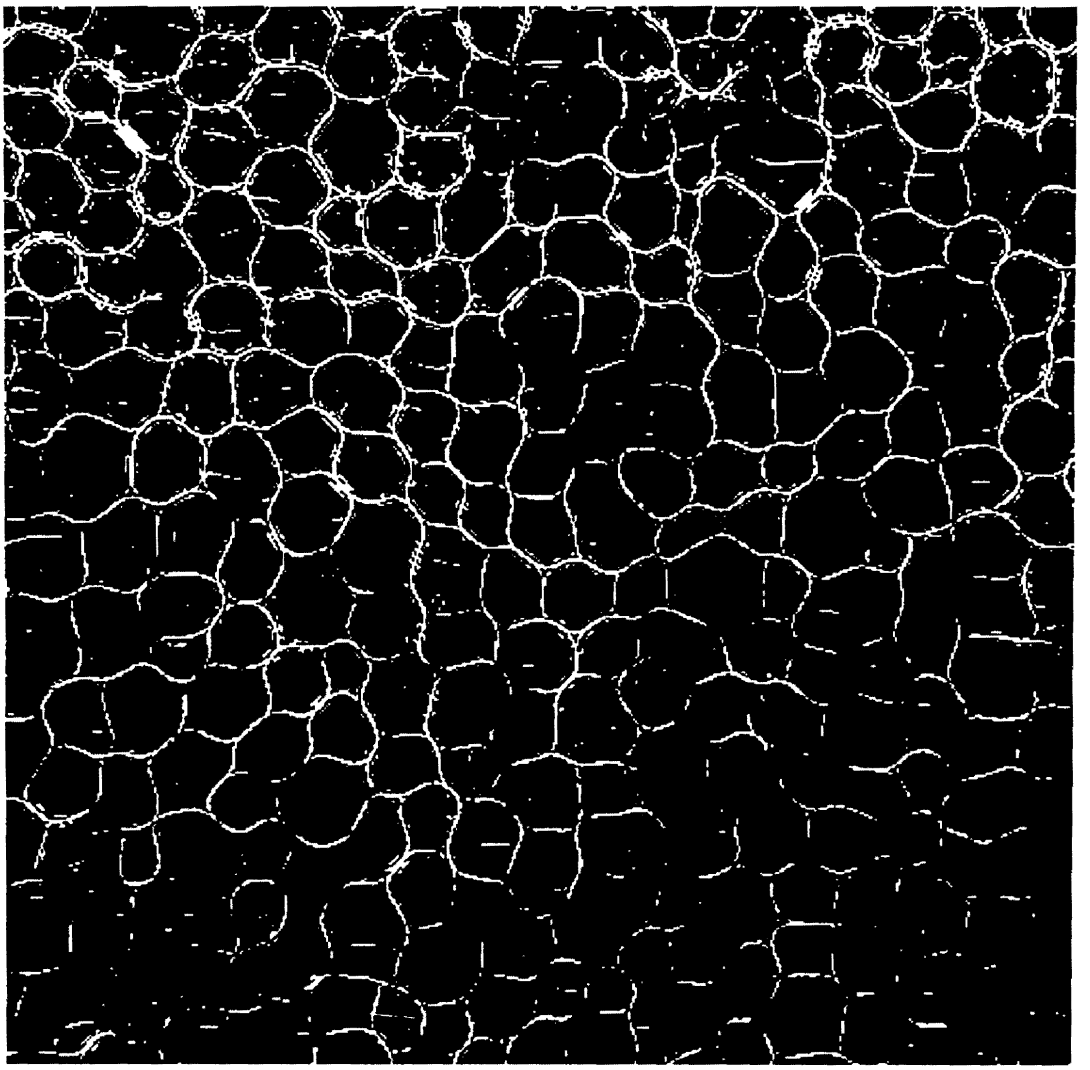

Figure 4.12: Result of binarizing the image in Fig. 4.10 by the angular variance measure ($\sigma_{th} = 1.9$).

CHAPTER 5

INVARIANT PATTERN RECOGNITION

5.1 Introduction

This chapter introduces a novel hybrid optical method, based on RKMT processing, for scale– and rotation–invariant pattern recognition. The method discussed exhibits invariance to shift and angular orientation and quasi–invariance to scale. In Chapters. 3 and 4 the RKMT method was applied to the enhancement of linear features in noisy imagery. Now the method is extended to the problem of recognizing objects with linear features (e.g., alphanumeric characters, airplanes, and industrial parts). In this extension [83], RKMT processing operation is used to extract an angular signature of the input object contour (i.e., edge). This signature is then compared to template signatures to effect the recognition. In the following a nonlinear mapping of the object contour information into an angular signature function is first defined. An algorithm for scale– and rotation–invariant pattern recognition is then presented, followed by numerical experiments. Sensitivity of the algorithm to noise is discussed. Effects that variations in the kernel dimension, the kernel profile, and the function f[Max, Min] have on the discrimination of objects are also discussed.

5.2 The Angular Signature Function

This section defines the angular signature function $P(\theta)$ for an image and gives examples of its calculation.

5.2.1 Definition of the Angular Signature

Calculation of the angular signature proceeds initially as for conventional RKMT processing: the input is convolved with a long, narrow 2–D kernel, and as the kernel rotates, the convolution output is monitored and the maximum [=Max(x,y)] and minimum [=Min(x,y)] values at each point (x,y) are stored. In addition, however, the angle $\theta_{Max}(x,y)$, at which the maximum value is found, is also stored. The processed image is given by some function f[Max, Min] of the Max and Min values. Once these values are available, each object point (x,y) is associated with the pair of values $(f[Max(x,y), Min(x,y)], \theta_{Max}(x,y))$.

The angular signature function $P(\theta)$ is calculated from $(f[Max, Min], \theta_{Max})$ in accord with the formula

$$P(\theta) = \int_{-\infty}^{\infty} \int_{-\infty}^{\infty} f[Max(x,y), Min(x,y)]\ \delta[\theta - \theta_{Max}(x,y)]\ dxdy, \qquad (5.1)$$

where $\delta[\ ]$ is a Dirac delta function and $0 \leq \theta < 360°$. In discrete case,

$$P(\theta_i) = \sum_m \sum_n f[Max(m,n), Min(m,n)]\ \delta^{(0)}[\theta_i - \theta_{Max}(m,n)], \qquad (5.2)$$

where $\delta^{(0)}[\ ]$ is the unit null function, i.e.,

$$\delta^{(0)}[\theta_i - \theta_{Max}(m,n)] = \begin{cases} 1 & \text{if} \quad \theta_i = \theta_{Max}. \\ 0 & \text{otherwise.} \end{cases} \qquad (5.3)$$

In Eq. 5.3 the kernel assumes only discrete angular orientations considered over 0 to 360 degrees and thus θ_{Max} will have one of the possible values of θ_i but it cannot have other values. $\theta_{Max}(x;y)$ is that angle θ for which the convolution output $S_\theta(x,y)$ is maximum, assuming that $S_\theta(x,y)$ contains a unique maximum over a period

($0° \leq \theta < 180°$ for a symmetric kernel). In other words, $S_{\theta_{Max}}(x,y) > S_\theta(x,y)$ for all $\theta \neq \theta_{Max}$, a definition that does not allow for multiple Max angles. Under certain conditions, the same Max value can be obtained at multiple Max angles. Two methods can be considered to take multiple Max orientations into account. One is to split $S_\theta(x,y)$ into multiple orientations at which multiple Max values are found. The idea would be to replace $\delta^{(0)}[\theta_i - \theta_{Max}]$ in Eq. 5.2 up into

$$\frac{1}{M}\sum_{k=1}^{M}\delta^{(0)}[\theta_i - \theta_{Max}^{(k)}(m,n)]$$

where $\theta_{Max}^{(k)}$ is the kth kernel orientation producing the (same) Max value at point (m,n). The other used in this thesis is to exclude those points with multiple Max angles [$= \theta_{Max}(x,y)$], eliminating them from consideration. The angular signature function $P(\theta)$ in Eqs. 5.1 and 5.2 gives a measure of the directionality of the input, as a function of orientation. If the object consists of a single line segment, for example, there is a peak at only one angle θ in the angular signature function $P(\theta)$.

For the remainder of the chapter, the function f[Max, Min] is referred to as the RKMT transform function, and the procedure to find the angular signature function $P(\theta)$ from the object contour is called an angular mapping operation. Note that this mapping operation depends on both the RKMT transform function f[Max, Min] and the kernel used.

5.2.2 Example of Angular Signature Function

An example of the angular signature function $P(\theta)$ is illustrated in Fig. 5.1. Figures 5.1(a) and (c) show an input object **E** and its angular signature for the four discrete kernel orientations shown in (b). Increasing the number of the kernel orientations results in an angular signature containing more information. However, only four kernel orientations were implemented for numerical experiments discussed in this thesis, because the object features used have only two, three, or four dominant orientations (i.e., 0°, 45°, 90°, and 135°). The symmetric kernel used was rectangu-

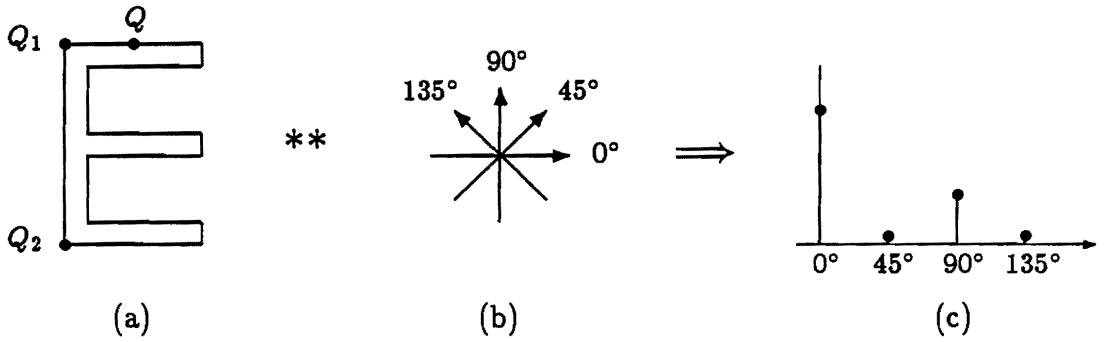

Figure 5.1: Illustration of the angular signature function $P(\theta)$ obtained by using $f[\ ,\ ] = Max^2(x,y)$ where $**$ represents 2–D convolution. (a) Object. At a point Q, Max is obtained at 0°. The points Q_1 and Q_2 are eliminated in finding $P(\theta)$. (b) Four kernel orientations with a long, narrow 2–D kernel which is symmetric. (c) $P(\theta)$.

lar in profile, its length being approximately 81 % of that of the vertical segment of the object **E**.

Consider the point Q on the horizontal edge of the object **E** contour shown in Fig. 5.1(a). As the kernel rotates on the point, the convolution output will be large for $\theta = 0°$ and small for other orientations. More generally, those points along the horizontal line segments (or features) give large convolution outputs for $\theta = 0°$, these outputs becoming the Max values. Similarly, those points along the vertical line segments yield large Max values for $\theta = 90°$. Certain points such as Q_1 and Q_2 are eliminated in finding the Max values, since they have multiple Max orientations at 0° and 90° for the particular kernel length used.

A simple Max operation can be used to find $P(\theta)$, i.e., $f[Max, Min] = Max(x,y)$. Alternatively, $P(\theta)$ can be obtained using $f[Max, Min] = Max^2(x,y)$, thereby further enhancing linear features oriented at certain angles. Figure 5.1(c) shows the angular signature function $P(\theta)$ obtained by using $f[Max, Min] = Max^2(x,y)$. In the figure $P(\theta)$ has two peaks, at 0° and 90°. The Max values obtained for $\theta = 45°$ and 135° are smaller in number, being achieved only at those points within the half kernel distance from the object contour. Increasing the number of kernel orienta-

tions may reduce the signature values obtained at 45° and 135° whereas significant angular signatures at 0° and 90° are still preserved. The angular signature function $P(\theta)$ could also be obtained by using $f[Max, Min] = Max(x,y) \cdot Min(x,y)$. Image points along the edge of the object (contour) achieve high Max values and small Min values. However, for points outside the object contour, both Max and Min are small. By calculating $f[Max, Min] = Max(x,y) \cdot Min(x,y)$, those points on the object contour contribute the most to $P(\theta)$.

5.2.3 Invariance to Scale

As the size of the object increases, each component contributing to the angular signature function $P(\theta)$ at angle θ will be increased, roughly in proportion to the scale. To obtain approximate scale invariance, $P(\theta)$ can be normalized by its area (evaluated over 0 to 360 degrees), producing $p(\theta)$:

$$p(\theta) = \frac{P(\theta)}{\int_0^{2\pi} P(\theta)\, d\theta}. \tag{5.4}$$

This latter function is similar to a probability density function of line segment orientations.

The normalized angular signature function $p(\theta)$ is largely insensitive to variation in scale of the input object. Figure 5.2 shows $P(\theta)$ and $p(\theta)$ for the letter **E**, with variations in scale over a 2.8:1 range. The mapping operation was performed using $f[Max, Min] = Max(x,y) \cdot Min(x,y)$. Those points at which multiple Max orientations (i.e., θ_{Max}) occur were not considered in finding $P(\theta)$. It is seen that the normalization operation greatly reduces sensitivity of the angular signature to variations in the scale of the objects. In the numerical calculation, the object contours were 2 pixels wide and the kernel used was rectangular in profile ($L = 39$ and $W = 1$). The kernel length was approximately 111 % of the longer side of the third object (scale = 1.0) in (c).

It is important to investigate how the approximate scale invariance behaves

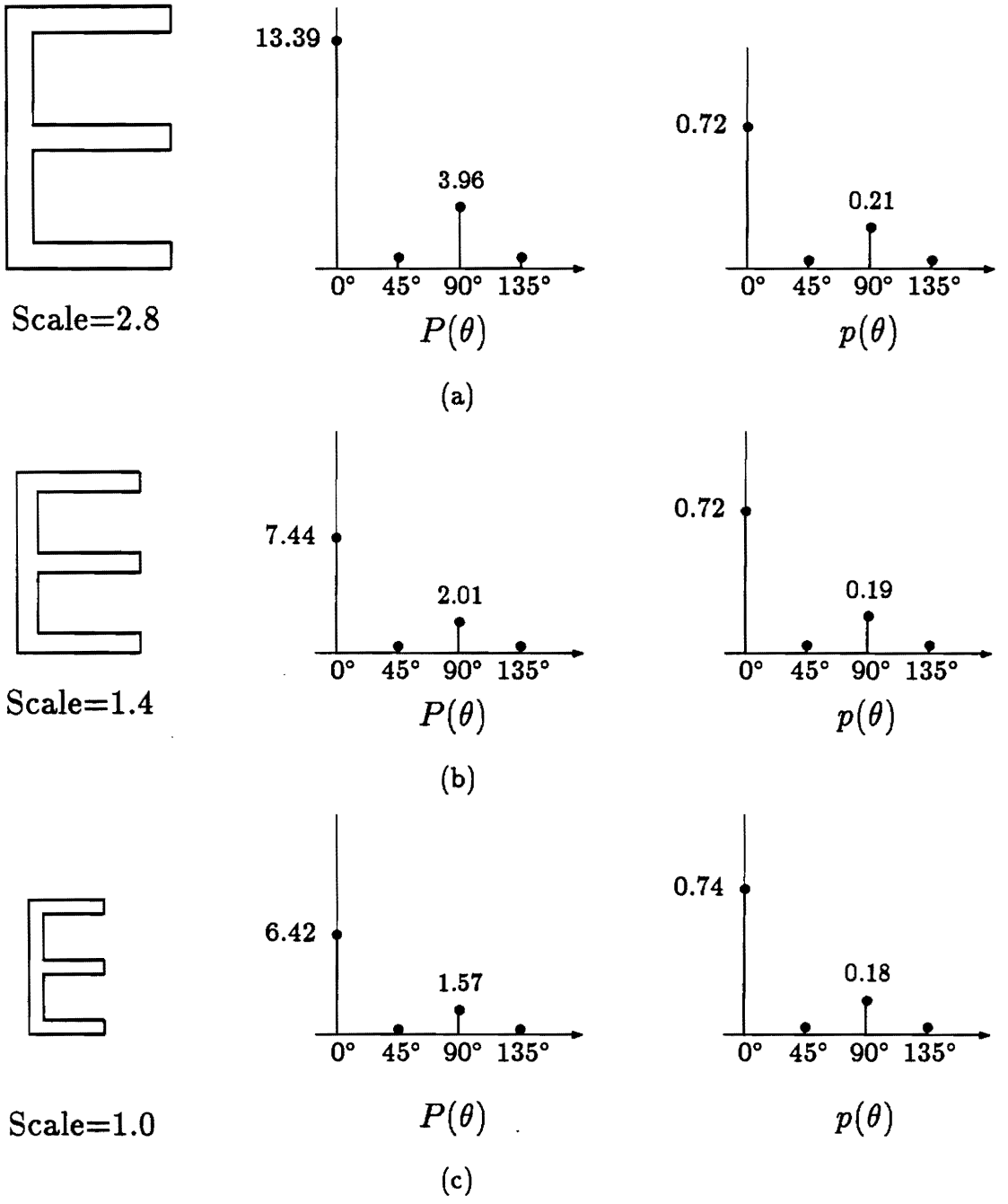

Figure 5.2: Approximate scale invariance obtained by normalizing the angular signature function $P(\theta)$ by its area to produce $p(\theta)$: (a) scale $\simeq$ 2.8; (b) scale $\simeq$ 1.4; and (c) scale = 1.0. Each signature function was obtained by using $f[Max, Min] = Max(x, y) \cdot Min(x, y)$. The kernel used is symmetric and rectangular in profile.

over a wide range of the kernel lengths L. Figure 5.3 shows a plot of the normalized angular signature function $p(\theta)$ versus the kernel length L for kernel orientations 0°, 45°, 90°, and 135°. The objects used are four scaled versions (scale=1.0, 1.4, 1.9, and 2.8) of the character **E** in Fig. 5.2(c). The kernel used is a symmetric rectangle function with $W = 1$; the RKMT function is $f[Max, Min] = Max(x, y) \cdot Min(x, y)$. Each angular signature of the objects at the kernel orientations are represented by the solid (scale=1.0), dashdot (scale=1.4), dashed (scale=1.9), and dotted (scale=2.8) lines. For the object with scale=1.0, the angular signature at $\theta = 90°$ shows a valley around $L = 34$ (the length of the longest vertical feature in this object). As L increases further, $p(\theta)$ at $\theta = 90°$ increases and then converges to a nearly constant value (0.31). Results with larger scaled versions of the object show the valley shifted to the right by an amount, roughly in proportional to the length of their longest vertical features. Note that the lengths of the vertical features of the scaled objects are 34, 48, 64, and 96 pixels. At other kernel orientations (e.g., 0°), $p(\theta)$ also increases, decreases, and then converges to a nearly constant value as the kernel length L increases. Thus, the maximum range for which the approximate scale invariance can be achieved depends on the kernel length used. The results shown in Fig. 5.3 suggest that the kernel length L should be chosen to be somewhat longer than the maximum scale of an input object. The approximate scale invariance can be expected to hold for a fairly large range (e.g., 1/5 to 5.0) of variations in scale.

5.2.4 Angular Similarity Measure

Consider the distance measure $D(\theta_o)$ between two area–normalized angular signatures:

$$D_{ij}(\theta_o) = \left\{ \int_0^{2\pi} [p_i(\theta) - p_j(\theta + \theta_o)]^2 \, d\theta \right\}^{1/2} \tag{5.5}$$

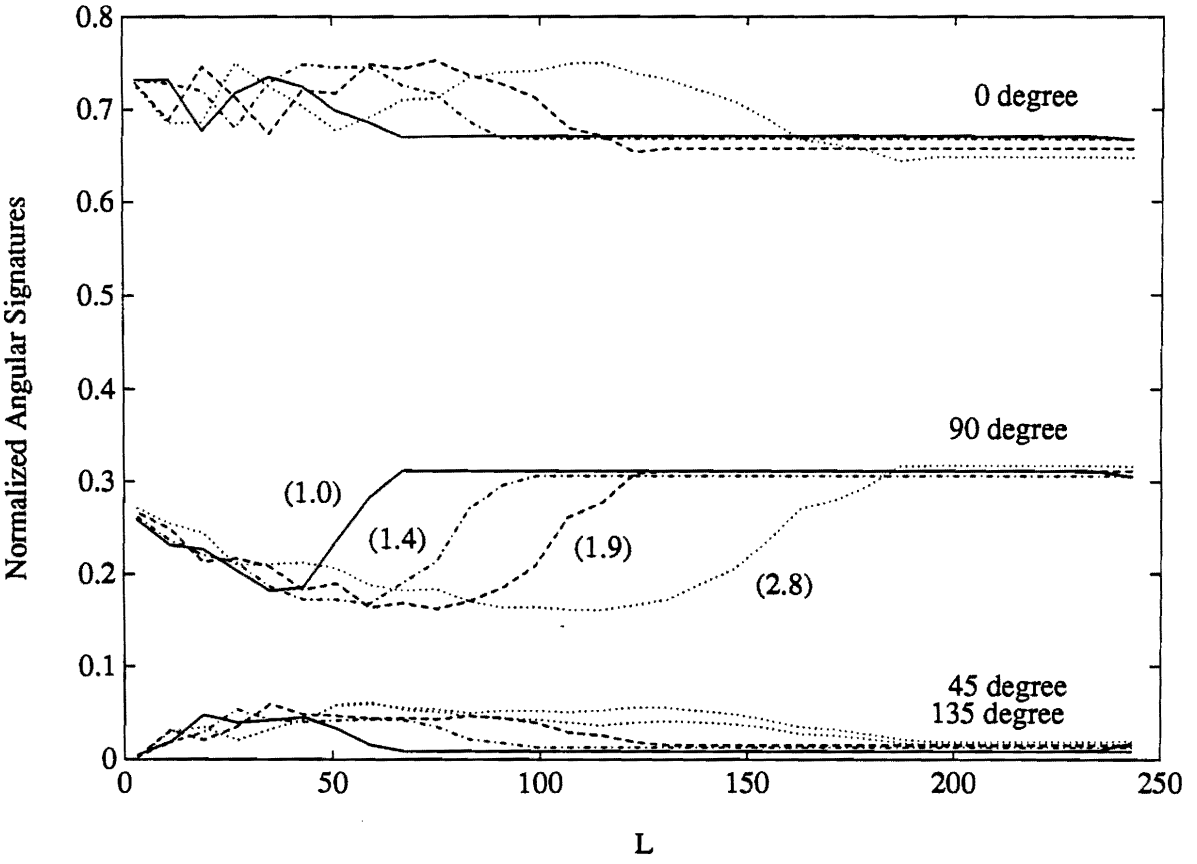

Figure 5.3: Normalized angular signatures $[= p(\theta)]$ for different kernel lengths L. The kernel used is a symmetric rectangle function with $W = 1$. The objects are four scaled versions of the character **E** (scale=1.0), the scales being given in parenthesis. The RKMT function used is f[Max, Min] = Max · Min. Above a certain kernel length (e.g., $L = 200$), each component tends to converge to a nearly constant value.

or, equivalently,

$$D_{ij}(\theta_o) = \left\{ \int_0^{2\pi} p_i^2(\theta) d\theta + \int_0^{2\pi} p_j^2(\theta) d\theta - 2 \int_0^{2\pi} p_i(\theta)\, p_j(\theta + \theta_o)\, d\theta \right\}^{1/2} \tag{5.6}$$

where $p_k(\theta)$ denotes the (area–normalized) angular signature associated with the kth object. The angle θ_o allows for changes in the relative angular orientation of the two objects. Note that the third integral in Eq. 5.6 corresponds to the (cyclic) crosscorrelation between $p_i(\theta)$ and $p_j(\theta)$. An alternative definition of the distance measure uses energy–normalized versions of the angular signatures, denoted by D':

$$D'_{ij}(\theta_o) = \frac{1}{\sqrt{2}} \left\{ \int_0^{2\pi} [p'_i(\theta) - p'_j(\theta + \theta_o)]^2\, d\theta \right\}^{1/2}$$

$$= \frac{1}{\sqrt{2}} \left\{ \int_0^{2\pi} p'^2_i(\theta) d\theta + \int_0^{2\pi} p'^2_j(\theta) d\theta - 2 \int_0^{2\pi} p'_i(\theta)\, p'_j(\theta + \theta_o)\, d\theta \right\}^{1/2} \tag{5.7}$$

where

$$p'(\theta) = \frac{P(\theta)}{\sqrt{\int_0^{2\pi} P^2(\theta) d\theta}}. \tag{5.8}$$

$D'_{ij}(\theta_o)$ can be written in the more compact form

$$D'_{ij}(\theta_o) = \left[1 - \int_0^{180^\circ} p'_i(\theta)\, p'_j(\theta + \theta_o)\, d\theta \right]^{1/2}$$

$$= \left[1 - C'_{ij}(\theta_o) \right]^{1/2} \tag{5.9}$$

Note that if $P_i(\theta) = \alpha P_j(\theta + \theta_R)$, the energy–normalized distance $D'_{ij}(\theta_o)$ evaluates to the minimum possible value of zero if $\theta_o = \theta_R$. Moreover, using the Schwartz inequality, it can be shown that $D'(\theta_o)$ can attain the minimum value of *zero only* when $P_i(\theta) = \alpha P_j(\theta + \theta_R)$.

The similarity measure S between the object and a template signature is defined by

$$S = \frac{1}{B + D'(\theta_R)}, \tag{5.10}$$

where $B(> 0)$ is a nonzero constant that controls recognition sensitivity. If B is too small, the recognition process may be overly sensitive to noise or other factors (e.g.,

object scale and distortion). When both the object and the template are identical, $D'(\theta_R) = 0$ and $S = 1/B$. Otherwise, S is less than $1/B$. A useful related quantity is given by

$$r_S = \frac{B}{B + D'(\theta_R)} \tag{5.11}$$

where $r_S (\leq 1)$ is the ratio of the similarity measure S (object) to $1/B$ (template). Note that $r_S = 1$ is obtained when the object is identical to the template. If the peak ratio r_S exceeds a certain threshold value r_{th}, the input object is recognized as an object that belongs to the same class of objects with possible variations in scale.

5.2.5 Algorithm

The algorithm for the invariant pattern recognition used in numerical experiments using Eq. 5.9 is summarized as follows.

- Algorithm:

  1. The description (f[Max, Min], θ_{Max}) for each input object is obtained by the RKMT processing.
  2. Given an input object, find the angular signature function $P(\theta)$ from

$$P(\theta) = \int_{-\infty}^{\infty} \int_{-\infty}^{\infty} f[Max, Min]\ \delta[\theta - \theta_{Max}]\ dxdy.$$

  3. Calculate the energy–normalized function $p'(\theta)$:

$$p'(\theta) = \frac{P(\theta)}{\sqrt{\int_0^{2\pi} P^2(\theta)\ d\theta}},$$

     where $p'(\theta) = P_O(\theta)$ for the object and $p'(\theta) = P_R(\theta)$ for the (reference) template.

  4. Find the angle θ_R for which the cyclic crosscorrelation $C'(\theta_o)$ is maximized,

$$C'(\theta_o) = \int_0^{2\pi} P_R(\theta)\ P_O(\theta + \theta_o)\ d\theta.$$

Then, calculate the angular signature difference measure $D'(\theta_R)$ for $\theta_o = \theta_R$:

$$D'(\theta_R) = [1 - C'(\theta_R)]^{1/2}.$$

5. The peak ratio $r_S(\leq 1)$ is given by

$$r_S = \frac{B}{B + D'(\theta_R)},$$

where $r_S = 1$ when the object is identical to the template.

Figure 5.4 shows the entire block diagram for the procedures required to perform the invariant pattern recognition by the angular difference measure $D'(\theta_R)$.

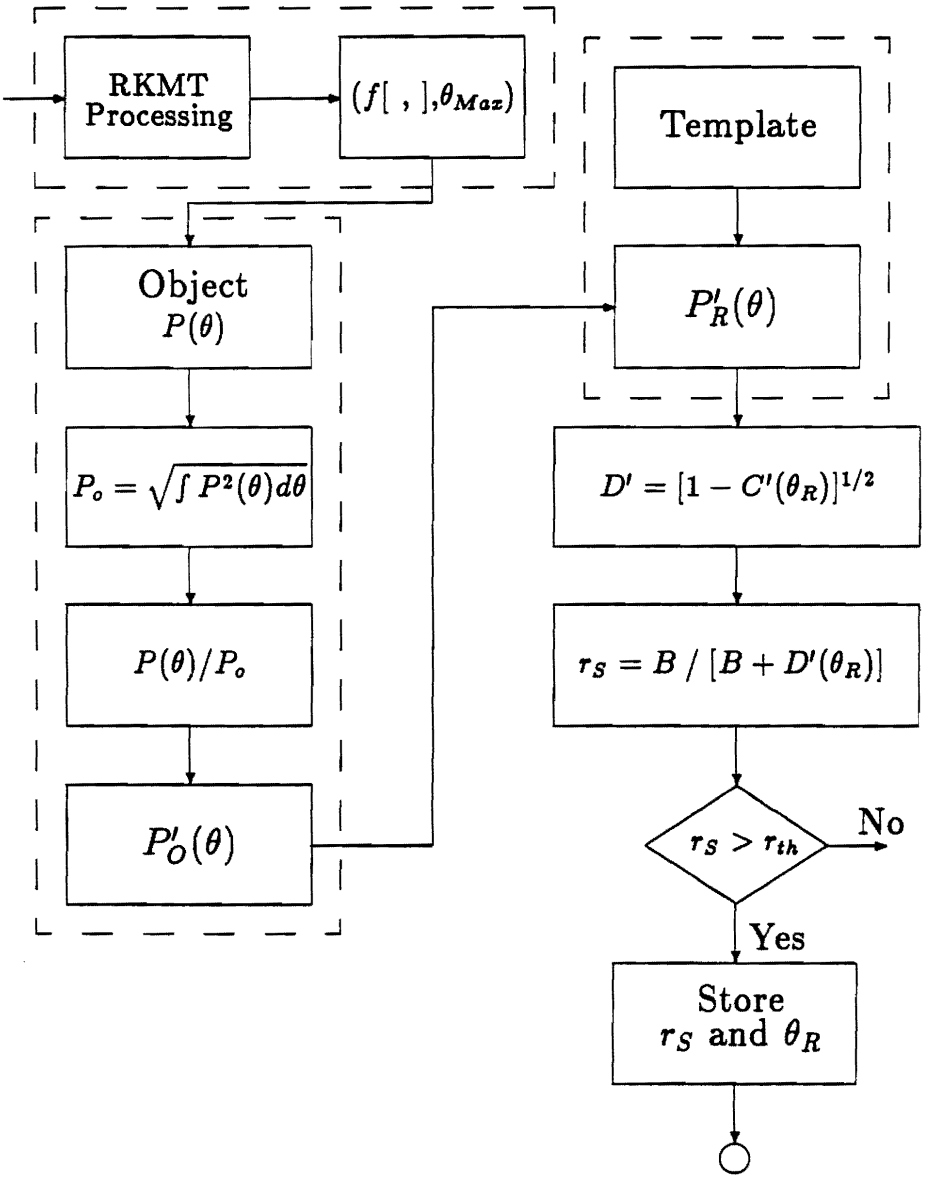

Figure 5.4: A block diagram of the entire systems to perform the invariant pattern recognition operation. $P_O(\theta)$ and $P_R(\theta)$ are the energy–normalized functions of the object and template, respectively. θ_R is the rotation angle of the object with respect to the template. $C'(\theta_R)$ is the cyclic crosscorrelation value for $\theta = \theta_R$ at which $C'(\theta_R)$ is maximized.

5.3 Numerical Experiments

The algorithm presented in Sec. 5.2 has been applied to edge images obtained from several binary alphabetic characters. Some effects of the kernel dimension, the kernel profile, and the RKMT transform function f[Max, Min] on pattern recognition performance are discussed.

5.3.1 Examples of Invariant Pattern Recognition

Figure 5.5 shows the results of applying the invariant algorithm with $B = 0.5$ to several binary alphabetic characters. The RKMT function used was $f[Max, Min] = Max(x, y) \cdot Min(x, y)$. The kernel used was a symmetric rectangle with $L = 39$ and $W = 1$. The kernel length was approximately 81 % of the longer (vertical) side of the template, whose edges are 2 pixels wide. Only four kernel rotation angles were used: 0, 45, 90, and 135°. Figure 5.5(a) demonstrates the pattern recognition capability for four objects. The character **E** was used as the template. The peak ratios [$= r_S$] are 1.0000, 0.6893, 0.4545, and 0.4180. Figure 5.5(b) illustrates the capability of recognizing the character **E** with variations in scale of 1.0 ($\mathbf{E}_1$), 0.7 ($\mathbf{E}_2$), 1.3 ($\mathbf{E}_3$), and 2.0 ($\mathbf{E}_4$). The template is located at the upper–left. Note in (b) that the peak ratio r_S tends to decrease slightly as the scale decreases or increases. Table 5.1 shows the numerical results obtained from the objects in Fig. 5.5. Listed are the angular signature functions $P(\theta)$, the normalized angular signature function $p(\theta)$, the energy–normalized function $p'(\theta)$, the angular signature difference measure $D'(\theta_R)$, and the peak ratio r_S.

To increase the recognition capability between different objects, B can be lowered. If B is too small, however, S or r_S may be excessively sensitive to noise or object distortion. Thus, it is necessary to understand how the peak ratio r_S is affected by varying B. Figure 5.6 shows the plot of r_S versus B for the objects with the same kernel and f[Max, Min] as used in Fig. 5.5. The character $\mathbf{E}_1$ was again

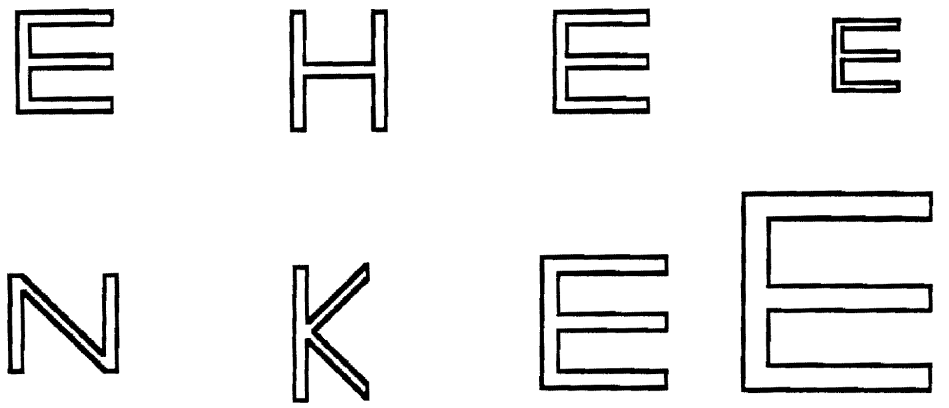

1.0000	0.6893
0.4545	0.4180

(a)

1.0000	0.9515
0.9262	0.9493

(b)

Figure 5.5: Experimental results for quasi–invariant pattern recognition. The character **E** is used as the template. The peak ratios r_S are shown inside the box below the objects for f[Max, Min] = Max · Min. (a) Results of recognizing four different objects. (b) Results showing the quasi–invariance to four different scales (approximately 1.00, 0.66, 1.33, and 2.00).

Angular Signatures: $P(\theta)$							
θ	$\mathbf{E}_1$	H	N	K	$\mathbf{E}_2$	$\mathbf{E}_3$	$\mathbf{E}_4$
0°	7.4394	1.6480	2.2322	2.2144	6.4198	9.0286	13.3884
45°	0.4467	1.2862	0.2814	3.5652	0.3498	0.7740	0.6881
90°	2.0096	5.5128	4.5592	4.6713	1.5662	2.6414	3.9604
135°	0.4467	1.2862	6.6498	3.5988	0.3498	0.7740	0.6861
Area–Normalized Functions: $p(\theta)$							
θ	$\mathbf{E}_1$	H	N	K	$\mathbf{E}_2$	$\mathbf{E}_3$	$\mathbf{E}_4$
0°	0.7193	0.1693	0.1627	0.1576	0.7391	0.6831	0.7151
45°	0.0432	0.1321	0.0205	0.2538	0.0403	0.0586	0.0368
90°	0.1943	0.5664	0.3322	0.3325	0.1803	0.1998	0.2115
135°	0.0432	0.1321	0.4846	0.2561	0.0403	0.0586	0.0366
Energy–Normalized Functions: $p'(\theta)$							
θ	$\mathbf{E}_1$	H	N	K	$\mathbf{E}_2$	$\mathbf{E}_3$	$\mathbf{E}_4$
0°	0.9622	0.2731	0.2667	0.3095	0.9688	0.9533	0.9566
45°	0.0578	0.2131	0.0336	0.4926	0.0528	0.0817	0.0492
90°	0.2599	0.9135	0.5447	0.6454	0.2364	0.2789	0.2830
135°	0.0578	0.2131	0.7944	0.4972	0.0528	0.0817	0.0490
$D'(\theta_R)$	0.0000	0.2254	0.6000	0.6962	0.0255	0.0398	0.0267
r_S	**1.0000**	0.6893	0.4545	0.4180	**0.9515**	**0.9262**	**0.9493**

Table 5.1: Numerical results obtained for the objects in Fig. 5.5. The RKMT function used is f[Max, Min] = Max(x,y) · Min(x,y). The kernel used is a symmetric rectangle function with $L = 41$ and $W = 1$. Kernel length is approximately equal to 81 % of the longer (vertical) side of the template $\mathbf{E}_1$ (scale = 1.0). The objects $\mathbf{E}_2$, $\mathbf{E}_3$, and $\mathbf{E}_4$ have scales 0.66, 1.33, and 2.00 with respect to the template $\mathbf{E}_1$ [=**E**].

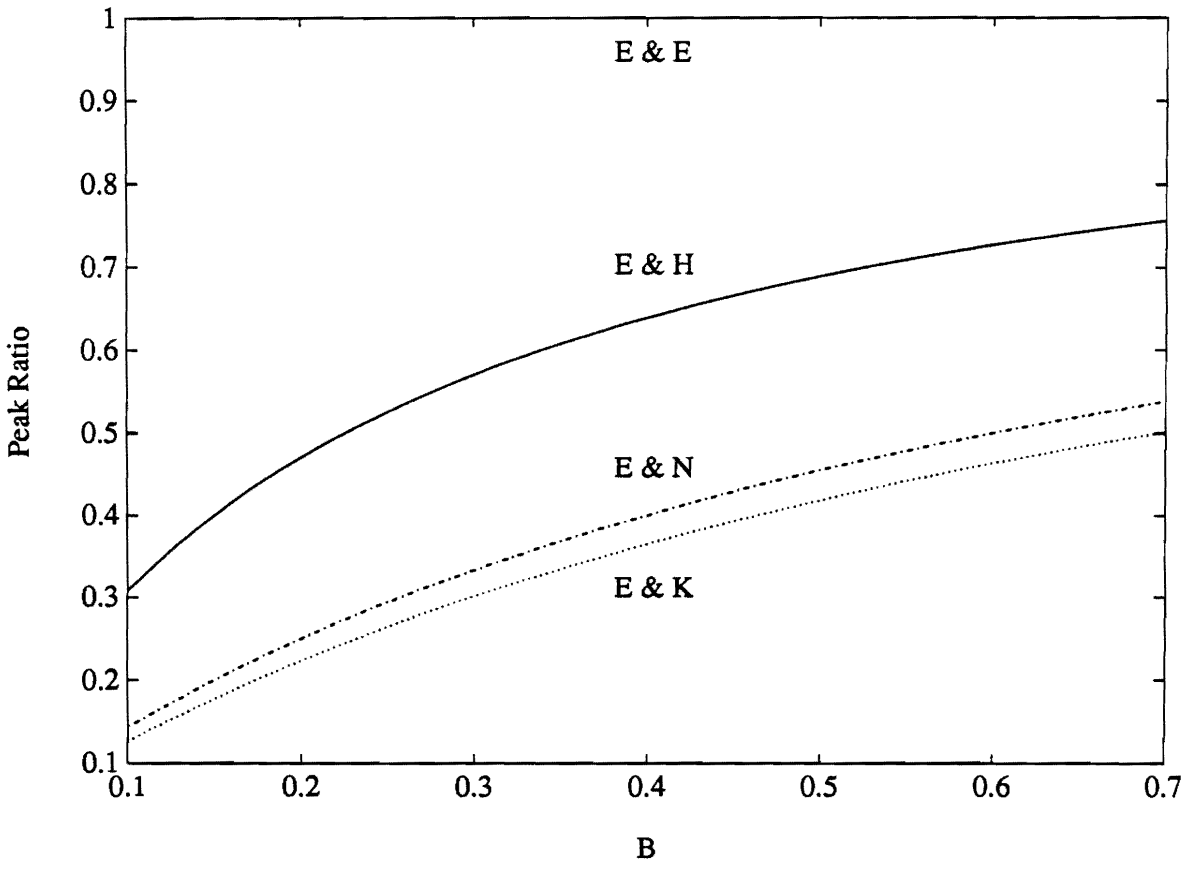

Figure 5.6: Plot of the peak ratio $r_S(= B/[B + D'])$ versus B where $\mathbf{E}$ is used as the template and the objects used are shown in Fig. 5.5(a).

	Object						
Template	$\mathbf{E_1}$	**H**	**N**	**K**	$\mathbf{E_2}$	$\mathbf{E_3}$	$\mathbf{E_4}$
$\mathbf{E_1}$ (1.0)	**1.0000**	0.6893	0.4545	0.4180	**0.9515**	**0.9262**	**0.9493**
H	0.6893	**1.0000**	0.5380	0.5095	0.6791	0.7245	0.6792
N	0.4545	0.5380	**1.0000**	0.5617	0.4548	0.4639	0.4474
K	0.4180	0.5095	0.5617	**1.0000**	0.4141	0.4306	0.4155
$\mathbf{E_2}$ (0.7)	**0.9515**	0.6791	0.4548	0.4141	**1.0000**	**0.8912**	**0.9116**
$\mathbf{E_3}$ (1.3)	**0.9262**	0.7245	0.4639	0.4306	**0.8912**	**1.0000**	**0.9150**
$\mathbf{E_4}$ (2.0)	**0.9493**	0.6792	0.4474	0.4155	**0.9116**	**0.9150**	**1.0000**

Table 5.2: Results of calculating the peak ratio r_S with $B = 0.5$. Those values greater than 0.8 are bold-faced. The objects used are shown in Fig. 5.5. The character E has four different scales indicated by $(\cdot)$ in the figure. The kernel used is a symmetric rectangle function with $L = 39$ and $W = 1$. Kernel length is approximately 81 % of the longer (vertical) side of the object $\mathbf{E_1}$.

used as the template. If the object $\mathbf{E}_1$ was used as the object, r_S is constant (= 1) regardless of B since $D'(\theta_R)$ is zero. Because B is large (e.g., 1), there will be small differences in r_S's obtained from different objects (e.g., **H**) with respect to the template $\mathbf{E}_1$. As B decreases, the difference in r_S between the objects increases. Thus, with an appropriately chosen B, the recognition process can preserve good recognition capability.

Table 5.2 shows the results of calculating r_S using the same kernel dimension and RKMT function f[Max, Min] as used for Fig. 5.5. In Tab. 5.2, the first row and column represent the objects and templates used for seven different cases, respectively. If the character **H** is used as an object, for example, r_S (=1) for the template **H** is significantly greater than for other templates in the first column of Tab. 5.2. From Tabs. 5.1 and 5.2, it is seen that the algorithm can preserve a good recognition capability, although only approximate scale invariance is achieved.

5.3.2 Discrimination Between Similar Objects

It is necessary to understand how the aforementioned algorithm responds to the objects similar to the template and to objects with some noise in shape and edge width. To demonstrate the recognition capability in such cases, three synthetic objects were generated: **F**, **C**, and **E**. The object **F** was generated by removing the horizontal line segments at the bottom of the template **E**. Similarly, the object **C** was generated by removing the horizontal line segments at the center of the template. A noisy object was generated by removing part of the horizontal line segments at the center of the template **E**. Note that the object **F** and **C** have very similar angular signatures.

Figure 5.7 demonstrates the recognition capability for edge images obtained from these synthetic objects. Figure 5.7(a) shows the results of recognizing these synthetic objects for which the character **E** in the upper left was used as the template. The peak ratio r_S is shown in the box below these objects in Fig. 5.7(a). The

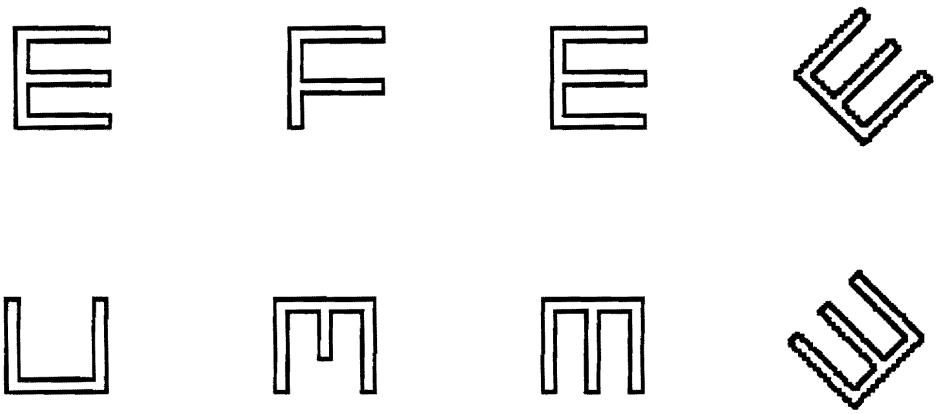

1.0000	0.7071
0.6606	0.8669

(a)

1.0000	0.8533
1.0000	0.8515

(b)

Figure 5.7: Numerical results of recognizing similar objects. The peak ratios r_S are shown in the boxes below the objects. The RKMT function used is f[Max, Min] = Max · Min. (a) First set: similar and distorted objects . (b) Second set: rotated and noisy versions of the character **E**.

	Object						
Template	**E**	**F**	**C**	$\mathbf{E}_d$	$\mathbf{E}_{45°}$	$\mathbf{E}_{270°}$	$\mathbf{E}_{135°}$
E	**1.0000**	0.7071	0.6606	**0.8669**	**0.8533**	**1.0000**	**0.8515**
F	0.7071	**1.0000**	0.7945	0.7772	0.6731	0.7071	0.6793
C	0.6606	0.7945	**1.0000**	0.7331	0.6484	0.6606	0.6539
$\mathbf{E}_d$	**0.8669**	0.7772	0.7331	**1.0000**	**0.8002**	**0.8669**	**0.8047**
$\mathbf{E}_{45°}$	**0.8533**	0.6731	0.6484	**0.8002**	**1.0000**	**0.8533**	**0.9823**
$\mathbf{E}_{270°}$	**1.0000**	0.7071	0.6606	**0.8669**	**0.8533**	**1.0000**	**0.8515**
$\mathbf{E}_{135°}$	**0.8515**	0.6793	0.6539	**0.8047**	**0.9823**	**0.8515**	**1.0000**

Table 5.3: Results of calculating the peak ratio [$= r_S$] obtained for similar objects in Fig. 5.7. The kernel used is a symmetric rectangle function ($L = 41$ and $W = 1$) with kernel length approximately 81 % of the longer side of the object **E** (scale = 1.0).

RKMT function used is $f[Max, Min] = Max(x, y) \cdot Min(x, y)$ for $B = 0.5$. The kernel used is rectangular in profile, and the kernel length is approximately 81 % of the longer side of the template **E** at upper–left. It is shown that the recognition capability is still noticeable, particularly when the distorted character **E** is used as the object.

In certain situations, nonuniform edge width may affect the recognition capability. Figure 5.7(b) shows the results of applying the same convolution kernel and f[Max, Min] used in (a) to three rotated objects (45°, 135°, and 270°) with noise and variations in the edge width. Since only four discrete kernel orientations separated by 45° were used, the objects were rotated to align with one of these kernel orientations. The peak ratio r_S is shown in the box below the rotated objects. The recognition capability is well preserved for such noisy and rotated objects.

Table 5.3 shows the numerical results of using the same kernel and f[Max, Min] used for the objects in Fig. 5.7 for $B = 0.5$. The first row and column represent the

input objects and the templates used for each case, respectively. It is not surprising that the peak ratio r_S between **F** and **C** is relatively high, since the method discussed takes into account only directional information.

5.3.3 Effects of the Kernel Dimension on the Performance

The invariant algorithm discussed depends on the kernel dimension, particularly the kernel length L. It is therefore important to understand how the recognition capability behaves as the kernel length increases. Consider two objects **E** and **H**, which have very similar angular signatures at 0° and 90°. For these two objects shown in Fig. 5.5(a), the similarity measure peak ratio r_S will be relatively high (e.g., close to 1) when the kernel is very short (e.g., $L = 3$ or 5). With such a short kernel, the nonlinear mapping to find $P(\theta)$ is close to a mapping that simply counts those points on line segments of the object contour at each kernel orientation. In other words, the mapping operation becomes simply a histogram of those points on the line segments at each orientation. In such cases, there will be no significant difference between the angular signatures obtained from the objects **H** and **E**, the recognition capability being lost. As L increases, however, the ambiguity tends to be resolved. The angular signature function $P(\theta)$ is no longer simply a histogram of those points on the line segments at each orientation.

Figure 5.8 shows the plot of r_S versus L for five objects using the same kernel and RKMT function used in Fig. 5.5. The character $\mathbf{E}_1$ (scale=1.0) is used as the template. The longer side of the template is 48 pixels long. Since L is very small, the peak ratio [$= r_S$] obtained from the objects **H** and $\mathbf{E}_1$ is close to 1, and thus there is no significant difference in their angular signatures. The ambiguity is resolved, however, as L increases. For both scaled versions $\mathbf{E}_2$ (scale$\simeq$0.7) and $\mathbf{E}_3$ (scale$\simeq$1.3), a valley or dip appears in the plot, the location of the dip tending to depend on the scale factor (e.g., 0.7 and 1.3). As the scale factor increases, the location of the valley tends to move to the right. When L exceeds a certain value

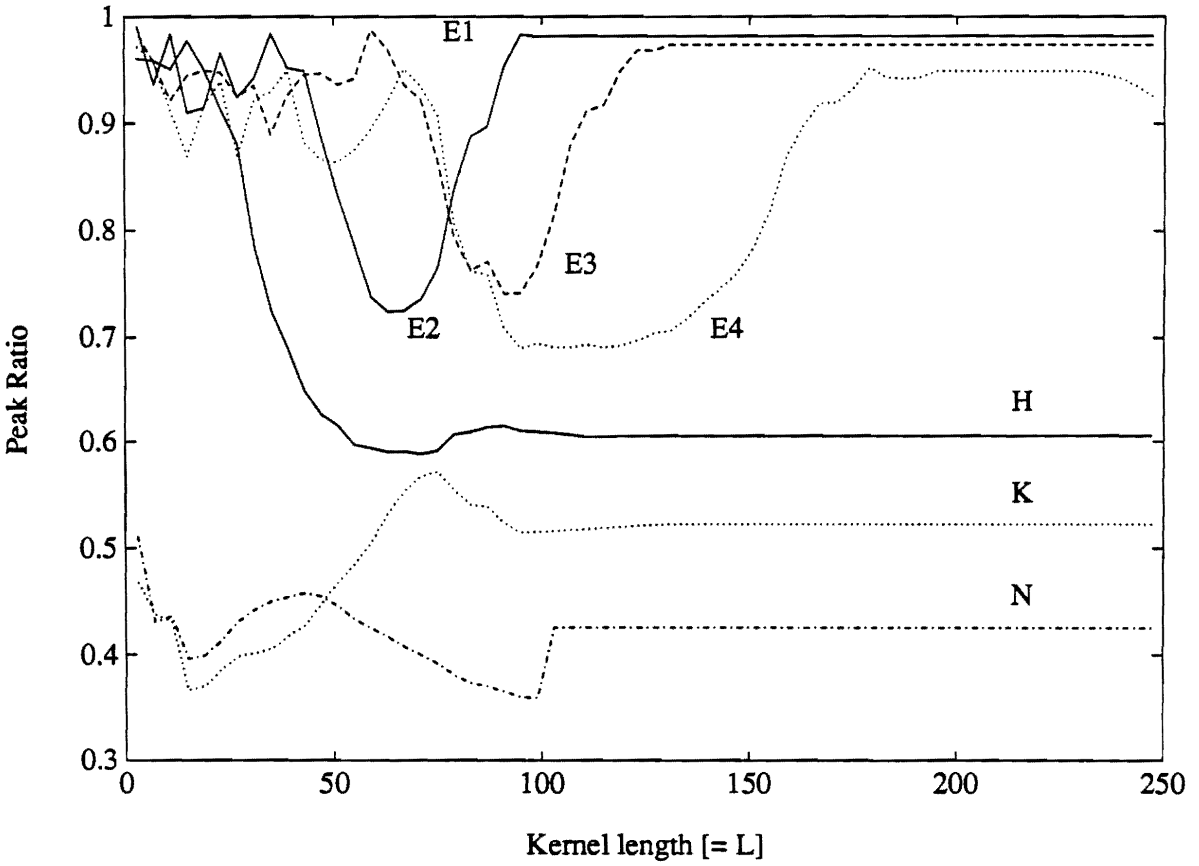

Figure 5.8: Plot of the peak ratio r_S versus L. The kernel used is a rectangle function with $W = 1$. The objects used are shown in Fig. 5.5. E_2, E_3, and E_4 are the scaled versions (0.71, 1.34, and 1.98) of E_1 (shown at the upper left in Fig. 5.5(b)), respectively.

(e.g., $L = 150$), the peak ratio r_S tends to converge to a certain value. Since the objects **K** and **N** are of significantly different angular signatures from those of the scaled versions of the template $\mathbf{E}_1$, there exist significant differences in the resulting peak ratios. It is shown that an appropriately chosen range of L (e.g., $31 \leq L \leq 51$ or $L \geq 110$) can be used for the invariant pattern recognition problems.

5.3.4 Effects of the Kernel Profile on the Performance

A variety of 2–D kernel profiles can also be used, including a rectangular kernel with or without an impulse at its center, a triangular profile, and a Gaussian profile. The kernel profile may affect the recognition capability. Figure 5.9 illustrates an example of the effect of the kernel profile on the recognition capability using a rectangular kernel with an impulse of the height h at its center. The RKMT function used is $f[Max, Min] = Max(x, y) \cdot Min(x, y)$, with $L = 39$ and $W = 1$. If h is close to zero, there are significant differences in r_S for different objects (e.g., **H** and $\mathbf{E}_4$). However, when h becomes significantly large (e.g., $h = 20$), the recognition process fails to discriminate the object **H** from the template $\mathbf{E}_1$. Thus, it is recommended that a rectangular kernel without an impulse be used in the application of the invariant pattern recognition. On the other hand, other objects like **N** and **K** have significantly different angular signatures, r_S being effectively insensitive to variations in h.

Other kernels with gray–scale profiles (e.g., triangular kernel) can yield results comparable with those obtained by using the rectangular kernel. Table 5.4 shows the peak ratio r_S using different kernel profiles for the objects in Fig. 5.5. The kernels with gray–scale or center–weighted profiles tend to decrease the recognition capability as the center portions of the kernels are more weighted. Thus, it is seen in Tab. 5.4 that the rectangular kernel tends to work better than other kernels.

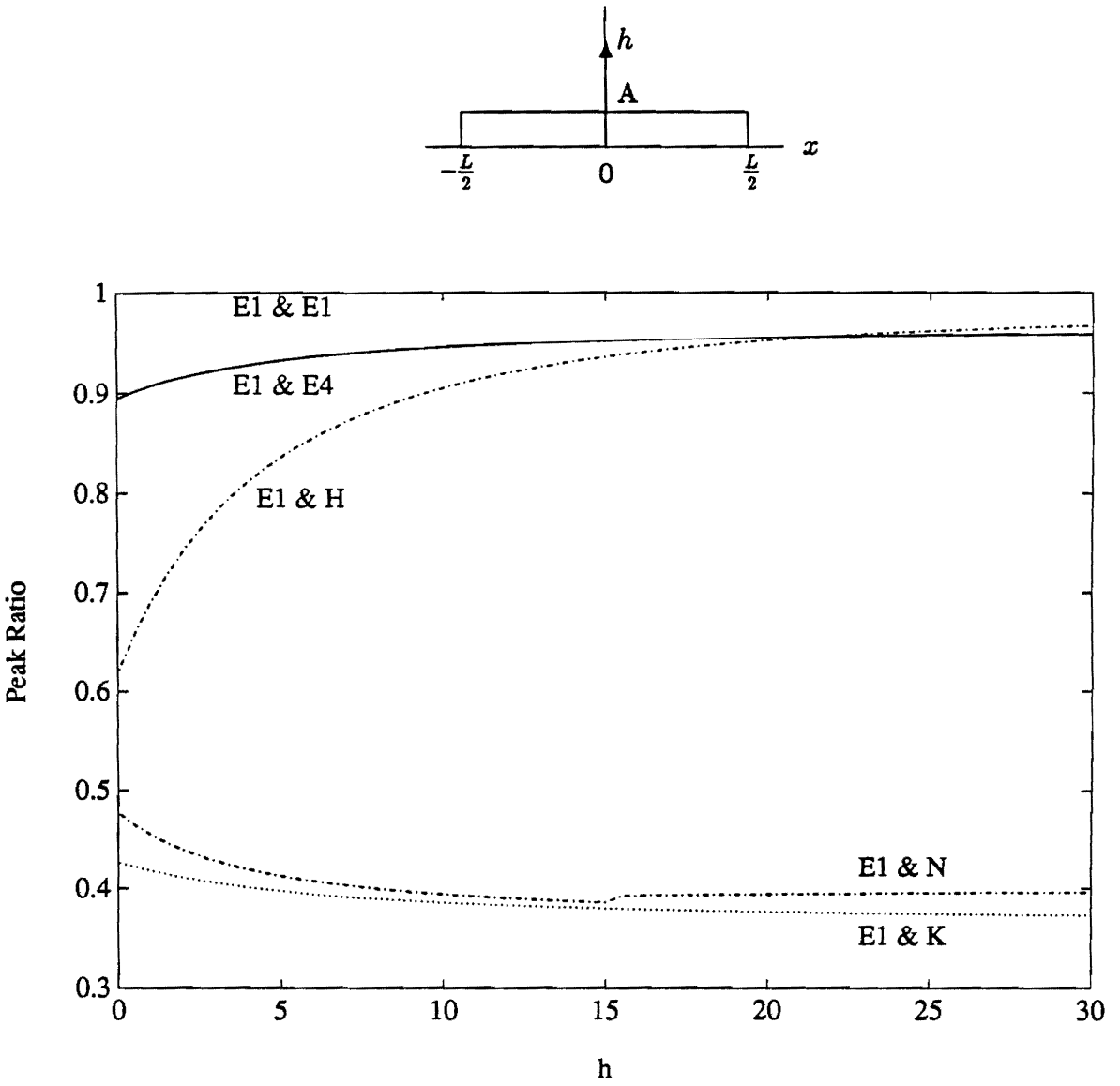

Figure 5.9: Plot of the peak ratio r_S versus h, where h is the height of an impulse at the center of a rectangular kernel. If h is large (e.g., $h = 20$, which is approximately 51 % of the kernel length ($L = 39$)), the recognition process fails to discriminate the objects H and E_4 from the template E_1. The objects used are shown in Fig. 5.5. E_4 (scale=1.98) is the scaled version of E_1 (scale=1.0) at upper-left in Fig. 5.5(b).

Kernel	E_1	H	N	K	E_2	E_3	E_4	B
Rect 1	1.0	0.6893	0.4545	0.4180	0.9515	0.9262	0.9493	0.50
Triangular	1.0	0.7872	0.2148	0.1844	0.9802	0.9280	0.8445	0.18
Gaussian	1.0	0.7072	0.2113	0.1833	0.9274	0.9587	0.8494	0.17
Parabola	1.0	0.7303	0.2497	0.2173	0.9279	0.9328	0.8591	0.21
Rect 5	1.0	0.8360	0.4127	0.3972	0.9740	0.9628	0.9586	0.50
Rect 11	1.0	0.9136	0.3922	0.3842	0.9870	0.9752	0.9651	0.50

Table 5.4: Effects of different kernel profiles ($L = 41$) on the recognition capability with the RKMT function f[Max, Min] = Max · Min. Rect 1, 5, and 11 represent a rectangular kernel with an impulse of the height h ($h = 1$, 5, and 11) at its origin. The standard deviation equals 10 pixels for the Gaussian profile kernel. The input objects are shown in Fig. 5.5 and 5.7.

f[Max, Min]	E_1	H	N	K	E_2	E_3	E_4	B
Max · Min	1.0	0.6893	0.4545	0.4180	0.9515	0.9262	0.9493	0.5
Max	1.0	0.7587	0.5452	0.5393	0.8961	0.9414	0.8716	0.5
Max^2	1.0	0.8825	0.3925	0.3928	0.8958	0.9810	0.9005	0.4
$Max^2 \cdot Min^2$	1.0	0.7950	0.4916	0.3439	0.9259	0.8854	0.8837	0.4
[Max − Min]	1.0	0.8518	0.5663	0.5371	0.8535	0.9602	0.8454	0.5
$[Max - Min]^2$	1.0	0.9015	0.4758	0.4551	0.8552	0.9617	0.8939	0.5
Max·[Max − Min]	1.0	0.8923	0.4067	0.3962	0.8571	0.9647	0.8857	0.4
$Max^2 \cdot [Max - Min]^2$	1.0	0.8387	0.4404	0.4840	0.8238	0.9424	0.9143	0.5

Table 5.5: Effects of the RKMT function f[Max, Min] on the recognition capability using a rectangular kernel ($L = 39$ and $W = 1$) for different RKMT functions f[Max, Min]. The input objects are shown in Fig. 5.5.

5.3.5 Effects of the RKMT Functions on Performance

A variety of RKMT transform functions can be used to obtain $P(\theta)$ and thus to perform the invariant pattern recognition:

$$f[Max, Min] = Max(x,y) \cdot Min(x,y), \tag{5.12}$$

$$f[Max, Min] = Max(x,y), \tag{5.13}$$

$$f[Max, Min] = Max^2(x,y), \tag{5.14}$$

$$f[Max, Min] = Max^2(x,y) \cdot Min^2(x,y), \tag{5.15}$$

$$f[Max, Min] = Max(x,y) - Min(x,y), \tag{5.16}$$

$$f[Max, Min] = [Max(x,y) - Min(x,y)]^2, \tag{5.17}$$

$$f[Max, Min] = Max(x,y) \cdot [Max(x,y) - Min(x,y)], \tag{5.18}$$

$$f[Max, Min] = Max^2(x,y) \cdot [Max(x,y) - Min(x,y)]^2. \tag{5.19}$$

The function $f[Max, Min] = Max(x,y)$ may be useful in certain situations since it can enhance linear features and is easy to measure in an opto–electronic implementation. The formula given by Eq. 5.19 is particularly useful when the object contour is embedded in noisy background. The first part, $Max^2(x,y)$, enhances the linear features whereas the second part, $[Max(x,y) - Min(x,y)]^2$, suppresses noise. By combining these functions as in Eq. 5.19, the recognition process becomes nearly insensitive to noise unless noise with highly oriented linear features exists.

Table 5.5 shows the peak ratio r_S for different RKMT transform functions using a rectangular kernel with $L = 39$ and $W = 1$. The RKMT functions in Tab. 5.5 work well for objects with different angular signatures (e.g., **E**, **N**, and **K**). See the characters $\mathbf{E}_4$ and **H**. A RKMT function like $f[Max, Min] = [Max - Min]$ does not discriminate these objects. Note that only four kernel orientations (0°, 45°, 90°, and 135°) were used in the numerical experiments. Increasing the number of kernel orientations can improve the discrimination capability for these objects,

excluding those points with multiple Max orientations outside their object contours and thus removing resulting spurious peaks. Using $f[Max, Min] = Max \cdot Min$, only those points on the object contour contribute most to finding the angular signature function. Thus, the function $f[Max, Min] = Max \cdot Min$ tends to exhibit the best recognition capability among other RKMT functions as in Tab. 5.5.

5.4 Summary and Discussion

We have discussed a novel hybrid optical method to perform scale– and rotation–invariant pattern recognition. In this method, the description (f[Max(x,y), Min(x,y)], $\theta_{Max}(x, y)$) is first obtained by RKMT processing, and the mapping operation to the angular signature function and the subsequent recognition process are performed on a computer. To obtain quasi–scale invariance, the angular signature function is normalized by its area. The area–normalized angular signature function exhibits an quasi–scale invariance, although the recognition capability still depends somewhat on the kernel length used relative to object scale. Since the kernel rotates, rotation invariance is achieved for input objects with different orientations.

Some effects that variations in the kernel length have on the discrimination of objects with similar angular signatures were discussed. As the kernel length increases, certain ambiguities can be resolved. With an appropriate RKMT transform function, a variety of kernel profiles can be used for the invariant recognition. A rectangular kernel works better than a rectangular kernel with an impulse at its center. In general, other kernels with gray–scale or weakly-weighted profile at their centers can also be used, yielding good recognition capability. Variations in the RKMT transform function are available for enhancing linear features and performing the invariant recognition. The RKMT functions that are particularly interesting include Max · Min, Max^2, and $Max^2 \cdot [Max - Min]^2$. The latter function may be useful for the invariant recognition in a noisy environment.

The foregoing method for the invariant pattern recognition can be implemented using a digital computer alone. However, the method is computationally expensive because of multiple convolutions and rotation operations. Therefore, a hybrid optical/digital system such as the one discussed in Sec. 3.5, can be employed to implement the procedures for the invariant recognition process. For certain objects, partial rotation of the convolution kernel may be sufficient to perform the invariant recognition for a certain class of objects.

CHAPTER 6

EDGE DETECTION AND ENHANCEMENT

In this chapter, the RKMT operation is applied to edge detection and enhancement by a hybrid optical/digital method. Two different classes of edge images are discussed: (1) a gray–scale edge image and (2) a binary edge image. Comparisons are made with conventional digital edge operators, along with a quantitative performance analysis by calculating the signal–to–noise ratio used in Sec. 3.4.

6.1 Introduction

In this section, a new hybrid edge detection method is introduced. For application to edge detection, an asymmetric rectangular or triangular profile kernel is used rather than a symmetric profile kernel. Figure 6.1 illustrates the edge detection operation using a binary input image and a rectangular profile kernel with both symmetry and asymmetry. When the symmetric kernel is convolved with the binary image, the Max value equals the Min value at the boundary in continuous case. Calculating $I_{out}(x,y) = Max(x,y) - Min(x,y)$, the points on the boundary have then zero edge magnitude. Similarly, the edge magnitude on the boundary is zero or quite small in discrete case, depending on the kernel dimension used. The edge magnitude in either side of the boundary increases monotonically with the maximum $W(L+W)/2$ at $x = W/2$, and decreases monotonically with zero magnitude at $x = L/2$. A double

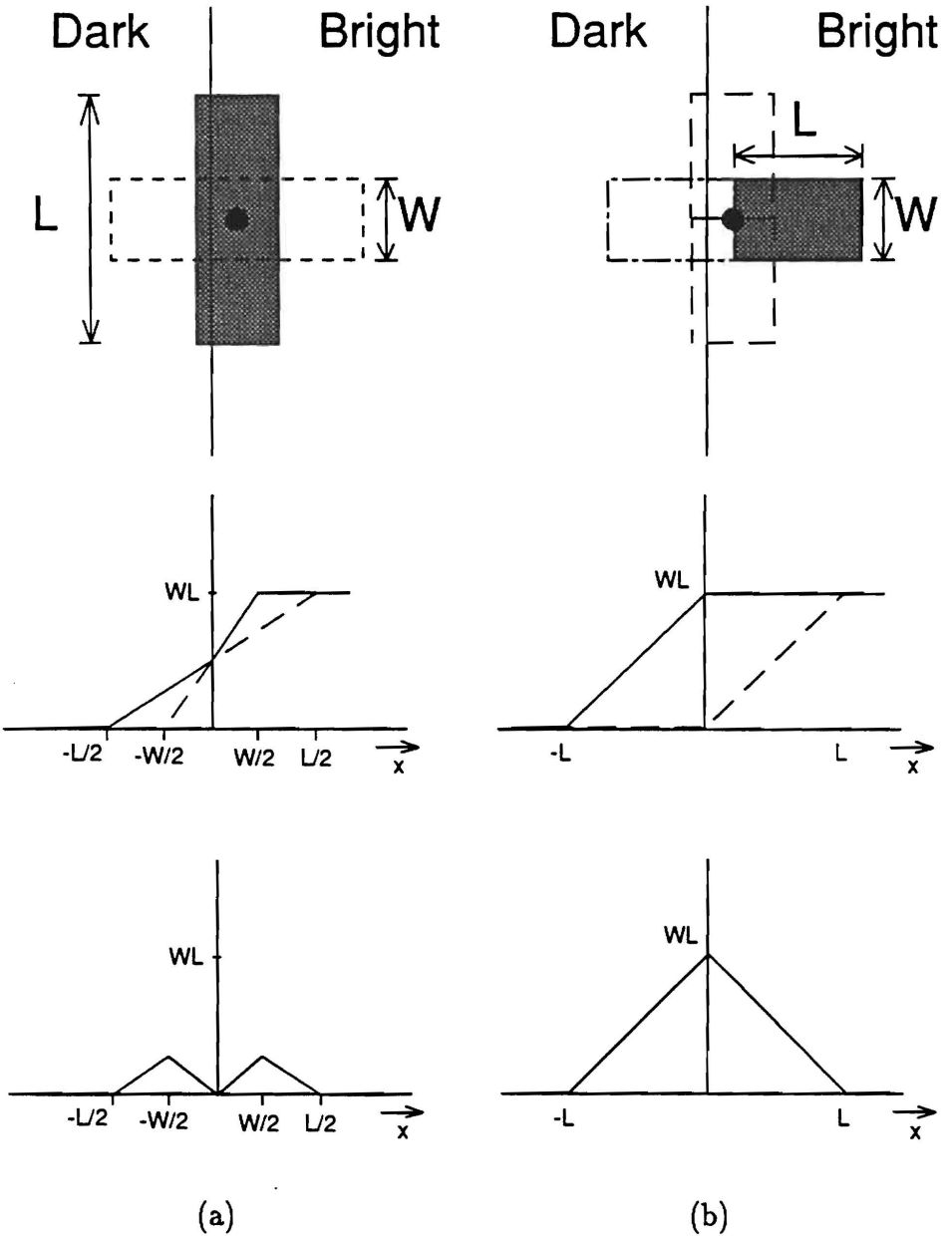

Figure 6.1: Edge detection on a binary image with (a) symmetric and (b) asymmetric rectangular profile kernels. Top to bottom: Binary images and kernels with Max orientations represented by black, Max (solid–line) and Min (dotted–line) values, and edge magnitudes. (•) represents the center of the kernel rotation.

edge will then result from the symmetry of the kernel, as shown in Fig. 6.1(a). On the other hand, Fig. 6.1(b) shows a single edge image obtained by using an asymmetric kernel with the maximum value WL at the boundary. When the kernel is too long, the edge will be thickened. To reduce this effect, the triangular profile or other nonrectangular profile kernels can be used.

6.2 Gray–Scale Edge

The method discussed for the gray–scale edge detection by RKMT processing is a gradient type edge detection method, combining directional information at each point in an input object. Two methods are discussed to obtain the gray–scale edge image using an asymmetric short, narrow kernel. One way to obtain the gray–scale edge image is simply to calculate the edge magnitude $d(x, y)$ at each point,

$$d(x, y) = Max(x, y) - Min(x, y). \tag{6.1}$$

The edge magnitude $d(x, y)$ considers only Max(x,y) and Min(x,y) values without considering of their orientations at each point. The other is to find the angularly rank–ordered edge magnitude $d_\theta(x, y)$ by incorporating the orientation of the convolution output $S_\theta(x, y)$ at an angle θ,

$$d_\theta(x, y) = |S_\theta(x, y) - S_{\theta+180°}(x, y)|. \tag{6.2}$$

The latter method involves calculating the difference between two convolutions obtained from two opposite–kernel orientations, for example, 0° and 180° or 45° and 225°. For 8 discrete rotation angles, four angularly rank–ordered edge magnitudes are obtained as d_1, d_2, d_3, and d_4, for which the highest ranked–edge magnitude is represented by d_1 (i.e., rank 1). The edge detection method using angularly ranked–magnitudes can be useful in certain situations, particularly when the input image is noisy and thus the direct edge magnitude $d(x, y)$ may be sensitive to noise and results in thickening of the edges.

(a)

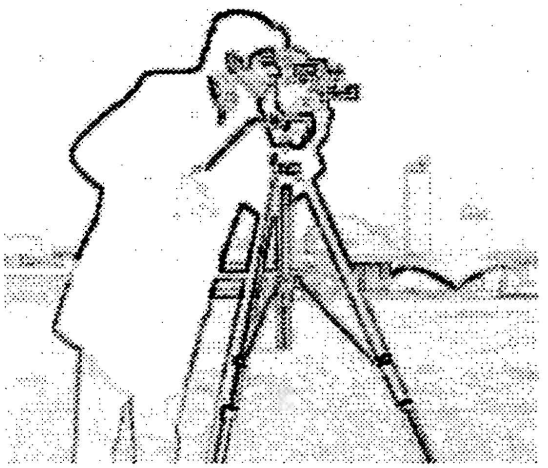

(b)

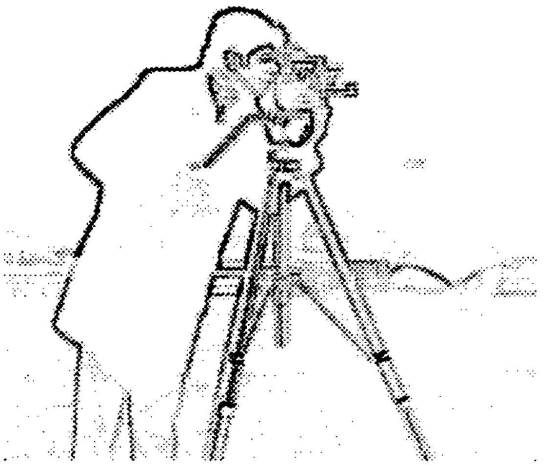

(c)

Figure 6.2: Gray–scale edges obtained by using a triangular profile kernel ($L = 4$ and $W = 1$): (a) original image; (b) $I_{out}(x, y) = d(x, y)$ with an asymmetric kernel; and (c) $I_{out}(x, y) = d(x, y)[1 - \rho^3(x, y)]$ with an asymmetric kernel.

Figure 6.2 illustrates several edge enhancement operations using an image with 256x256 pixels. Figure 6.2(a) shows the original image. Figures 6.2(b) and (c) show the results obtained by calculating $I_{out}(x,y) = d(x,y)$ and $I_{out}(x,y) = d(x,y)[1-\rho(x,y)]$, respectively. The brightness of each image in Fig. 6.2 was rescaled with 256 gray levels. The kernels used for (b) and (c) were triangular in profile ($L = 4$ and $W = 1$) with asymmetry, and rotated through 8 discrete rotation angles: 0°, 45°, 90°, 135°, 180°, 225°, 270°, and 315°. For the edge enhancement application, it may not be necessary to scan all of the orientations from 0 to 360°. A few orientations may be sufficient to quickly locate most significant object boundaries.

Figure 6.3 shows the results obtained finding angularly ranked–edge magnitudes with an asymmetric triangular kernel with $L = 4$ and $W = 1$: (a) $I_{out}(x,y) = d_2(x,y)$; (b) $I_{out}(x,y) = d_3(x,y)$; (c) $I_{out}(x,y) = d_2(x,y)[1-\rho^3(x,y)]$; and (d) $I_{out}(x,y) = d_3(x,y)[1-\rho^3(x,y)]$. It can be shown in (c) and (d) that background noise was significantly reduced by combining $[1-\rho^3(x,y)]$ with $d_2(x,y)$ and $d_3(x,y)$ as demonstrated in Tab. 4.1. Most significant edges with high directionality were enhanced by calculating the ranked–edge magnitude $d_i(x,y)$.

Figure 6.4 shows the results obtained using a noisy image with an asymmetric triangular kernel of $L = 5$ and $W = 1$, followed by thresholding–hard limiting. A threshold value was chosen to obtain comparatively similar edge widths from the gray–scale edge images. Figure 6.4(a) shows the image in Fig. 6.2(a) corrupted by adding the Gaussian noise with zero mean and $\sigma = 40$ (standard deviation). The results of calculating $I_{out}(x,y) = d(x,y)$ and $I_{out}(x,y) = d_2(x,y)$ are shown in Figs. 6.4(b) and (c), respectively. In the numerical simulation, the kernel was rotated through only 8 discrete angles used for the images in Fig. 6.2. Note that the maximum number of rotation angles is eight for 3x3 mask size in the discrete implementation of the RKMT edge enhancement operation. As the kernel becomes longer or wider, the discrete implementation of the RKMT operation may become difficult, particularly when a nonrectangular kernel must be used to reduce thicken-

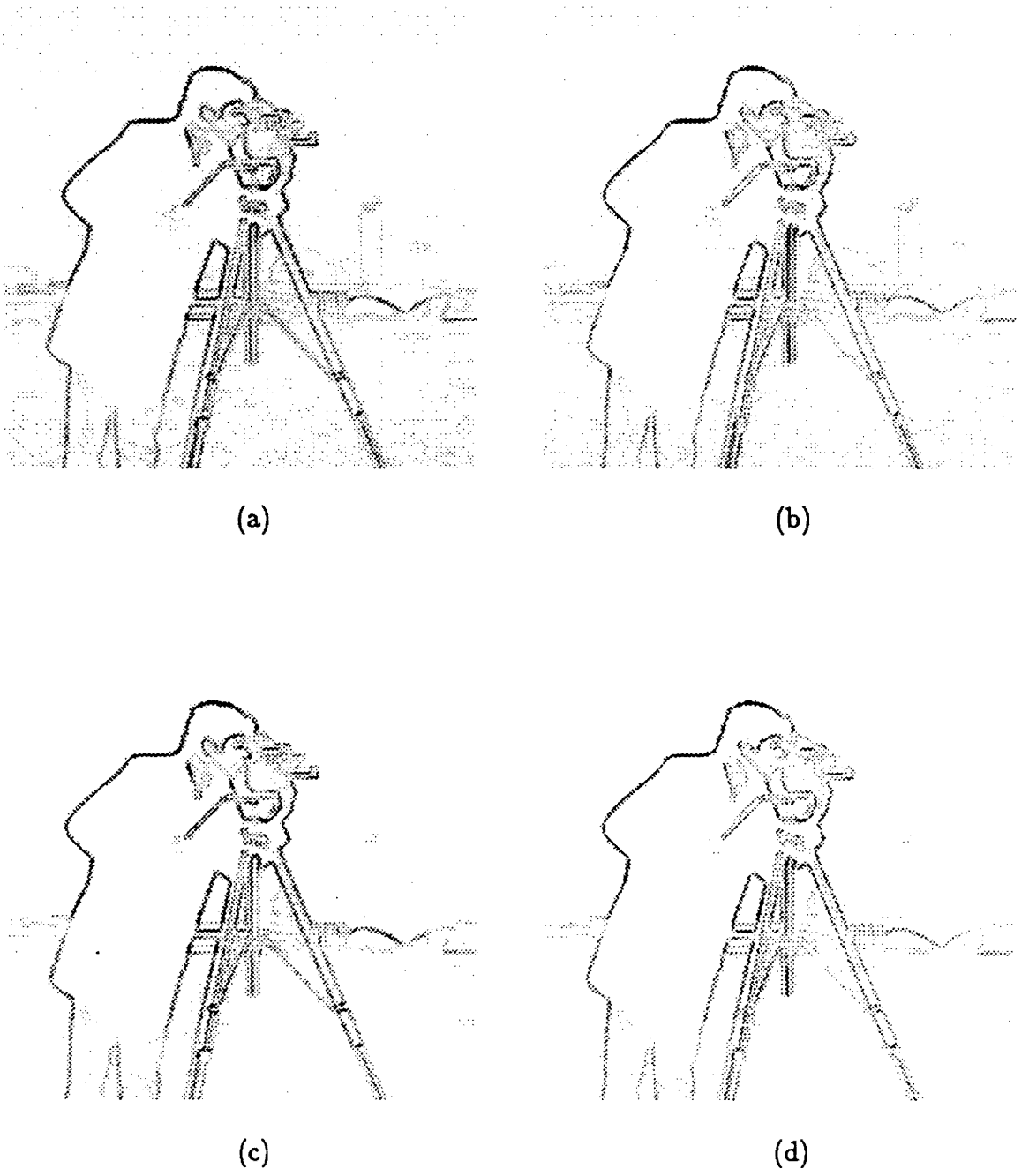

Figure 6.3: Gray–scale edges obtained by using an asymmetric triangular kernel ($L = 4$ and $W = 1$): (a) $I_{out}(x, y) = d_2(x, y)$: (b) $I_{out}(x, y) = d_3(x, y)$: (c) $I_{out}(x, y) = d_2(x, y)[1 - \rho^3(x, y)]$: and (d) $I_{out}(x, y) = d_3(x, y)[1 - \rho^3(x, y)]$.

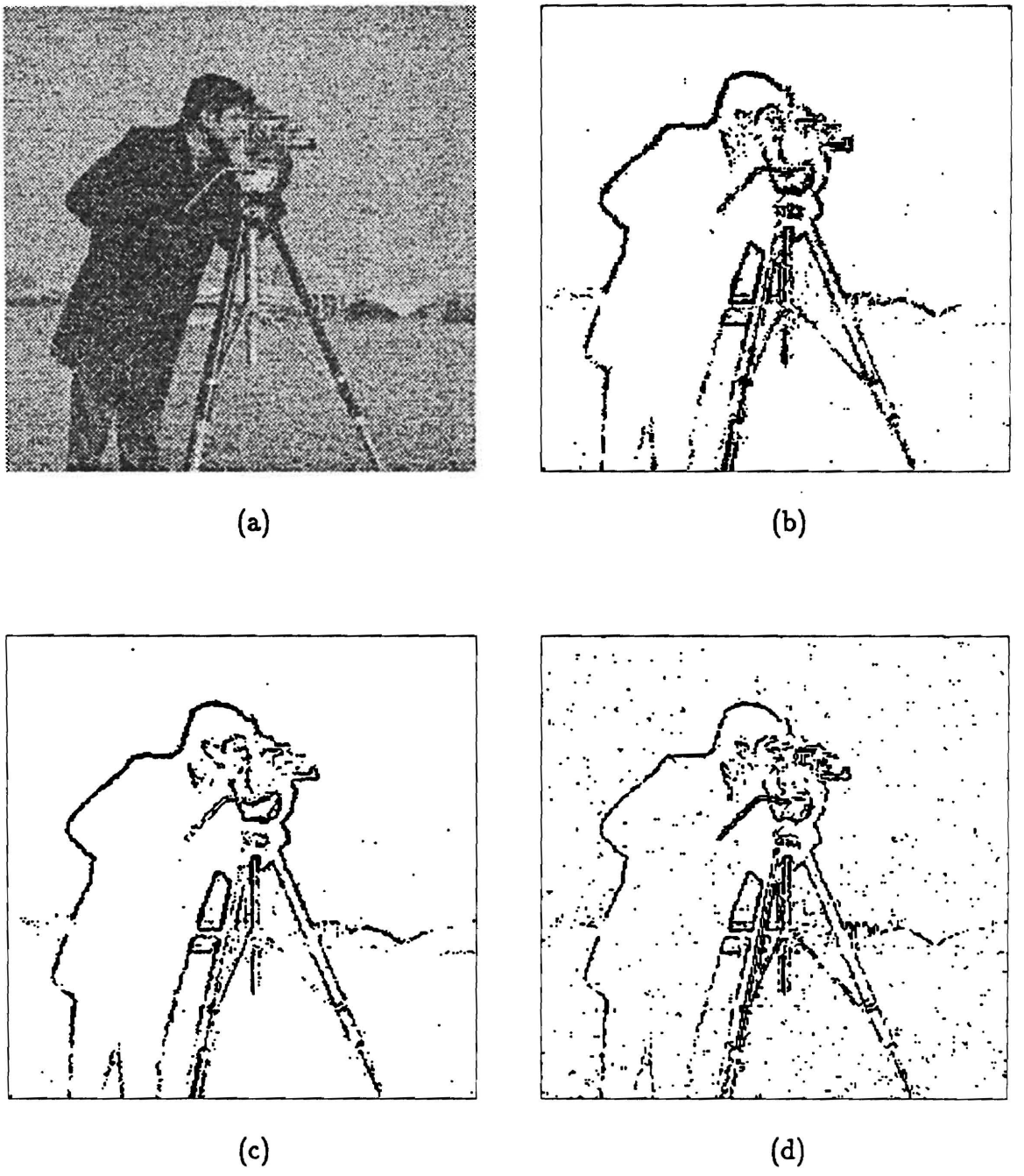

Figure 6.4: Results from the noisy image corrupted with Gaussian noise of $\sigma = 40$ using an asymmetric triangular kernel with $L = 5$ and $W = 1$. (a) Noisy image. (b) Result of calcaulting $I_{out}(x, y) = d(x, y)$. (c) Result of calcaulting $I_{out}(x, y) = d_2(x, y)$. (d) Result of applying the Sobel's digital edge operator with 3x3 mask.

ing of enhanced edges and background noise. In an optical implementation of the RKMT edge enhancement operation, however, this problem is not found. Better results could be expected if more rotation angles were used in the optical implementation of the enhancement method. For comparison, the Sobel's digital edge operator [49] with a 3x3 mask was applied to the image in Fig. 6.4(a). The result of applying the Sobel's operator is shown in Fig. 6.4(d). A larger mask (e.g., 5x5 or 7x7 mask) can be used to reduce background noise, but resulting in great thickening of the edges and losing certain details because the Sobel's edge operator detects well only horizontal and vertical edges in the input image.

6.3 Binary Edge

The concept behind binary edge detection and enhancement is similar to a morphological operation [52,91,92]. In one application of the latter method to edge detection, an input image is processed finding the maximum gray value in a structuring element (e.g., 3x3 mask or 5x5 mask). An edge detection operation is then performed by calculating the difference in pixel values at each point between the processed image and the input image [93]. The edge detection operation by RKMT processing is performed by finding Max or Min value of the convolution outputs with a certain kernel rather than individual pixel values in the input image.

In the application of the RKMT method to the binary edge detection, a Max operation with an asymmetric short kernel (e.g., 3x1) tends to expand bright objects in an image whereas a Min operation shrinks bright objects. The kernel dimension [$=LxW$] can be either $L > W$ or $L < W$. Figure 6.5 illustrates the results of applying the Max and Min operations with an asymmetric kernel. The kernel used is rectangular in profile with $L = 3$ and $W = 1$. Figure 6.5(a) shows a camera man image with 256x256 pixels. The images processed by the Max and Min operations are shown in (b) and (c), respectively. In (b), certain bright regions in the tripod legs were expanded into comparatively dark regions. In (c), the bright line features in the left leg of the tripod was significantly reduced by the Min operation. Both Max and Min operations result in smoothing, particularly at the boundaries as seen in (b) and (c), but preserving most desired features. The property of expanding the object by the Max operation can be used for detecting the edges in such a way that the processed image is subtracted by the original image, followed by a certain thresholding operation to obtain a binary image. Similarly, the input image can also be subtracted by the image obtained in the Min operation, followed by a thresholding operation.

The binary edge detection operation is summarized as follows.

(a)

(b)

(c)

Figure 6.5: Examples of expanding and shrinking objects by Max and Min operations, respectively, where the kernel used is rectangular in profile with $L = 3$ and $W = 1$. (a) Original image. (b) Result of applying a Max operation. (c) Result of applying a Min operation.

1. For the input image $O(x,y)$, obtain the intermediate image

$$I'_{out}(x,y) = Max(x,y) \;/\; V_o, \tag{6.3}$$

where V_o is the volume of the convolution kernel used. The image obtained in the Max operation is normalized by the volume V_o to remove dependence on the kernel dimension.

2. Compute the difference image $d_b(x,y)$,

$$d_b(x,y) = c \cdot I'_{out}(x,y) - O(x,y) \tag{6.4}$$

where $c(< 1)$ is a constant to control the difference. The constant c also depends on image contrast. For example, c is relatively small for the image with high contrast.

3. Obtain the binary edge image $I_{out}(x,y)$,

$$\begin{aligned} I_{out}(x,y) &= 1, \qquad \text{if} \quad d_b(x,y) \geq 0. \\ I_{out}(x,y) &= 0, \qquad \text{if} \quad d_b(x,y) < 0. \end{aligned} \tag{6.5}$$

Alternatively, $I'_{out}(x,y) = Min(x,y)/V_o$ can also be used instead of taking $I_{out}(x,y) = Max$. In this case, Eq. 6.4 is replaced by $d_b(x,y) = c \cdot O(x,y) - I'_{out}(x,y)$.

Figure 6.6 shows the results of applying the detection method to a gray-scale image in Fig. 6.5(a). The kernel used is rectangular in profile with $L = 2$ and $W = 1$ $(L > W)$. The images in Figs. 6.6(a) and (b) show the results of calculating $d_b(x,y) = c \cdot I'_{out}(x,y) - O(x,y)$ (Eq. 6.4) with $c = 0.71$ and 0.81, respectively. The kernel with $W > L$ is also useful for the binary edge detection method as the image is noisy, reducing background noise and thickening of the edges. Comparisons are made with the Sobel's edge operator and a morphological operation. Figure 6.6(c) shows the result of applying the Sobel's edge operator with a 3x3 mask, followed by thresholding–hard limiting. The threshold value was chosen

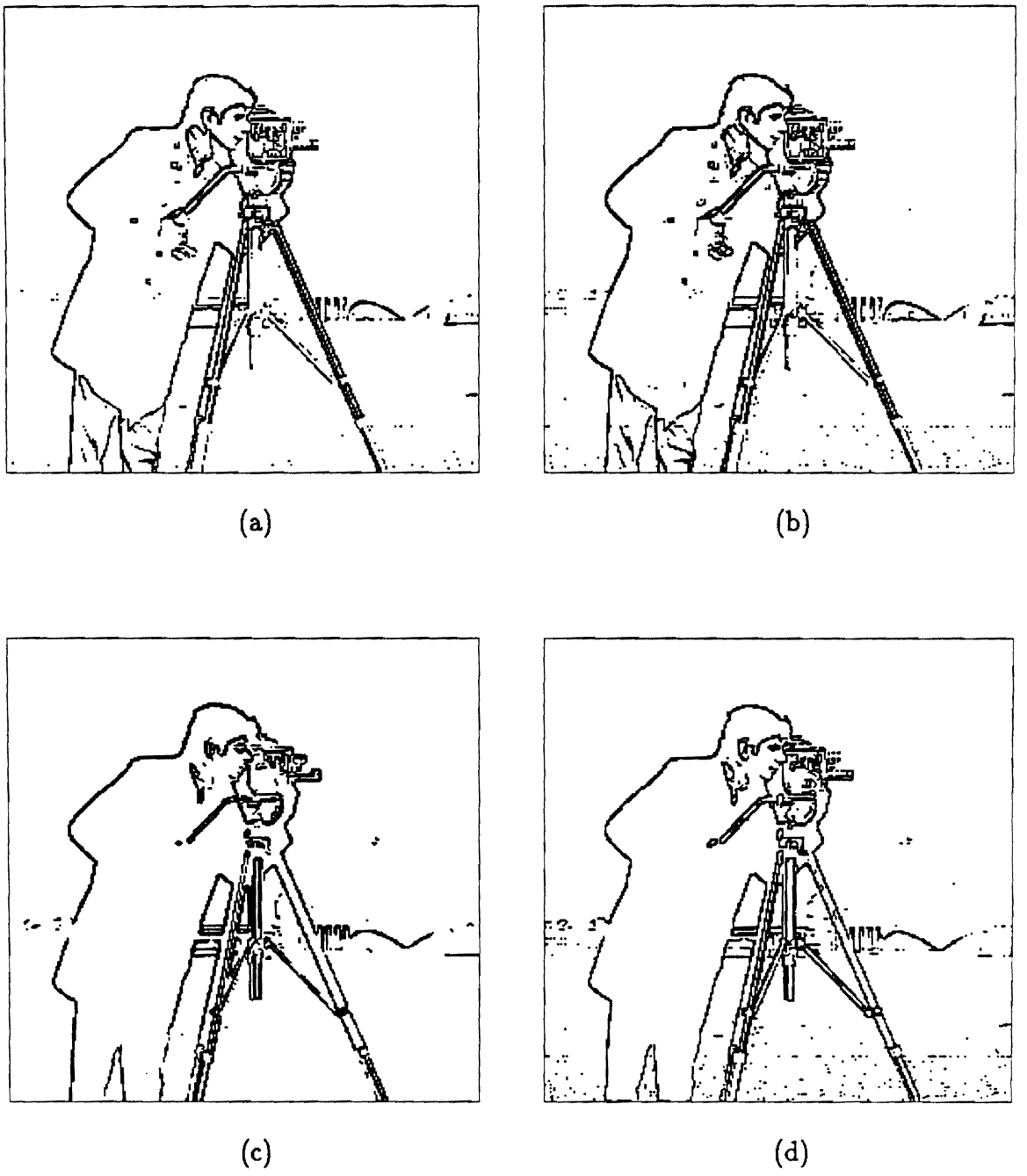

Figure 6.6: Results of the edge detection operation. (a) and (b) RKMT binary edge detections using an asymmetric rectangular kernel ($L = 2$ and $W = 1$) with $c = 0.71$ and $c = 0.81$, respectively. (c) Sobel's edge operator with 3x3 mask. (d) Morphological operation with 3x3 mask.

to obtain comparatively similar edge widths to those of the images in Figs. 6.6(a) and (b). The result of applying a morphological operation is shown in Fig. 6.6(d), for which the input image in Fig. 6.5(a) was processed by finding the maximum value in a 3x3 structuring element (i.e., filtering mask) and the processed image was then subtracted by the input image, followed by thresholding–hard limiting.

6.4 Quantitative Performance Measure

It is useful to investigate quantitatively how the RKMT edge enhancement operation performs under various conditions of varying the kernel dimension and profiles. The peak mean–square error measure method as discussed in Sec. 3.4 was used to estimate similarity between ideal edge components in a noiseless edge image and edge components obtained from a noisy image, calculating the signal–to–noise ratio (SNR). Figure 6.7 shows the images used for the quantitative performance analysis. The noiseless test image used for this analysis is shown in Fig. 6.7(a) and consists of 12 triangles and uniform backgrounds with 150 and 100 in 256 gray levels, respectively. The noiseless edge components of the image in (a) are shown in (b), where each edge width is two pixels. The image in (a) was corrupted by adding the Gaussian noise with zero mean and $\sigma = 10$ (standard deviation). The resulting noisy image is shown in (c).

Two digital edge detection methods are evaluated for purposes of comparison: (1) gradient–type digital edge operators (e.g., Sobel's and Prewitt's operators) [49] and (2) a morphological operation. Note that the RKMT gray–scale edge enhancement method discussed in Sec. 6.2 is also a gradient–type operator. The edge detection method using the Sobel's and Prewitt's edge operators has been optically implemented using a multiple–exposure matched spatial filter (and computer–generated hologram) in a coherent optical system [53] and using an optical symbolic substitution technique [54]. The optical implementations of such digital edge op-

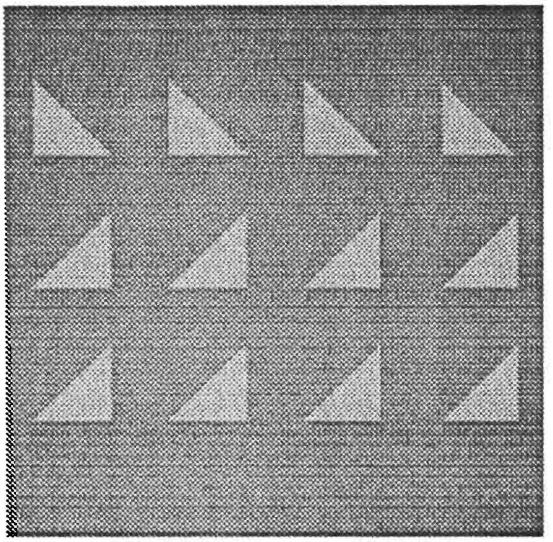

(a)

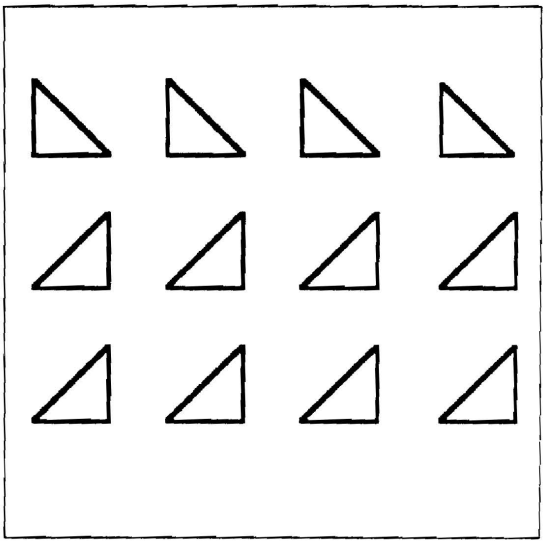

(b)

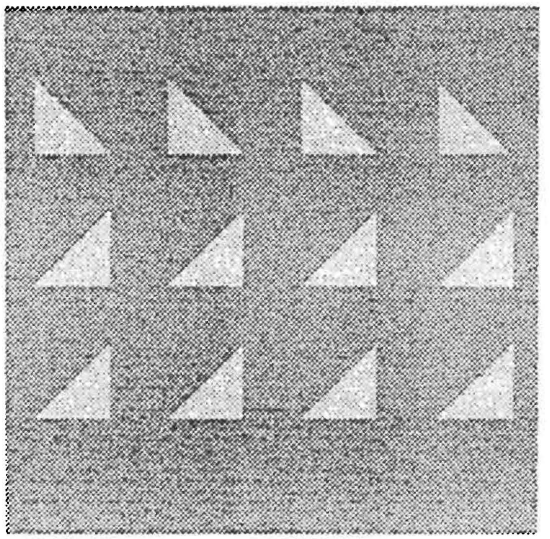

(c)

Figure 6.7: Test images. (a) Noiseless image where the bright (dark) region has 150 (100) in 256 gray levels. (b) Edge image of (a), where the edges are 2 pixels wide. (c) Noisy image corrupted by Gaussian noise with zero mean and $\sigma = 10$ (standard deviation).

erators suggest the use of the Sobel's and Prewitt's edge operators to evaluate the performance of the RKMT edge enhancement operation. Another comparison can be obtained using a simple morphological edge operator used for Fig. 6.6(d), since the concept for finding Max and Min values of the convolution outputs in the RKMT processing is somewhat similar to such a morphological edge detection method.

The noisy image in Fig. 6.7(c) is subjected to various RKMT edge enhancement operations and digital edge operators. Figure 6.8 shows the edge images obtained by calculating various RKMT functions: $I_{out}(x,y) = d(x,y)$ and $I_{out}(x,y) = d_i(x,y)$ for i=1, 2, and 3. The kernel used is triangular in profile with $L = 5$ and $W = 1$. (Note that the number of nonzero weights of the triangular kernel is only 4.) Each image was thresholded at a gray level at which the maximum SNR was obtained. Similarly, Fig. 6.9 shows the results of applying the digital edge operators. The images obtained from the Sobel's edge operators with 3x3 and 5x5 masks are shown in Figs. 6.9(a) and (b), respectively. Figures 6.9(c) and (d) show the results of using the Prewitt's edge operators with 3x3 and 5x5 masks, respectively. Two filtering mask sizes were used because the small one (i.e., 3x3) can be sensitive to noise.

Table 6.1 shows the numerical results of calculating the SNRs for the binarized edge images in Figs. 6.8 and 6.9, where S3(S5), P3(P5), and M3 (M5) represent the Sobel's operator, the Prewitt's operator, and the morphological operation with 3x3 (5x5) mask, respectively. The SNRs represent the similarity between the noiseless edge image in Fig. 6.7(b) and the processed images in Figs. 6.8 and 6.9. In other words, the SNRs measure how accurately each edge detection operator locates and enhances the edge components of the noisy image in Fig. 6.7(c). It is shown in Tab. 6.1 that both 3x3 Sobel's and Prewitt's operators can detect accurately the desired edge components for $\sigma = 0$ (i.e., SNR=∞). Otherwise, the SNRs obtained using these digital operators remain approximately the same (SNR$\simeq$19 dB for 3x3 mask and SNR$\simeq$21 dB for 5x5 mask). The morphological operation (M3 for 3x3 mask and M5 for 5x5 mask) may detect well the edges, the detection operation

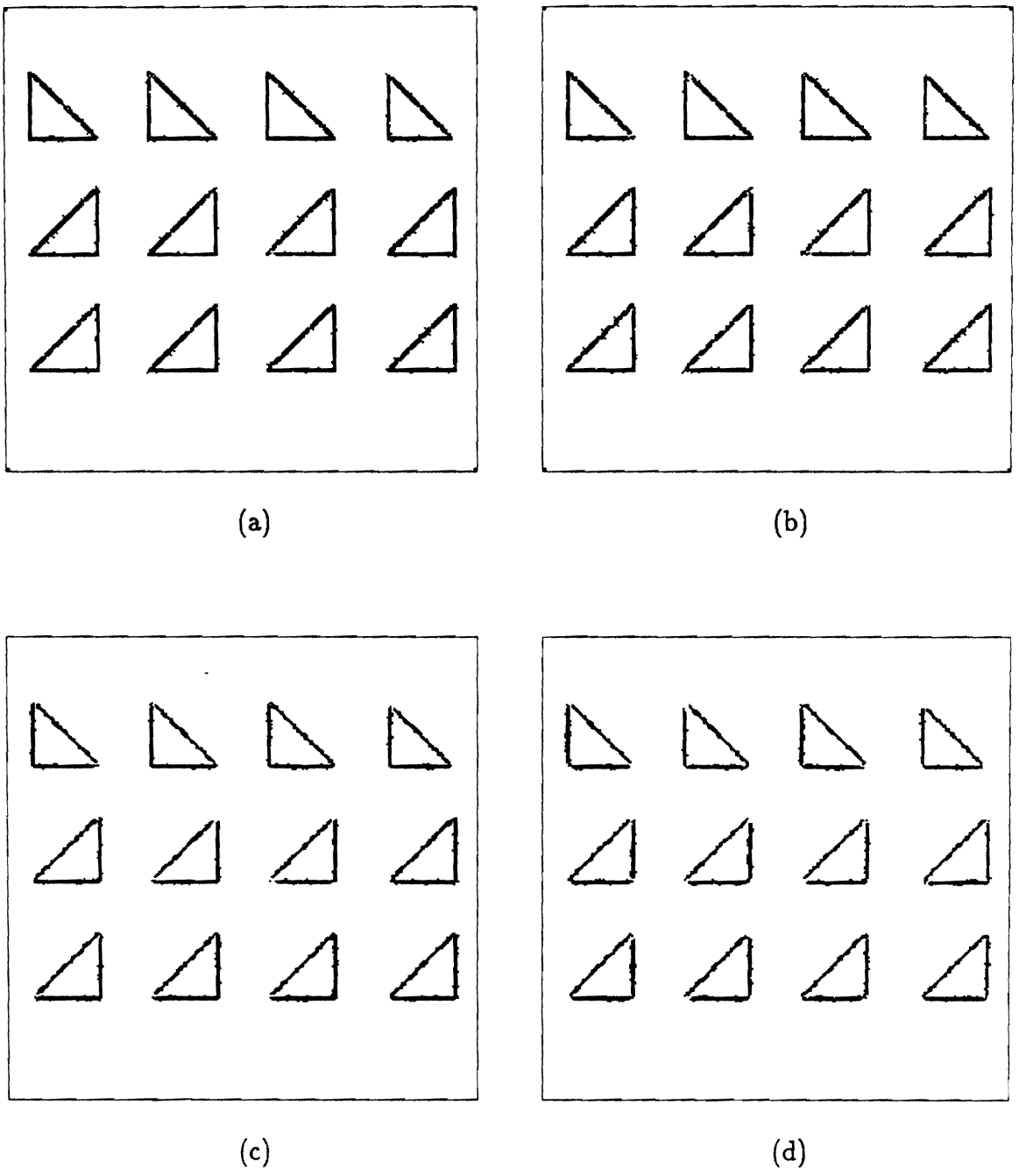

Figure 6.8: Results of applying various RKMT functions, followed by thresholding–hard limiting: (a) $I_{out}(x, y) = d(x, y)$; (b) $I_{out}(x, y) = d_1(x, y)$; (c) $I_{out}(x, y) = d_2(x, y)$; and (d) $I_{out}(x, y) = d_3(x, y)$.

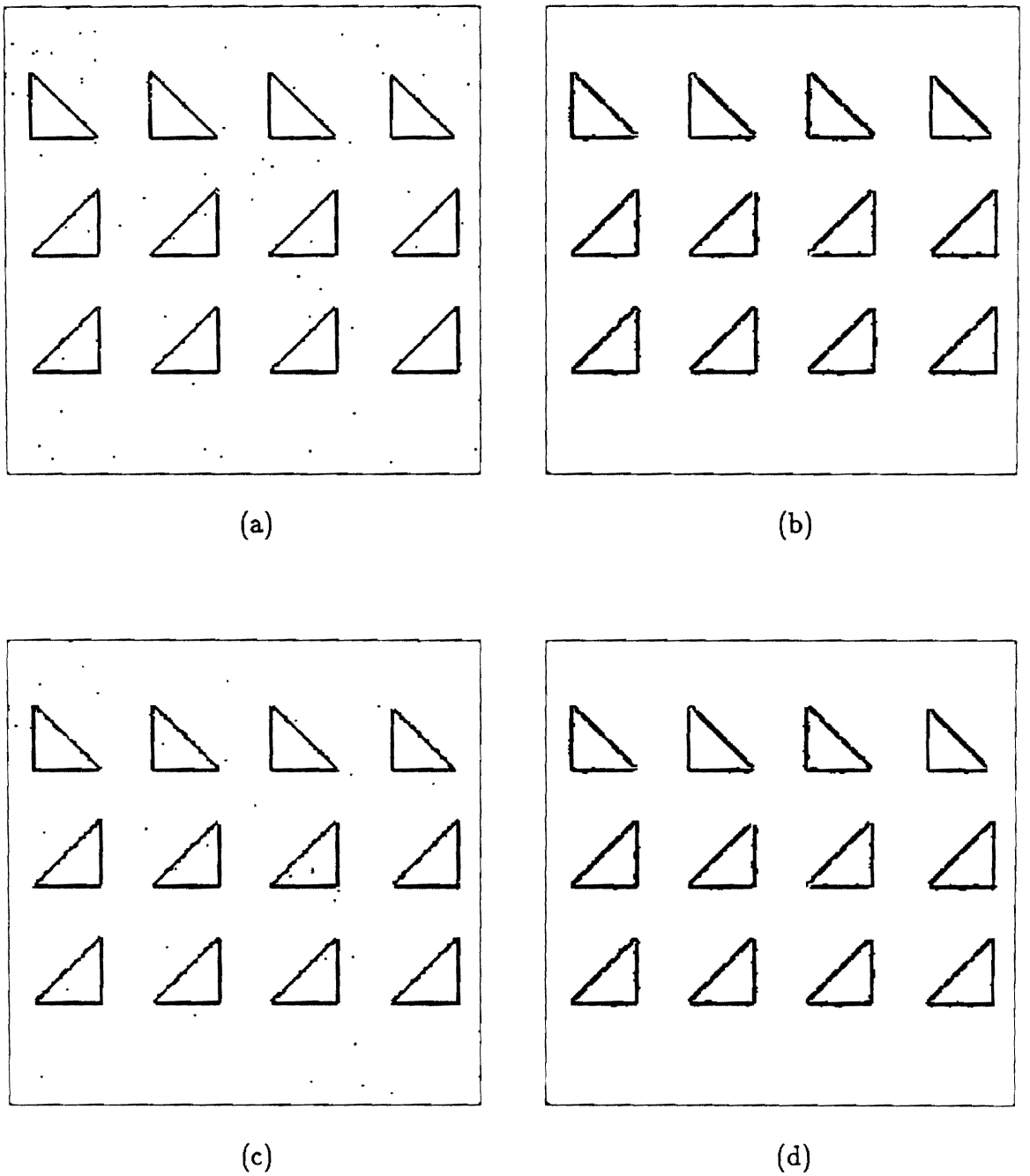

Figure 6.9: Results of applying digital gradient edge operators: (a) and (b) 3x3 and 5x5 Sobel's edge operators; (c) and (d) 3x3 and 5x5 Prewitt's edge operators.

Signal–To–Noise Ratios [=SNR] dB										
σ	d	d_1	d_2	d_3	S3	S5	P3	P5	M3	M5
0	34.36	31.35	18.25	16.32	∞	27.37	∞	26.96	16.00	12.71
10	**23.84**	22.04	19.07	17.98	18.55	21.94	19.47	21.93	14.77	13.29

Table 6.1: Numerical results obtained for various edge operators, where S3 (P3) and S5 (P5) represent the Sobel's (Prewitt's) digital edge operators with 3x3 and 5x5 filtering masks, respectively, and M3 (M5) is a morphological edge operator with 3x3 (5x5) mask. The kernel used for $d(x,y)$ and $d_i(x,y)$ is triangular in profile with $L = 5$ and $W = 1$.

being sensitive to noise. However, the SNRs for these morphological edge operators are quite low, because they do not locate accurately. Note that the morphological operation was performed by finding the maximum pixel value within a structuring element and thus the bright regions of the triangles expand into dark background regions. This means that the edge components are found in only dark regions (i.e., outside the triangles). Thus, in a certain case, only one pixel edge width is obtained.

The kernel used for the RKMT processing is triangular in profile with $L = 5$ and $W = 1$. The RKMT edge enhancement operation with $L = 5$ and $W = 1$ does not yield SNR $= \infty$ for $\sigma = 0$, because such a long kernel results in thickening of the edges and then reducing the SNR. Alternatively, a shorter kernel can be used to yield SNR $= \infty$. (See Tab. 6.2.) The SNRs for $I_{out}(x,y) = d(x,y)$ and $I_{out}(x,y) = d_1(x,y)$ are slightly higher than those of digital opertors. For only comparison, the SNRs for other angularly rank-ordered edge magnitudes are also given in Tab. 6.1. The SNRs for such low rank–ordered edge magnitudes (e.g., $d_2(x,y)$ and $d_3(x,y)$) are much lower than those of [Max - Min] operation and $d_1(x,y)$, simply because they lose certain edge components (e.g., vertices of the triangles) and result in some thinning of the edges.

	Triangular Kernel					Rectangular Kernel				
σ	L=3	L=4	L=5	L=6	L=7	L=2	L=3	L=4	L=5	L=6
0	∞	∞	34.36	34.36	31.35	∞	34.36	31.35	29.59	28.34
10	21.46	**25.54**	23.84	22.55	21.42	21.42	22.20	20.18	18.59	17.90

Table 6.2: SNRs obtained calculating $I_{out}(x,y) = Max(x,y) - Min(x,y)$ with two kernel profiles [W=1] for various kernel lengths [=L]. Note that the number of nonzero weights of the triangular kernel with the length L is $(L-1)$.

Table 6.2 shows the SNRs obtained varying the kernel length L for two kernel profiles ($W = 1$): triangular and rectangular kernels. The kernels with L=3 (and 4) for the triangular kernel and L=2 for the rectangular kernel yield SNR=∞, since these kernels can detect the same edge components as those of the noiseless edge image in Fig. 6.7(b). The maximum SNR was obtained for the triangular kernel with L=4, which is 3.6 dB higher than that of the 5x5 Sobel's edge operator in Tab. 6.1. The SNRs for other longer kernels decrease because these kernels result in thickening of the edges as discussed in Tab. 6.1. Similarly, the SNR tends to decrease because of noise effects as L becomes short. In Tab. 6.2, the triangular profile kernel tends to show the better performance than the rectangular profile kernel. It is not difficult to choose a proper kernel dimension for a certain application. As the input is noisy, the kernel can also be widened to reduce background noise.

It is shown from Tabs. 6.1 and 6.2 that the overall results obtained in the RKMT edge enhancement operations are close to those obtained from Sobel's and Prewitt's digital edge detection operators. However, such digital operators may not work well for objects with arbitrary edge orientations, because they locate and detect well only the horizontal and vertical edges. In an optical implementation of the RKMT operation, most significant edges regardless of their orientations can be located and enhanced, since the convolution kernel rotates through 360 degrees.

In addition, a nonrectangular profile kernel can easily be generated holographically with various kernel dimensions, reducing noise effects and thickening of enhanced edges.

CHAPTER 7

CONCLUSIONS

7.1 Summary of Results

In this work we have described robust opto–electronic procedures for the reliable extraction of information on size and shape parameters. The focus has been on developing a novel optical rotating kernel transformation (RKMT) method for enhancing linear features (e.g., endothelial cell boundaries) in noisy background. Related works, which are offshoots from the RKMT endothelial image preprocessing, have been discussed, including invariant pattern recognition and edge enhancement.

7.1.1 Pattern Analysis by Fourier Transform Methods

Two different procedures have been discussed for extracting statistical information on cell parameters such as size, size variation, and shape of cells. One procedure involves illuminating and optically Fourier transforming a large number of cells in the input pattern. The other procedure limits the illuminated area to a small region approximately the size of one cell, thus enabling the estimation of shape characteristics.

The first procedure was used to obtain the radial projection of the Fourier intensity pattern, introducing robust automated algorithms for size measures. The raw radial projection was median–filtered to reduce the effects of noise and then subjected to fifth–order polynomial curve fitting. For the average size or density, the maximum point B_p was located in the first lobe of the fitted polynomial curve.

For the size variation, the normalized mean–square difference measures e_{13} and e_{23} (i.e., contrast measure) were calculated between the fitted polynomial and the mean of median–filtered values. It was shown that the latter measure e_{23} tends to cluster better than the former measure.

To obtain shape characteristics, a numbered cell pattern containing 24 cells was scanned, one cell at a time, with a beam size slightly larger than a single cell. Twenty–four angular correlation functions of angular projections obtained from the Fourier intensity distributions were summed and averaged. It was observed that the location and width of the peaks in the mean correlation function relate rather well, at least qualitatively, to the average shape and average variation of number of sides of the 24 scanned cells.

7.1.2 Optical Rotating Kernel Transformation

RKMT processing has been introduced and demonstrated, in computer simulations, for nonlinear image processing including linear feature (e.g., straight–line segments) enhancement operation. A variety of 2–D noncircular symmetric (and asymmetric) kernels and RKMT functions were introduced. Two types of kernels were particularly useful for the enhancement of linear features: a long, narrow rectangular profile and a long, narrow nonrectangular (e.g., triangular) profile.

Algorithms for enhancing linear features were introduced and applied to noisy images, including [Max - Min] operation and more generally multipass operation iteratively combining a Max operation and a [Max - Min] operation. The multipass operation demonstrated quantitatively and qualitatively better performance than the basic [Max – Min] operation. Continuing the multipass operation may increase smoothing and thickening of enhanced line segments, while reducing noise.

While the RKMT processing can be implemented on a digital computer, perhaps its most important advantage lies in the fact that it is particularly well suited for optical–electronic implementation. Since the kernels used are typically nonneg-

ative, an incoherent spatial filtering system was discussed to implement the RKMT processing. In such an optical implementation, a prism–hologram combination is used in the pupil plane to produce the desired kernel rotation. Such a realization would retain much of the flexibility of a digital–electronic implementation, while tapping the traditional speed and throughput advantages of optics.

7.1.3 Nonlinear Image Processing: Preprocessing

RKMT processing was applied to the enhancement of cell boundaries (i.e., straight–line segments) in endothelial cell images characterized by low contrast and spatially varying average background brightness in noisy background. While a simple [Max - Min] operation achieved useful enhancement of the cell boundaries, better results were obtained for multipass operation combining a Max operation with the [Max - Min] operation. Furthermore, two iterations of the multipass operation yielded still better results. Lengthening the kernel resulted in greater connectivity in the output line segments, but increased thickening of line segments and smoothing at the intersections of cell boundaries. The triangular profile kernel resulted in reduced thickening of the cell boundaries.

Two binarization methods, based on the Min–Max deviation measure and the angular variation measure, were also introduced and applied to the gray–scale image enhanced by the RKMT processing for subsequent pattern analysis. The former measure is simple and suitable for optical–electronic implementation. Comparisons were made with conventional digital filtering methods, including bandpass spatial filtering and directional nonlinear processing with wedge–shaped spatial filters. Experimental results showed that RKMT processing compared extremely well with such digital techniques.

7.1.4 Invariant Pattern Recognition

A novel hybrid optical method to perform pattern recognition with rotation and quasi–scale invariance has been introduced and discussed using alphabetic characters. Based on numerical experiments, the quasi–scale invariance was obtained over 1:3 range. More generally, such scale invariance can also be expected over a wide range (e.g., 1:5) using an appropriate kernel dimension. Since the kernel was rotated, the rotation invariance was achieved. The recognition process was performed by calculating the angular crosscorrelation function between the energy–normalized angular signature functions obtained from both the input object and the template. The rotation angle of the object with respect to the template was found to correspond to the point where the correlation achieves the maximum.

Also discussed were some effects that variations in the kernel length and profile have on the discrimination of objects with similar angular signatures. The RKMT function $f[Max, Min] = Max(x, y) \cdot Min(x, y)$ performed best among other RKMT functions with four kernel orientations. Increasing the number of kernel orientations improves the recognition capability by excluding those points with multiple Max orientations, which may not be excluded using a small set of kernel orientations.

7.1.5 Edge Detection and Enhancement

The RKMT processing has also been extended to edge enhancement operation, using a short, narrow asymmetric kernel. Two types of edge images were obtained: gray–scale and binary edge images. For the gray–scale edge image, two methods were discussed to quickly locate edges: direct edge magnitude $[=d(x, y)]$ and angularly rank–ordered edge magnitude $[=d_i(x, y)]$. The methods for the direct edge magnitude and binary edge image are highly attractive for optical–electronic implementation. Quantitative analysis on the performance of RKMT edge enhancement operation was also performed for test images with and without noise. A triangular kernel performed better than a rectangular kernel, reducing thickening of edges and

thus yielding higher signal–to-noise ratio. More generally, a nonrectangular profile kernel with a large dimension can be used without great thickening of edges, searching most edge orientations in the input image.

7.2 Recommendations for Future Research

The RKMT processing developed in this thesis appears to be a promising hybrid optical–electronic technique for nonlinear image processing and pattern recognition. In this regard, it is recommended that the RKMT method be investigated further for future research in various areas. In one of these areas, RKMT processing can be generalized to an angularly rank–ordered filtering (AROF) operation for which the Max and Min values are treated as the highest– and lowest–ranked values of the directional convolution outputs. One example of such an AROF operation may be demonstrated by directional smoothing [49], which reduces noise but preserves sharp boundaries in noisy imagery. This argues for further investigation into the applications of the AROF operation.

RKMT processing can be developed for detecting and enhancing striated patterns like fingerprints and airport runways, and nonlinear features like line intersections. It is possible to use a '+' shaped kernel for enhancing such striated patterns and periodic line structures (e.g., mesh structures) in a matter similar to endothelial image preprocessing. With basic RKMT processing operations, it may also be possible to enhance line intersections embedded in noisy gray–scale images. A simple case of enhancing vertices in a binary cell boundary pattern was demonstrated (Sec. 3.2.2) by two consecutive Min operations. In addition, various types of image enhancement or feature detection and enhancement operations can also be found for biomedical and industrial applications.

In the invariant pattern recognition application, numerical experiments were performed for only four kernel orientations. Increasing the number of kernel orien-

tations can improve the recognition capability. The invariant algorithm discussed can be particularly useful for determining the quasi–scale invariance for small targets. For more general applications, a more thorough investigation is needed into how well the invariant algorithm works for other objects with linear features (e.g., airplanes and industrial parts) rather than alphabetic characters.

Most challenging is an optical implementation of the RKMT processing operation. Currently, RKMT processing can be demonstrated using a hybrid incoherent spatial filtering system incorporated with a CCD camera and a digital computer. However, much greater speed can be achieved if a smart focal plane array processor with simple peak–detection electronic circuitry can be used as a Min–Max processor in the output plane. Such an optical implementation of the RKMT processing requires a physical rotation of the convolution kernel in the pupil plane. Another method for achieving such a kernel rotation can be considered if a smart spatial light modulator were to be available to electronically write the kernel at each kernel orientation. Thus, it is recommended that such a smart spatial light modulator be investigated for future work.

For cell pattern analysis in clinical treatment, further investigation is needed into how the parameters (e.g., B_p and e_{23}) obtained by optical Fourier transform methods relate with computer morphometric cell parameters. This is another subject for potential investigation. In order for these investigations to proceed, it is essential that an optical system be constructed with a real wedge–ring detector in the Fourier transform plane and a great deal of clinical data be incorporated.

Bibliography

[1] G. Rao, J. Aquavella, S. Goldberg, and S. Berk, "Pseudophakic bullous keratopathy: Relationship to preoperative corneal endothelial status," *Ophthalmol.*, vol. 91, pp. 1135–1140, 1984.

[2] M. Sawa and T. Tanishima, "The morphometry of the human corneal endothelium and follow–up of postoperative changes," *Jpn. J. Ophthalmol.*, vol. 23, pp. 337–350, 1979.

[3] J. Lester, J. McFarland, S. Bursell, R. Laing, and J. Brenner, "Automated morphometric analysis of corneal endothelial cells," *Invest. Ophthalmol. Vis. Sci.*, vol. 20(3), pp. 407–410, 1981.

[4] L. Hirst, R. Sterner, and D. Grant, "Automated analysis of wide–field specular photomicrographs," *Cornea*, vol. 3, pp. 883–887, 1984.

[5] B. R. Masters, "Characterization of corneal specular endothelial photomicrographs by their Fourier transform," in *Proc. SPIE*, vol. 938, pp. 246–252, April 1988.

[6] Y. K. Lee and W. T. Rhodes, "Nonlinear image processing by rotating kernel transformation," *Optics Letters*, vol. 15(23), pp. 1383–1385, 1990.

[7] Y. K. Lee and W. T. Rhodes, "Feature detection and enhancement by a rotating kernel min–max transformation," in *Proc. SPIE*, vol. 1297, pp. 154–159, 1990.

[8] J. G. Verly and E. Peli, "Circular harmonic analysis of PSFs corresponding to separable polar–coordinate frequency responses with emphasis on fan filtering," *IEEE Transactions on ASSP*, vol. ASSP–33, pp. 300–307, 1985.

[9] L. M. Murphy, "Linear feature detection and enhancement in noisy images via the Radon transform," *Pattern Recognition Letters*, vol. 4, pp. 279–284, 1986.

[10] Z. Zhu and Y. Kim, "Algorithm for automatic road recognition on digitized map images," *Optical Engineering*, vol. 28(9), pp. 949–954, 1989.

[11] E. Peli, "Adaptive enhancement based on a visual model," *Optical Engineering*, vol. 26(7), pp. 655–660, 1987.

[12] W. L. Anderson and R. E. Beissner, "Counting and classifying small objects by far–filed light scattering," *Applied Optics*, vol. 10(7), pp. 1503–1508, 1971.

[13] A. L. Wertheimer and W. L. Wilcock, "Light scattering measurements of particle distributions," *Applied Optics*, vol. 15(6), pp. 1616–1620, 1976.

[14] H. Stark, D. Lee, and B. W. Koo, "Counting quasicircular particles by an optical–digital method," *Applied Optics*, vol. 15(9), pp. 2246–2249, 1976.

[15] B. C. R. Ewan, "Fraunhofer plane analysis of particle field holograms," *Applied Optics*, vol. 19(8), pp. 1368–1372, 1980.

[16] G. G. Lendaris and G. L. Stanley, "Diffraction–pattern sampling for automatic pattern recognition," in *Proc. IEEE*, pp. 198–216, February 1970.

[17] N. George and H. L. Kasdan, "Diffraction pattern sampling for recognition and metrology," in *Proc. Electro–Optics Systems Design*, pp. 494–503, 1975.

[18] H. L. Kasdan, "Industrial applications of diffraction pattern sampling," *Optical Engineering*, vol. 18(5), pp. 496–503, 1979.

[19] N. George and S. G. Wang, "Neural networks applied to diffraction pattern sampling," in *Technical Digest MX3 (OSA Annual Meeting)*, October 1989.

[20] R. K. O'Toole and H. Stark, "Comparative study of optical–digital vs all–digital techniques in textural pattern recognition," *Applied Optics*, vol. 19(15), pp. 2496–2506, 1980.

[21] B. Pernick, R. E. Kopp, J. Lisa, M. Mendelsohn, H. Stone, and R. Wohlers, "Screening of cervical cytological samples using coherent optical processing," *Applied Optics*, vol. 17(1), pp. 21–33, 1978.

[22] J. R. Leger and S. H. Lee, "Signal processing using hybrid systems," in *Applications of Optical Fourier Transforms* (H. Stark, ed.), New York, NY: Academic Press, 1982.

[23] A brochure obtained from a private communication between Dr. William T. Rhodes and Dr. C. N. George at Automatic Recognition & Control Inc.

[24] C. Gorecki, "Optical/digital analyzer of Fe_2O_3, FeO substrate by Fourier techniques," *Optical Engineering*, vol. 27(6), pp. 466–470, 1988.

[25] M. S. Brown, "A multifacet holographic field lens for diffraction pattern sampling," *Optica Acta*, vol. 31(5), pp. 507–503, 1984.

[26] D. P. Casasent, S. F. Xia, J. Z. Song, and A. J. Lee, "Diffraction pattern sampling using a computer–generated hologram," *Applied Optics*, vol. 25(6), pp. 983–989, 1986.

[27] M. J. Simpson, "Diffraction pattern sampling using a holographic optical element in an imaging configuration," *Applied Optics*, vol. 26(9), pp. 1786–1791, 1987.

[28] H. Stark and B. Dimitriadis, "Minimum-bias spectral estimation with a coherent optical spectrum analyzer," *J. Optical Society of America*, vol. 65(4), pp. 425–431, 1975.

[29] H. Stark, D. Lee, and B. Dimitriadis, "Smoothing of irradiance spectra with finite-bandwidth windows, with application to particle–size analysis," *J. Optical Society of America*, vol. 65(12), pp. 1436–1442, 1975.

[30] J. K. Kauppinen, D. J. Moffatt, H. H. Mantsch, and D. G. Cameron, "Smoothing of spectral data in the Fourier domain," *Applied Optics*, vol. 21(10), pp. 1866–1872, 1982.

[31] J. Radon, "Uber die bestimmung von funktionen durch ihre integralwerte tangs gewisser mannigfaltigkeiten (on the determination of functions from their integrals along certain manifolds)," *Math. Phys. Klass.*, vol. 69, pp. 262–277, 1917.

[32] S. R. Deans, *The Radon Transform and Some of Its Applications.* New York: John Wiley, 1982.

[33] J. Goodman, *Introduction to Fourier Optics.* New York, NY: McGraw–Hill, 1968.

[34] D. P. Casasent and D. Psaltis, "Position, rotation, and scale invariant optical correlation," *Applied Optics*, vol. 15(7), pp. 1795–1799, 1976.

[35] R. C. Sherman, D. Grieser, F. Gamble, C. M. Verber, and T. Dolash, "Hybrid incoherent optical pattern recognition system," *Applied Optics*, vol. 22(22), pp. 3579–3582, 1983.

[36] Y. Hsu and H. H. Arsenault, "Pattern discrimination by multiple circular harmonic components," *Applied Optics*, vol. 23(6), pp. 841–844, 1984.

[37] R. Wu and H. Stark, "Rotation-invariant pattern recognition using a vector reference," *Applied Optics*, vol. 23(6), pp. 838–840, 1984.

[38] G. F. Schils and D. W. Sweeney, "Rotationally invariant correlation filtering," *J. Optical Society of America A*, vol. 2(9), pp. 1411–1418, 1985.

[39] G. F. Schils and D. W. Sweeney, "Rotationally invariant correlation filtering for multiple images," *J. Optical Society of America A*, vol. 3(7), pp. 902–908, 1986.

[40] G. F. Schils and D. W. Sweeney, "Iterative technique for the synthesis of distortion-invariant optical correlation filters," *Optics Letters*, vol. 12(5), pp. 307–309, 1987.

[41] J. Rosen and J. Shamir, "Circular harmonic phase filters for efficient rotation-invariant pattern recognition," *Applied Optics*, vol. 27(14), pp. 2895–2899, 1988.

[42] Y. Sheng, C. Lejeune, and H. H. Arsenault, "Frequency-domain Fourier-Mellin descriptors for invariant pattern recognition," *Optical Engineering*, vol. 27(5), pp. 354–357, 1988.

[43] D. Mendlovic, E. Marom, and N. Konforti, "Improved rotation or scale invariant matched filter," *Applied Optics*, vol. 28(18), pp. 3814–3819, 1989.

[44] P. V. C. Hough, "Method and means of recognizing complex." U.S. Patent 3,069,654, 1962.

[45] R. O. Duda and P. E. Hart, "Use of the Hough transformation to detect lines and curves in pictures," *Commun. ACM*, vol. 15(1), pp. 11–15, 1972.

[46] D. P. Casasent and S. I. Chien, "Efficient (ϕ, s) string code symbolic feature generation," *Optics Communications*, vol. 67, pp. 103–106, 1988.

[47] Y. Naor and J. Shamir, "Angular feature mapping–an optical method," *Applied Optics*, vol. 29(5), pp. 713–716, 1990.

[48] W. Frei and C. C. Chen, "Fast boundary detection: a generalization and a new algorithm," *IEEE Transactions on Computers*, vol. 26(10), pp. 988–998, 1977.

[49] A. K. Jain, *Fundamentals of Digital Image Processing.* Englewood Cliffs, NJ: Prentice–Hall Inc., 1989.

[50] D. Marr and E. Hildreth, "Theory of edge detection," in *Proc. R. Soc. Lond. B 207*, pp. 187–217, 1980.

[51] R. M. Haralick, "Digital step edges from zero crossing of second directional derivatives," *IEEE Transactions on Pattern Analysis and Machine Intelligence*, vol. PAMI–6(1), pp. 58–68, 1984.

[52] J. S. J. Lee, R. M. Haralick, and L. G. Shapiro, "Morphological edge detection," *IEEE J. Robotics and Automation*, vol. RA–3(2), pp. 142–156, 1987.

[53] D. P. Casasent and J. Chen, "Nonlinear local image preprocessing using coherent optical techniques," *Applied Optics*, vol. 22, pp. 808–814, 1983.

[54] A. K. Cherri and M. A. Karim, "Optical symbolic substitution: edge detection using Prewitt, Sobel, and Robert operators," *Applied Optics*, vol. 28(21), pp. 4644–4648, 1989.

[55] R. W. Yee, M. M. Matsuda, R. O. Schultz, and H. F. Edelhauser, "Changes in the normal corneal endothelial cellular pattern as a function of age," *Current Eye Research*, vol. 4(6), pp. 671–678, 1985.

[56] T. Charn-Ling and J. Curmi, "Changes in corneal endothelial morphology in cats as a function of age," *Current Eye Research*, vol. 7(4), pp. 387–392, 1988.

[57] B. R. Masters, Y. K. Lee, and W. T. Rhodes, "Fourier transform method for statistical evaluation of corneal endothelial morphology," in *Noninvasive Diagnostic Techniques in Ophthalmology* (B. R. Masters, ed.), pp. 122–141, New York, NY: Springer–Verlag, 1990.

[58] J. D. Gaskill, *Linear Systems, Fourier Transforms, & Optics.* New York, NY: John Wiely & Sons, 1978.

[59] D. Joyeux and S. Lowenthal, "Optical Fourier transform: what is the optimal setup?," *Applied Optics*, vol. 18(5), pp. 4368–4372, 1982.

[60] R. C. Smith and J. S. Marsh, "Diffraction patterns of simple apertures," *J. Optical Society of America.*, vol. 4(1), pp. 798–803, 1974.

[61] Private communication: information obtained at vertices of cell boundaries can be useful for statistical shape estimation.

[62] S. A. Dudani and A. L. Luk, "Locating straight–line edge segments on outdoor scenes," *Pattern Recognition*, vol. 10, pp. 145–157, 1978.

[63] Y. J. M. Pouliquen, "Fine structure of the corneal stroma," *Cornea*, vol. 3, pp. 168–177, 1985.

[64] E. Peli, T. R. Hedges(III), and B. Schwartz, "Computerized enhancement of retinal nerve fiber layer," *Acta Ophthalmol.*, vol. 64, pp. 113–122, 1986.

[65] A. F. Lehar and R. A. Gonsalves, "Locally adaptive enhancement, binarization, and segmentation of images for machine vision," in *Applications of Digital Image Processing VII* (A. G. Tescher, ed.), vol. 504, pp. 183–188, 1985.

[66] K. Y. Huang, K. S. Fu, T. H. Sheen, and S. W. Cheng, "Image processing of seismograms: (a) Hough transformation for the detection of seismic patterns; (b) thinning processing in the seismogram," *Pattern Recognition*, vol. 18, pp. 429–440, 1985.

[67] R. H. Bamberger, *The Directional Filter Bank: A Multirate Multidimensional Filter Bank for the Directional Decomposition of Images.* PhD thesis, School of Electrical Engineering, Georgia Institute of Technology, December 1990.

[68] D. B. Harris, *Design and Implementation of Rational 2-D Digital Filters.* PhD thesis, Department of Electrical Engineering and Computer Science, Massachusetts Institute of Technology, November 1979.

[69] E. Peli and J. G. Verly, "Digtal line–artifact removal," *Optical Engineering*, vol. 22(4), pp. 479–484, 1983.

[70] S. Marcelja, "Mathematical description of the responses of simple cortical cells," *J. Optical Society of America*, vol. 70, pp. 1297–1300, 1980.

[71] C. Kimme, D. Ballard, and J. Sklansky, "Finding circles by an array of accumulators," *Commun. ACM*, vol. 18, pp. 120–122, 1975.

[72] H. Wechler and J. Sklansky, "Finding the rib cage in chest radiographs," *Pattern Recognition*, vol. 9, pp. 21–30, 1977.

[73] S. Tsuji and F. Matsumoto, "Detection of ellipses by a modified Hough transfomation," *IEEE Transactions Computers*, vol. C–27, pp. 777–781, 1981.

[74] D. Ballard, "Generalizing the Hough transform to detect arbitrary shapes," *Pattern Recognition*, vol. 13, pp. 111–118, 1981.

[75] D. P. Casasent and R. Krishnapuram, "Curved object location by Hough transformations and inversions," *Pattern Recognition*, vol. 20, pp. 181–186, 1987.

[76] F. O'Gorman and M. B. Clowes, "Finding picture edges through collinearity of feature points," *IEEE Transactions on Computers.*, vol. C–25, pp. 449–456, 1976.

[77] J. Sklansky, "On the Hough technique for curve detection," *IEEE Transactions on Computers*, vol. C–27, pp. 923–926, 1978.

[78] S. R. Deans, "Hough transform from the Radon transform," *IEEE Transactions Pattern Analysis and Machine Intelligence*, vol. PAMI–2, pp. 185–190, 1981.

[79] G. Eichman and B. Z. Dong, "Coherent optical production of the Hough transform," *Applied Optics*, vol. 22(6), pp. 830–834, 1983.

[80] W. H. Steier and R. K. Shori, "Optical Hough transform," *Applied Optics*, vol. 25(16), pp. 2734–2738, 1986.

[81] P. Ambs, S. H. Lee, Q. Tian, and Y. Fainman, "Optical implementation of the Hough transform by a matrix of holograms," *Applied Optics*, vol. 25(22), pp. 4039–4045, 1986.

[82] J. Richards, P. Vermeulen, E. Barnard, and D. P. Casasent, "Parallel holographic generation of multiple Hough transform slices," *Applied Optics*, vol. 27(21), pp. 4540–4545, 1988.

[83] Y. K. Lee and W. T. Rhodes, "Scale– and rotation–invariant pattern recognition by a rotating kernel min–max transformation," in *Proc. SPIE*, vol. 1347, pp. 146–155, 1990.

[84] Y. K. Lee and W. T. Rhodes, "Edge detection and enhancement by a rotating kernel transformation," in *Technical Digest WL6 (OSA Annual Meeting)*, Optical Society of America, November 1990.

[85] W. K. Pratt, *Digital Image Processing.* New York, NY: John Wiley, 1978.

[86] I. Glaser, "Incoherent information processing," in *Progress in Optics, XXIV* (E. Wolf, ed.), North–Holland, 1987.

[87] W. T. Rhodes and A. A. Sawchuk, "Incoherent optical processing," in *Optical Information Processing* (S. H. Lee, ed.), New York, NY: Springer–Verlag, 1987.

[88] H. Battret, S. K. Case, and R. Hauck, "Incoherent optical processing," in *Applications of Optical Fourier Transforms* (H. Starkf, ed.), New York, NY: Academic Press, 1983.

[89] W.-H. Lee, "Computer–generated holograms: techniques and applications," in *Progress in Optics, XVI* (E. Wolf, ed.), North–Holland, 1978.

[90] R. H. Bamberger. (Private communication). School of Electrical Engineering, Georgia Institute of Technology (1990).

[91] I. Dinstein, A. Fong, L. Ni, and K. Wong, "Fast discrimination between homogeneous and textured regions," in *IEEE Proceedings, Seventh International Conference on Pattern Recognition*, (Montreal, Canada), pp. 361–363, July 1984.

[92] Y. Nakagawa and A. Rosenfeld, "A note on the use of local min and max operations in digital picture processing," *IEEE Transactions on Systems, Man, and Cybernetics*, vol. SMC–8(8), pp. 632–634, 1978.

[93] J. Serra, *Image Analysis and Mathematical Morphology.* New York, NY: John Wiely & Sons, 1982.

Vita

Yim–Kul Lee, the second son of Myung–Choon Lee and Nahm–Kyu Park, was born in Seoul, Korea on March 8, 1958. He was engaged to Jong–Sook Park on April 19, 1984 and married to her on February 19, 1985.

He graduated from the Department of Electronic Engineering, Seoul Engineering High School, Seoul, Korea in 1977. In 1982, he received a BSEE degree with High Honors (within top 5 %) from Hanyang University, Seoul, Korea. He started his graduate program in January 1986 and received the MSEE degree from the Georgia Institute of Technology in 1987, at which time he entered the doctoral program. He has defended his Ph.D. on December 18, 1990.

From 1979 to 1982, Mr. Lee held a scholarship from the Hanyang University regarding his academic achievement. In August, 1980, he was selected as the student representative of Hanyang University to visit Japan as one of the student activities between Korea and Japan, supported by the Department of Education, Korea. From 1986 to 1987, from January to March in 1988, and from 1989 to 1991, he was a Graduate Research Assistant in the School of Electrical Engineering, Georgia Institute of Technology. From September to December in 1988 he was a Graduate Research Assistant in the Department of Ophthalmology, Emory University in Atlanta, Georgia.

Before he entered the area of optical image/information processing, he has worked with Prof. Richard P. Kenan in the area of electro–optics from 1987 to 1988, leading to a journal publication.

He is a member of the institute of Electrical and Electronic Engineers, the Optical Society of America, and the Society of Photo–Optical Instrumentation Engieers.